



Variations spatio-temporelles dans l'exhumation Cénozoïque de la chaîne Pyrénéo-catabrienne : couplages entre tectonique et processus de surface

Charlotte Fillon

► To cite this version:

Charlotte Fillon. Variations spatio-temporelles dans l'exhumation Cénozoïque de la chaîne Pyrénéo-catabrienne : couplages entre tectonique et processus de surface. Sciences de la Terre. Université de Grenoble; Universitetet i Bergen, 2012. Français. NNT : 2012GRENU002 . tel-00683929

HAL Id: tel-00683929

<https://theses.hal.science/tel-00683929>

Submitted on 30 Mar 2012

HAL is a multi-disciplinary open access archive for the deposit and dissemination of scientific research documents, whether they are published or not. The documents may come from teaching and research institutions in France or abroad, or from public or private research centers.

L'archive ouverte pluridisciplinaire **HAL**, est destinée au dépôt et à la diffusion de documents scientifiques de niveau recherche, publiés ou non, émanant des établissements d'enseignement et de recherche français ou étrangers, des laboratoires publics ou privés.

UNIVERSITÉ DE GRENOBLE UNIVERSITY OF BERGEN

THÈSE

Pour obtenir le grade de

DOCTEUR DE L'UNIVERSITÉ DE GRENOBLE

Spécialité : **Sciences de la Terre, de l'Univers, et de l'Environnement**

Arrêté ministériel : 7 août 2006

THESIS

Submitted for the degree of

DOCTOR OF PHILOSOPHY (Ph.D.)

Charlotte FILLON

Thèse dirigée par **Peter Van der Beek**
et codirigée par **Ritske Huismans**

Préparée au sein de l'**Institut des Sciences de la Terre de Grenoble (ISTerre)**
dans l'**École Doctorale Terre Univers Environnement**

Spatial and temporal variations in Cenozoic exhumation
of the Pyrenean-Cantabrian mountain belt :
coupling between tectonics and surface processes

Variations spatio-temporelles dans l'exhumation
Cénozoïque de la chaîne Pyreneo-cantabrique :
couplages entre tectonique et processus de surface

Thèse soutenue publiquement le 24 Janvier 2012

devant le jury composé de:

M. Sean Willett

Rapporteur

M. Hugh Sinclair

Rapporteur

Mme Patience Cowie

Examinatrice

M. Jacques Malavieille

Examineur

M. Daniel Garcia-Castellanos

Examineur

M. David Pedreira

Examineur



Remerciements

Je n'en serai certainement pas arrivée là sans la compagnie, le soutien et l'aide de toutes ces personnes,

un GRAND MERCI / a BIG THANK YOU/ MUCHAS GRACIAS à/to/a :

Peter (super grand merci même), pour m'avoir appris à chercher (et à trouver parfois !), encadré en me laissant mon indépendance (la méthode Peter : toujours disponible mais jamais sur ton dos !), et surtout m'avoir donné envie de continuer. Ne change rien, c'est trop bien de travailler avec toi.

Ritske, for welcoming me in Bergen, introducing me to numerical modeling, learning me to be critical, to work with method ("one parameter at a time") and to always double-check my results!

The Jury: Patience Cowie, Sean Willett, Hugh Sinclair, Jacques Malavieille, Daniel Garcia-Castellanos and David Pedreira for their review of my work and for being here to my defense. Particularly, I thank Sean and Hugh for reading my manuscript during their Christmas holidays!

The Pyrtec team: Ritske, Peter, Josep Anton, David, Roy, Ronald, Suzon, Zoltan, Irene, Martin and Ivar. I will really miss the meetings and field trips, and above all, the discussions about the Cantabrian Mountains! Muchas gracias David (once again) for introducing me to the Cantabrians, coming with me on the field (even under the snow) and for your nice (and singing sometimes ;) company.

Merci à tous ceux qui m'ont particulièrement aidé dans mes travaux de recherche à ISTerre et ailleurs :

Francis et François, qui se sont occupé d'une grande partie de la préparation de mes échantillons et qui m'on fait gagner un temps fou, leur travail est précieux, surtout quand on ramène dans les 300 kg de cailloux ! Merci aussi à Martine de m'avoir accueilli dans son labo pour mes petites expériences de dissolution de carbonates. Même si ça n'a rien donné au final, l'expérience fut enrichissante et surtout très sympathique.

Matthias, qui m'a accueilli dans le labo de thermochronologie, m'a appris à reconnaître les minéraux, préparer les échantillons, compter les traces et comprendre les données en général, et tout ça avec sa bonne humeur et sa gentillesse habituelle. Heureusement que tu étais là pour « aligner » mes échantillons quand j'avais envie de les jeter par la fenêtre ! Au passage, je remercie Vincent (qui ne lira probablement jamais ces lignes) de m'avoir appris et beaucoup aidé pour la préparation et le comptage, c'est un travail très fastidieux...

Pierre (mon voisin Totoro), merci de ta patience quand j'ai commencé à bidouiller Pecube, et à m'intéresser à l'Helium. Tu m'as toujours accueilli avec le sourire, même quand je venais te poser des questions 10 fois par jour ! Au passage, merci au bureau 349, à Chichi pour la thermochro et à Romain (de l'autre côté du mur) pour l'ambiance !

Jean, pour m'avoir aidé avec Pecube, et permis d'utiliser tes ordi. Merci aussi d'être toujours là pour m'expliquer, ou plutôt me raconter les subtilités de la modélisation numérique, en transformant, comme ça en parlant, les phrases en équations !

Cécile, une autre exilée parisienne, pour m'avoir initié à l'Helium, aux joies du picking (y a une inclusion, là !), et surtout m'avoir permis d'aller un peu plus loin dans la compréhension et l'interprétation des âges He. J'ai adoré décortiquer avec toi ces résultats que d'autres auraient laissé tomber.

Julien, pour m'avoir accompagné sur le terrain (et dans les boutiques) !

Enfin, merci à Xavier de m'avoir initié aux joies et Pecube et de Linux !

Cette thèse a aussi été l'occasion de rencontrer une multitude de personnes et de personnages, et de me faire des nouveaux amis ; ils ont aussi contribué à cette thèse, et je suis persuadée que je n'aurai pas pu garder ma « bonne humeur » (comme dit Peter) sans les petites blagues de couloir, les soirées, les gâteaux du jeudi (ça c'est pour bergen), les pauses cafés, etc etc..

Je vais essayer de n'oublier personne, si j'ai oublié quelqu'un, vous connaissez mon mail et/ou mon numéro de téléphone, ça fera une occasion de papoter...

Priorité à la capitale (hihi), merci à Laure, ma collègue de Master, et mon chauffeur préféré, qui m'a accompagnée en Espagne pour aller taper du caillou et explorer la Cantabrie et les Asturies. Merci aussi à 2 autres parisiens, Seb et Céline qui m'ont aidé à trouver un appart et à m'installer à Grenoble.

Du côté grenoblois, je remercie particulièrement Violaine et Morgane, mes 2 généreuses-rigolotes-sympathiques co-bureaux, et qui ont fait de cet endroit le meilleur bureau du 3^{ème}, en tout cas, le seul où on peut toujours trouver des petits gâteaux fait maison, du café chaud, une ambiance agréable, bref, un vrai bureau de fille.

Merci à ma ptite ion-ion, reine des colonnes et des soirées labo, partenaire de fêtes, de lendemain de fête aussi, de week-end, d'apéro LaiTUE, et surtout de toutes ces pauses café Promis, je l'aurai mon permis, et tu auras un accès illimité à mon bolide !

Une pensée particulière aussi pour ceux avec qui j'ai partagé ces années de thèse, Yohann et Nico, ou comment rester ado en étant bac+8 (et c'est un compliment) !!!

Une bise aussi à tous ceux qui m'ont fait aimer vivre à Grenoble, les potes du labo, jeunes et moins jeunes, permanents et provisoires, en vrac : TSL (papa tibo), Manu, Emilie, Pierre (le prochain ?), Abir (princesse Leila), Sébastien, Maria (et ses araignées du mercredi), Carole, Marc (super-kiwi !!), Alex

(prouiiiiit), Jérôme (l'idole des jeunes), Marie, Catherine, Nick (on va à la piscine ?), Clément, Shasa (Hihihi), Vivi (on change de crèmerie ?), Stéphane, et tous les autres que je pourrai oublier...

A kiss also to my friends from Bergen: Katharina, Vaneeda (Ca y est, c'est fini!!!!), Louise, Kosuke (you should stop smoking...), Matteo, Sebastien, Erling, Fabian, Ingjerd and the Cake Club family. Et surtout à mes deux compagnons (de galère), Suzon (on va au spa ?) et Cédric (le roi du café). Heureusement que vous étiez là pour supporter ces longues nuits d'hiver norvégiennes, et pour mettre un peu d'ambiance dans les couloirs !

Enfin, j'en arrive aux personnes les plus importantes pour moi. Merci Maman et Papa, Frangin et Tata, Françoise et François, Geneviève et Gérard, Céline et Christophe et merci à mon Frédéric. Merci à tous de m'avoir soutenue, aidé, et supporté parfois.

Merci à Papa et Françoise pour m'avoir conseillé un jour d'arrêter de vouloir avoir la tête dans les nuages et de continuer à étudier la Terre.

Merci Dada pour le coup de main Photoshop (la couverture, c'est lui !).

Merci Maman pour tout (la liste serai trop longue) et pour le pot.

Merci aux Mouthereau/Simon pour votre soutien.

Merci Frédéric, de m'avoir fait aimer les montagnes, le terrain, la géol, de m'avoir aiguillé (l'air de rien) vers Peter, de m'avoir soutenue ces trois ans, supportée pendant la fin de la rédaction et surtout la préparation de la soutenance, tu as été parfait.

Abstract

The Cenozoic evolution of the Pyrenean-Cantabrian mountain belt was driven by both internal and external processes, such as tectonics, erosion and deposition. This alpine belt is made up by the Pyrenees and the Cantabrian Mountains, and is characterized by significant lateral variations in total shortening, structural styles and topography. This thesis aims to better constrain the controls on exhumation and topography development during syn- to post-orogenic times, from the Eocene to the Pliocene, by focusing on two characteristic parts of the belt: the Southern Central Pyrenees and the Central Cantabrian Mountains. To this purpose, a multi-disciplinary approach is developed, combining low-temperature thermochronology with different numerical modeling tools. To better understand lateral variations in exhumation of the belt, a new low-temperature thermochronology dataset is presented for the Cantabrian domain. The first part of this thesis presents new apatite fission-track data and (U-Th)/He analysis on zircons, constraining the timing and amount of exhumation along the central Cantabrian cross-section. In particular, the Eocene to Oligocene ages obtained from the different thermochronometers allow us to infer a more important amount of burial and, consequently, a thicker Mesozoic sedimentary section than previously considered, thereby also refining the structural style of the section at the upper crustal scale.

The extensive thermochronological dataset existing in the central Pyrenees is then used to reconstruct the late-stage evolution of the South Central Axial Zone by thermo-kinematic inverse modeling. The model predicts rapid exhumation of the area during late Eocene (late syn-orogenic) times, followed by a post-orogenic evolution that is strongly controlled by base-level changes. As a consequence of the establishment of endorheic conditions in the adjacent Ebro foreland basin, together with the strong erosion of the Axial Zone, the southern foreland area was infilled by an important amount of erosional deposits in late Eocene to early Oligocene times. The models allow us to constrain the level of infilling at ~2.6 km and to date the excavation of these sediments at ~10 Ma, following opening of the Ebro basin toward the Mediterranean Sea. The thickness of sediments draping the foreland fold-and thrust belt was verified using fission-track analysis and (U-Th)/He measurements on apatites from foreland sediments. Thermal modeling of the data provides an estimate of 2 to 3 km of sediments on top of the foreland and confirms its incision in Late Miocene times. The effect of syn-orogenic deposition on the building and late evolution of the southern Pyrenean fold-and-thrust belt has been modeled in the last chapter of this thesis using a 2D thermo-mechanical numerical modeling approach. The models highlight the potential effect of syn-tectonic sedimentation on thrust kinematics at several stages of wedge building. Our modeling also shows that the addition of an Oligocene sediment blanket perturbs the thrusting sequence by stabilizing the central part of the external wedge and enhancing both frontal and internal accretion; a pattern that reproduces the observed deformation in the Southern Central Pyrenees.

Résumé

L'évolution Cénozoïque de la chaîne Pyreneo-Cantabrienne est contrôlée par des processus internes et externes, comme la tectonique et les processus d'érosion et de sédimentation. Les effets de ces différents mécanismes font actuellement l'objet de nombreuses études, en particulier dans les systèmes orogéniques, pour comprendre les contrôles de la tectonique et du climat (via les processus de surface) pendant les différentes phases d'exhumation d'une chaîne de montagne. La chaîne Pyrénéo-Cantabrienne est une chaîne alpine se composant des Pyrénées à l'Est et des Montagnes Cantabriennes à l'Ouest, et qui présente d'importantes variations latérales en termes de raccourcissement total, de style structural et de topographie. Cette thèse a donc pour but de mieux contraindre ces variations le long de la chaîne depuis l'Eocène au Pliocène, c'est-à-dire pendant et après l'inversion lithosphérique Cénozoïque, et en se concentrant particulièrement sur deux zones caractéristiques : le Sud des Pyrénées centrales et le centre des Montagnes cantabriennes. L'étude de ces deux zones permet également d'identifier et d'analyser les interactions entre la tectonique et les processus de surface au syn- et post-orogénique, et notamment les couplages entre la chaîne et son avant-pays. Pour ce faire, une approche multi-disciplinaire combinant la thermochronologie basse température avec différents modèles numériques en 2 et 3 dimensions, a été adoptée.

En effet, la thermochronologie basse température est un outil fréquemment utilisé pour étudier l'exhumation d'une zone orogénique ; en combinant différents thermochronomètres, on peut déduire des périodes d'exhumations ainsi que des vitesses de soulèvement, renseignant ainsi directement sur les phases d'exhumations d'une zone. Contrairement aux Pyrénées, la chaîne cantabrienne centrale est une région où très peu de datations thermochronologiques ont été effectuées. Pour illustrer les variations latérales d'exhumation dans la chaîne, de nouveaux âges thermochronologiques effectués dans les Cantabrides centrales sont présentés dans une première partie de cette thèse. Ces nouvelles données de traces de fission sur apatites et d'analyses (U-Th)/He sur zircons donnent ainsi une bonne estimation de la quantité d'exhumation le long d'une coupe Nord-Sud, indépendamment contrainte par sismique réflexion. En particulier, les âges Eocène ((U-Th)/He sur zircons) à Oligocène (traces de fission sur apatite) obtenus nous ont permis de donner un calendrier précis de la déformation alpine dans cette zone, concordant avec les observations géologiques en mer, ainsi qu'une quantité d'enfouissement (et donc une épaisseur de sédiments ante-orogéniques) plus importante que ce qui avait été proposé auparavant. De plus, ces nouvelles données nous permettent d'apporter des contraintes supplémentaires afin de raffiner la coupe structurale à l'échelle de la croûte supérieure.

Les chapitres suivants se concentrent sur l'évolution syn- à post-orogénique des Pyrénées centrales. Dans une première partie, l'importante base de données thermochronologiques dans le centre-Sud de la Zone Axiale est utilisée pour reconstruire l'évolution tardive du Sud de la chaîne et de son avant-pays, jusqu'au bassin de l'Ebre. Des données (U-Th)/He sur apatite et trace de

fission sur apatites et zircons sont incorporées au modèle thermo-cinématique *Pecube*, qui, couplé à une méthode d'inversion (*Neighbourhood Algorithm*) prédit des valeurs de vitesses d'exhumation pour différentes périodes de temps ainsi que les quantités de sédiments déposés dans les vallées nécessaires pour reproduire avec la meilleure probabilité les données thermochronométriques. Ainsi, le modèle prédit une exhumation rapide à l'Eocène supérieur, puis une évolution post-orogénique contrôlée par les variations du niveau de base du bassin de l'Ebre au Sud. En effet, l'endorhéisme du bassin conjugué à la forte érosion de la Zone Axiale ont favorisé le remplissage du flanc Sud de la Zone Axiale depuis l'Eocène supérieur par une quantité importante de sédiments, produits de l'érosion des zones internes. Les modèles nous ont également permis de dater l'incision de ces sédiments à ~10 Ma, date que nous interprétons comme correspondant à l'ouverture du bassin de l'Ebre vers la Méditerranée.

Dans le chapitre suivant, une extension des conclusions du chapitre précédent à l'avant-pays Sud-Pyrénéen est proposée par la datation thermochronologique en plusieurs sites situés dans les bassins de Tresp-Graus et d'Ager. L'épaisseur des sédiments ayant recouvert la chaîne plissée d'avant-pays Sud-Pyrénéen est donc précisément contrainte par des analyses trace de fission et des mesures (U-Th)/He sur des apatites prélevées dans les grès du Crétacé supérieur. Ce chapitre s'attache également à démontrer que des grains détritiques avec des âges (U-Th)/He faiblement reproductibles peuvent provenir d'une même histoire thermique, en prenant en compte deux facteurs prépondérants : la valeur du eU (concentration effective d'uranium) et l'histoire anté-déposition du grain. Ainsi, une fois ces facteurs identifiés, la modélisation thermique de ces données nous permet de trouver par inversion un même chemin temps-température pour les différents échantillons. Les résultats donnent en effet une estimation de 2 à 3 km de sédiments recouvrant le bassin Sud-Pyrénéen, et confirment également le signal d'une incision de ces sédiments au Miocène supérieur.

Enfin, après avoir quantifié dans la sédimentation syn-orogénique dans le temps, le dernier chapitre se concentre sur l'effet de cette sédimentation sur la construction puis l'évolution tardive de la chaîne plissée d'avant-pays. Un modèle dynamique en 2 dimensions a été utilisé pour reconstruire les différentes étapes de la construction de la chaîne, de façon à reproduire la géométrie et la cinématique des chevauchements de l'avant-pays sud-pyrénéen. Les résultats mettent en lumière les contrôles potentiels de la sédimentation syn-tectonique à différentes étapes de la croissance du prisme, sur la croissance et la cinématique des chevauchements. En période de construction de la chaîne, une sédimentation syn-tectonique même modérée contrôle au premier ordre la longueur des unités chevauchantes et la largeur du prisme, tout comme la flexure de lithosphère. L'ajout d'une sédimentation tardi-orogénique importante perturbe la séquence de déformation en stabilisant la partie centrale du prisme externe et en favorisant l'accrétion interne et frontale. Ces observations sont d'ailleurs en accord avec la séquence de déformation observée dans les Pyrénées centrales.

Pour conclure, l'approche combinant thermochronologie et modélisation numérique m'a permis de préciser l'évolution Cénozoïque de la chaîne Pyrénéo-Cantabrienne. Les nouvelles données provenant des Cantabrides centrales démontrent les variations latérales d'exhumation de la chaîne, avec des âges d'exhumation plus récents d'Est en Ouest. En effet, pendant que les Pyrénées subissent un pic d'exhumation rapide à l'Eocène supérieur, l'exhumation alpine commence dans les Cantabrides centrales. Ensuite, alors que la tectonique apparaît comme le mécanisme principal d'exhumation des Cantabrides à l'Oligocène, l'évolution tardi-orogénique des Pyrénées centraux est fortement influencée par la sédimentation syn-orogénique, puis par les variations du niveau de base du bassin de l'Ebre jusqu'au Miocène supérieur.

Table of contents

| | |
|--|-----------|
| Part I- Introduction and Methodology | 10 |
| Chapter I-1 Introduction | 12 |
| I-1.1 Collisional orogeny | 12 |
| I-1.1a Wedge development..... | 12 |
| I-1.1b Doubly-vergent wedges | 14 |
| I-1.1c Foreland basin systems | 15 |
| I-1.1d Feedback between tectonics and surface processes..... | 17 |
| I-1.2 The Pyrenean-Cantabrian mountain belt | 19 |
| I-1.2a General overview | 19 |
| I-1.2b Variscan orogeny | 21 |
| I-1.2c Mesozoic kinematics..... | 21 |
| I-1.2d Cenozoic contractional deformation..... | 23 |
| I-1.2e Spatial exhumation patterns | 25 |
| I-1.2f The Duero and Ebro basins | 29 |
| I-1.2g Cenozoic climatic evolution | 33 |
| I-1.3 Motivations and outline of the manuscript | 35 |
| Chapter I-2 Methodology..... | 38 |
| I-2.1 Introduction..... | 38 |
| I-2.2 Low-temperature Thermochronology | 39 |
| I-2.2a (U-Th)/He thermochronometry | 39 |
| I-2.2b Apatite (U-Th)/He thermochronometry | 40 |
| I-2.2c Zircon (U-Th)/He analysis | 40 |
| I-2.2d Apatite fission-track thermochronology | 41 |
| I-2.3 Numerical modeling | 44 |
| I-2.3a 3-D Thermo-kinematic modeling..... | 44 |
| I-2.3b 2D thermo-mechanical modeling..... | 47 |
| Part II- Alpine exhumation of the Cantabrian Mountains..... | 52 |
| II.1 Introduction..... | 54 |
| II.2 Geological background | 55 |
| II.2-1 Structural inheritance | 55 |

| | |
|---|----|
| II.2-2 Alpine deformation in the Central Cantabrians..... | 57 |
| II.2-3 Evolution of the Duero foreland basin | 58 |
| II.3 Methodology..... | 58 |
| II.3-1 Sampling sites..... | 58 |
| II.3-2 Apatite Fission-Track dating | 59 |
| II.3-3 (U-Th)/He analyses on zircons..... | 62 |
| II.4 Results..... | 62 |
| II.5 Implications | 67 |
| II.6 Unsuccessful apatite He analyses | 70 |
| II.7 Conclusions..... | 74 |

Part III- Cenozoic evolution of the South-Central Pyrenees: thermochronology and thermo-kinematic modeling..... 76

Chapter III-1 Post-orogenic Evolution of the Southern Pyrenees: constraints from Inverse Thermo-Kinematic Modeling of Low-Temperature Thermochronology Data 78

| | |
|--|-----|
| III-1.1 Abstract | 78 |
| III-1.2 Introduction..... | 79 |
| III-1.3 Geological setting..... | 80 |
| III-1.3a Structure and Geodynamic Evolution of the Pyrenees..... | 80 |
| III-1.3b Ebro basin drainage history..... | 83 |
| III-1.3c Thermochronological data and exhumation of the central Pyrenees | 85 |
| III-1.4 Numerical modeling..... | 86 |
| III-1.4a Model set up..... | 86 |
| III-1.4b Pecube inversions..... | 88 |
| III-1.4c Parameter space..... | 89 |
| III-1.5 Results | 91 |
| III-1.5a Exhumation history | 92 |
| III-1.5b Topographic evolution | 92 |
| III-1.5c Comparison with observed ages..... | 97 |
| III-1.6 Discussion | 98 |
| III-1.6a Limitations of the model | 98 |
| III-1.6b Neogene acceleration in exhumation rates? | 99 |
| III-1.6c Age and thickness of conglomerate deposits | 100 |
| III-1.6d Timing of and controls on post-orogenic incision | 103 |
| III-1.7 Conclusions | 103 |

| | |
|---|------------|
| Chapter III-2 Quantifying the timing and extent of post-orogenic sedimentation in the southern Pyrenean foreland | 106 |
| III-2.1 Introduction | 106 |
| III-2.2 Tectono-sedimentary evolution..... | 107 |
| III-2.3 Pre-depositional history | 109 |
| III-2.4 Low-temperature thermochronology | 111 |
| III-2.4a Apatite Fission-Track (AFT) thermochronology | 111 |
| III-2.4b Apatite (U-Th)/He analysis | 111 |
| III-2.5 Results | 112 |
| III-2.5a Data | 112 |
| III-2.5b Thermal modeling | 116 |
| III-2.5c Inferred thermal histories | 117 |
| III-2.5d Eocene additional constraint | 119 |
| III-2.6 Discussion | 121 |
| III-2.6a Exhumation scenario | 121 |
| III-2.6b Sedimentary extent..... | 121 |
| III-2.6c Sensitivity to eU variations | 122 |
| III-2.6d Influence of the pre-depositional history | 122 |
| III-2.7 Conclusions | 126 |
| Part IV- 2-D Modeling of the Southern Pyrenees..... | 128 |
| Chapter IV-1 Syn-tectonic sedimentation effects on the growth of fold-and-thrust belts..... | 130 |
| IV-1.1 Abstract..... | 130 |
| IV-1.2 Introduction..... | 131 |
| IV-1.3 Model set up..... | 131 |
| IV-1.4 Model Results | 133 |
| IV-1.5 Discussion..... | 136 |
| IV-1.6 Comparison to natural systems | 137 |
| IV-1.7 Conclusions..... | 138 |
| IV-1.8 Supplementary Material..... | 139 |
| Supplementary models | 140 |
| Chapter IV-2 Influence of surface processes on the late-stage evolution of the southern Pyrenees..... | 146 |
| IV-2.1 introduction | 146 |
| IV-2.2 Geological setting | 147 |

| | |
|--|----------------|
| IV-2.2a General context | 147 |
| IV-2.2b South central Pyrenean thrusting sequence..... | 150 |
| IV-2.3 Model description | 151 |
| IV-2.3a Model geometry and Materials | 152 |
| IV-2.3b Boundary conditions | 153 |
| IV-2.3c Surface processes | 154 |
| IV-2.4 Results..... | 154 |
| IV-2.4a Base model (1) – no secondary sedimentation..... | 155 |
| IV-2.4b Models including Secondary sedimentation | 158 |
| Low elevation, short extent (model 2)..... | 158 |
| Low elevation, moderate extent (model 3)..... | 159 |
| Low elevation, long extent (model 4) | 162 |
| High elevation, moderate extent (model 5) | 162 |
| IV-2.5 Interpretations and discussion..... | 165 |
| IV-2.5a Effects of secondary sedimentation on the thrusting sequence..... | 165 |
| IV-2.5b Comparison to the Pyrenees..... | 167 |
| IV-2.5c Climatic triggering of the erosional pulse? Preliminary results..... | 168 |
| IV-2.6 Conclusions..... | 171 |
| Additional runs | 172 |
| Part V - Synthesis and Outlook..... | 180 |
| References | 186 |

Part I- Introduction and Methodology

The aim of this thesis is to study the lateral and temporal variations of exhumation patterns of the Pyrenean-Cantabrian mountain belt, and the links between the orogenic growth and the foreland basins evolution. In this thesis, I present a comparative study between two representative parts of the belt: the Central Pyrenees (to the east) and the central Cantabrian Mountains (to the west). In the Cantabrian domain, very few low-temperature thermochronology data are available and we will thus bring more constraints by dating more precisely the Alpine exhumation (Part II).

Then, the Parts III and IV will be focused on the Central Pyrenees, where I will present new low-temperature thermochronology and different type of modeling, evidences for the important feedbacks between the orogen and its adjacent foreland basin. We will in particular investigate the timing and amount of syn-tectonic sedimentation deposited on the southern foreland and study its implications. The notions developed in each chapter and the general geodynamical history of the Pyrenean-Cantabrian mountain belt will first be detailed in this introduction.

Chapter I-1 Introduction

I-1.1 Collisional orogeny

Plate convergence and ensuing continental collision is accompanied by important thickening of the lithosphere by folding and thrusting. The Critical Coulomb wedge model (Chapple 1978; Davis et al. 1983; Dahlen 1984; Dahlen et al. 1984) has proved very successful in explaining many features of the upper and outer brittlely deforming parts of collisional orogens. To set the stage for my study, I will start by detailing the basics of the critical wedge model and its application to doubly-vergent-wedges, as well as the associated foreland systems. I will then review the possible interactions between surface processes and tectonics in orogenic settings, and focus in particular on the potential effects of base level change on a mountain belt.

I-1.1a Wedge development

Many collisional orogen develop an overall wedge shape during their evolution. In particular, the expression of wedge growth is well imaged by the propagation of the foreland fold-and-thrust belt, the most external part of an orogen. The understanding of the process of orogenic wedge propagation has its roots in work developed in the 1970's and 1980's. Development of an orogenic prism as a wedge has been first hypothesized by Elliott (1976), for whom the main factor controlling the gravitational forces acting on a thrust belt is the regional surface slope. Chapple (1978) then presented an analytical model for wedge development based on the fundamental assumptions that (1) both the foreland and the fold-and thrust belt are wedge-shaped, thinning toward the foreland; (2) the whole wedge is thickened, and most of shortening concentrates at its back; and (3) a very weak basal layer delimits the domain where deformation is concentrated and shortening occurs. He also suggested that most of the natural thin-skinned thrust belts could not be reproduced by the conceptual model without this very weak layer at the base and horizontal parallel compression.

In this framework, the first formulation of the critical behavior for wedge development was proposed by Davis et al. (1983). They described the prism evolution as a function of a critical taper: the wedge deforms until it reaches a steady state and then slides stably. Deformation of the rocks is assumed to follow a Coulomb criterion for failure, which linearly links the normal and shear stresses. Two factors act against the failure of a material: the cohesion and the internal friction. The combination of these two factors defines a failure envelope as:

$$\tau = C_0 + \mu(\sigma_n - P_f) \quad (1)$$

With τ , the shear stress; C_0 , the Cohesion; μ , the coefficient of internal friction, such that $\mu = \tan \phi$ (ϕ is the internal friction angle); σ_n , the normal stress; and P_f , the fluid pressure.

Throughout the wedge, three main forces act on a unit segment: the gravitational forces ($\rho g H \beta$), the frictional resistance to sliding along the basal décollement (τ_b) and the normal stress (σ_x), as represented in Figure I - 1.

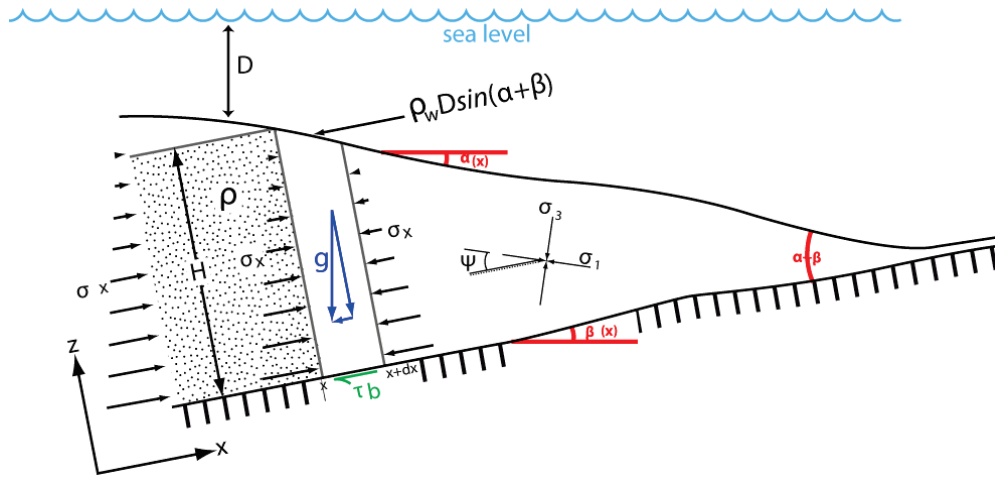


Figure I - 1. Schematic representation of the forces acting on a wedge, under a compressional regime. Modified from Davis et al. (1983).

Using a small-angle approximation and in the absence of pore fluid, the equilibrium state in a wedge can be formulated as follows (Davis et al. 1983):

$$\rho g H \beta + \tau_b + \frac{d}{dx} \int_0^H \sigma_x dz = 0 \quad (2)$$

From the equilibrium of forces, the solution for the taper angle definition for a dry, frictional and cohesionless material has been written as (Dahlen 1990):

$$\alpha + \beta = \frac{(1 - \sin \phi)}{(1 + \sin \phi)} (\beta + \tan \phi_b) \quad (3)$$

With α , the topographic slope; β , the basal slope; ϕ , the internal friction angle of the wedge material and ϕ_b , the basal friction angle. Therefore, the critical taper ($\alpha + \beta$), at which the wedge is

on the verge of failure is only controlled by the topographic and basal slopes, and the rheology of the materials. A combination of α and β defines different domains for the critical behavior (Figure I – 2). The critical envelope (blue curve in Figure I – 2) bounds the different domains and represents the combination of the taper values for which the wedge is critical. For these values, sliding and so wedge propagation occurs. When the values of α and β are located in the stable domain, there is no Coulomb failure because of a low stress state, and so the wedge can deform by sliding without any internal deformation. The subcritical domain represents the values for which the taper is less than the critical value. A wedge located in that domain will increase its taper until attaining the critical state. For reference, most of the fold-and-thrust belts have α value between 10° and -10° and β between 0° and 20° .

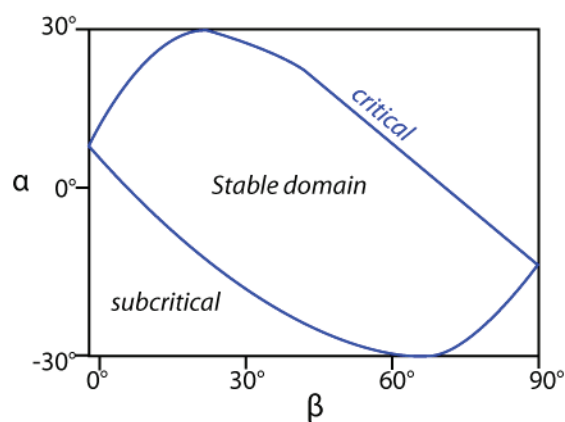


Figure I - 2. Stability domains defined by the values of the topographic slope (α) and the basal slope (β). Modified after Willett (1992).

I-1.1b Doubly-vergent wedges

A strong assumption of the critically tapered models is that they have a rigid backstop, which forces the deformation to propagate in only one direction. In natural settings, an orogenic wedge is built from the subduction and the collision of two plates. Deformation is therefore distributed over the whole system. The first numerical modeling of a doubly-vergent wedge was published by Willett et al. (1993). They modeled, in a 2-D plane, the underthrusting of one plate below another, at a meeting point called S (or singularity) point. The subduction and the deformation from this S-point thus lead to the creation of a doubly vergent wedge, with a pro-wedge on the side of the subducting plate and a retro-wedge on the side of the overriding plate (Figure I-3).

The general evolution of such a doubly-vergent system can be divided into three stages, as shown in Figure I - 3. First (stage 1), shear zones rooted at the singularity point develop at 45° , in agreement with the plastic Coulomb rheology used for this modeling, and accommodate the deformation in a triangular-shaped zone bounded by two major thrusts. Then (stage 2) deformation propagates toward the side of the subduction, defining the pro-wedge. Finally (stage 3), the retro-wedge area deforms and the retro-front propagates toward the external part.

We will see in the following that the evolution of a doubly-vergent wedge will be strongly dependent of climatic conditions through erosion. Moreover, we will show in section I.1.2 that this

evolution can also be perturbed by the inherited (pre-orogenic) structure of the margin, as is the case in the Pyrenees.

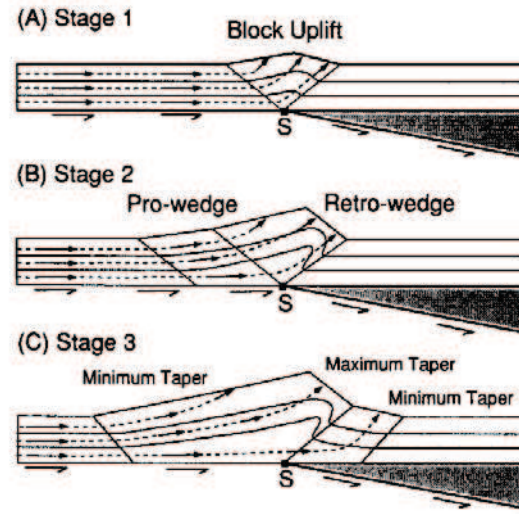


Figure I - 3. First numerical model of a doubly-vergent wedge by Willett et al. (1993). Stages 1,2 and 3 represent the main steps of wedge development as detailed in the text.

I-1.1c Foreland basin systems

Synchronous to the wedge development, crustal thickening leads to increase the load on the underlying lithosphere. Thus the lithosphere is deflected and creates a flexural depression (foreland basin) that is deepest at the termination of the orogenic wedge (Figure I - 4). The shape of the basin is directly controlled by the flexural parameters of the elastic lithosphere. One of the most important of them is the flexural rigidity (D), representing to what degree the plate can bend (Watts 2001):

$$D = \frac{ET_e^3}{12(1-\nu^2)} \quad (4)$$

With D the flexural rigidity in Nm; T_e the equivalent elastic thickness of the lithosphere (km); E Young's modulus ($\sim 10^{10}$ Pa) and ν , the Poisson (~ 0.5) are the elastic parameters.

The equivalent elastic thickness of a lithospheric plate (T_e) represents the portion of the plate that is not plastically or viscously deformed, and is still elastic. This is a main parameter controlling the shape of the foreland basin (Figure I - 4). For instance, if T_e is very high, the rigidity will be strong and so the plate will deflect with a large wavelength. The foreland basin will consequently be wide and shallow, as in the Appalachians, where $T_e \sim 100$ km (Watts 2001). Conversely, a plate with a thin elastic thickness will experience a strong deflection under the loading and so will create a deep and narrow foreland basin, as in the southern Pyrenees, where the T_e of the Iberian plate is

~20 km under the Ebro basin (Zoetemeijer et al. 1990a). Lithospheric flexure thus creates the space for the foreland basin system (Figure I - 5).

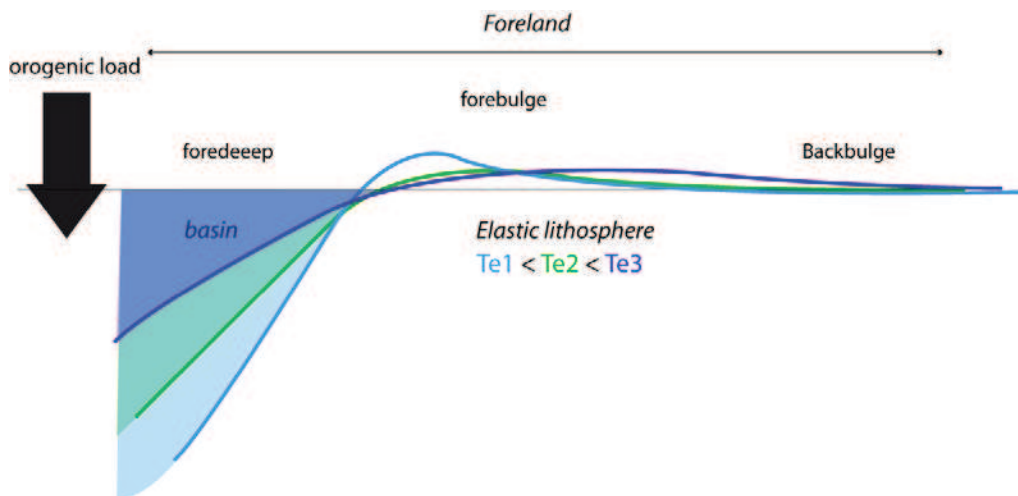


Figure I - 4. Effect of the orogenic load on an elastic lithosphere . The plate is deflected towards the belt defining a depresional area (basin).

The hinterland of an orogenic wedge is the place where erosion dominates through fluvial or glacial processes and the products of this erosion are deposited in the adjacent foreland basin. Several zones of deposition have been defined in a foreland basin system (Figure I - 5) called wedge-top, foredeep, forebulge and back-bulge depozones according to the classification of DeCelles and Giles (1996) . The three more external zones comprise areas where sediments are deposited without being involved in the orogenic deformation; the geometry and thickness of the different zones is mainly constrained by the flexural profile.

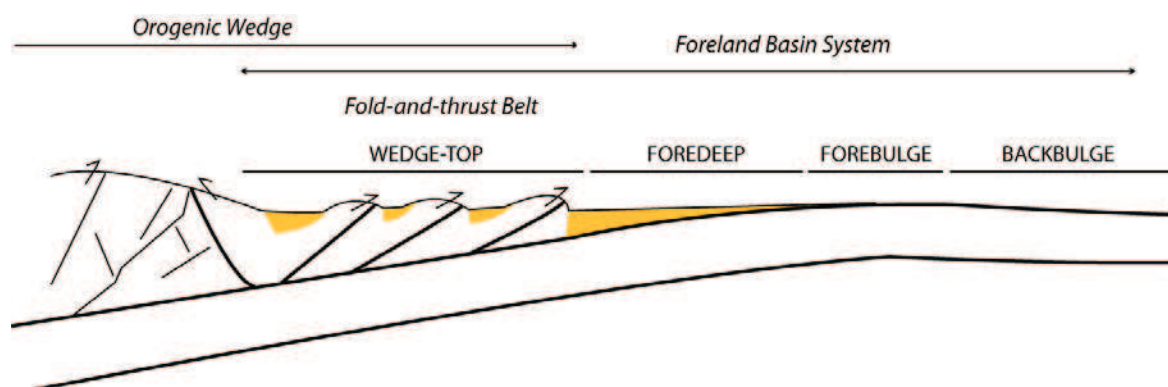


Figure I - 5. Schematic cross-section of the external domain of an orogenic wedge and its associated foreland basin, with the denominations of the main areas constituting the foreland system, redrawn from DeCelles and Giles (1996).

The wedge-top depozone is the area of sedimentation that is incorporated in the propagating fold-and-thrust belt. Due to their relatively short transport distance from the hinterland, wedge-top sediments are usually the coarsest in the basin, with conglomerates and sandstones drained by the fluvial or alluvial systems. As wedge-top basins develop while the wedge continues to grow, wedge-top sedimentation is contemporaneous with activity of either the frontal thrust or the out-of-sequence thrusts and backthrusts, carried as “piggy-back” basins of the deformed wedge (Ori and Friend 1984). The deposition on an active thrust leads to characteristic growth strata geometries (DeCelles and Giles 1996; Vergés et al. 2002b). Moreover, their continental facies make them a useful tool for dating the deformational history of a wedge by magnetostratigraphy (Burbank et al. 1992a for example). I will focus in particular on wedge-top sedimentation for the comprehension of fold-and-thrust belt evolution.

I-1.1d Feedback between tectonics and surface processes

Surface processes tend to affect the topographic slope of an orogenic wedge, and thus modify the critical taper and perturb the orogen growth process. Feedbacks between tectonics and surface processes are still debated today (Johnson and Beaumont 1995a, Molnar and England 1990, Kooi and Beaumont 1996). Erosion and deposition are the main surface processes influencing the growth of an orogenic wedge. Whereas deposition of sediments occurs in the most external part, erosion affects the internal range.

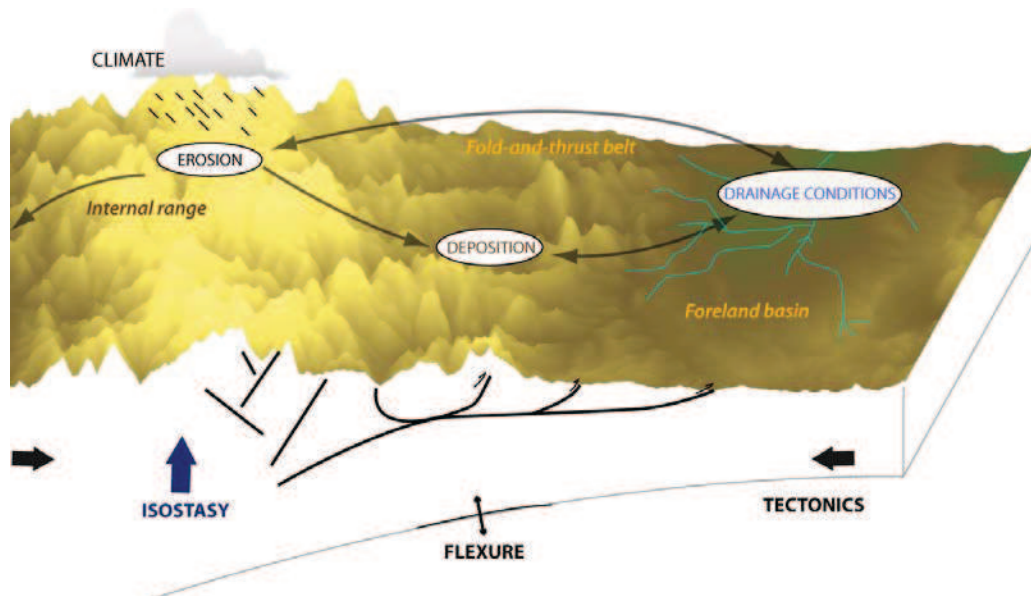


Figure I - 6 Schematic representation of the pro-wedge of an orogen and the main parameters influencing its growth.

Erosion effects on a mountain building are numerous, modifying the width of the belt and the exhumation pattern, as suggested by numerical models (Willett 1999b). Depending on the topography, the rock type and the climate, erosion affects the orogenic core (Figure I - 6) by

removing materials from the highest mountains, and so participating actively in the exhumation of rocks. Moreover, it forces isostatic compensation that can lead to increase the peak elevation of the range. Conversely, tectonic uplift and climate change are the main mechanisms enhancing erosion. The more erosion perturbs the internal evolution, the more sediments will be produced and deposited in the foreland system. Their deposition is controlled by the capacity of the rivers to transport the sediments, which is itself affected by both climatic variations and tectonic uplift (Whipple 2001) as well as by the base level. The base level is a boundary condition to an orogenic system, defined as the limit for river incision, and so it delimits the area of predominance of deposition. In general cases, base level refers to the sea level, but locally it can be an intra-mountainous level or the foreland basin level when the foreland basin is endorheic as has been the case in the Southern Pyrenees.

Base level evolution and the feedbacks with the orogenic system have been principally studied in terms of response to base-level lowering, which can be triggered by sea-level fall or opening of the foreland basin. By several modeling techniques (see Burbank and Anderson 2005, for example), the main consequence of this change in drainage conditions is the propagation of a wave of incision upstream, toward the hinterland. The effects of base-level rise have also been studied using analogue and numerical modeling (Babault et al. 2005a, Carretier and Lucazeau 2005). The main results of these experiments show that piedmont sedimentation in the foreland perturbs the erosion dynamics of the range (Figure I - 7), and prevent it from attaining its steady state while the aggradation of the sediments is faster than the relief uplift. Therefore the system of erosion/sedimentation in an orogenic context is fully coupled and especially when conditions are favorable for sediment accumulation (endorheic foreland basin, enhanced erosion). The Pyrenean pro-wedge effectively experienced such drainage conditions and we will investigate the effects of wedge-top sedimentation of the fold-and-thrust belt in Parts III and IV.

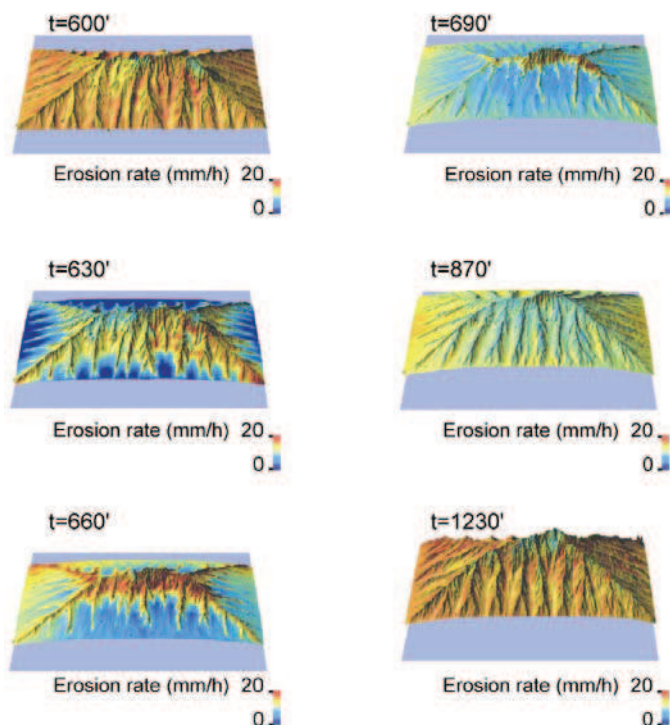


Figure I - 7. analogue modeling results of the response of orogenic topography to a sudden increase in base level, (from Babault 2004).

I-1.2 The Pyrenean-Cantabrian mountain belt

I-1.2a General overview

The Pyrenean-Cantabrian mountain belt extends ~1000 km from east to west and is ~100 km wide. The Pyrenean part straddles the border between Spain and France and the Cantabrian part follows the Spanish coast of the Bay of Biscay.

The belt is divided into several units, the Pyrenees to the East, the Basque-Cantabrian basin in the center and the Cantabrian Mountains to the west. Several denominations have been used for defining the Cantabrian domains of this belt (see the review of Barnolas and Pujalte 2004); Figure I - 8 shows the terminology that I will use in this thesis.

The Pyrenean-Cantabrian belt has been formed from Late Cretaceous to Oligocene-Miocene times, and is a consequence of the closure of the Tethys Ocean, that led to the onset of building of the Alpine-Himalayan belt, of which the Pyrenean-Cantabrian belt is the western termination.

The outcropping rocks reflect the polyphased history experienced by the range, from the Variscan orogeny to the Alpine compression. Basement rocks outcrop in the Pyrenean part and the Central and Western Cantabrian Mountains; Mesozoic and Cenozoic sediments are present in the foreland areas and in the Basque-Cantabrian basin.

The Central Pyrenees and the Central Cantabrians are the area of highest relief, with the highest peaks reaching 3404 m for the Pic d'Aneto in the Central Pyrenees and 2648 m in the Picos de Europa massif in the central Cantabrians. Even if the mountain belt has not been active since Oligocene-Miocene times, the high areas are associated with strong relief.

In the following, I will review the main characteristics of the geological and geodynamic history of the range and of its adjacent southern basins. Details on the geological history of the central Pyrenean and central Cantabrian Mountains will be provided at the beginning of each chapter.

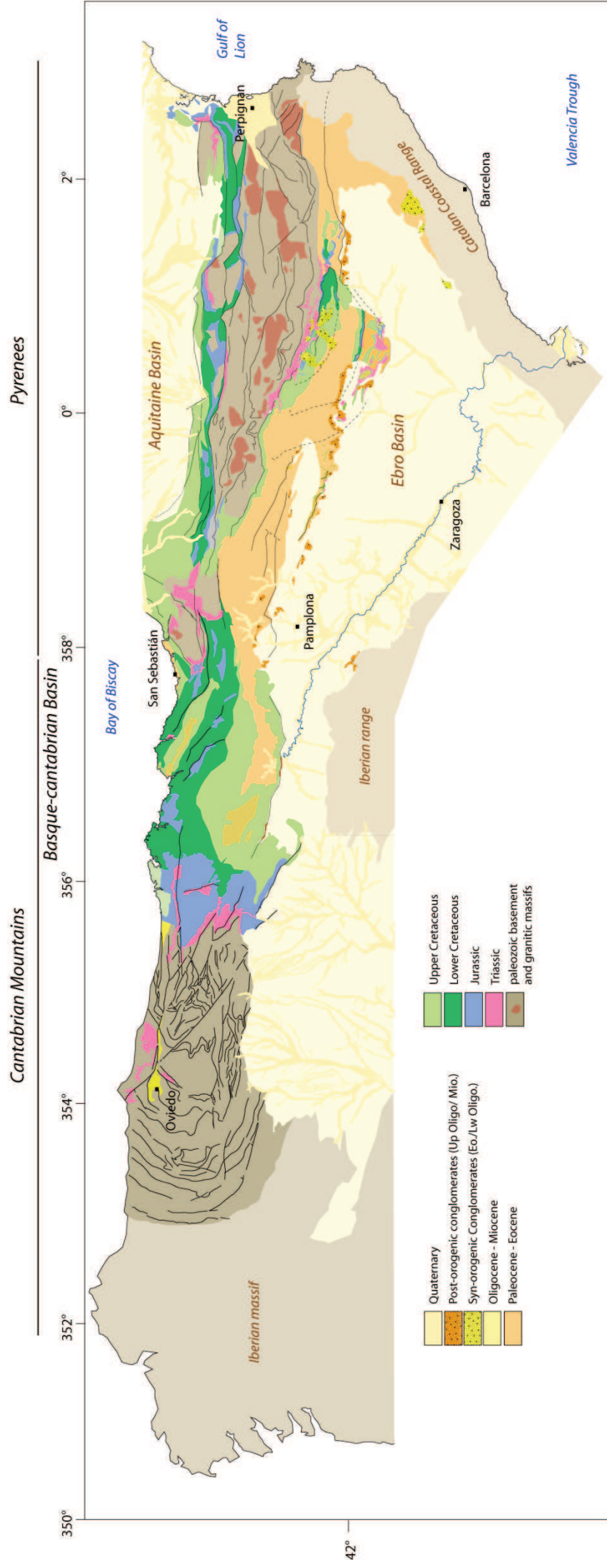


Figure I - 8 Geological map of the Pyrenean-Cantabrian mountain belt.

I-1.2b Variscan orogeny

Well before the alpine orogeny, structuration of the two ranges has been influenced by a complex kinematic evolution. A major phase of deformation took place during the Variscan orogeny, which led to the creation of the Armorican arc. Building of the Variscan belt occurred from 500 to 250 Ma and resulted from the collision of several plates against Gondwana. The belt was subsequently broken up during the Mesozoic opening of the Atlantic Ocean. In the north-west of Spain, the heart of the Armorican arc is called the Asturian arc (Julivert 1971; Pérez-Estaún et al. 1988) that formed during the late Stephanian to early Permian, although its origin is still matter of debate. In the center of the asturian arc, the Cantabrian zone represents the external part of the Variscan belt (Figure I - 9). The first phase of deformation in that area was driven by east-west compression that produced a thin-skinned imbricate thrust structure progressing from west to east. Then, the formation of the arc tightened the structures. The Central Coal basin unit and Ponga units (that we will further study Part II) were therefore the latest to be emplaced.

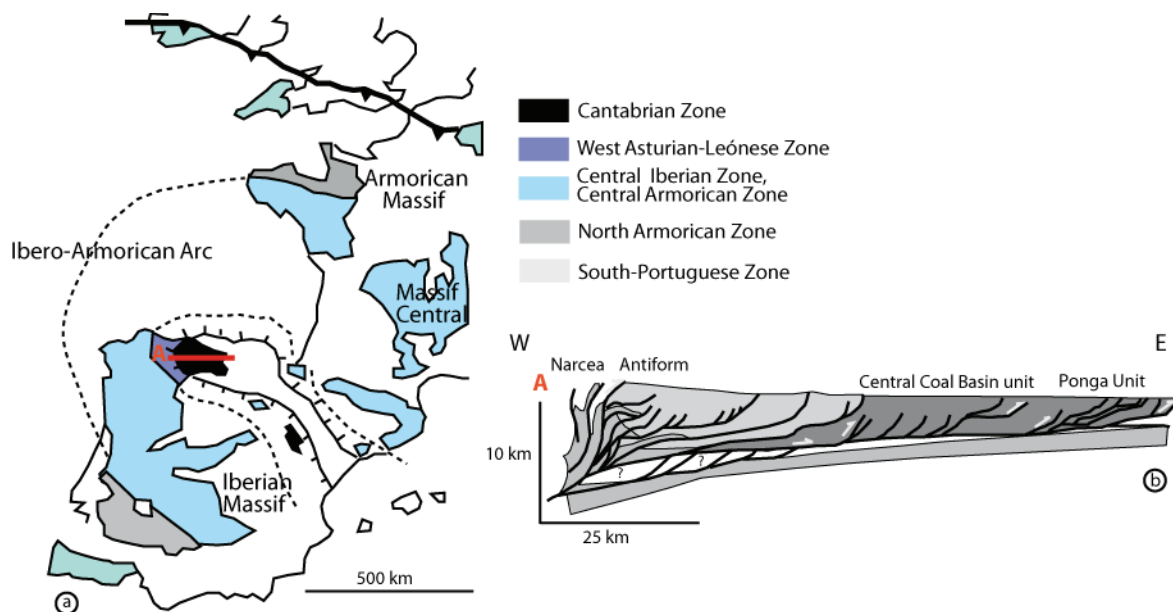


Figure I - 9. (a) Map of the Ibero-Armorican arc and its main zones. (b) E-W cross section through the Cantabrian Zone. Modified from Carrière (2006) and Pérez-Estaún et al. (1988).

I-1.2c Mesozoic kinematics

The evolution of the proto-Pyrenean-Cantabrian belt was influenced by its pre-Cenozoic structuration, and the patterns of convergence (*e.g.* the tectonic regime) of the Iberian plate to the European plate are therefore determinant. Two Mesozoic rifting periods led to the formation of the extensional Pyrenean basins, in late Jurassic and in early Cretaceous times (Puigdefabregas and

Souquet 1986, Sibuet et al. 2004). These rifted basins connected the Atlantic Ocean to the west with the Tethys to the east.

The Mesozoic geodynamic history has recently been strongly debated in terms of kinematics. There are several scenarios for the reconstitution of the Mesozoic movement of the Iberian plate and the opening of the Bay of Biscay (Srivastava et al. 1990; Olivet 1996; Sibuet et al. 2004; Jammes et al. 2009); one of the most popular models, proposed by Olivet (1996) is presented in Figure I - 10.

To summarize, these studies are mainly based on the magnetic anomaly patterns in the Atlantic ocean and the Bay of Biscay, the uncertainties of which leave room for several interpretations. The common feature among the several models is the presence of major left-lateral strike slip movement from late Jurassic to early Cretaceous depending on the models. The difference in timing for this movement is associated to the different mode of opening of the Bay of Biscay. The two end-members models for this opening are 1) driven by the left-lateral strike-slip movement along the North Pyrenean Fault (Figure I - 10, Olivet 1996; Jammes et al. 2009); or 2) driven by a scissor-type opening (Roest and Srivastava 1991; Srivastava et al. 2000; Sibuet et al. 2004). The consequences of the two models are determinant for the study of the mountain growth. The first model implies oblique convergence and a synchronous collision from east to west; the second model implies a diachronous collision starting in the Eastern Pyrenees. From thermochronological data shown in the following, we will see that the signal of a diachronous collision is not very well constrained.

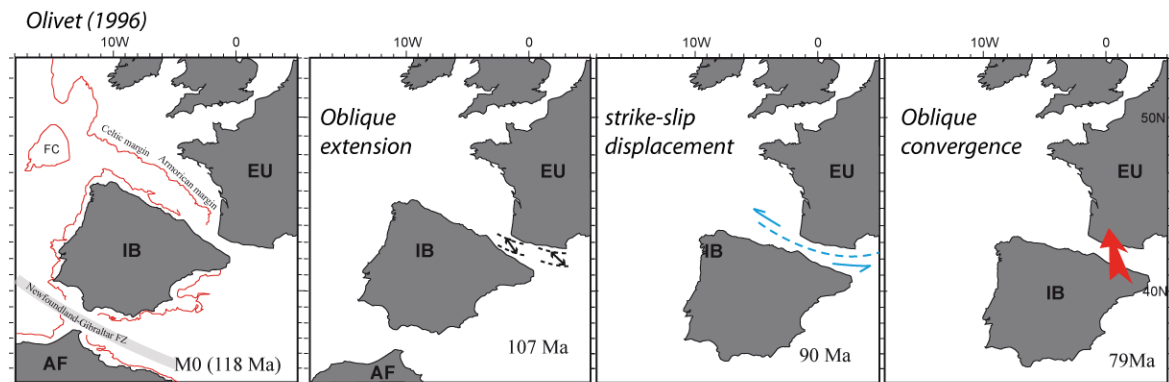


Figure I - 10. Kinematic reconstruction of the Iberian plate (IB) movement in respect to the European plate (EU). Modified from Olivet (1996).

Opening of the Bay of Biscay occurred until the Santonian-Campanian (85-70 Ma), when the inversion of the Mesozoic basins started (Sibuet et al. 2004). This extension phase resulted in creating from east to west the present-day Pyrenean-Cantabrian range the Organya basin, the Basque Cantabrian basin, and affected the central Cantabrians by reactivating east-west structures and creating new small basins.

I-1.2d Cenozoic contractional deformation

Consequently to the Mesozoic extension, the convergence of the Iberian micro-plate toward the European plate started in Late Cretaceous times by inversion of the Mesozoic basins followed by underthrusting of the Iberian crust underneath the European crust. The collision led to a doubly-vergent orogen, presenting several structural variations along-strike. The polyphased regional history developed previously (Variscan orogeny in the Cantabrian domain and Mesozoic extension) inferred a pre-structuration that led to varying collisional patterns along-strike. Moreover, the Pyrenees developed as a classical continental collisional belt (see section I.1) whereas the Cantabrian Mountains were built by the inversion of the Iberian continental margin.

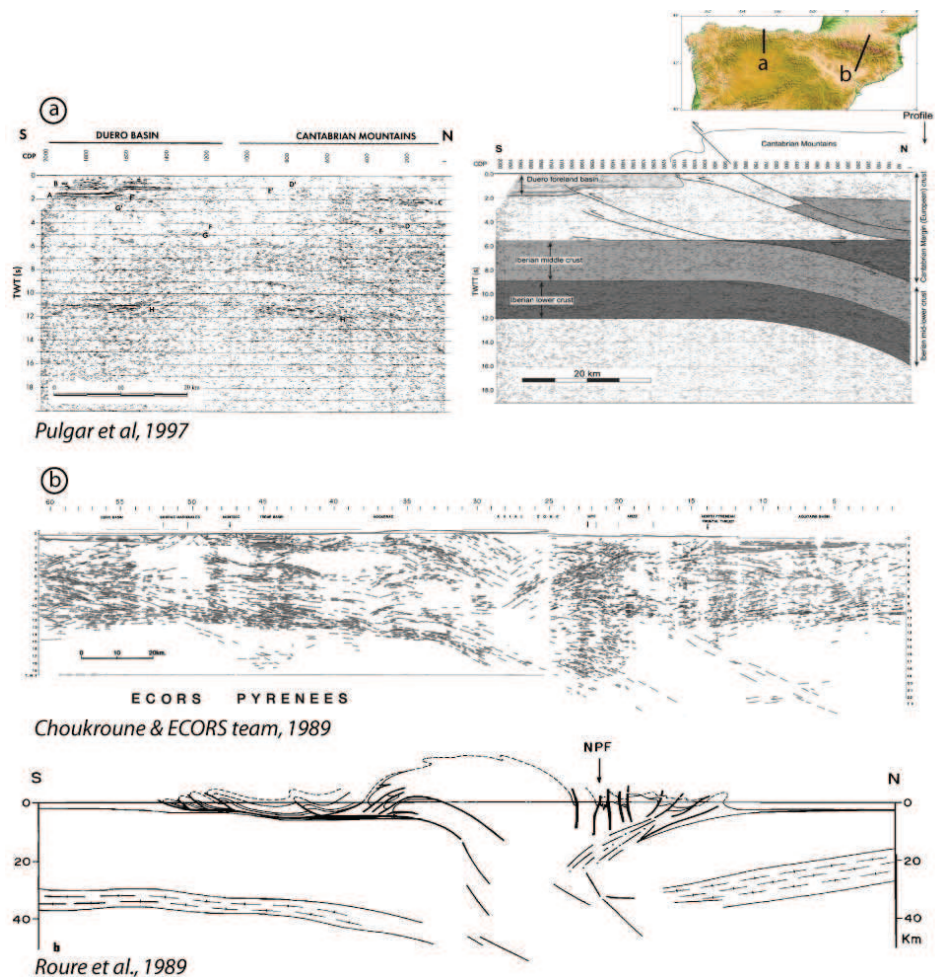


Figure I - 11. Deep Seismic profiles and their interpretations for the central Pyrenees and the central Cantabrian mountains. a) ESCIN-2 seismic profile; b) ECORS seismic profile

The continuity of the northward underthrusting of the Iberian crust from the Pyrenees to the Cantabrians has been demonstrated by numerous deep seismic reflection profiles, such as ECORS in the Pyrenees (Figure I - 11b, ECORS Pyrenees Team 1988) and ESCI-N in the Cantabrian

mountains (Figure I - 11a, Pulgar et al. 1997). In the eastern Cantabrian Mountains (Basque-Cantabrian basin) this continuous pattern has also been confirmed by the 3-D modeling of gravity and seismic data (Pedreira et al. 2003; Pedreira 2007).

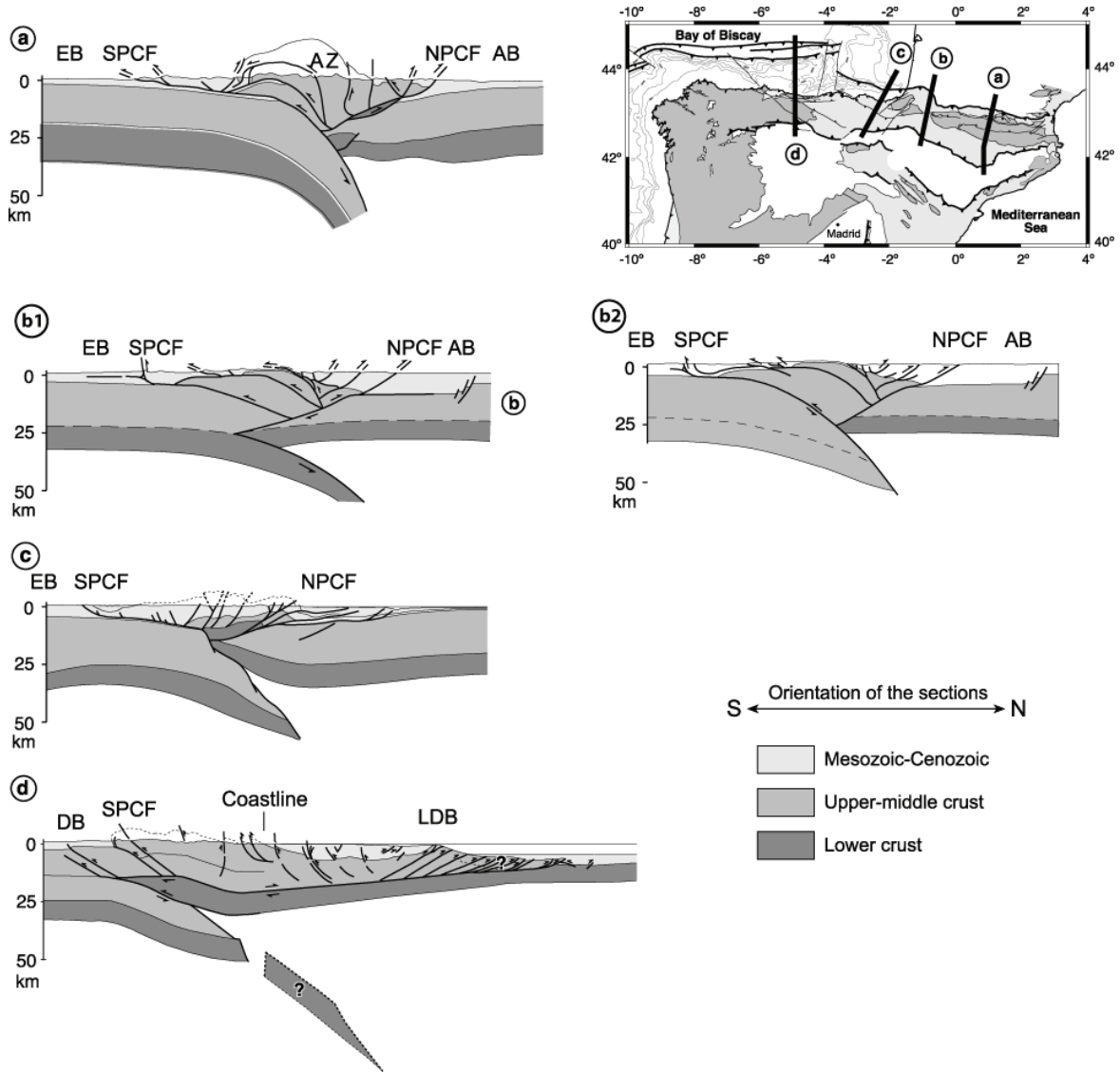


Figure I - 12. Crustal cross-sections along-strike of the Pyrenean-Cantabrian mountain range. From Pedreira (2007). a) Central Pyrenees (Muñoz 1992), b) Western Pyrenees (Teixell 2004), c) Western Cantabrian mountains (Pedreira 2005), d) Central Cantabrian mountains (Gallastegui 2000). AB, Aquitaine Basin; AZ, Axial Zone; EB, Ebro basin; LDB, Le Danois Bank; NPCF, North Pyrenean-Cantabrian front; SPCF, South Pyrenean-Cantabrian front.

These authors conclude that the contractional deformation between the Pyrenees and the Cantabrian mountains is partitioned by large NE-SW lateral structures in the Basque-Cantabrian basin.

The amount of shortening also varies from west to east; from 82 km in the Eastern Pyrenees (Vergés et al. 1995) to 165 km in the Central Pyrenees (Beaumont et al. 2000), 125 km in the Western Pyrenees (Teixell 1998), and 96 km of shortening in the Central Cantabrians (Gallastegui 2000). The different crustal structural styles are presented in Figure I - 12.

We will see in the following section that the peak of exhumation, as recorded by low-temperature thermochronology, was not synchronous along-strike of the Pyrenean-Cantabrian mountain belt. The bounds for frontal activity are synchronous in the Pyrenees but young towards the west.

Timing estimates of the frontal thrusting activity are provided by continental deposits that are well preserved in most of the frontal area of the Pyrenean-Cantabrian belt. The latest frontal activity was dated to Chattian times in the Eastern (28 Ma, Vergés et al. 1995; Vergés et al. 2002a), Central (26 Ma, Meigs et al. 1996) and Western Pyrenees (Teixell 1998). More details on the thrusting sequence of the central Pyrenees are presented in Chapter IV-2.

To the west, in the Cantabrian Mountains, the frontal activity has been estimated to be more recent, even though the dating of the Oligocene-Miocene sediments is less precise there. In the Eastern Cantabrians (Basque-Cantabrian basin), early Miocene sediments are deformed by Alpine compressional structures and therefore date the latest activity (Camara 1997). Finally, the frontal activity of the Central Cantabrian mountains is dated by the conglomeratic deposits sealing the syn-tectonic sediments, which are late Miocene in age (Vallesien, 11.6-9 Ma). Precise dating of the syn-tectonic conglomerates is in progress at the University of Oviedo (see Part II), the ages reported by the geological map (Guardo, 1:50000) are Oligocene to middle Miocene.

I-1.2e Spatial exhumation patterns

By studying the variations in apatite fission-track (AFT) ages, we can obtain an overview of the large-scale patterns of exhumation in the Pyrenean-Cantabrian belt. Low-temperature thermochronology (and AFT in particular) has been extensively used, to discuss both the tectonic activity and the geomorphologic evolution (Jolivet et al. 2007 and Gunnell et al. 2009 for instance). In this section, we will use the numerous AFT results (Figure I - 13) to support a description of the exhumation patterns and their variations.

On the Pyrenean side, the oldest AFT age (106.3 ± 5.3 Ma) has been measured in the Arize massif (Morris et al. 1998), to the north (retro-side) of the central range; whereas the youngest AFT age (10.9 ± 1 Ma, Jolivet et al. 2007) comes from the Bielsa granite to the south-west. In between, the majority of the ages are Eocene-Oligocene in age. On the Cantabrian side, the oldest age is in the western Cantabrians and is dated to Permian times (262 ± 18 Ma), whereas the youngest date is Oligocene in age (27.4 ± 4.8 Ma) and located in the Central part (both dated by Carrière 2006); the majority of the Cantabrian ages are Permian to Mesozoic. The youngest ages of exhumation are therefore found in the Pyrenees and the Alpine exhumation is concentrated in Eocene to Oligocene times.

But the most interesting information produced by these ages is their spatial distribution. In the Pyrenees, the AFT ages show clear pattern, with oldest (Cretaceous to Eocene) ages in the north and youngest (Eocene to Miocene) to the south, in agreement with the geodynamic reconstructions of Verges et al. (1995) ; Teixell (1998) or Beaumont et al (2000) that all predict more important exhumation at the early stages of compression in the retro-side of the wedge, which then migrates to the pro-side. This evolution is quite different from the classical model of doubly-vergent orogen development (Willett et al. 1993) that predicts the first deformation on the pro-side. The existence of a weak and thinned area around the North-Pyrenean Fault could explain the concentration of deformation on the retro-side.

In contrast to the Pyrenees, no north to south progression of exhumation is evidenced in the Cantabrian Mountains; the low number of Cenozoic ages and also the structural style can be the cause for this. Conversely, east-west patterns of denudation are clearer in the Cantabrian Mountains. The AFT ages are not reset (Mesozoic) in the western part and a few Oligocene ages are present in the center, implying that the central Cantabrians probably experienced the most exhumation. We will see in Part II that this trend is confirmed by our AFT and (U-Th)/He on zircons (ZHe) results.

In the Pyrenees, this east-west propagation of exhumation is not evident. In the Western part, Oligocene ages are present in the south-western and central area. To the west, the young Miocene ages published by Jolivet et al (2007) are interpreted more in terms of out-of sequence thrusting of the Bielsa thrust.

Finally, exhumation rates obtained by combining different thermochronometers and their thermal modeling date the maximum of Pyrenean exhumation. Results from the Eastern and Central Pyrenees lead to similar conclusions. Gunnel et al. (2009) report rapid cooling of their samples in the 40-30 Ma interval, followed by quiet conditions (very slow to no exhumation) until present. In the Central Pyrenees, the estimations are more precise, owing to the presence of age-elevation profiles. From their dataset, Fitzgerald et al. (1999) predicted exhumation rates between 2 and 4 km.Myr⁻¹ between 36 and 30 Ma, and then ~0.06 km.Myr⁻¹ until 6 Ma. From their thermal modeling, Gibson et al (2007) predicted an exhumation rate of 1.5 mm.yr⁻¹ between 31 and 29 Ma and then 0.03 to 0.09 mm.yr⁻¹ from that time to present. Even if the two estimations are slightly different, they both agree with a peak of exhumation in late Eocene-early Oligocene.

Patterns of exhumations of the central Cantabrian Mountains will be studied in Part II In the Western Cantabrian Mountains, the dataset produced by Grobe et al.(2010) and Martin-Gonzalez et al. (2011), suggest exhumation rates in the rate of 0.05 mm.yr⁻¹ between 100 and 50 Ma, then 0.02 mm.yr⁻¹ in the Paleogene and 0.06 mm.yr⁻¹ in Neogene.

In summary, with this extensive dataset, we can follow an Eocene-Oligocene main exhumation phase from the eastern Pyrenees to the central Cantabrian Mountains. We can also see the development of the doubly-vergent Pyrenean wedge, from north to south, pattern that is not visible

in the Cantabrian Mountains area. Finally, the main phase of exhumation occurred in late Eocene-early Oligocene times and was very important in the Central Pyrenees, whereas, there is not enough information on the Cantabrians to deduce Cenozoic exhumation rates. In this thesis, additional constraints will be brought to the Central Cantabrians and Central Pyrenean history by (U-Th/He) on apatites (AHe), AFT and ZHE dating. Low-temperature thermochronological data are missing in the Basque-Cantabrian basin, to link the two parts of the range; sampling and dating are currently in preparation in the framework of the Pyrtec project (Irene de Felipe Thesis, Oviedo).

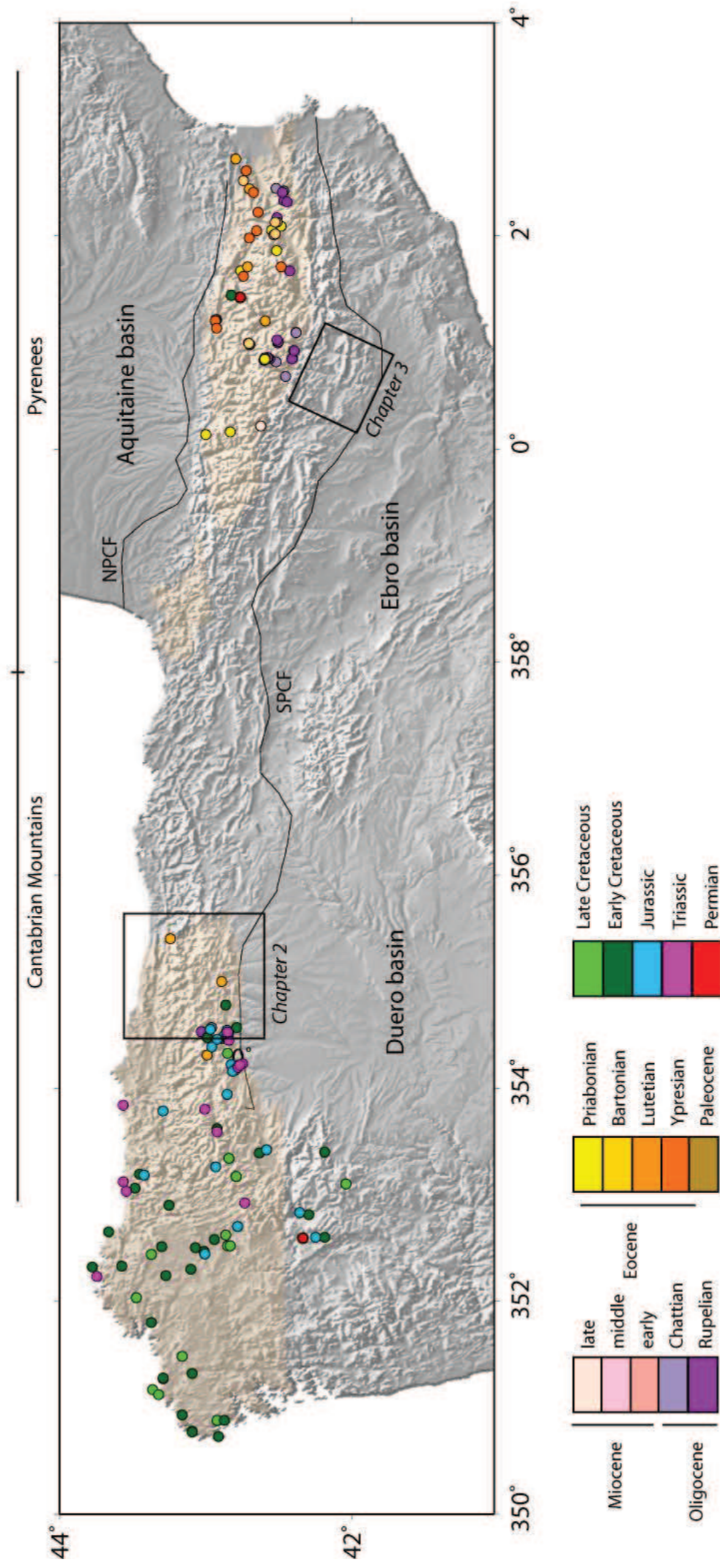


Figure I - 13 . Compilation of apatite fission-track dating results in the Pyrenean-Cantabrian mountains, published by Yelland 1990; Morris et al. 1998; Fitzgerald et al. 1999; Sinclair et al. 2005; Carrière 2006; Gibson et al. 2007; Jolivet et al. 2007; Maurel et al. 2007; Gunnell et al. 2009; Metcalf et al. 2009; Grobe et al. 2010; Martin-Gonzalez et al. 2011. Balck boxes represent the areas for which new low-temperature thermochronology data are presented in this thesis.

I-1.2f The Duero and Ebro basins

As outlined in the introduction, the evolution of a mountain range is strongly linked to the evolution of its adjacent foreland basin. On the pro-side of the Pyrenean-Cantabrian domain, two large basins, the Duero and the Ebro basins, take part in the Cenozoic evolution of the mountain belt. These two basins experienced independent evolution until Pliocene times, when a connection between them was established.

The Ebro basin was formed in response to the flexural load of the Pyrenean orogenic wedge; the loading of the two other Alpine ranges surrounding the basin (the Catalan Coastal Range to the southeast and the Iberian Range to the southwest) also contributed to its formation (Desegaulx and Moretti 1988a; Zoetemeijer et al. 1990a). The sedimentology of Paleocene-early Eocene sediments in the basin clearly shows that it initially deepened and opened toward the Atlantic Ocean in the West (Puigdefabregas and Souquet 1986). The connection of the Ebro basin with the Atlantic Ocean was closed at 36 Ma (Costa et al. 2009) and the basin became endorheic. From that time, the sedimentation is continental at its border to lacustrine in its center. The modeling performed by Garcia-Castellanos et al.(2003) showed that the basin evolved as an asymmetric main lake. The preservation of the endorheic conditions for ~25 Myr was helped by the uplift of the Catalan coastal ranges and the climatic conditions (dry and warm). The onset of the connection of the Ebro River to the Mediterranean has been discussed by several authors (Garcia-Castellanos et al. 2003; Babault et al. 2006; Urgeles et al. 2011) and we will see in Chapter III-1 that the modeling of thermochronological data is in favor of a pre-Messinian opening to the Mediterranean Sea.



Figure I - 14. Picture of the south Pyrenean mountain front and the Ebro foreland basin, in the Western Pyrenees. View from the top of one of the conglomeratic relief, looking toward the south-east.

The Duero basin drains the Iberian Chain to the east, the Cantabrian Mountains to the north and the Spanish Central System to the south. Until Paleocene times, the basin was open to the Atlantic ocean and its sedimentation was marine to terrestrial (Santisteban et al. 1996). The basin became endorheic in Paleocene times, with the closure of the connection to the Atlantic to the north by the

onset of uplift of the western Pyrenean massifs. The capture of the fluvial network in the southwest of the basin (in early Miocene times) re-opened the basin toward the Atlantic. Exorheic drainage then extended progressively to the center of the basin but the conditions remained endorheic in the northern part. Complete capture of the basin only occurred in late Miocene-Pliocene times (Mediavilla et al. 1996).

Both basins had their drainage system perturbed by uplift of the surrounding mountain ranges, which led to their closing and tuned them into long-lived, internally drained basins before re-opening again when the main Alpine contraction was over. This is a common feature of the basins developed in contractional settings and that are controlled by their adjacent orogen. Moreover, as shown by Figure I - 15 and Figure I - 16, their sedimentary environments are imprinted by the uplift of the Pyrenean–Cantabrian belt. While the large sediment input supplied by the Pyrenees mainly occurred in Oligocene times in the north of the Ebro basin, sedimentation in the Duero basin was maximum in late Oligocene-Miocene times. This time offset from east to west thus reflects the propagation of the exhumation from the Pyrenees to the Cantabrian mountains, that is, however, not so striking at smaller scale.

It is important to note, however, that the contribution of the Pyrenean-Cantabrian range to the two basins is not similar. The Pyrenees extended along the entire northern margin of the Ebro basin, making them the primary contributor in both sediment supply and flexural control. The Duero basin is fed by several other important orogenic systems such as the Spanish Central system and the Iberian range, and is also strongly controlled by them. Therefore, the ratio between fluvial network area and basin size is much less in the case of the Duero basin and one can think that the influence of the Cantabrians was of less importance on the range in terms of erosion and sedimentation than the Ebro evolution.

The Duero basin drainage was exorheic since Miocene times but it has never been totally excavated compared to the Ebro, which leads to a very different topographic profile between the two basins (Figure I - 17). Indeed, in the Central Cantabrian profile, we can see that the southern flank has been poorly incised, as the base level is still 1000m high today, which will have had a significant effect on the late-stage exhumation of the southern Cantabrians.

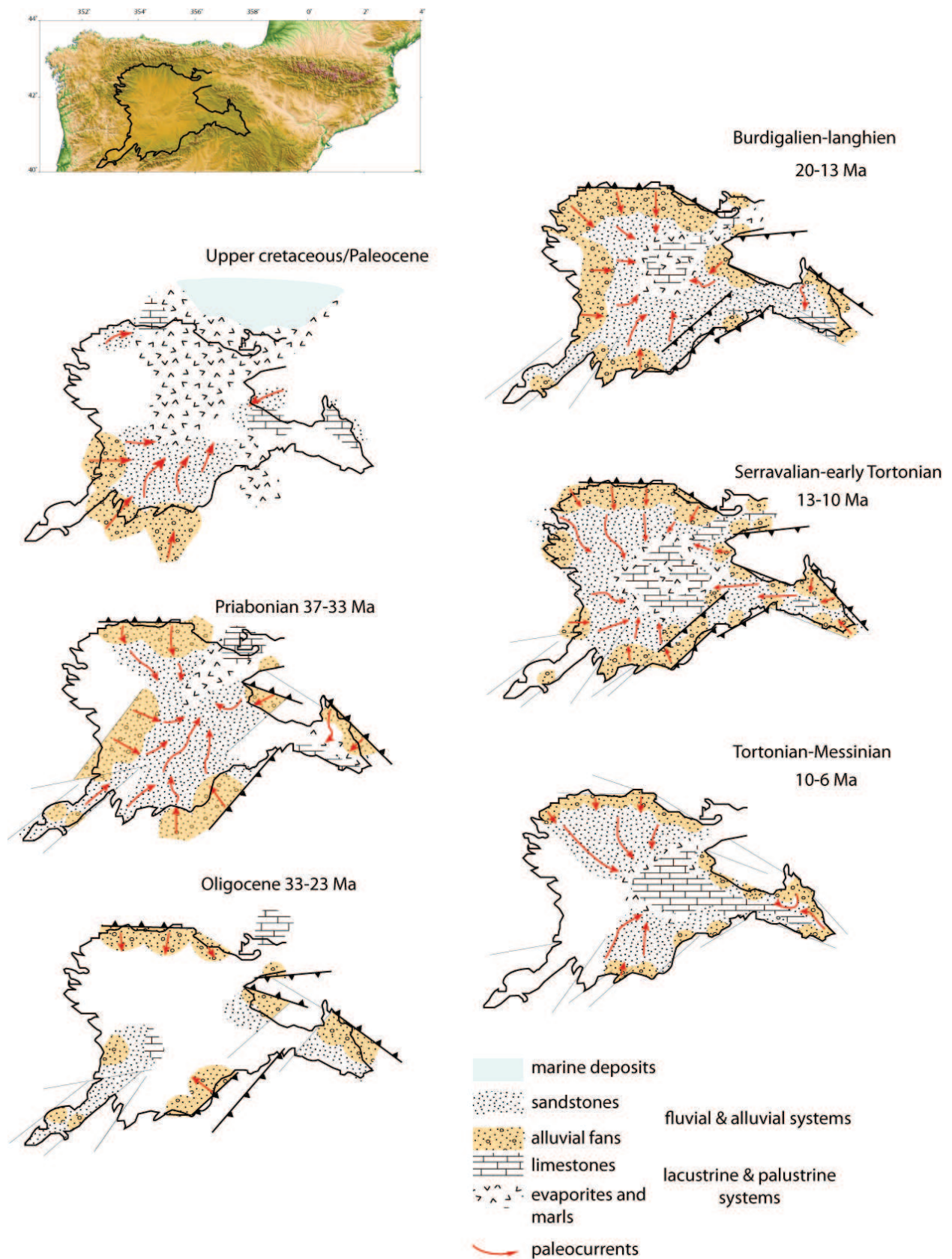


Figure 1 - 15. Paleoenvironmental reconstructions of the Duero basin, from Late Cretaceous to Messinian times. Redrawn from Vera (2004).

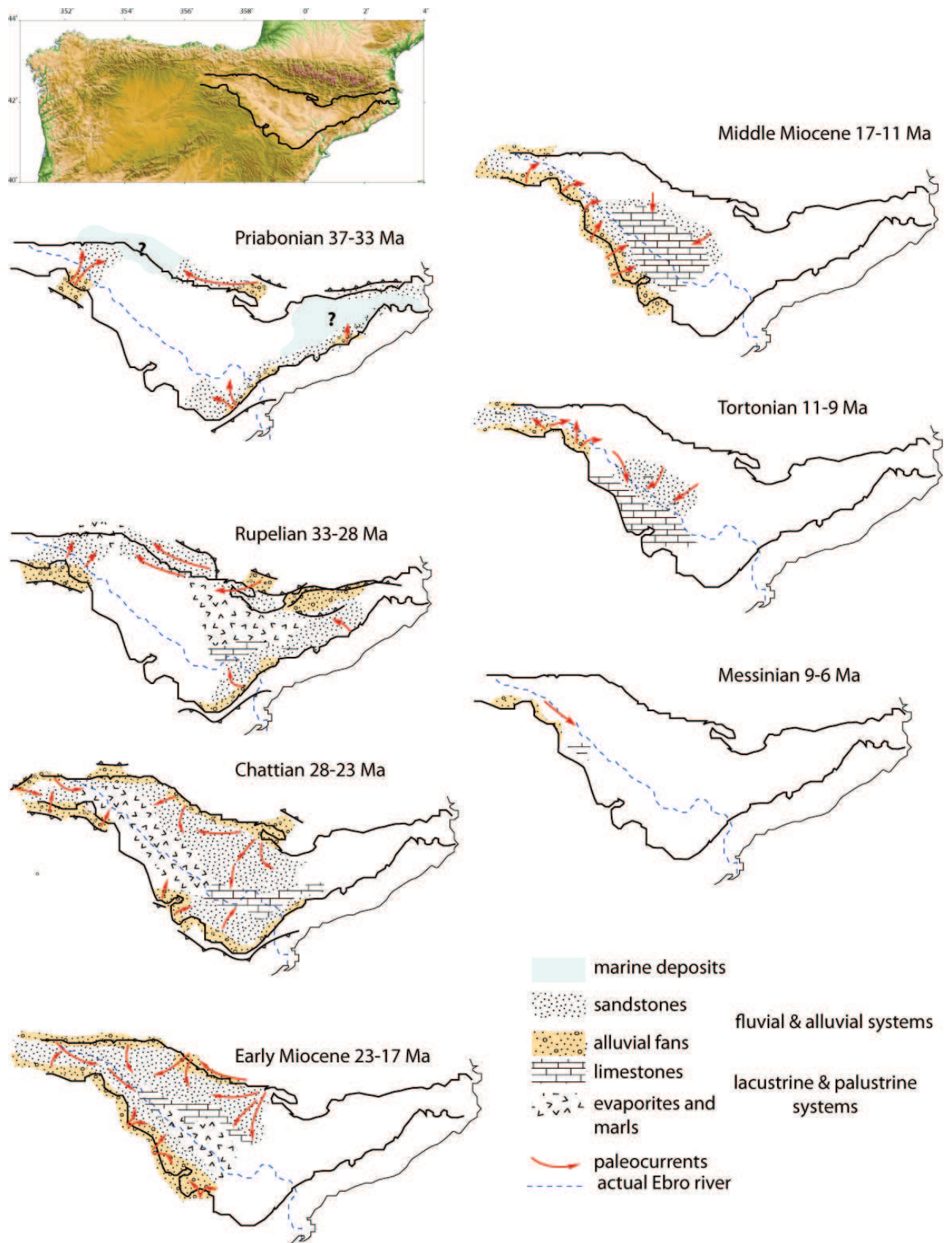


Figure 1 - 16 Paleoenvironmental reconstructions of the Ebro basin, from late Eocene to Messinian times. Redrawn from Vera (2004).

Finally, the Duero basin is linked to the history of the high-elevated central area of the Iberian sub-continent (called the Meseta), of which the present-day patterns and the formation are still a matter of debate. Several processes have been invoqued for explaining this high-elevation area. The most recent ones are 1) lithospheric folding of the Iberian plate (Cloetingh et al. 2002; de Vicente et al. 2007), and 2) the conjugated effect of the infilling of the endhorheic basin by the uplift of the Alpine ranges around, conjugated with isostatic adjustment from crustal thickening (Casas-Sainz and de Vicente 2009).

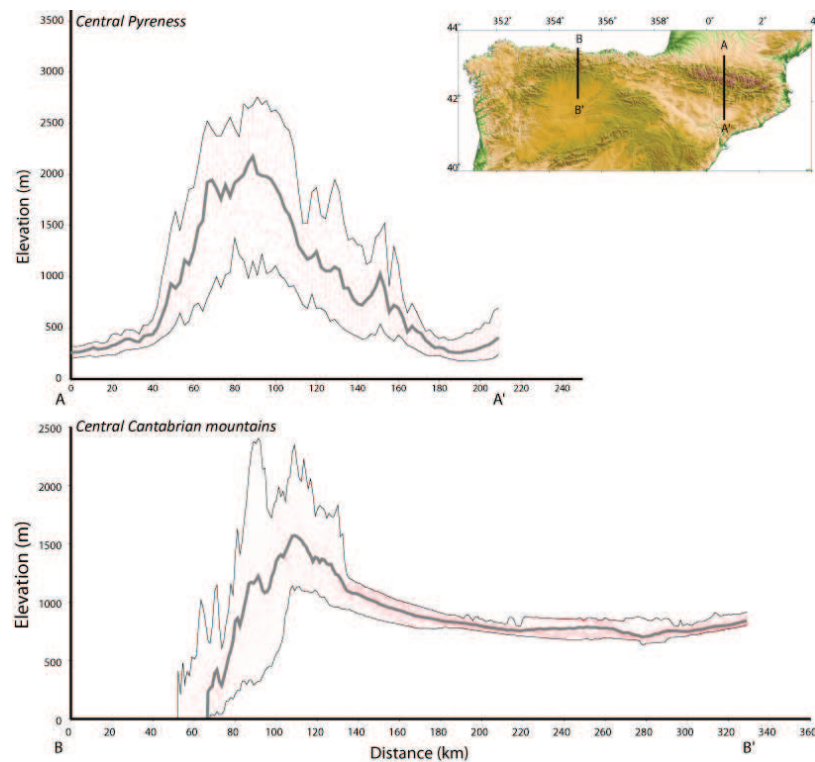


Figure I - 17. *Topographic profiles of the central Pyrenees and central Cantabrian Mountains. Maximum, minimum and mean elevations are indicated.*

I-1.2g Cenozoic climatic evolution

The Cenozoic era is characterized by a climate that has deeply modified by the emplacement of ice sheets. With the numerous studies using stable isotopes like ^{18}O or ^{13}C (see , For instance, Zachos et al. 2001) several main climatic events have been defined, like the Early Eocene climatic optimum, the Eocene-Oligocene cooling event, and the late Miocene warming , characterized by extreme changes in temperatures or by onset of changing climatic conditions. Among these climatic events, the Eocene–Oligocene climatic transition is one of the largest global cooling events (Figure I - 18) of the Cenozoic (Katz et al. 2008). The establishment of large permanent

Antarctic ice sheets (Coxall et al. 2005; Lear et al. 2008) was accompanied by the decrease in carbon dioxide concentration and a major sea-level fall.

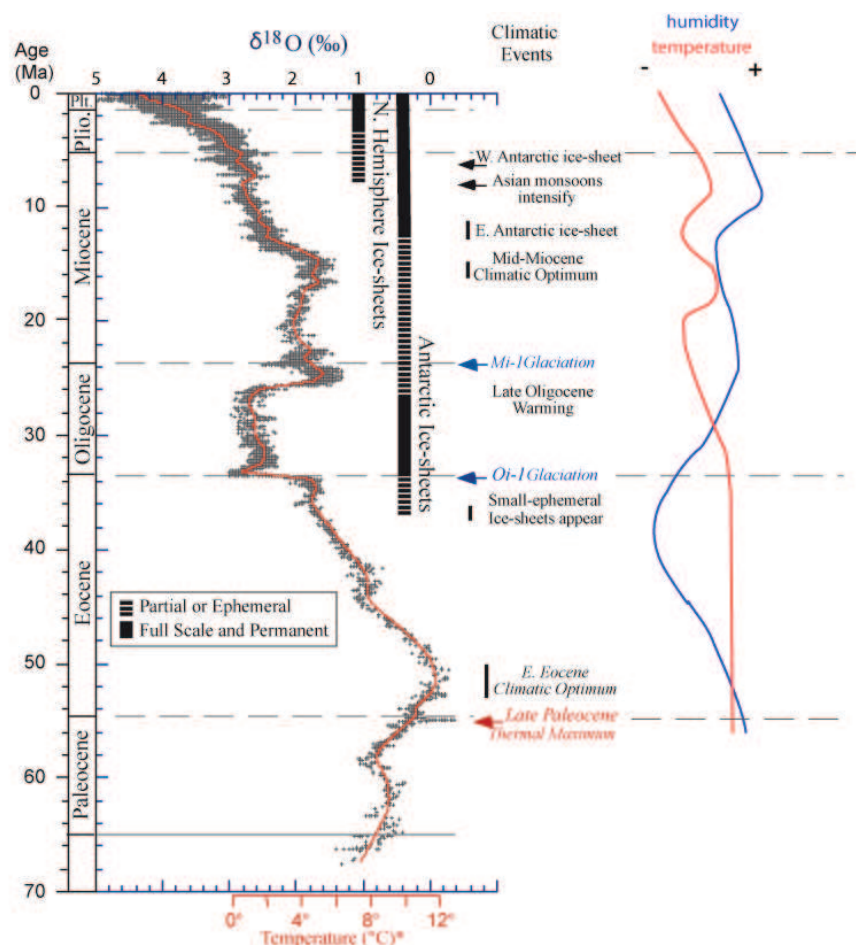


Figure 1 - 18. Cenozoic climatic data. Left-hand side, $\delta^{18}\text{O}$ compilation of Zachos et al. 2001. Right-hand side, summary of the climatic data for the northern Spain (by Garcia-Castellanos et al. 2003).

Climatic conditions have been inferred for northern Spain by several studies performed in the Spanish Pyrenees and Ebro basin. In the Spanish Pyrenees, Schmitz and Pujalte (2007) found evidence for a drastic change in the hydrological cycles during the Paleocene-Eocene thermal maximum, with conditions becoming more humid, and important seasonal rains.

Subsequently, the Eocene-Oligocene boundary has also been reported in northern Spain by the palynological study of Cavagnetto and Anadon (1996), who relate the transition from a tropical to a dryer and more contrasted (increased seasonality) climate in the early Oligocene.

The late Oligocene was the time of very warm and humid conditions, recorded by clay assemblages in the Ebro basin (Mayayo et al. 2011); these authors also note a passage to drier conditions consequently to the Mi-1 glaciations at the Oligocene-Miocene boundary. During the Miocene, a maximum of humid and cool conditions was identified at 9.4 (Vallesian) by the

analysis of palustrine sediments (Alonso-Zarza and Calvo 2000) and stable isotopes (Arenas et al. 1997). Since that time, the regional climate became warmer and drier.

I-1.3 Motivations and outline of the manuscript

The Pyrenean-Cantabrian mountain range is characterized by significant lateral variations in topography, amount of shortening (Muñoz 1992; Teixell 1998; Beaumont et al. 2000; Gallastegui 2000; Vergés et al. 2002a) and structural style (section I.1.2, Pedreira 2007). The Central Pyrenean part of the range presents all the characteristics of a classical collisional orogen, with a well-developed thin-skinned foreland (Muñoz 1992). The Cantabrian Mountains are a thick-skinned belt (Alonso et al. 1996; Pulgar et al. 1999), much more asymmetric and with a well-developed submarine fold-and-thrust belt on the retro-side. On the pro-side, the orogen core directly overthrusts the Duero foredeep basin without an intervening fold-and-thrust belt (Figure I - 12).

The lateral variations of exhumation patterns as shown by the thermochronological data are much less clear. A majority of Eocene to Oligocene ages are represented in the Pyrenees (section I.2.5), whereas most of the low-temperature data in the Central and Western Cantabrian Mountains indicate Mesozoic cooling ages. Only a few samples provide evidences for Eocene-Oligocene exhumation in that part of the range.

Moreover, the two areas did not experience the same pre-collisional history. The Cantabrian domain was strongly imprinted by the Variscan orogeny and the different episodes of Mesozoic extension while the Pyrenean domain has been strongly influenced by the Mesozoic rifting period. Therefore, tectonic inheritance appears to have conditioned the inversion of the two areas by leading to different tectonic styles.

However, external controls such as erosion in the internal parts and deposition in the foreland basins are integrally part of the orogenic system and could also have influenced the belt evolution. Indeed, the Pyrenean and the Cantabrian belts are both bounded to the South by large basins (the Ebro and the Duero respectively) that have been endorheic during a major part of the Cenozoic. The Duero basin has been filled by an important amount of Oligocene-Miocene foredeep sediments while the Southern Pyrenean foreland is suspected to have experienced a syn- to post-tectonic burial by wedge-top sediments sourced from the hinterland. Therefore, the Pyrenean-Cantabrian belt is favourable for investigations of feedbacks between the orogen dynamics and the variations in the foreland basins.

Better understanding the controls on lateral variations of these feedbacks and thereby on orogen dynamics, passes through a more complete description of the exhumation history of the Pyrenean-Cantabrian mountain belt, including its potential lateral variability, combined with numerical modelling of the tectonic evolution of the belt and its surface response as well as the coupling between these.

But the central Cantabrian range clearly misses constraints on exhumation, compared to the Pyrenees. For this reason, **part II** focuses on obtaining new age constraints on the Alpine exhumation of the central Cantabrians by low-temperature thermochronology. A few apatite fission-track ages already showed Eocene and Oligocene exhumation, and the aim is to bring more constraints to shed light on potential north-south and/or east-west variability as is the case in the Pyrenees. Apatite fission-track and (U-Th)/He thermochronology data will thus be presented that provide important information and basic constraints on the exhumation as well as on the Alpine structure.

In the next part (**part III**), we first use the low-temperature thermochronological data that already exists in the Central Pyrenees, to understand the feedbacks between the internal range uplift and its foreland and to investigate a possible Neogene acceleration in exhumation rate. Using a 3D thermal-kinematic modelling, we present a new interpretation of the data, by testing the effects of a significant wedge-top sedimentation during syn-orogenic times, and its incision by base-level fall in post-orogenic times. In the second chapter, the extent and thickness of syn- to post-orogenic sediments predicted in the southern flank of the Axial zone to the Southern Pyrenean foreland are tested by new low-temperature thermochronology data ((U-Th)/He on apatite data from the foreland fold-and-thrust belt), and their thermal modelling, using a new inversion model to predict time-temperature paths.

Finally, we present in **part IV** a study of the effects of wedge-top sedimentation at the early and late stages of the development of the Pyrenean range on the thrusting sequence of the foreland fold-and-thrust belt by 2D thermo-mechanical modelling of an orogenic wedge. In the first chapter, we apply to the growing wedge a first syn-tectonic sedimentation at the early stage of its development. In the second chapter, the wedge undergoes different amounts and styles of wedge-top sedimentation in its late evolution, reproducing the important conglomeratic sedimentation that covered the southern Pyrenean foreland in Oligocene times.

This multi-disciplinary approach will lead us to emphasize the influence of the coupling between surface processes and base level changes on the mountain belt evolution.

The next chapter will outline the different methods employed in this study: low-temperature thermochronology (AHe, AFT, ZHe), forward and inverse thermo-kinematic models, 2-D thermo-mechanical model.

Chapter I-2 Methodology

I-2.1 Introduction

As outlined in the introduction, a mountain belt is the locus of numerous interactions between tectonics and surface processes. We are focusing here on the evolution of the Pyrenean-Cantabrian range during their syn-orogenic and post-orogenic phases; therefore we have to consider the whole system, including processes of erosion/deposition, tectonics, and also drainage conditions (*e.g.* piedmont evolution) that are all linked together (Figure I-19). The diversity of processes involved implies to use multiple methodologies. In this thesis, characterization and quantification of the patterns of exhumation is performed using different low-temperature thermochronometers ((U-Th)/He on apatite and zircon, apatite fission track) as well as two different numerical models. The first is the 3D thermo-kinematic model *Pecube* (Braun 2003) that uses the thermochronological data to deduce exhumation as well as topographic evolution through time. It will be used here with in-situ data located in the southern central Axial Zone of the Pyrenees, and will help us to quantify exhumation rates and the late syn-orogenic to post-orogenic topographic evolution of the orogen. The results will be used as an input for the second modeling technique; in which the evolution of the foreland fold-and-thrust belt will be modeled with the 2D thermo-mechanical model *Sopale* (Fullsack 1995). This model is used to study the evolution of the foreland-fold-and-thrust belt and in particular the interactions between syn-tectonic sedimentation and the thrusting sequence at a critical period of orogen growth.

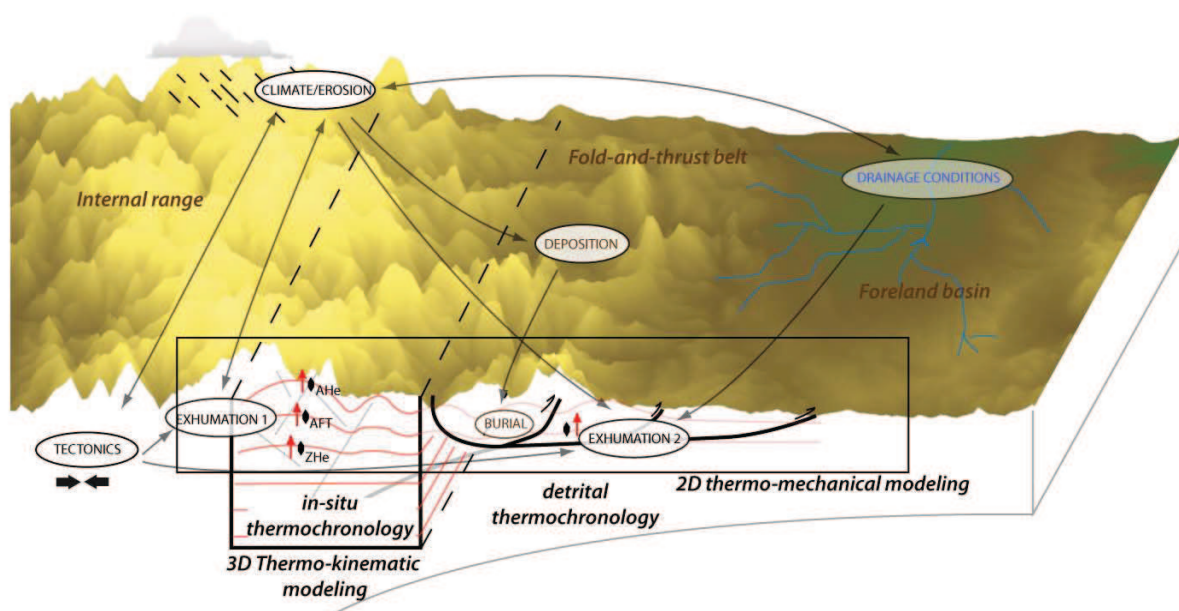


Figure I-19. Summary of the methods developed in this chapter and their relationship with the principal geological processes involved in the evolution of a mountain belt and its foreland.

In the following chapters, we will also investigate the evolution of the Pyrenean-Cantabrian mountain belt in terms of the timing and amount of exhumation/burial and therefore use different low-temperature thermochronometers : (U-Th)/He in apatite and zircon as well as fission-track analysis in apatites. For instance, the fission-track thermochronometer in apatite will inform us on when the sample passed through the 120°C isotherm (its closure temperature) and kinetic parameters as the track length and the width of the etch pits (Dpar) will return information about how long the sample stayed in the Partial Annealing Zone, from which we derive the rock exhumation rate. The use of several thermochronometers provide an efficient way to obtain robust time boundaries on the timing and rates of exhumation. In chapter III-2, (U-Th)/He thermochronology on zircon and apatite fission tracks allow us to delimit the timing of the onset and end of Alpine exhumation in the Cantabrian Mountains and also to locate the structural units that experienced most exhumation, shown by samples in which both thermochronometers were reset.

In the following sections, I will briefly review the basics of the different methods as well as their implementation in my thesis work.

I-2.2 Low-temperature Thermochronology

I-2.2a (U-Th)/He thermochronometry

The (U-Th)/He method is based on the measurement of α particles (^4He) produced during the radioactive decay of ^{238}U , ^{235}U and ^{232}Th , and on the diffusion of these particles within the host mineral. The closure temperature of the system was calibrated at 180 ± 20 °C (Reiners et al. 2002; Reiners et al. 2004) for zircon, and at 75 ± 15 °C (Wolf et al. 1998; Farley 2000) for apatite.

Several biases can interfere in the age determination, of which the principal one is α -ejection. The α -particles that are produced during the radioactive decay of U and Th can travel up to 20 μm in the crystal lattice. The stopping-distance is slightly different for apatite and zircon, with values of 19.68, 22.83 and 22.46 μm for ^{238}U , ^{235}U and ^{232}Th respectively in apatite and 16.65, 19.64, and 19.32 μm for ^{238}U , ^{235}U and ^{232}Th in zircons Farley et al. 1996. These stopping distances imply that the α -particles can be ejected from the crystal or be assimilated (implantation) from an adjacent crystal of apatite, zircon or monazite. The crystal should therefore be large enough (more than 60 μm) and well-shaped to be able to precisely infer the age from the U, Th and He measurements.

Thus, the size and shape of the mineral have to be taken into account by a correction factor called F_t Farley et al. 1996. Based on the assumption that the parent elements are homogeneously distributed in the crystal, F_t approximates the loss of ^4He by α -ejection (assuming that implantation is insignificant).

The F_t correction factor is calculated from measurements of the length, thickness and width of the grain and from the U/Th ratio, following the equations (Farley 2002):

$$F_T = 1 + a_1\beta + a_2\beta^2 \quad (5)$$

$$mean F_t = a_{238}^{^{238}\text{U}}F_t + (1 - a_{238})^{^{232}\text{Th}}F_t \quad (6)$$

With a_1 and a_2 geometric mineral coefficient; β the surface to volume ration; a_{238} derived from the Th/U ratio. Every individual He age is corrected by dividing it by its F_t factor.

I-2.2b Apatite (U-Th)/He thermochronometry

All apatites used in this study were prepared in the Grenoble laboratory. After crushing and seaving of the samples, the apatites were separated by magnetic (Frantz) and heavy liquid separation protocol that allows to separate the different minerals by densities (F. Senebier). The grains were then selected according to their morphology (euhedral, rounded) during picking selection under an optical microscope, and each grain was placed into a platinum basket. Particular attention was paid to the presence of inclusions of actinide-rich minerals such as zircons or monazite during grain selection. These minerals do not fully dissolve during the apatite preparation phase and therefore an excess in He concentration appears, leading to an overestimate in the apatite He ages. Therefore the clearest apatite grains were chosen.

He extraction and U and Th measurement were performed in the Thermochronology laboratory at Orsay-Paris-sud university in collaboration with Cécile Gautheron. Details of the analytical procedure for He extraction are provided in Chapter III-2.

Ejection factors have been determined using the Monte Carlo simulation technique of Gautheron et al.(2006) and the equivalent-sphere radius has been determined using the procedure outlined by Gautheron et al.(2010) (http://h0.web.u-psud.fr/UTHeNe_MonteCarloSimulation). The influence of damage caused by radioactive decay reactions in the apatite mineral on He retention has recently been demonstrated by Flowers et al. (2009) and Gautheron et al. (2009), who proposed methods to incorporate this effect in He-diffusion models. The α -recoil damage appears to lead to significantly increased retention of He and can be a predominant cause for errors in the age determination, especially in slowly cooled samples.

I-2.2c Zircon (U-Th)/He analysis

Zircons present several characteristics that make their (U-Th)/He age determination easier and more accurate than for apatite: it has high concentrations of U and Th and is one of the most resistant minerals to weathering. Finally, as zircons are much more U-rich than apatites, problems of inclusions are of less importance.

Sample preparation for zircon is the same as for apatite, except that they are found in the $>3.3\text{g.cm}^{-3}$ -density fraction after heavy liquid separation. Subsequently to measuring and picking, 3 grains per sample were selected using a binocular microscope and each of them was placed in a Nb tube. They were sent to the thermochronology laboratory of the University of Tübingen (Germany) for analysis. In general we analyzed 3 aliquots per sample. The samples were analyzed in the Patterson helium-extraction line at the University of Tübingen, and after Helium analysis the grain packages were sent to the University of Arizona at Tucson for U and Th measurements using an ICP-MS. The analytical procedure is detailed in Part II .

I-2.2d Apatite fission-track thermochronology

The fission-track dating technique is based on the recognition of crystal-lattice damage caused by the spontaneous fission of ^{238}U in Uranium-rich minerals like apatite, zircon and titanite.

Uranium decays through emission of α and β particles, but also by fission of the atom, creating a linear track of ionization damage in the mineral. Fission of ^{238}U nuclei occurs spontaneously, but it can also be induced in ^{235}U by neutron irradiation in a nuclear reactor.

Counting of spontaneous fission tracks permits quantifying how much decay of ^{238}U has occurred, the amount of tracks in a crystal will strongly depend on the initial concentration of ^{238}U , and the rate of ^{238}U decay. The thermochronometric age equation is:

$$t = \frac{1}{\lambda_d} \ln \left(\frac{\lambda_d N_s}{\lambda_f U_{238}} + 1 \right) \quad (7)$$

With λ_d the total decay constant for ^{238}U , λ_f the spontaneous fission decay constant for ^{238}U , N_s the number of spontaneous fission tracks, and U_{238} the number of ^{238}U atoms in the samples.

The ^{238}U concentration is determined by irradiating the sample with thermal neutrons in a nuclear reactor. This causes ^{235}U to fission, creating induced tracks that will provide an estimate of the amount of ^{235}U and, as the ratio 235/238 is constant, of the ^{238}U abundance. Initial sample preparation for fission-track analysis is similar to that for apatite (U-Th)/He. After separation, apatite grains were mounted in epoxy, polished to reveal an internal surface and etched with 5.5 M HNO_3 for 20 seconds at 21 °C. The external detector method was used to determine variations in U concentration between the grains. A low-U mica sheet (the external detector) is attached to the grain mounts before irradiation, and will register the induced fission tracks. After irradiation, the user counts the density of tracks on a given surface of the grain and on the same position on the mica that is fixed to the mount. Thus, the number of spontaneous (N_s) and induced (N_i) tracks is derived from the same grain and therefore results from the same concentration.

Finally, Zeta calibration (Hurford and Green 1983) is used to reduce uncertainties in the constants and in the neutron fluence received, as well as the counting technique that can vary according to the counter. In Grenoble, the calibration parameter Zeta was determined using Durango and Fish Canyon Tuff standards, dated by different methods ($\text{Ar}^{40}\text{-Ar}^{39}$, U-Pb) at 31.02 ± 0.22 Ma (McDowell et al. 2005) and 27.8 ± 0.2 Ma (Hurford and Hammerschmidt 1985), respectively. Standards from five different irradiations were counted and the resulting Zeta value is in the Table I - 1. The glass dosimeter used is IRMM-540.

| Irradiation code | standard | mean Zeta | Standard Error |
|------------------|----------|-----------|----------------|
| 04-2007 | Dur | 255.2 | 8.2 |
| | Dur | 228.6 | 7.3 |
| 13-2007 | Dur | 226.1 | 21.4 |
| | FCT | 255.7 | 30.7 |
| 12-2007 | FCT | 261.4 | 18.1 |
| | FCT | 180.5 | 19.2 |
| 05-2010 | Dur | 188.1 | 14.1 |
| | Dur | 184.8 | 7.6 |
| | FCT | 183.4 | 12.9 |
| | FCT | 189.1 | 13.4 |
| 09-2010 | Dur | 222.1 | 14.1 |
| | FCT | 263.2 | 16.1 |
| mean | Zeta | 217.9 | 3.5 |
| 12/01/2011 | | | |

Table I - 1 Zeta measurements from Durango (Dur) and Fish Canyon Tuff (FCT) standard apatites

The fission tracks can be repaired and even erased (annealing) when the crystal is kept at a temperature higher than 120 ± 10 °C; this temperature defines the upper limit of the Partial Annealing Zone (PAZ). This zone, between 60°C and 120 °C, is the temperature range where the crystal lattice damage will tend to repair by shortening from both ends, therefore, the longer the sample has stayed in the PAZ, the shorter the tracks will be. The PAZ is thus defined as the temperature range in which annealing takes place at rates that are comparable to track production. It has been shown by several annealing experiments that the annealing kinetics of fission tracks in apatite depend on the chemical composition (Green et al. 1986; Carlson et al. 1999; Barbarand et al. 2003), especially on the Chlorine content although cation substitution such as REE, Mn, Sr also appears to play a role. The track etch pit size, and particularly its length parallel to the c-

crystallographic axis (called D_{par}) can be a proxy for estimating the composition of an apatite. The experiments of Green et al.(1986) and Carlson et al. (1999) showed also that the annealing rate depends on the crystallographic orientation of the tracks in the crystal, the tracks parallel to the c-axis anneal slowly. Therefore, only track lengths parallel to the c-axis and D_{par} were measured at 1250-magnification, using an Olympus BH2 optical microscope and the FTStage 4.04 system (Dumitru 1993). As the tracks register the thermal history of the grain, their distribution is a key parameter in evaluating variable cooling rates.

I-2.3 Numerical modeling

I-2.3a 3-D Thermo-kinematic modeling

There is now an important amount of thermochronological data in south-central Pyrenees that have generally been interpreted and modeled independently. In Chapter III-1, I use this important dataset as an input for thermo-kinematic models to constrain the complete denudation and topographic history of the area from Eocene to present times.

Model description

The thermo-kinematic modeling is based on *Pecube* (Braun 2003; see also Braun et al. in review), a finite-element code that solves the heat-transfer equation (Carslaw and Jaeger 1959) in 3 dimensions, following this formulation:

$$\rho c \left(\frac{\partial T}{\partial t} + v \frac{\partial T}{\partial z} \right) = \frac{\partial}{\partial x} k \frac{\partial T}{\partial x} + \frac{\partial}{\partial y} k \frac{\partial T}{\partial y} + \frac{\partial}{\partial z} k \frac{\partial T}{\partial z} + H \quad (8)$$

With $T(x,y,z,t)$ the temperature ($^{\circ}\text{C}$), ρ the rock density (kg.m^{-3}), c the heat capacity ($\text{J.kg}^{-1}.\text{K}^{-1}$), v the rock uplift velocity with respect to the base of the crustal block (km.Myr^{-1}), and H the radioactive heat production (W.m^{-3}).

This equation is solved in a crustal block for a prescribed exhumation (rock advection) and topographic history. In this version of the code, rock advection is controlled by a single fault, carrying a velocity field, with a variable geometry and located outside the model domain, to avoid boundary effects.

Topographic changes are implemented by modifying two parameters (called here amplitude and filling) applied to a Digital Elevation Model of the present-day topography. The amplitude $A(t)$ can be assumed as the paleo-relief, varying from a plateau to the present-day relief (incised valleys in the case of the Pyrenees). In the modeling study presented in chapter 3 $A(t)$ was fixed to 1, *i.e.* the paleorelief is at the present-day relief, because we found that the thermochronological dataset could not sufficiently resolve this parameter.

The filling factor $F(t)$ was specifically added to the code to simulate the deposition of prograding conglomerates on the south-central Pyrenees area. It imposes a minimum value of the elevation on each point of the grid to reproduce infilling and excavation of the Pyrenean paleo-valleys (see Figure I-20), through the equation:

$$z_{x,y,t} = \max(z_{x,y,t_{\text{now}}} A(t), F(t)) \quad (9)$$

With z the elevation through time, $A(t)$ the amplitude of the relief and $F(t)$ the reference filling value. The value of $F(t)$ was explored by inversions presented in Chapter III-1.

Other important parameters have to be defined, in particular the basal and surface temperatures, heat production and elastic thickness; they can be fixed or inverted as well.

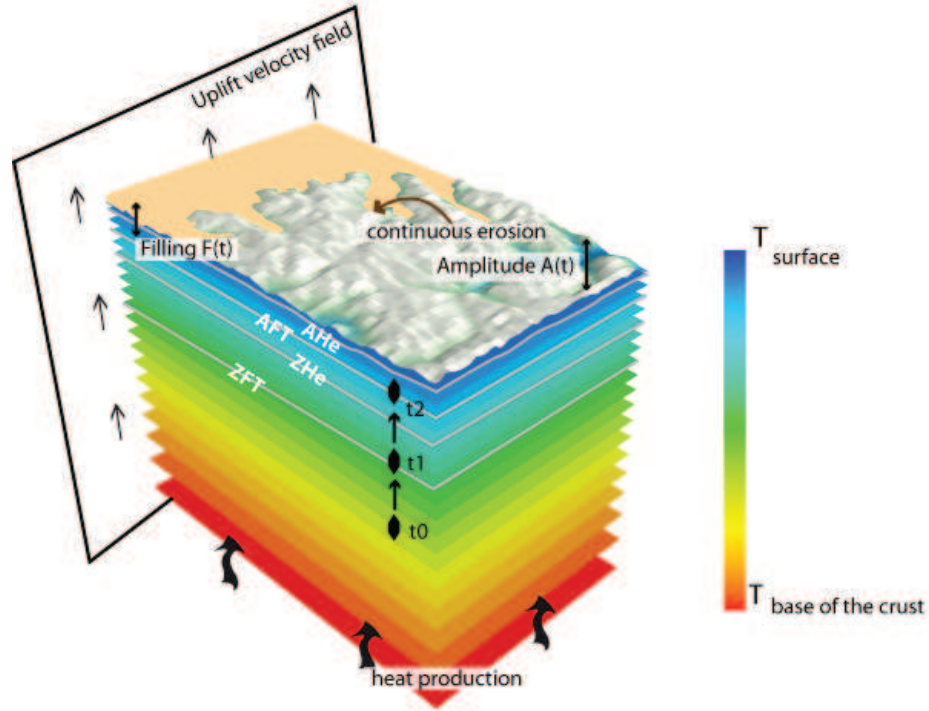


Figure I-20. Schematic representation of the parameters controlling a *Pecube* model run.

For each node, *Pecube* calculates time-temperature paths for particles that end up at the surface. Thermochronological age-prediction models are used to calculate thermochronometric ages that are compared to the input dataset. Here, we use the AFT annealing model of Stephenson et al. (2006), the ZFT annealing model of Tagami et al. (1998), and the AHe diffusion model of Farley (2000) for reasons outlined in Chapter III-1.

The calculated ages are then compared to the input data to estimate the fit of the model. The statistic evaluation of this misfit is defined by the objective function (Glottzbach et al. 2011; Braun et al. in review) :

$$\mu = \sum_{i=1}^n \left(\frac{m_i - o_i}{\sigma_i} \right)^2 \quad (10)$$

With μ the misfit value, n the number of data and, for each data point i , o_i the observed value (age or mean track length), m_i the modeled (predicted) value, and σ_i the observed (1 σ) error.

This approach is very useful to set first-order constraints on exhumation scenarios but a precise evaluation of each parameter (such as exhumation rates and topographic parameters at different timesteps) requires an inverse approach.

Inverse modeling

For inverse modeling, *Pecube* was coupled with the Neighborhood Algorithm (Sambridge 1999b; a). This approach defines an optimal model (*i.e* a best-fitting set of parameters) within a predefined parameter space, and then evaluates the level of constraint that the data resolve for each parameter. These two steps (Figure I-21) are called sampling stage (Sambridge 1999b) and appraisal stage (Sambridge 1999a), respectively.

In more detail, during the sampling stage the parameter space is divided into Voronoi cells centered on each model. During an initial iteration, 96 randomly chosen forward models are run and their misfit is assessed using Equation 5. Subsequent iterations also use 96 forward models but for which the parameter space is gradually restricted to the best-fitting 83% of models from the previous iteration. Note that this resampling value is high, in order not to force the convergence and to fully explore the parameter space, just eliminating the most unlikely parameter values. At the end of the sampling stage, we thus have a large collection of models that converge to an optimal combination of parameter values as a function of their misfit (see scatter plots Chapter III-1), but these solutions are strongly dependant on the calibration of the sampling stage itself. Indeed, with this procedure, it is obvious that the number of iterations should be proportional to the number of free parameters. For instance, inversions of 10000 models and of 20000 models returned roughly the same results but with a much better defined convergence in the second case. The limit to the number of models run is set by the computational time, which can become very long if the user does not have access to a large number of CPUs to run the code.

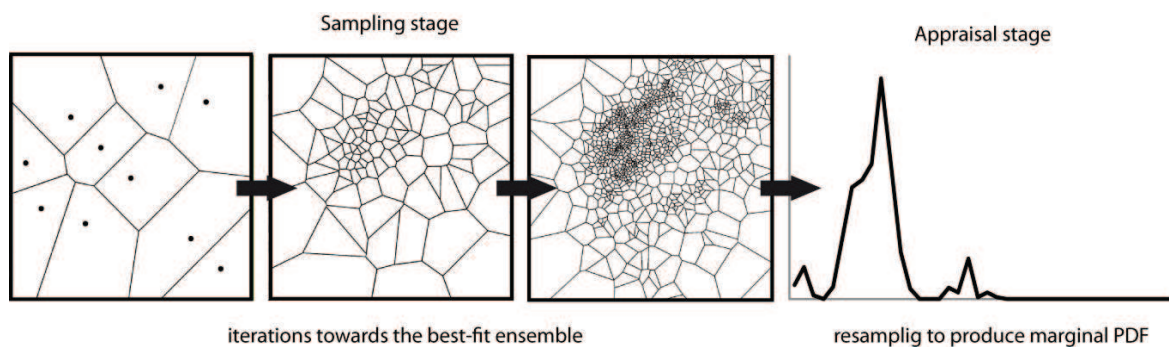


Figure I-21. Representation of the sampling stage and appraisal stage. At the initial stage, the parameter space is delimited by large Voronoi cells, that are precising through iterations. The sampling stage allows to define a best-fit model ensemble (combination of parameter values) and then the appraisal stage calculates the probability density function of each parameter value.

To more quantitatively assess these results, a Bayesian estimate of parameter values is calculated during the appraisal stage by re-sampling the models and calculating the marginal posterior probability density function (L) of each parameter, following the equation (Sambridge 1999a):

$$L = \prod_{i=1}^N \exp\left(-\frac{1}{2} \sum_{j=1}^M \mu\right) \quad (11)$$

The PDF directly provides a measure of the distribution of likely parameters value, in most of the case with one or two peak-values. From the PDFs, we can graphically infer the optimal parameter value (peak) and deduce its incertitude by taking the values at the half-gaussian height of the peak.

I-2.3b 2D thermo-mechanical modeling

In order to reproduce the development of the southern pyrenean wedge (Chapter IV-2), we use the Arbitrary Lagrangian Eulerian (ALE) finite-element numerical model Sopale (Fullsack 1995), which computation of deformation of visco-plastic materials at a range of scales. The model has been used to study geodynamic processes at large scale (lithosphere-asthenosphere) and at the scale of the upper crust (see examples in Figure I-22). Sopale is a thermo-mechanical model, computing both mechanical deformation and thermal evolution. Therefore the temperature field and the rheologies are coupled to control the mechanical behavior. The materials are deforming primarily by the stress exerted by the boundary conditions, and according to their own rheological properties. In our case, we will consider the upper crustal scale, confining our materials to a plastic temperature independent rheologies.

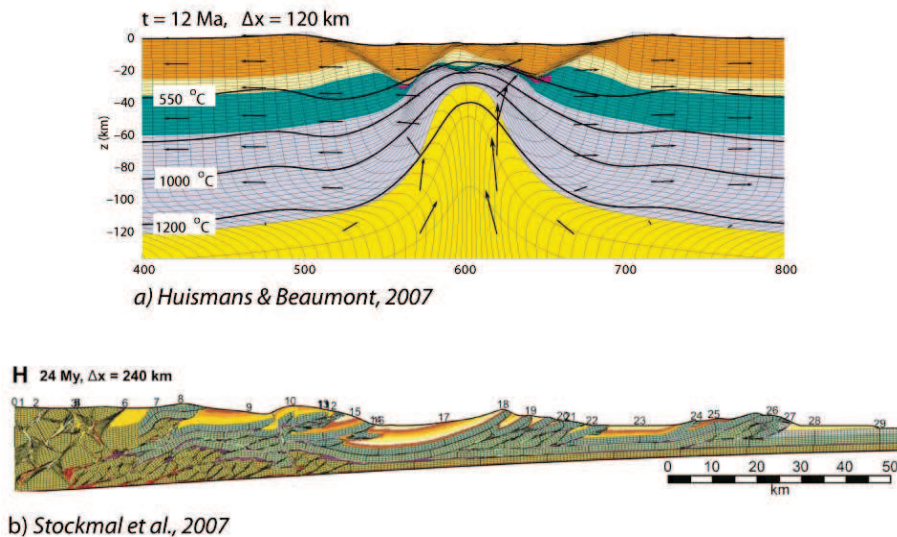


Figure I-22. Examples of different scales of modeling using Sopale. a) Modeling of extension at lithospheric scale (Huisman and Beaumont 2007). b) Modeling of the evolution of a fold-and-thrust belt with surface processes at the upper crustal scale (Stockmal et al. 2007).

The model is used to solve the creeping-flow deformation of plastic materials in 2 dimensions (Fullsack 1995; Willett 1999a; Huismans and Beaumont 2003). The equation of motion for the creeping-flow deformation of materials is governed by the quasi-static force balance and conservation of mass equations:

$$\frac{\partial P}{\partial x_j} + \frac{\partial}{\partial x_i} \left(\eta_{eff} \frac{\partial v_j}{\partial x_i} \right) + \rho g = 0, j=1, 2 \quad (12)$$

With P the pressure, η_{eff} the effective viscosity, v_j the components of velocity, ρ the density, and g the vertical gravitational acceleration.

The constitutive law relating the stress to strain rate is:

$$\sigma = P \delta_{ij} + 2\eta_{eff} \dot{\epsilon}_{ij} \quad (13)$$

With $\dot{\epsilon}_{ij}$ the strain rate tensor defined by:

$$\dot{\epsilon}_{ij} = \frac{1}{2} \left(\frac{\partial v_i}{\partial x_j} + \frac{\partial v_j}{\partial x_i} \right) \quad (14)$$

Material properties are mainly represented by the density, the cohesion and the internal friction angle (Φ). The values used in Part IV correspond to values that have been used previously by Stockmal et al (2007) to model fold-and-thrust belt evolution.

To localize strain in plastic shear zones, the model uses the Drucker-Prager yield criterion (equivalent to Mohr-Coulomb) to model the plastic behavior for incompressible deformation in plane strain. Yielding occurs when:

$$(J'_2)^{\frac{1}{2}} = p \sin \phi_{eff} + c \cos \phi_{eff} \quad (15)$$

Where $J'_2 = \frac{1}{2} \sigma'_{ij} \sigma'_{ij}$ is the second invariant of the deviatoric stress, p is the dynamic pressure (mean stress) c is the cohesion and ϕ_{eff} is the effective internal friction angle. The values of c and ϕ_{eff} were chosen to reproduce frictional sliding of rocks. The angle ϕ_{eff} includes the variations of Pore fluid pressure (P_f), which reduces the effective stress and is defined by

$$P \sin \phi_{eff} = (P - P_f) \sin \phi \quad (16)$$

Several mechanisms can lead to brittle weakening of rocks (Huismans and Beaumont 2007 and references therein), including cohesion loss, mineral transformations, and increased pore fluid pressures. In the models presented here strain weakening is introduced using a parametric approach. The friction angle $\phi_{eff}(\epsilon)$ decreases linearly with increasing strain in the range $0.5 < \epsilon < 1.0$, where ϵ represents the square root of the second invariant of deviatoric strain (Figure I-23).

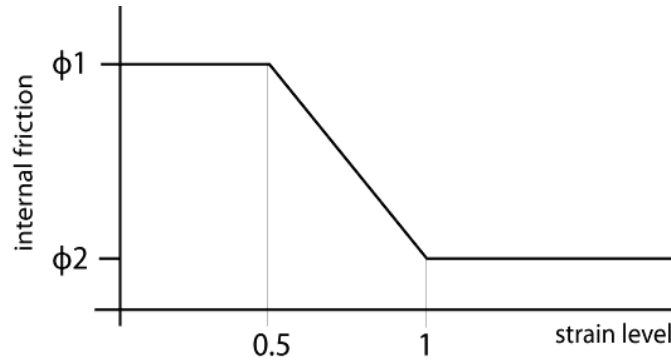


Figure I-23. Strain softening behavior of materials used in the thermo-mechanical models. In Part IV, it is applied to materials I and II. The material has a defined internal friction angle until a certain state of strain is attained. It then decreases linearly towards the lower friction angle and stays with that value until the end of the run.

Three main mechanisms can lead to strain weakening of rocks (see Huismans and Beaumont 2007 and references therein) : cohesion loss of the material, mineral transitions that affect the internal friction angle , and increase in pore fluid pressure. Moreover, Huismans and Beaumont (2007) showed from numerical tests that the main controlling parameter on the model behavior is the value of ϕ_{eff} when softening starts, then transition to the weaker state is rapid due to the important positive feedback between strain softening and strain accumulation.

To compute the deformation at large scales, two grids are superposed: an Eulerian and a Lagrangian grid (ALE formulation, Fullsack 1995). The Eulerian grid is the finite element discretization grid and is used to compute the velocity and the pressure. The Lagrangian grid carries material properties and the accumulated strain. The Lagrangian grid moves according to the velocity field calculated on the Eulerian grid.

Part II- Alpine exhumation of the Cantabrian Mountains

The low-temperature thermochronological data can give a good estimate of the timing and amount of uplift of the Pyrenean-Cantabrian mountain range. In particular, we observed in the introduction that the AFT data were revealing a progression of exhumation from north to south in the Pyrenees. It also shows that the signal of a continuation of this alpine exhumation is lost around the central Cantabrian mountains (with a few Cenozoic ages) while the Western Cantabrian Mountains present only Mesozoic ages. We can interpret these different dates as showing an east-west propagation of the exhumation of the Pyrenean-Cantabrian belt, but there is still a lack of data in the Eastern (Basque-Cantabrian basin) and Central Cantabrians. Moreover, the central Cantabrian structure has been revealed by the interpretations of the deep seismic reflexion profiles ESCI-N, but the surface evolution is still enigmatic, mostly because of the overprinting of Alpine and Variscan structures.

We will present in this chapter new apatite fission-track (AFT) data and (U-Th)/He measurements on zircons (ZHe) to investigate the Alpine exhumation of the central part of the Cantabrian Mountains. In the future, this study will be combined with the data produced by Luis Barbero (University of Cadiz) to publish a consistent low-temperature thermochronological dataset of the area, and discuss the consequences of these data on the structure of the range.

II.1 Introduction

From Eocene to Miocene times, Pyrenean deformation linked to the Iberian and European plate convergence is known to have propagated from the Eastern Pyrenees to the Cantabrian mountains via the Basque-Cantabrian basin. This Mesozoic basin with a complex history does not allow to follow clearly the Alpine (e.g. Eocene to Miocene N-S compression phase) patterns of exhumation to the west. Nevertheless, several geophysical studies have imaged the southern Pyrenean contractional front continuing westward until the center of the Cantabrian mountains, where its orientation turns towards the north (e.g. Martin-Gonzalez and Heredia 2011). Moreover, the ESCI-N deep seismic reflection profiles have permitted to image the deep structure of the Cantabrian Mountains and adjacent Bay of Biscay margin in some details (Alvarez-Marron et al. 1996; Pulgar et al. 1996; Fernández-Viejo et al. 1998; Fernández-Viejo et al. 2000; Gallastegui 2000; Pedreira et al. 2003). The most common interpretation is that north-verging underthrusting of the Iberian lower crust and mantle, well established under the Pyrenees, is continuous towards the west under the Cantabrian Mountains. The ESCIN-2 seismic profile, in the central part of the range, suggests for the upper crustal structure a single south-vergent wedge, underlain by a crustal-scale décollement and thrust ramp, emerging at the southern front of the mountain belt (Figure II-1). To the south of the Cantabrian Mountains, the Duero foreland basin comprises Cenozoic syn- to post-orogenic sediments that are not precisely dated, rendering them of limited use to constrain the age of Cenozoic deformation. Moreover, the Variscan orogeny has strongly imprinted the Cantabrian basement rocks, making the Alpine folds and faults very difficult to observe in the field. The shortening calculated from structural reconstructions is maximum in the central part of the Cantabrian mountains (96 km, Gallastegui 2000) and the timing of deformation has been constrained by several field studies onshore and tectono-sedimentary observations offshore (Alonso et al. 1996; Alvarez-Marron et al. 1996; Pulgar et al. 1999). N/S compression is thus estimated to have affected the Cantabrian Mountains from Late Eocene until Oligocene-Miocene times. Thermochronological ages published in the western Cantabrians (Carrière 2006; Grobe et al. 2010; Martin-Gonzalez et al. 2011) do not show any evidence of significant Alpine exhumation in the Asturian Arc, west of our study area. Published apatite fission-track (AFT) ages range from Triassic to upper Cretaceous (cf. Figure I-13), and there is a lack of data in the central Cantabrians, where the Alpine shortening is supposed to be the most important; only two AFT samples to the east have yielded Oligocene ages (Carrière 2006).

Thermochronology is used here to help constraining both the timing and pattern of Alpine exhumation in the Cantabrian Mountains. This chapter aims to unravel the Alpine history by dating more precisely the main episode of deformation as well as quantifying the amount of Alpine exhumation. To that purpose, we present in the following apatite AFT ages and (U-Th)/He analyses on zircons that allow us to clarify the Alpine deformation history and to add some constraints on the structural cross-section. Finally, the last section reports (U-Th)/He

measurements on apatites which were not used in the interpretation due to their poor reproducibility, and discusses potential reasons for their scatter.

II.2 Geological background

The present-day Cantabrian Mountains represent the western continuation of the Pyrenean orogen and result from the collision of the Iberian plate with the European plate. To the east the Iberian plate has underthrust the European plate to build the Pyrenees (Choukroune and ECORS Team 1989; Muñoz 1992; Vergés et al. 1995; Teixell 1998; Pedreira et al. 2003). To the west, the Cantabrian Mountains reflect inversion of the northern Iberian margin rather than a full continental collision, the onset of margin inversion occurred within the Iberian plate itself. The Cantabrian Mountains are bounded by the Iberian massif to the west, the Mesozoic Basco-Cantabrian basin to the east, and the Duero foreland basin to the south.

II.2-1 Structural inheritance

To understand the Cenozoic deformation of the Cantabrian Mountains (as shown in Figure II-1), one needs to take into account that this area experienced a long-term polyphased deformation history, starting with the Variscan orogeny.; followed by two phases of Mesozoic extension and finally the Alpine deformation phase. The Variscan orogeny, which affected the Cantabrian Mountains during the Carboniferous, had a major impact on the structure of the belt. It led to the construction of the western arcuate structure called the Asturian Arc (Julivert 1971; Pérez-Estaún et al. 1988). In the center of the Asturian Arc, the Cantabrian zone represents the external part of the Variscan belt. The Variscan phase of deformation in that area is driven by east-west compression that produced a thin-skinned imbricate thrust structure progressing from west to east. The Central Coal Basin unit and Ponga units (Picos de Europa area) are therefore the external units of the Variscan belt. These units were then unconformably overlain by Stephanian sandstones that date the end of Variscan deformation. The orogenic episode led to the development of major E/W trending thrusts in the eastern and central part of range and N/S trending arcuate faults to the west; most of the large structures observed today were formed during this first orogenic event. Some of the E/W faults in the Eastern Cantabrians were reactivated during the subsequent phase of Mesozoic extension as well as during the Alpine convergence phase (Alonso et al. 1996; Pulgar et al. 1999).

The first Mesozoic extension episode started during Permian and Triassic times (Lepvrier and Martinez-Garcia 1990) and a second phase affected the area from the Late Jurassic to the early Cretaceous, consequently to the opening of the Bay of Biscay (Olivet 1996). Extension was maximum during Albian-Aptian times, leading to create and reactivate E-W faults that define horst

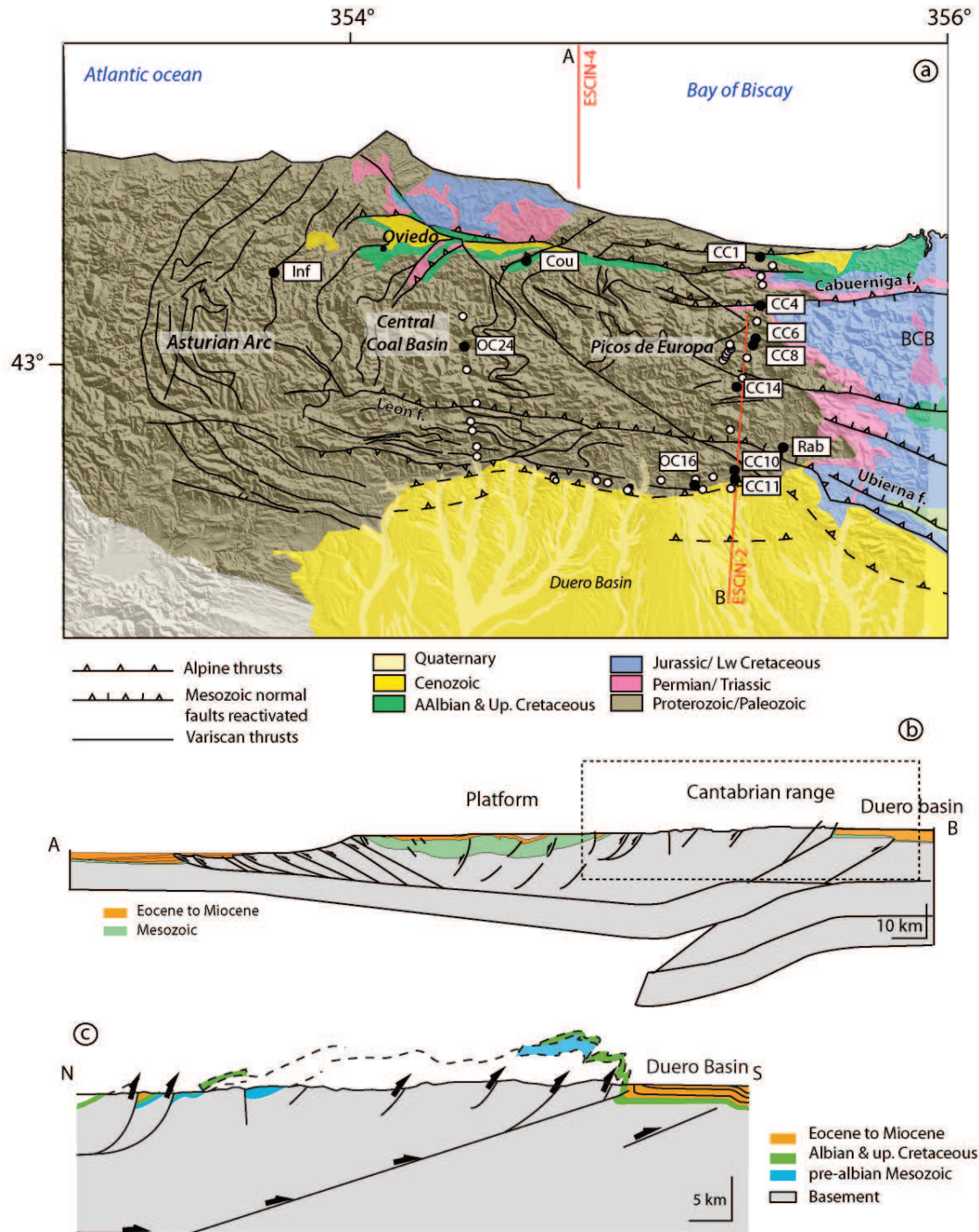


Figure II - 1 (a) Geological map of the Cantabrian Mountains with relief from the SRTM digital elevation model. White dots represent samples that could not be analyzed because of a lack of apatites. The black dots are the sampling sites where AFT and ZHe analysis could be performed. (b) Crustal-scale cross section based on the ESCIN-2 and ESCIN-4 profiles (see map for localization); modified from Gallastegui (2000); (c) upper crustal cross-section showing Alpine onshore structures, modified from Pulgar et al. (1999). BCB: Basque-Cantabrian Basin.

and graben systems, mostly in the present-day eastern Cantabrian Mountains and in the Basque-Cantabrian Basin. The Mesozoic basins then experienced a long phase of subsidence before the Cenozoic reactivation of the structures. This last inversion is striking in the Oviedo Basin, of which the normal faults were inverted to create a piggy-back Tertiary basin propagating toward the south.

II.2-2 Alpine deformation in the Central Cantabrians

The Alpine phase of deformation initiated in the northern Cantabrian margin during the Late Eocene with inversion of extensional structures to form a south-vergent accretionary wedge (Figure II-1b). Dating of this phase is constrained by offshore syn-tectonic sediments that are late Eocene in age (Alonso et al. 1996, Alvarez-Marron et al. 1997, Gallastegui 2000). The end of N-S compression can be extrapolated from the age of the uppermost syn-tectonic and the lowermost post-tectonic strata south of the southern front of the range, in the Duero basin (Figure II-2).



Figure II - 2 Panoramic view of the southern Cantabrian mountain front, with Oligocene-Miocene conglomerates of the Cuevas alluvial system, showing impressive growth strata. Further south, these syn- tectonic sediments are unconformably overlain by horizontal Miocene sediments (Photo Peter Van der Beek).

From the geological map (Guardo, 1:50000) syn-tectonic strata are dated to the Paleogene-Neogene, and are unconformably overlain by Late Miocene strata. Their absolute age still lacks precision due to their continental depositional environment, which renders biostratigraphic dating of these rocks difficult. Absolute dating of the syn-tectonic sediments is in progress at the University of Oviedo. The structural cross-section published by Alonso et al. (1996, Figure II-1c) is based on field observations. These authors interpreted the structure of the range as a crustal-scale fault-bend-fold accommodated by a major ramp that roots at 15-20 km depth and emerges at the southern front of the belt. From the bending of the Mesozoic layers, the authors extrapolated a dip of the ramp of 18° towards the north.

All other Alpine thrusts that emerge at the surface are north verging. They mainly crop out in the northern and southern parts of the section. That is where they are visible because they offset Mesozoic sediments; in the center of the belt, where only deformed basement crops out, Alpine

thrusts are very hard to distinguish from Variscan ones. The deformation is of thick-skinned style, and cover and basement deformed jointly during the Alpine deformation.

II.2-3 Evolution of the Duero foreland basin

The Duero basin is a large intracontinental basin that drains several mountain ranges surrounding it: the Iberian Chain to the east, the Cantabrian Mountains to the north and the Central System to the south. Before the Alpine uplift of these ranges, the basin was open to the north and east and sedimentation was marine to terrestrial (Santisteban et al. 1996). The onset of uplift of the western Pyrenean massifs in Paleocene times closed this connection and the basin became endorheic. The south-west of the basin re-opened toward the Atlantic by capture of the fluvial networks in the early Miocene. From that moment, exorheic drainage extended progressively but in the north-east, alluvial fans still continued to be connected to central lacustrine environments. Complete capture of the basin only occurred in late Miocene-Pliocene times (Mediavilla et al. 1996).

The Northern part of the basin has been filled by 2.5 km of Oligocene to Miocene deposits, most of which were sourced from the Cantabrian Mountains. Alpine loading within the Cantabrian Mountains led to a flexural isostatic subsidence of around 1.5 km (Alonso et al. 1996). Assuming that the basin was at sea level before the onset of Alpine deformation; filling and subsidence values account for the present-day elevation of the basin of 1000m. The basin is thus significantly overfilled, which can be explained by its endorheic character during much of the Cenozoic, as well as its semi-arid and little erosive climate.

At the Cantabrian Mountain front, the Oligocene-early Miocene infilling of the basin was perturbed by the development of a fault-propagation fold on top of the main crustal ramp. This is especially clear in the eastern part of the range, where the deposits show spectacular growth strata geometries (Figure II - 2). These formations record the evolution of the Cantabrian drainage system, with two groups of alluvial fan deposits. In the oldest one, pebble provenance indicates a distant source at least in the central parts of the range, whereas in the younger alluvial fans, the sources of the deposits were identified mainly in the frontal Cretaceous limestones and Carboniferous massifs (Alonso et al, 1996), illustrating the migration of the source from the hinterland to the foreland.

II.3 Methodology

II.3-1 Sampling sites

Two field trips were necessary to collect sufficient material to produce the ages; all the collected samples are plotted in Figure II-1a. The initial sampling strategy was to collect along the ESCIN-2 seismic profile, from the Atlantic coast to the Duero basin. We collected ~20 samples, mostly in

sandstones (Triassic, Albian and Stephanian); one sample comes from the Peña Prieta granodiorite and we sampled a vertical profile as well (e.g. 6 samples along a profile from the valley bottom to mountain top, with ~1200 m difference in height) in the center of the section. However, all but 3 samples (CC4, CC14 and CC10) proved to be nearly devoid of apatite.

The subsequent sampling trip (~30 samples) targeted to sample a N-S profile across the Central Coal Basin (Westphalian and Stephanian sandstones), an E-W profile along the northern limit of the Duero basin (Stephanian sandstones, Cretaceous Utrillas Fm. and Paleogene Vegaquemada Fm.), and also to go back to samples which provided a few apatites from the first field trip. We also sampled in the syn-tectonic conglomeratic deposits of the Cuevas system (on top of the Vegaquemada Fm.), at the southern front of the eastern section shown in Figure II-2.

We collected and prepared 50 samples of > 5 kg each, but only 5 of these produced sufficient apatites for fission-track analysis (see Figure II - 1a for location), while most of the samples yielded sufficient high-quality zircons for ZHe dating. The stratigraphic position of the samples that provided usable amounts of apatite and zircon is shown in Figure II-3.

II.3-2 Apatite Fission-Track dating

For this study, apatite grains were separated from overall fine to medium grained sandstone samples using heavy liquid and magnetic separation techniques (cf. Chapter 2). Apatite aliquots were mounted in epoxy, polished to expose internal crystal surfaces, and etched with 5.5 M HNO₃ for 20 seconds at 21 °C. Low-U muscovite sheets were fixed to the mounts, to be used as external detectors, and then samples were sent for irradiation in the FRM II Research Reactor at the Technische Universität München (Germany). Apatite samples were irradiated together with IRMM 540R dosimeter glasses and Durango and Fish Canyon Tuff age standards. After irradiation the mica sheets of all samples and standards were etched for 18 min at 21 °C in 48% HF. The samples and standards were counted dry at 1250-magnification, using an Olympus BH2 optical microscope and the FTStage 4.04 system of Dumitru (1993). Due to the low yield of grains in most samples, as many grains as possible were counted for each sample.

Fission track ages were calculated using the zeta-calibration method and the standard fission-track age equation (Hurford and Green, 1983). The X²-test and age dispersion (Galbraith and Green 1990; Galbraith and Laslett 1993) were used to assess the homogeneity of AFT ages. Two samples (both from the southern front) yielded dispersed ages incompatible with a single age component, the grain-age distributions of these samples were decomposed into major grain-age components or peaks, using binomial peak fitting (Stewart and Brandon 2004).

We were able to measure horizontal confined track lengths in three samples. The widths of tracks crossing the etched internal surface (Dpar) were measured using the same digitizing techniques as used for measuring track length.

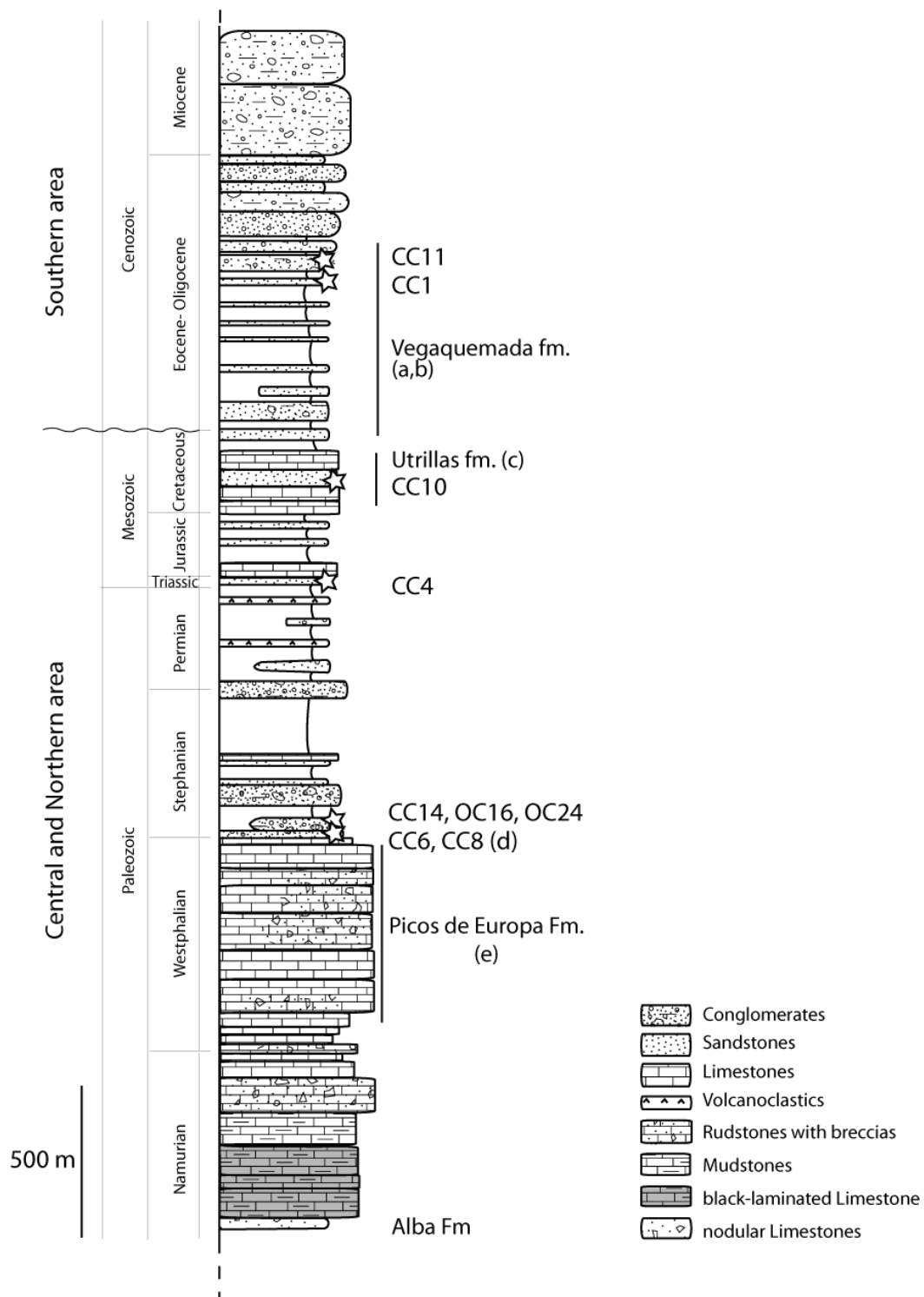


Figure II - 3. Synthetic stratigraphic column with sample positions. Letters refer to the photos of characteristic sampled formations presented in Figure II- 4. Modified after Garcia-Ramos and Gutierrez-Claveral (1995) ; Alonso et al.(1996) ; Gomez-Fernandez et al.(2000) and Herrero et al.(2010).

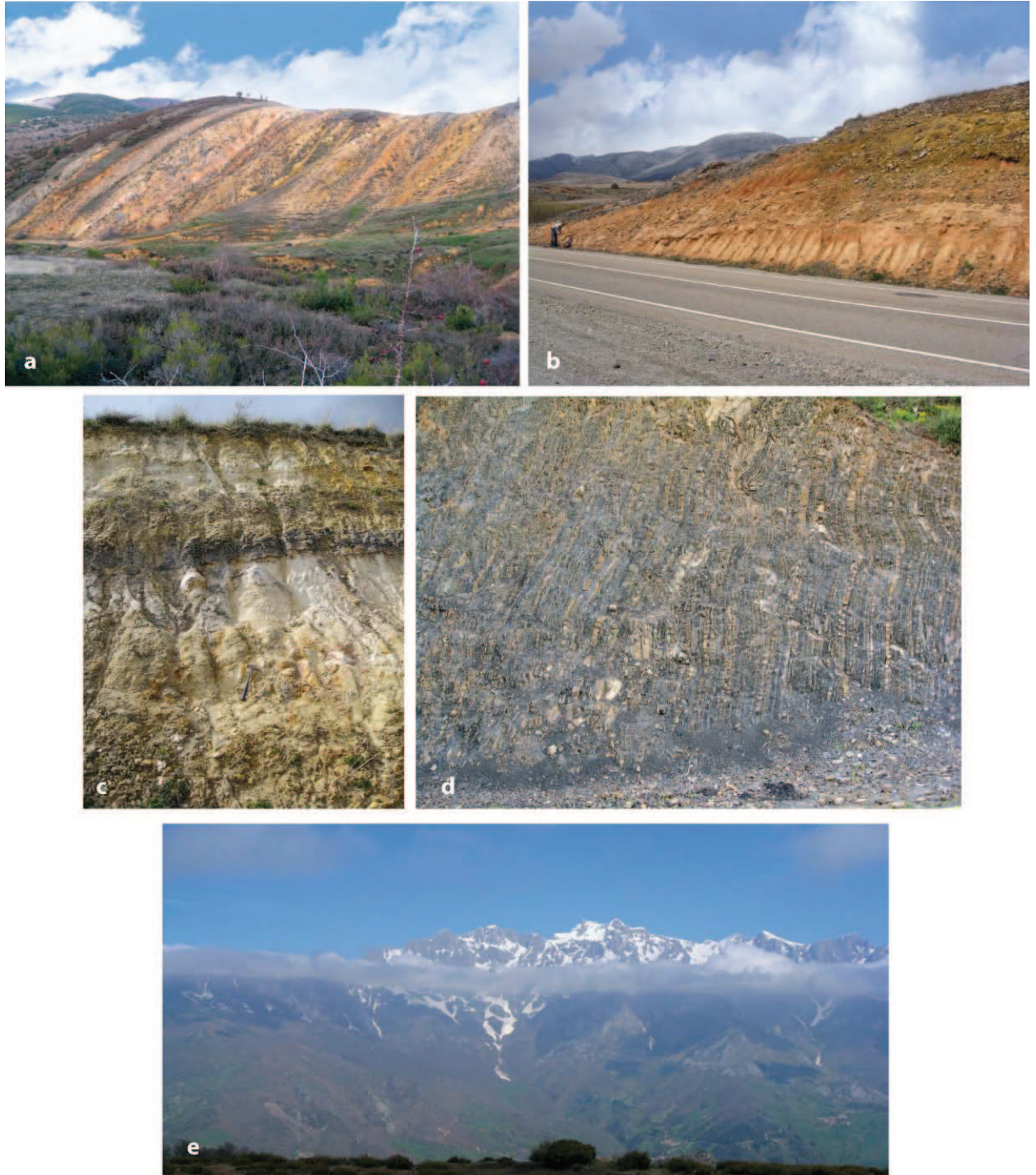


Figure II - 4 Field photos showing characteristic formations of the Cantabrian Mountains area. White letters localize these formations on the stratigraphic column of Figure II - 3. A) Cuevas alluvial fan deposits ,b): Vegaquemada Fm. at the southern front, sampling site of CC11; c):Upper cretaceous Utrillas Fm., at the southern front, located between the eastern profile and CCB profile; d):Stephanian turbidites (center of the eastern profile), photo of the CC8 sample outcrop; e): View of the Picos de Europa limestone massif near by the city of Potes.

II.3-3 (U-Th)/He analyses on zircons

Among the samples yielding sufficient zircons, 6 were selected for (U-Th)/He dating, according to the quality of the grains and their geographic distribution along the eastern cross-section.

Clear and undisturbed zircon grains without inclusions were selected using a binocular microscope. The grain dimensions were measured for the calculation of the α -correction factor F_t (Farley et al. 1996). Single grains were subsequently packed in Nb-tubes for (U-Th)/He analysis. We analyzed 3 aliquots per sample in the Patterson helium-extraction line at the University of Tübingen (Germany), which is equipped with a 960 nm diode laser to extract the helium gas. Zircon grains were heated for 10 minutes at 20 Amps. Each grain was heated and analyzed a second time to make sure that the grain was degassed entirely in the first step. The re-extracts generally released <1% of the amount of gas released during the first step. After helium analysis, the grain packages were sent to the University of Arizona at Tucson (USA) for U and Th measurements using an ICP-MS. The analytical error of the mass spectrometer measurements are generally very low and do not exceed 2%. In contrast, the reproducibility of the sample age constitutes a much larger error. We therefore report the mean (U-Th)/He age and the standard deviation of the measured aliquots as the sample error.

II.4 Results

Results are reported in Tables 1, 2 and 3, plotted on the geological map (Figure II - 5) and will also be presented on structural cross sections (Figure II - 7) in order to discuss the structural implications of these new data. In the following, ages will be interpreted in terms of Alpine exhumation, therefore we will name refer to Cenozoic ages as “reset” ages.

Apatite fission-track results show three samples with a single grain-age population and two with multiple populations (Figure II-6 and Table II-3). Measurements of mean track length were only possible for samples OC16, CC10 and OC24 (Figure II - 6); even though only a small number of lengths could be measured, they all show very short mean track lengths implying slow cooling through the AFT Partial Annealing Zone (PAZ). In contrast, the zircon (U-Th)/He ages are very well constrained, only the CC4 sample has more than 10 % uncertainty. Interestingly, this sample is located between a sample to the north with old (Triassic) ages and the group of young samples to the south; it may thus record partial resetting of the ZHe system.

| sample | Formation/ stratigraphic age | lat | Lon | elevation (m) | no grains | P_s (N s) 10^5 cm^{-2} | P_i (N i) 10^5 cm^{-2} | P_d (N d) | P (X^2) (%) | age disper- sion | Central age ($\pm 1 \sigma$, Ma) | MTL (μm) | no tracks | sd (μm) | Dpar (μm) |
|-------------|---------------------------------|-------|-------|------------------|--------------|---------------------------------------|---------------------------------------|--------------|----------------------|------------------------|---------------------------------------|-----------------------|--------------|-------------------------|---------------------------|
| CC4 | Triassic (220 Ma) | 43.25 | -4.58 | 421 | 20 | 6.662 (888) | 14.292 (1905) | 5.51 (4192) | 18.8 | 0.11 | 30.4 \pm2.1 | | | | |
| CC14 | Stephanian (300 Ma) | 43.05 | -4.65 | 1125 | 14 | 3.81 (197) | 8.664 (448) | 5.522 (4192) | 56.9 | 0.02 | 28.9\pm2.9 | | | | |
| OC16 | Stephanian (300 Ma) | 42.79 | -4.78 | 1116 | 35 | 16.36(2388) | 8.6022 (1256) | 6.44 (4262) | <<1 | 0.24 | 128.8\pm7.7 | 8.979 | 26 | 1.99 | 1.3 |
| CC10 | Utrillas fm. Albian (110 Ma) | 42.83 | -4.65 | 1203 | 29 | 21.11 (3509) | 11.142 (1852) | 5.515 (4292) | <<1 | 0.29 | 124.5\pm10.0 | 10.113 | 31 | 2.02 | 1.4 |
| OC24 | Stephanian (300 Ma) | 43.13 | -5.56 | 528 | 41 | 5.354 (1182) | 13.099 (2892) | 6.467 (4262) | 13.2 | 0.12 | 26.8\pm1.3 | 11.201 | 12 | 2.74 | 1.82 |

Table II - I Apatite fission track results for the Cantabrian Mountains. ρ_s and ρ_i are the measured spontaneous and induced track densities; ρ_d is the induced track density in the external detector, in brackets are the number of tracks counted; $P(X^2)$ is the X^2 -probability; $P(X^2) < 1$ indicates that the data distribution has multiple populations; MTL is the measured mean track length, with sd its standard deviation; Dpar is the average etch-pit lengths.

| sample | lat | lon | elevation (m) | 4-He (mol) | 238-U (mol) | 232-Th (mol) | Uncorr. Age (Ma) | F_t | Corr. age (Ma) | mean age (Ma) | std.dev |
|--------|-------|-------|------------------|---------------|-------------|--------------|---------------------|-------|----------------|------------------|---------|
| CC1_A | 43.38 | -4.59 | 34 | 1.776E-12 | 5.869E-12 | 1.369E-12 | 218.09 | 0.792 | 274.0 | | |
| CC1_B | | | | 1.583E-12 | 5.247E-12 | 2.210E-12 | 209.19 | 0.804 | 259.0 | | |
| CC1_C | | | | 3.263E-12 | 1.144E-11 | 4.658E-12 | 198.60 | 0.811 | 243.9 | 259.0 | 15.0 |
| CC4_A | 43.25 | -4.58 | 421 | 6.486E-13 | 2.105E-12 | 1.263E-12 | 206.16 | 0.743 | 275.8 | | |
| CC4_B | | | | 1.060E-12 | 4.449E-12 | 1.800E-12 | 166.50 | 0.742 | 223.3 | | |
| CC4_C | | | | 1.948E-12 | 1.259E-11 | 1.189E-11 | 97.82 | 0.752 | 129.7 | 209.6 | 74.0 |
| CC6_A | 43.17 | -4.59 | 368 | 6.228E-13 | 1.262E-11 | 2.973E-12 | 36.15 | 0.809 | 44.6 | | |
| CC6_B | | | | 7.672E-14 | 1.825E-12 | 1.630E-12 | 26.99 | 0.788 | 34.2 | | |
| CC6_C | | | | 9.460E-14 | 1.889E-12 | 2.223E-12 | 30.50 | 0.749 | 40.7 | 37.5 | 4.6 |
| CC8_A | 43.15 | -4.60 | 310 | 7.851E-14 | 2.055E-12 | 6.640E-13 | 27.48 | 0.720 | 38.1 | | |
| CC8_B | | | | 2.038E-13 | 5.278E-12 | 1.735E-12 | 27.75 | 0.740 | 37.5 | | |
| CC8_C | | | | 6.029E-13 | 1.504E-11 | 6.260E-12 | 28.27 | 0.798 | 35.4 | 37.0 | 1.4 |
| CC14_A | 43.04 | -4.65 | 1125 | 7.151E-13 | 1.710E-11 | 2.595E-12 | 31.20 | 0.787 | 39.6 | | |
| CC14_B | | | | 4.326E-13 | 1.091E-11 | 2.131E-12 | 29.30 | 0.763 | 38.4 | | |
| CC14_C | | | | 1.257E-12 | 2.878E-11 | 1.003E-11 | 31.24 | 0.780 | 40.0 | 39.3 | 0.9 |
| CC11_A | 42.81 | -4.65 | 1118 | 2.984E-12 | 8.297E-12 | 1.420E-12 | 261.59 | 0.812 | 320.4 | | |
| CC11_B | | | | 2.044E-12 | 6.197E-12 | 2.664E-12 | 227.94 | 0.806 | 281.5 | | |
| CC11_C | | | | 1.394E-12 | 3.368E-12 | 2.546E-12 | 267.34 | 0.777 | 341.9 | 314.6 | 30.6 |

Table II - 2 Zircons (U-Th)/He results. F_t is the geometric correction factor for age calculation. He measurements were performed at the University of Tübingen (Germany); U and Th measurement at the University of Arizona (USA).

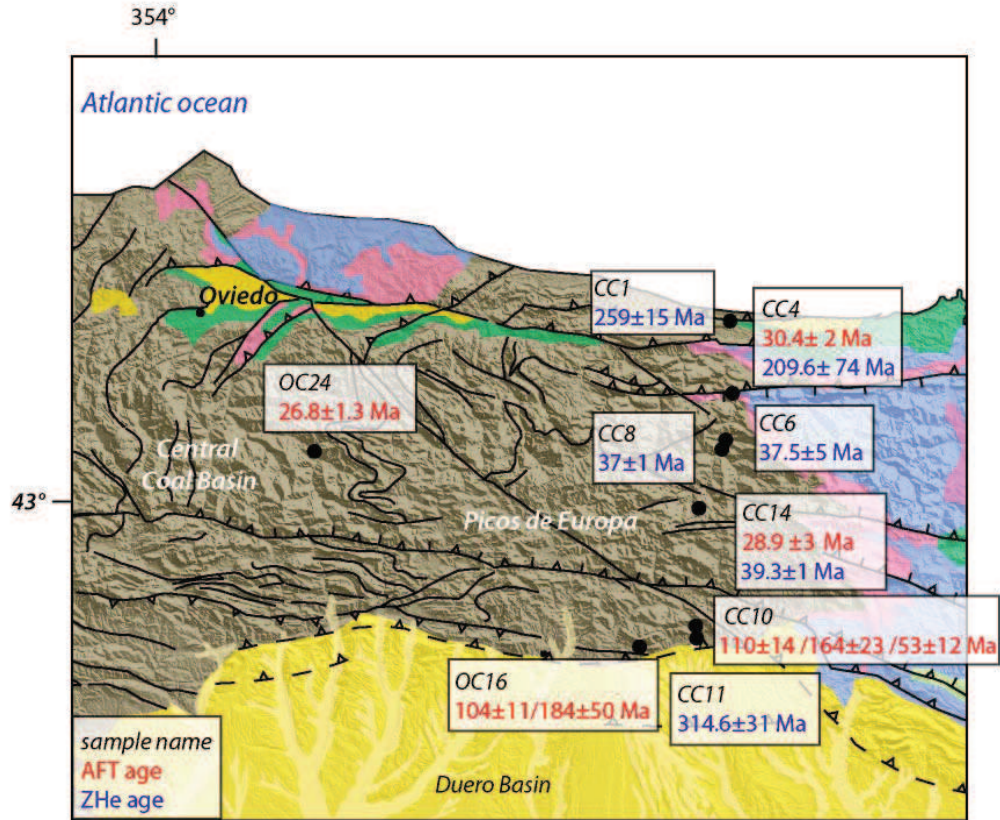


Figure II - 5. New AFT and ZHe ages plotted on the geological map. ZHe ages are in blue and AFT ages in red. OC 16 and CC10 gave ages with multiple populations, the first age written represents the main age peak.

Most of the data are located along a transect across the central Cantabrians. The AFT and ZHe data delimit three areas characterized by distinct age patterns. From the northern extremity to the CC4 sample, the data indicate an Alpine AFT age (CC4, 30.4 ± 2.1 Ma) associated with non- or partially-reset ZHe ages (CC1, $259 \pm$ Ma; CC4, 209.6 ± 74 Ma).

| sample | Stratigraphic age (Ma) | P1 $\pm 1 \sigma$ (Ma) | P2 $\pm 1 \sigma$ (Ma) | P3 $\pm 1 \sigma$ (Ma) |
|--------|------------------------|------------------------|--|---------------------------|
| OC16 | 300 | | 109.3 \pm 5.3 (79.4 %) | 198.6 \pm 22.3 (20.6 %) |
| CC10 | 110 | 56.5 \pm 6.4 (6.9 %) | 110.7 \pm 14.9 (50 %) | 164.3 \pm 11.9 (43.1 %) |

Table II - 3. Details of AFT results for samples with multiple populations. P1,2 and 3 are the best-fit values of the peak ages calculated by Binomfit software.

The second region regroups samples from CC6 to the center of the section, and is characterized by both Alpine reset AFT and ZHe ages. In this area, the ZHe ages are very similar and associated

with low uncertainties (ages of 37.5 ± 5 Ma; 37 ± 1 Ma; and 39.3 ± 1 Ma for respectively CC6, 8 and 14). The combination of both the young AFT (28.9 ± 2.9 Ma, CC14) and ZHe ages clearly indicates that this is the area that experienced most exhumation during Alpine deformation. Moreover, the combination of these two ages in sample CC14 indicates that it took ~ 10 Myr (39 Ma to 29 Ma) to the sample to travel from the lower limit of the ZHe PRZ (160°C) to the lower limit of the AFT PAZ (100°C). Based on the thermal gradient measurements of Fernández et al. (1998), the average geothermal gradient in the Cantabrian Mountains area is of $20 \pm 3^\circ\text{C.km}^{-1}$, thus the CC14 sample provides an estimated exhumation rate of 0.3 km.Myr^{-1} from middle Eocene to Oligocene times. Finally, the third set of data, located in the southern part of the cross-section shows AFT ages with multiple populations (Figure II - 6) and an unreset Variscan ZHe age.

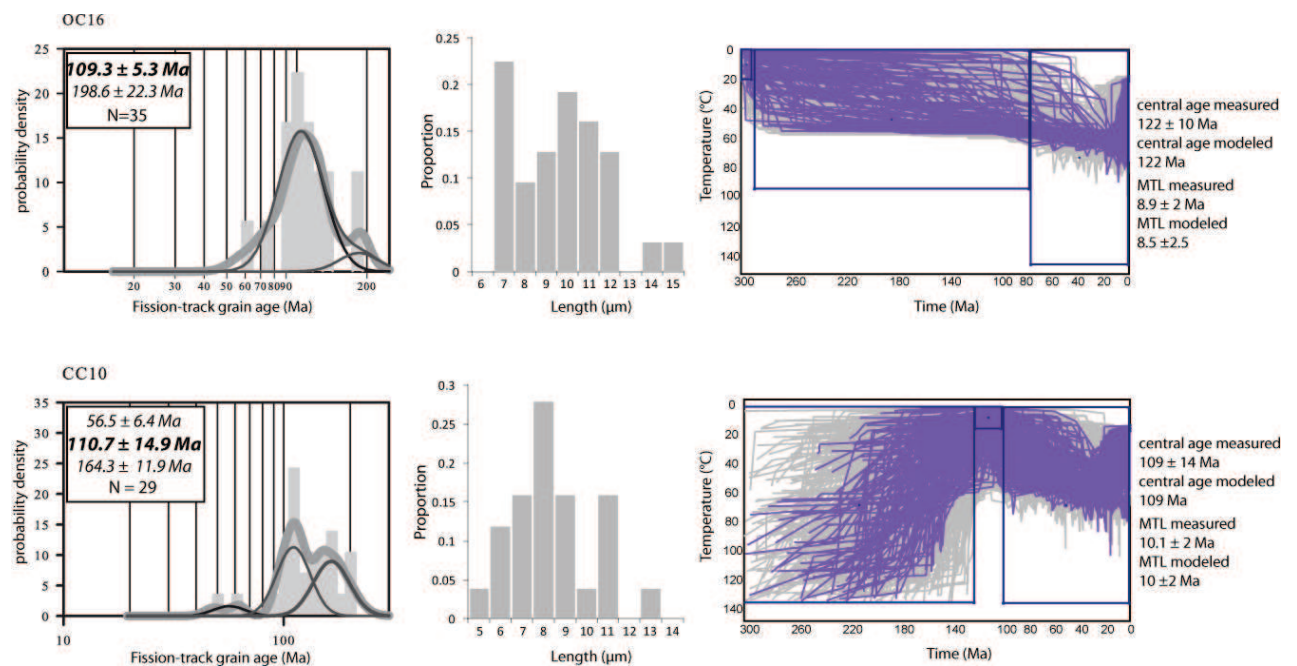


Figure II - 6. Grain-age population, track length measurements and HeFTy modeling of t-T paths for samples CC10 and OC16.

Samples OC16 and CC10 (deposited respectively during Stephanian and Albian times) both have Albian peak ages (109 ± 5 Ma and 111 ± 5 Ma respectively) and secondary Jurassic peak ages (199 ± 22 Ma and 164 ± 12 Ma). Measured track lengths are very short in both samples, with a mean track length of $8.9 \mu\text{m}$ for OC16 ($n=26$) and $10.1 \mu\text{m}$ for CC10 ($n=31$), indicating that the samples were not deeply buried after deposition and stayed a long time in the PAZ. Individual thermal modeling of the data was performed with HeFTy using AFT annealing model of Ketcham (2007). Forward models were run to fit the track length and Dpar distribution as well as the central age (i.e. not taking into account the different age populations). Modeled T-t paths do not show the same Mesozoic history for the two samples (even though they have similar peak ages), sample CC10 experienced Jurassic exhumation and Cretaceous re-burial, whereas the sample OC16 only

shows a slow and progressive Mesozoic burial until Cenozoic times. This difference is probably constrained by the depositional ages (Albian for CC10, Stephanian for OC16) and by the MTL value that is a bit larger for CC10. Moreover, note that these modeling results should be interpreted carefully as the number of track lengths counted is only of 26 and 31 whereas it should be around a hundred in order to obtain statistically well constrained T-t paths. It is interesting to note that even if the samples do not have Alpine reset AFT ages, the modeling shows a similar timing of Cenozoic exhumation to the samples from the north (CC14 for instance), i.e. since 20-30 Ma. Finally, the sample OC24, located to the west in the Central Coal Basin, also indicates Oligocene exhumation, with an age of 26.8 ± 1.3 Ma. Unfortunately, the other samples collected in this area did not provide enough apatites to be analyzed; we will therefore discuss this result later by confronting it to the AFT ages produced by Carrière (2006).

II.5 Implications

These new AFT and ZHe ages allow us to better constrain Alpine exhumation of the central Cantabrian Mountains in terms of its timing and spatial distribution. The ZHe ages provide a minimum estimate of the onset of Alpine inversion in the Bartonian (39 Ma), which is synchronous to the thrusting in the accretionary wedge offshore, dated at late Eocene (Alvarez-Marron et al. 1996; Gallastegui 2000). The maximum ending time of this deformation phase is constrained by the youngest AFT ages that are late Oligocene in age. It is also worth noting that the “reset ages” located in the center of the eastern structural section do not show any propagation of exhumation from north to south.

Central Cantabrian cross-section

In the central part of the Cantabrian Mountains (Figure II - 7a), the thermochronological ages highlight the exhumation patterns that are, to first order, in agreement with the structural interpretation of Alonso et al. (1996) and Pulgar et al. (1999). Unreset ages are encountered in the northern and southern extremities of the range, where burial and exhumation is supposed to be less, and the reset ages are located in the center of the section, between the Cabuerniga fault and the Ubierna fault. These two major faults are known to be Mesozoic extensional faults reactivated during the Cenozoic compression. They both played a major role in the Basque-Cantabrian Basin; the Cabuerniga fault continues until the Picos de Europa unit, whereas the Ubierna fault extends until the Central coal basin area, where it is named Leon fault. The reset zircon ages imply, however, larger amount of burial than previously predicted by Alonso et al. (1996), who constrained the continuation of the Mesozoic cover from the outcrops of Jurassic and Cretaceous strata in the northern area. When projecting the amount of burial needed to reset the AFT and ZHe systems, assuming that the thickness of Paleocene and early Eocene is not significant and that the

geothermal gradient is 20°C/km (Fernández et al. 1998), 1.5 to 4 km of additional Mesozoic sediments are required, with respect to what was previously hypothesized (see Figure II - 7). This addition leads to a reconstructed Mesozoic cover of a maximum of 7 km thick, which is equivalent to the thickness of the Mesozoic cover reconstructed by Espina et al. (1996) in their section of the western Cantabrian basin (~10 km to the east of the II/II' section in Figure II-7) shown in Figure II - 8. This observation leads to position the projected Mesozoic strata in the footwall of the Cabuerniga fault at the same level as in footwall of the Ubierna fault. Therefore, the structure becomes more symmetric in terms of burial, which also probably implies some differences in the deeper structure. A more symmetric pop-up structure defined by the Cabuerniga and Ubierna faults could fit our data better than the fault-bend-fold structure drawn by Alonso et al. (1996). I am currently working in collaboration with David Pedreira from the University of Oviedo on a new balanced cross-section of the eastern Cantabrians that is consistent with both the structural and geophysical data and with my new thermochronological ages.

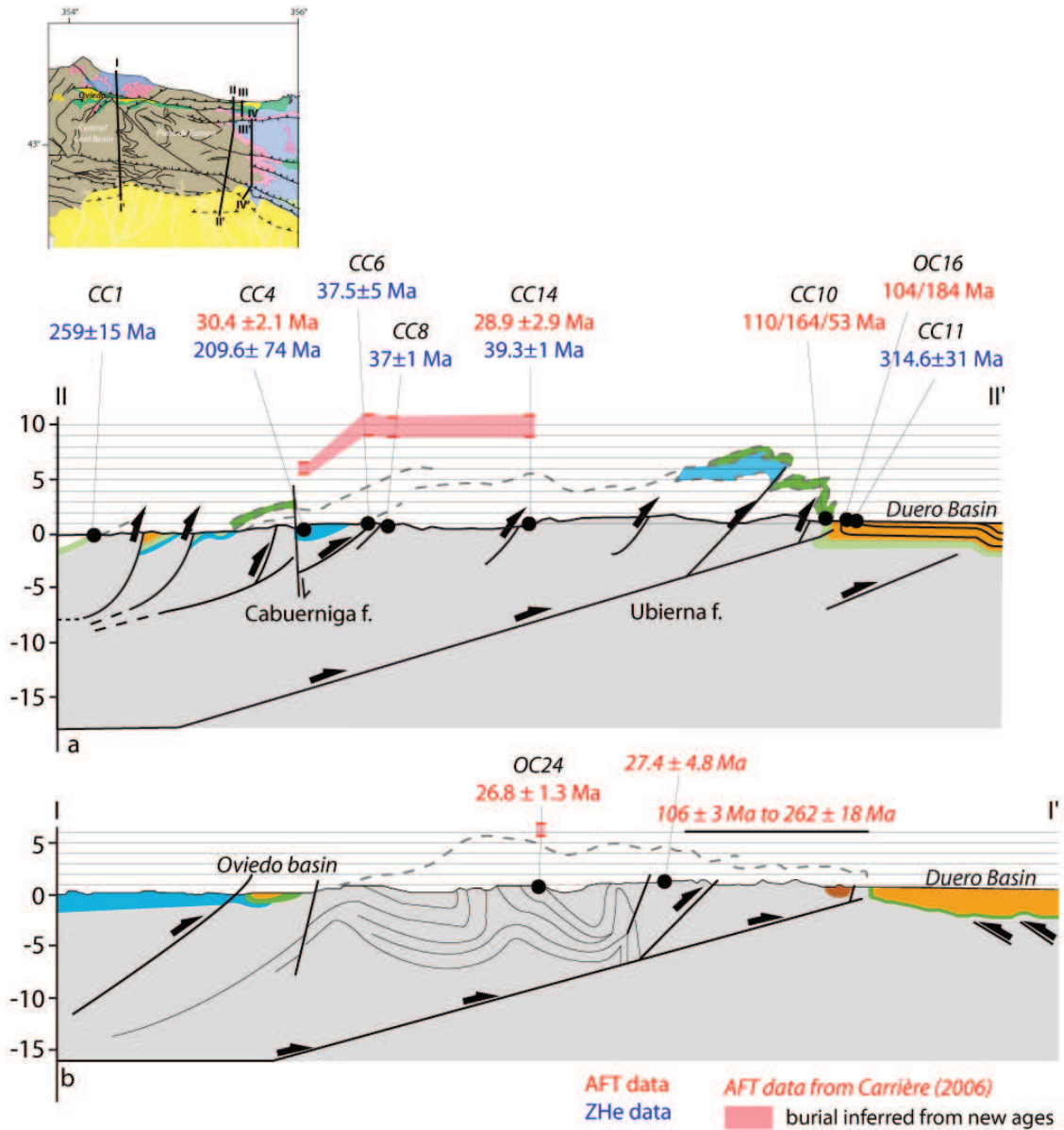


Figure II - 7. N/S cross-sections located in the central (a, section II/II') and in the western Cantabrians (b, section I/I'), with projected ages from this study and Carrière (2006). Aft ages are in red; ZHE ages in black. Structural cross-section are redrawn from Pulgar et al. (1999). The red area represents the projection of the limits of the observed ZHe PRZ (160-200°C) for samples CC6, CC8 and CC14 and of the AFT PAZ (100-120°C) for CC4. This area represents the minimum burial needed to obtain the ZHE and AFT ages, and so therefore marks the estimated top of Mesozoic sediments limit.

West-Central Cantabrian cross-section

Due to the lack of suitable samples, exhumation patterns along the west-central cross-section are much less constrained. Our single AFT age in the center of the Central Coal Basin (OC24) suggests a burial of 5 to 6 km (with an AFT PAZ between 100 and 120°C and assuming a

geothermal gradient of 20°C/km) that is consistent with the 3 to 4 km of projected Mesozoic sediments inferred by Pulgar et al. (1999). The AFT ages produced by Carrière in his PhD thesis (2006) are also in agreement with the published structure, as he reports an Oligocene AFT age 10 km to the south of our sample, and the unreset ages to the south, where the amount of Alpine exhumation is supposed to be less.

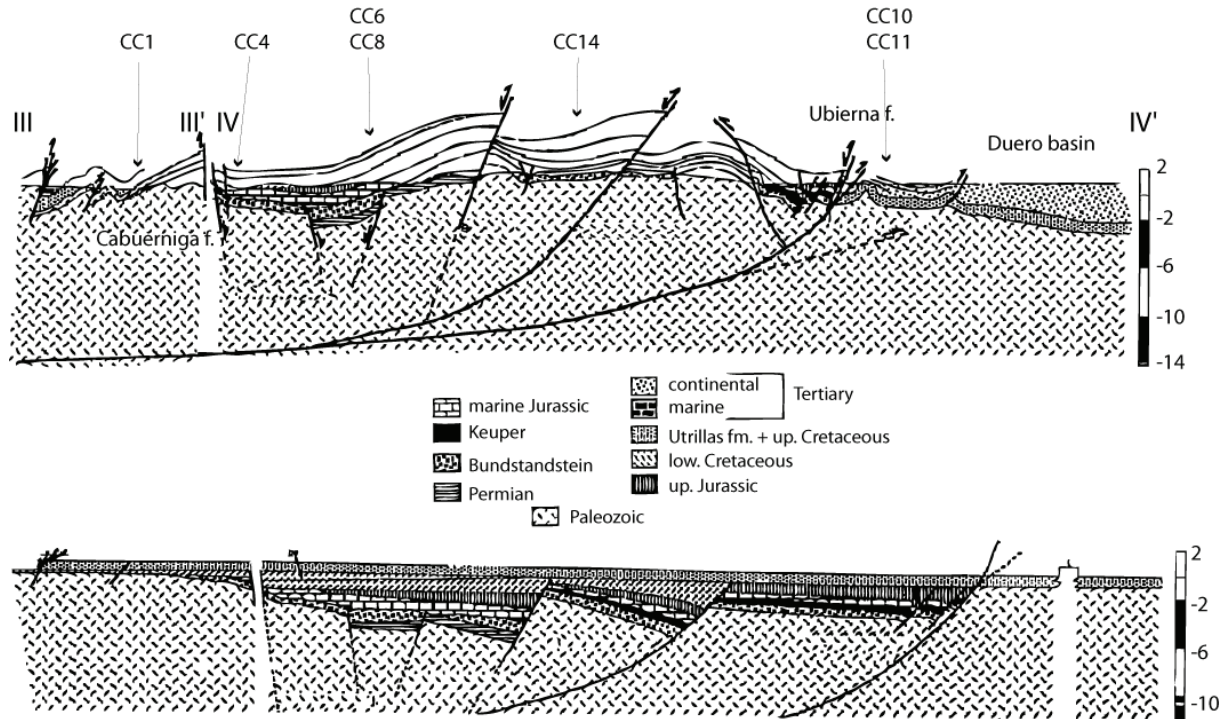


Figure II - 8. Present-day and reconstructed pre-Alpine cross-section of the Western Basque-Cantabrian Basin (from Espina et al. 1996), corresponding to the section III/III' and IV/IV' localized in Figure II-7. Position of samples in the eastern cross-section was projected for comparison.

II.6 Unsuccessful apatite He analyses

In order to refine our understanding of the Cenozoic exhumation history of the Cantabrian Mountains, four samples, with several aliquots each, were selected for apatite (U-Th)/He analysis. The samples are derived from Variscan granitoids (IN, Ra and Pi09) and Triassic sandstones (LIN) outcrops located in the north, center and south of the central Cantabrians, and were collected by Luis Barbero (University of Cadiz). The apatites were picked in Grenoble and a single grain per aliquot was put in a Pt tube before sending them to Paris-Sud University (Orsay) for analysis. He-degassing as well as U and Th measurements were performed by Cécile Gautheron.

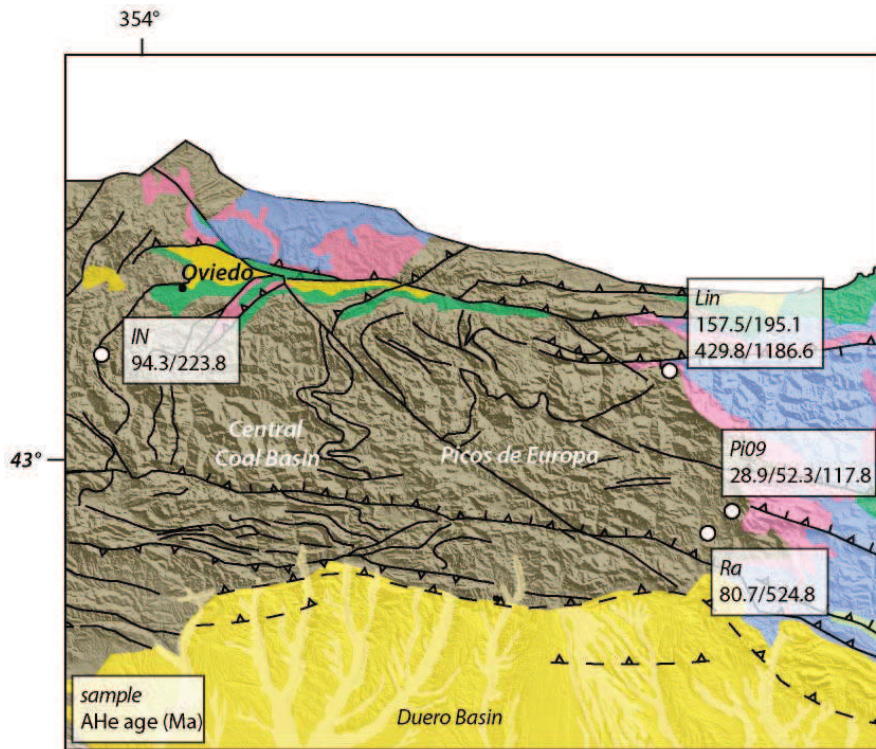


Figure II - 9. Localization of the four samples with their AHe results.

The results are presented in Table II - 4, and present several evident inconsistencies that led us to reject this dataset for interpretation, only one grain in sample Pi09 presenting an Alpine age. The main issues inferred from these results are:

- 1) None of these ages are reproducible. Individual aliquots from the same sample are very different from each other; the Pi09 sample, for instance, has three grains dated at 28.9, 52.3 and 117.8 Ma.
- 2) Nearly all the AHe ages are older than the corresponding AFT ages reported in Table 1, whereas the AHe closure temperature (T_c) is 75 ± 15 °C and the AFT T_c is 110 ± 10 °C. For example, the LIN sample, which is equivalent to the CC4 sample (dated by AFT and ZHe, Tables II-1 and II-2), has an AFT age of 30.4 Ma and AHe ages ranging from 157 Ma to 1186 Ma.
- 3) Some of the AHe ages derived from granodiorites are older than the emplacement age of the host rock. The oldest AHe age derived from a granodiorite is Cambrian in age (Ra3, 525 Ma) whereas the age of emplacement of these granodiorites is Permian (Fernández-Suárez et al. 2000).

Several causes can explain these problems. The most obvious one is the presence of U-rich mineral inclusions in the apatites, like zircon or monazite inclusions. Even if the apatites were picked very carefully, there is still the possibility of little inclusions that are not visible under an optical microscope but could have produced an important amount of He. Secondly, the presence of U and Th-rich mineral neighbors could also have biased the He measurement

in these apatites that are relatively poor (<50 ppm) in U/Th (Spiegel et al. 2009), as well as chemical zonation of Uranium and Thorium in the minerals (Meesters and Dunai 2002). Moreover, several authors have pointed out that dispersion of replicate ages is often encountered in samples from slowly-cooled terrains (Fitzgerald et al. 2006; Gautheron et al. 2009). From our AFT ages, we know that exhumation was probably quite slow, as the mean track lengths are $\sim 10 \pm 1$ μm . Moreover, the (U-Th)/He analysis on zircons combined with AFT ages allows us to obtain an estimated maximum cooling rate of $6^\circ\text{C}.\text{Myr}^{-1}$, that can be considered as moderately low.

More generally, numerous studies document problems of measuring AHe ages older than corresponding AFT ages (Persano et al. 2002; Hendriks and Redfield 2005; Green et al. 2006; Green and Duddy 2006). Some authors hypothesized that the AFT ages are “too young” (e.g. Hendriks and Redfield 2005), but the majority of them postulated that differences between AFT ages and AHe ages are not coming from anomalous fission track annealing behavior but effectively from the (U-Th)/He system itself. More precisely, Shuster et al. (2006) inferred from diffusion experiments that the kinetics of He diffusion is affected by the amount of radiation damage in the crystal, which may be a principal cause responsible for unexpectedly old He ages. The effect of radiation damage and the way the defects caused by the emission of α -particles are themselves annealed are further investigated by Gautheron et al. (2009) and Flowers et al. (2009). These authors proposed different He-diffusion models including build-up and annealing of radiation damage, which help to explain some problematic (U-Th)/He ages. Unfortunately, the age scatter between aliquots in the samples analyzed here is too important to try to use these models with our data.

To conclude, there are several ways for explaining these ages and the valuable explanation would probably be a combination of all the causes developed earlier. One of the most probable explanations for our scattered AHe ages remain the presence of U-rich mineral inclusions.

| Sample | lat | lon | Weight(g) | U (ppm) | Th (ppm) | 4He (cc/g) | Th/U | Age (Ma) | FT | corr. age (Ma) |
|---------------|--------|--------|-----------|---------|----------|------------|------|----------|------|----------------|
| Ra1 | 42.897 | -4.477 | 6.4 | 4.5 | 14.5 | 6.22E-05 | 3.2 | 64.88 | 0.80 | 80.68 |
| Ra3 | | | 2.6 | 9.5 | 24.7 | 7.16E-04 | 2.6 | 386.31 | 0.74 | 524.88 |
| IN01 | 43.348 | -5.364 | 4.7 | 1.9 | 13.8 | 1.08E-04 | 7.2 | 173.85 | 0.78 | 223.80 |
| IN02 | | | 6.1 | 8.4 | 24.9 | 1.33E-04 | 3.0 | 77.48 | 0.82 | 94.28 |
| LIN1 | 43.253 | -4.581 | 3.5 | 17.6 | 23.0 | 2.51E-03 | 1.3 | 899.68 | 0.76 | 1186.59 |
| LIN2 | | | 1.4 | 23.2 | 27.4 | 1.12E-03 | 1.2 | 312.89 | 0.73 | 429.85 |
| LIN3 | | | 2.1 | 17.8 | 18.2 | 3.97E-04 | 1.0 | 148.54 | 0.76 | 195.06 |
| LIN5 | | | 3.7 | 23.4 | 14.8 | 3.88E-04 | 0.6 | 119.47 | 0.76 | 157.51 |
| PI09-1 | 43.033 | -4.407 | 1.2 | 8.8 | 23.2 | 3.50E-05 | 2.6 | 20.25 | 0.70 | 28.95 |
| PI09-2 | | | 1.0 | 20.4 | 28.2 | 2.65E-04 | 1.4 | 80.85 | 0.69 | 117.82 |
| PI09-3 | | | 2.1 | 7.0 | 10.7 | 4.51E-05 | 1.5 | 39.16 | 0.75 | 52.33 |

Table II - 4 Apatite (U-Th)/He results (Orsay-Paris Sud University). These samples were collected from granodioritic intrusions and sandstones by Luis Barbero. The LIN sample is equivalent to the CC4 sample (see previous tables).

II.7 Conclusions

The strong imprint of the earlier Variscan deformation phase experienced by the higher (central) part of the Cantabrian Mountains as well as the lack of appropriate rocks for thermochronological analysis have revealed the isolation of the Alpine deformation patterns difficult. Nevertheless, the combination of apatite fission-track analysis and (U-Th)/He measurements on zircons has allowed us to define more precisely the timing and evolution of Alpine exhumation. In the eastern part of the range, where alpine shortening is known to be maximum, the combined AFT and ZHe data provide a precise timing of the onset of exhumation during at least late Eocene times at latest, as well as its ending time during or after the Oligocene. Moreover, the spatial distribution of reset and unreset ages allowed us to re-interpret the amount of burial and exhumation in the center of the section, and consequently the structure. AFT ages produced independently by Luis Barbero (University of Cadiz) in the east and center of the range confirm our observations of Eocene-Oligocene Alpine exhumation.

Part III- Cenozoic evolution of the South-Central Pyrenees: thermochronology and thermo-kinematic modeling

According to the thermochronological data, while the central Cantabrian Mountains were uplifting in Oligocene times, the main phase of exhumation was ending in the Pyrenees. The onlap of conglomeratic erosional products on the southern flank of the Axial Zone was hypothesized by Coney et al. (1996), and been proved by magnetostratigraphic studies. Nevertheless, the amount, extend and timing of in- and un- filling of these conglomerates still need to be quantified.

In this Part, we will first demonstrate by 3D thermo-kinematic modeling that the thermochronological dataset existing can be re-interpreted when adding this conglomeratic infilling in the model. The maximum elevation of the deposit and the timing of their incision will be quantified by inverse modeling; and compared to the geological history of the Southern Pyrenees and of the Ebro basin. This study has recently been accepted to Basin Research for publication. In the second chapter, we attempt to extend our conclusions to the southern foreland fold-and-thrust belt. By producing new AFT and (U-Th/He) measurements on apatites and incorporating them in a new thermal inverse model, to study the late-stage burial/exhumation history of samples located in the southern foreland. Despite the scatter of the AHe data, we will show that they all agree for the same Neogene exhumation phase.

Chapter III-1 Post-orogenic Evolution of the Southern Pyrenees: constraints from Inverse Thermo-Kinematic Modeling of Low-Temperature Thermochronology Data

Charlotte Fillon and Peter van der Beek

Institut des Sciences de la Terre, Université Joseph Fourier – Grenoble 1,

BP 53, 38041 Grenoble Cedex, France

Basin Research, *in press*

III-1.1 Abstract

The late-stage evolution of the southern central Pyrenees has been well documented but controversies remain concerning potential Neogene acceleration of exhumation rates and the influence of tectonic and/or climatic processes. A popular model suggests that the Pyrenees and their southern foreland were buried below a thick succession of conglomerates during the Oligocene, when the basin was endorheic. However, both the amount of post-orogenic fill and the timing of re-exhumation remain controversial. We address this question by revisiting extensive thermochronological datasets of the Axial Zone. We use an inverse approach that couples the thermo-kinematic model *Pecube* and the Neighborhood inversion algorithm to constrain the history of exhumation and topographic changes since 40 Ma. By comparison with independent geological data, we identified a most probable scenario involving rapid exhumation ($>2.5 \text{ km Myr}^{-1}$) between 37 and 30 Ma followed by a strong decrease to very slow rates (0.02 km Myr^{-1}) that remain constant until the present. Therefore, the inversion does not require a previously inferred Pliocene acceleration in regional exhumation rates. A clear topographic signal emerges however: the topography has to be infilled by conglomerates to an elevation of 2.6 km between 40 and 29 Ma and then to remain stable until ~ 9 Ma. We interpret the last stage of the topographic history as recording major incision of the southern Pyrenean wedge, due to the Ebro basin connection to the Mediterranean, well before previously suggested Messinian ages. These results thus demonstrate temporally varying controls of different processes on exhumation: rapid rock uplift in an active orogen during late Eocene, whereas base-level changes in the foreland basin control the post-orogenic evolution of topography and exhumation in the central Pyrenees. In contrast, climate changes appear to play a lesser role in the post-orogenic topographic and erosional evolution of this mountain belt.

III-1.2 Introduction

The evolution of mountainous topography and of sediment flux to foreland basins is generally considered to be controlled by tectonics and surface processes (e.g., Flemings and Jordan 1989; Johnson and Beaumont 1995b). Base-level changes in the foreland have received less attention, but should also influence mountain belt evolution, as both numerical and analogue models have demonstrated strong coupling between eroding upland ranges and adjacent sedimentary basins (Babault et al. 2005a; Carretier and Lucazeau 2005; Densmore et al. 2007). This influence is enhanced in an internally drained foreland basin, where sediments will accumulate and be stored until the system opens again (Sobel et al. 2003; Garcia-Castellanos 2007). Syn-orogenic accumulation of sediments provides a regional load on the system, which will influence the deformation of the orogenic wedge (e.g., Storti and McClay 1995; Mugnier et al. 1997; Ford 2004) and modify patterns of tectonic and/or erosional exhumation. During the post-orogenic phase, the history of foreland basin fill and erosion constitutes an important, but not easily interpretable, record of climatic and / or geodynamic events that have affected the “dead” mountain belt (e.g., McMillan et al. 2006; Wobus et al. 2010).

The southern Pyrenees constitute a key region to study the interaction between mountain-belt development and foreland basin evolution, because of an exceptionally preserved syn- and post-orogenic stratigraphic record (e.g., Puigdefàbregas et al. 1992; Vergés et al. 2002a; Sinclair et al. 2005). However, although the main orogenic phase is well constrained by an extensive dataset including seismic imagery (ECORS Pyrenees Team 1988), structural and thermochronological data (Muñoz 1992; Fitzgerald et al. 1999; Beaumont et al. 2000; Vergés et al. 2002a; Sinclair et al. 2005; Metcalf et al. 2009), the post-orogenic evolution of the belt remains subject to debate in terms of its geomorphic evolution and the potential tectonic and climatic controls thereon.

In the southern central Pyrenees, the peak of exhumation during upper Eocene times (Fitzgerald et al. 1999; Sinclair et al. 2005) coincides with the closure of its southern foreland basin, the Ebro basin (Riba et al. 1983). The basin remained endorheic until Late Miocene or Pliocene times. During this long period, the basin experienced a phase of infilling by the erosion products of the internal zone of the belt, which are characterized in the southern fold-and-thrust belt by a thick pile of conglomeratic deposits.

Although the general evolution of the southern Pyrenean foreland outlined above is commonly accepted, controversies exist regarding its influence on the morphologic evolution of the mountain belt, the timing of opening of the basin and the geodynamic significance of late-stage incision. It has been argued that the base-level change associated with filling of the endorheic basin led to the development of high-elevation low-relief surfaces within the internal zone of the belt (the ‘Pyrenean peneplain’ Babault et al. 2005b) but both this interpretation and the actual existence of such a peneplain have been called into question (Gunnell and Calvet 2006). Opening of the Ebro

basin to the Mediterranean has been argued to coincide with the Messinian Salinity Crisis (Coney et al. 1996) but also to either pre- (Garcia-Castellanos et al. 2003) or post- (Babault et al. 2006) date it (see Arche et al. 2010 for a recent review). Re-incision of the Pyrenees and their foreland basin has been related to Pliocene climatic change (Babault et al. 2005b) or to headward propagation of the base-level fall associated with basin opening (Coney et al., 1996; Garcia-Castellanos et al., 2003). Finally, low-temperature thermochronological data from the central Pyrenees have been variously interpreted in terms of requiring increased late-Neogene exhumation (Fitzgerald et al. 1999) or slow steady post-orogenic exhumation since the Oligocene (Gibson et al. 2007).

This paper revisits these questions by using numerical modeling to integrate all of the existing thermochronology data that have played a key role in quantifying the post-orogenic erosion history of the Pyrenees. Specifically, we aim to quantify the thickness of post-orogenic conglomerates that accumulated in the southern foreland during the phase of endorheism, to date the onset of their incision, and to test the inferred increase of exhumation rates during Pliocene-Quaternary times in the mountain belt. By doing so, we aim to link the history of the Ebro basin with the evolution of the thick sequence of Oligocene conglomerates and the post-orogenic exhumation history of the internal part of the orogen. Our results therefore also provide an independent constraint on the timing of opening of the basin to the Mediterranean Sea, as we interpret the onset of valley incision as resulting from the base-level drop associated with this opening. In the following, we first briefly outline the geological setting of the southern Pyrenees and Ebro foreland basin, synthesize the existing thermochronological dataset and describe our numerical inversion technique. We then present our model results and discuss their significance for the inferred post-orogenic history of the southern Pyrenean foreland and its tectonic, climatic and base-level controls.

III-1.3 Geological setting

III-1.3a Structure and Geodynamic Evolution of the Pyrenees

The Pyrenean mountain belt is a doubly-vergent orogenic wedge resulting from inversion of a highly extended basin between the Iberian and European plates. Collision started during the Late Cretaceous and reached its peak in the central Pyrenees during Eocene-Oligocene times (Muñoz 1992; Beaumont et al. 2000; Vergés et al. 2002a). The belt is structured into three main tectonic units Muñoz 1992: the North Pyrenean unit, which corresponds to the retro-wedge, the central Axial Zone and the South Pyrenean unit, together making up the pro-wedge (Figure III-1). The narrow northern Pyrenean wedge imbricates basement and cover rocks north of the North Pyrenean Fault (NPF) and is bounded by a large retro-foreland basin, the Aquitaine Basin. The southern pro-wedge is much wider, with a succession of well-marked tectonic units including a

central antiformal stack of basement rocks (Axial Zone), a foreland fold-and-thrust belt (the South Pyrenean unit) and the Ebro pro-foreland basin (Muñoz 1992; Vergés et al. 2002a). The amount of shortening varies along the belt and reaches a maximum of around 165 km (Muñoz 1992; Beaumont et al. 2000) in our study area along the ECORS seismic profile.

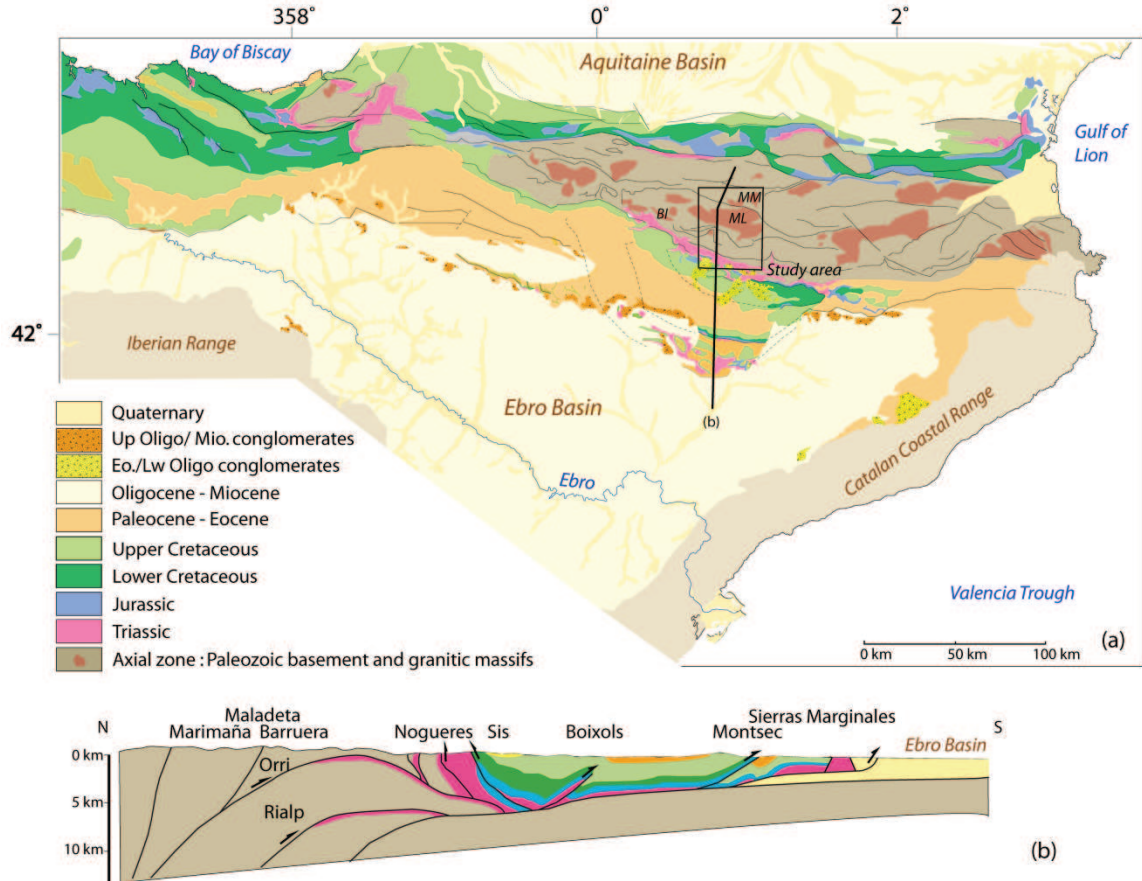


Figure III- 1. (a) Geological map of the Pyrenees (modified from BRGM-IGME, 2008). BI: Bielsa massif; ML: Maladeta massif; MM Marimaña massif. Line indicates cross-section (b); box indicates study area shown in Figure III-2. (b) Cross-section of the southern (pro-) wedge of the Pyrenees, based on the ECORS seismic profile (modified from Muñoz, 1992).

Due to the pre-collisional structure of the northern Iberian margin, the north-south collision led to temporal migration of compressional deformation from East to West and from North to South. This along- and across-strike migration is well reflected in the patterns of both exhumation and foreland deposition (Puigdefàbregas et al. 1992; Vergés et al. 2002a; Sinclair et al. 2005). Exhumation patterns are constrained by an extensive thermochronological database, consisting mainly of apatite fission-track (AFT) data, with subordinate zircon fission-track (ZFT), K-feldspar and mica $^{40}\text{Ar}/^{39}\text{Ar}$ and apatite (U-Th)/He (AHe) data. To summarize, exhumation started in the early Eocene (~50 Ma) in the central Pyrenees, as recorded by AFT data from the northern Pyrenean zone (Yelland 1990; Morris et al. 1998; Fitzgerald et al. 1999) and ZFT and K-feldspar

$^{40}\text{Ar}/^{39}\text{Ar}$ data from the Axial Zone (Sinclair et al. 2005; Metcalf et al. 2009). A late Eocene (~36-30 Ma) phase of very rapid exhumation is recorded by AFT data in the southern Axial Zone (Fitzgerald et al. 1999; Sinclair et al. 2005; Gibson et al. 2007; Metcalf et al. 2009). The youngest AFT and AHe ages (~10-15 Ma) are encountered in the southernmost part of the Axial Zone in the central (Barruera zone; Gibson *et al.*, 2007) and the southwestern (Bielsa massif, Jolivet et al. 2007) Pyrenees.

In this study, we focus on three domains of the central Pyrenees, along the ECORS profile (Figure III-1): the central Axial Zone, the southern foreland fold-and-thrust belt and the southern foreland basin. The Axial Zone is an antiformal stack built by three thrust sheets (Rialp, Orri and Noguères) that were emplaced between Late Cretaceous (Noguères) and early Oligocene (Rialp) times (Muñoz 1992; Beaumont et al. 2000). The foreland fold-and-thrust belt developed generally in-sequence from north to south. The onset of exhumation in the Noguères Zone (northern limit of the foreland) coincided with activation of the Boixols thrust in the foreland during Late Cretaceous times (Beaumont *et al.*, 2000; Sinclair *et al.*, 2005). Deformation subsequently migrated southward with activation of the Montsec thrust in the Paleocene and the Sierras Marginales system in the middle Eocene, while the Orri and Rialp units were piling up farther north. At the same time, out-of-sequence thrusting was active in the Noguères zone (Capote et al. 2002; Sinclair et al. 2005). The most recent deformation in the fold-and-thrust belt has been dated to the early Miocene (20-25 Ma; Meigs et al. 1996), since then, the belt is considered as tectonically inactive.

The foreland fold-and-thrust belt exposes a continuous succession of Cretaceous to upper Oligocene marine to continental sediments that record the syn-tectonic infilling and piggy-back progression of the foreland basin (Vergés and Muñoz 1990; Puigdefàbregas et al. 1992). Remarkable late-orogenic conglomerate deposits started covering the basin from late Eocene times onward (Coney et al. 1996). These were fed by the rapidly exhuming Axial Zone, as revealed by pebble provenance studies (Vincent 2001). Three main conglomeratic remnants have been preserved from subsequent erosion in the central southern Pyrenees: the Sis, Gorp and Pobla de Segur massifs (from west to east; Figure III-2). The depositional sequence of these conglomerates has recently been clarified by magneto-stratigraphy (Beamud et al. 2003, 2011), which dates the onset of infilling to the middle Eocene (~40 Ma) while the youngest preserved deposits are Oligocene (27-28 Ma). Detrital AFT ages from granitic pebbles in the conglomerates (Beamud et al. 2011; Rahl et al. 2011) are 43-61 Ma at the bottom of the succession to 27-42 Ma at the top, confirming the simultaneity of exhumation of Axial Zone rocks and the infilling of the fold-and-thrust belt valleys by conglomerates a few tens of km to the south.

III-1.3b Ebro basin drainage history

The Ebro foreland basin was formed in response to the flexural load of the Pyrenean orogenic wedge, although it was also influenced by loading of the two other alpine ranges surrounding the basin: the Catalan Coastal Range to the southeast and the Iberian Range to the southwest (Desegaulx and Moretti 1988b; Zoetemeijer et al. 1990b). During late Eocene times, the connection with the Atlantic Ocean was closed (36 Ma; Costa et al. 2009) and the basin became endorheic. Continental and lacustrine sedimentation continued until at least the middle Miocene (13 Ma), the age of the youngest sediments dated by magneto-stratigraphy and outcropping in the center of the basin (Pérez-Rivarés et al. 2004). Some time after this, the modern connection of the Ebro River to the Mediterranean should have been established, but there are different possible scenarios for the timing of opening to the Mediterranean Sea.

In the 1990's, it was commonly accepted that the Ebro connected to the Mediterranean during the Messinian Salinity Crisis (5.9-5.3 Ma; Krijgsman et al. 1999), and the connection was understood to be driven by margin incision due to the large associated sea-level drop in the Mediterranean (Nelson and Maldonado 1990). Coney *et al.* (1996) further developed this idea and made the link between conglomerate “backfilling” (cf. above) and the drainage history of the Ebro basin. In their model, the southern Pyrenees were all but buried under their own erosional products during the endorheic phase of the basin and were re-excavated since the Messinian reopening of the Ebro basin toward the Mediterranean. The Messinian timing of basin opening has, however, been challenged by several authors. On the one hand, Babault *et al.* (2006) suggested, using numerical models and morphological analyses that the connection to the Mediterranean should have occurred after the Messinian, probably during Pliocene times. Their main argument is the absence of evidence for Messinian canyons incising the Ebro basin, in contrast to other large rivers draining into the Mediterranean. On the other hand, Garcia-Castellanos *et al.* (2003) modeled the Ebro basin evolution using a 3D model combining surface processes and crustal-scale deformation; they argue that the Messinian sea-level drop could not have triggered opening of the basin because its duration was too short to induce capture. From consideration of the sediment budget between the Pyrenees, the Ebro basin and the Ebro delta, they predicted that opening occurred between 13 and 8.5 Ma. In their model, capture was triggered by erosional lowering of the Catalan Coastal Range topographic barrier, sediment overfilling of the basin and/or changing climatic conditions, from dry to humid, during late Miocene times. These issues were further discussed by Arche et al. (2010), who infer capture of the Ebro around 9-8.5 Ma from analysis of pre-Messinian sediments in the Valencia Trough (the Castellon group). Finally, recent 3D seismic data from the Ebro delta (Urgeles et al. 2011) show clear evidence for a late Miocene “proto-Ebro” river, as they image a major through-going river just below the Messinian Erosion Surface (MES) as well as clinoform geometries, dated to the Serravalian-Tortonian (13.8 to 7.2 Ma) and inferred to correspond to a paleo-Ebro delta.

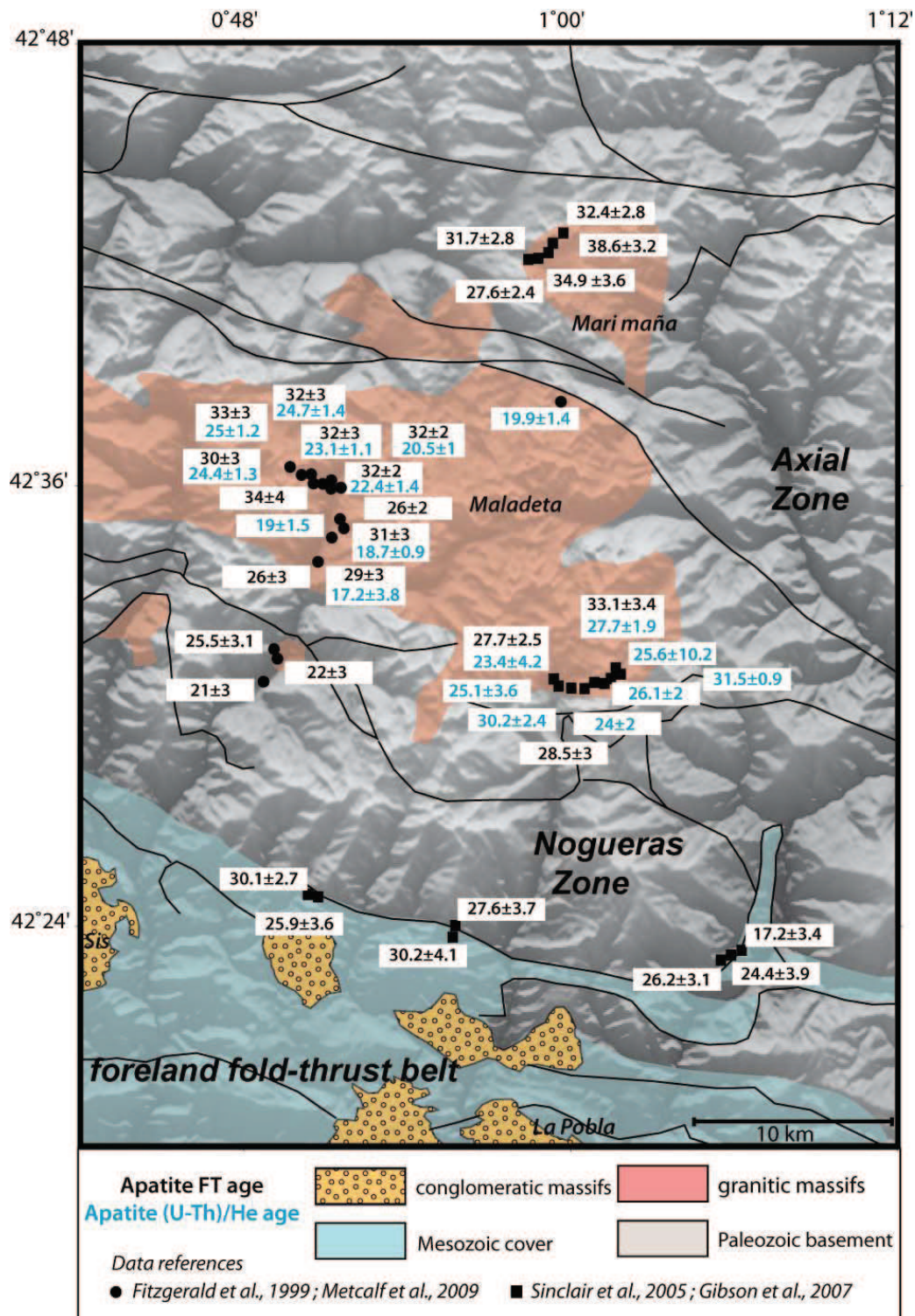


Figure III- 2. Schematic geological map of the study area, showing distribution of main units and location of thermochronological data (AFT ages in black, AHe ages in blue), from Fitzgerald et al. (1999), Sinclair et al. (2005), Gibson et al. (2007) and Metcalf et al. (2009).

III-1.3c Thermochronological data and exhumation of the central Pyrenees

Our thermo-kinematic modeling is based on 31 published AFT ages and 17 published AHe ages (Fitzgerald *et al.*, 1999; Sinclair *et al.*, 2005; Gibson *et al.*, 2007; Metcalf *et al.*, 2009). The data were collected in the Maladeta and Marimaña massifs, located within the Orri thrust sheet in the footwall and the hanging wall of the Gavarnie thrust respectively, as well as from the Nogueras zone, the southernmost part of the Orri thrust sheet (Figure III-2). Samples from the Maladeta and Marimaña massifs are from Late Carboniferous granites and the Nogueras zone samples are from Cambrian to Triassic volcanic rocks. To improve the constraint on predicted T-t paths, we also use track-length data from 29 AFT samples.

AFT ages range from a maximum of 38.6 ± 3.2 Ma for the topographically highest sample in the Marimaña massif to 17.2 ± 3.4 Ma for the lowest sample in the Nogueras zone; AHe ages similarly range from 31.6 ± 0.9 Ma to 17.2 ± 3.8 Ma (Figures III-2 and III-3). The mean track lengths (MTL) vary between $12.3 \mu\text{m}$ (for a sample toward the base of the Maladeta profile) to $14.3 \mu\text{m}$. Samples from elevations >2000 m generally have $\text{MTL} > 14 \mu\text{m}$, indicating rapid cooling through the AFT Partial Annealing Zone (PAZ), while lower-elevation samples are characterized by MTL between $13\text{--}14 \mu\text{m}$. Although somewhat different etching procedures were used to reveal tracks in the different studies, no systematic offsets in either AFT ages or MTL are observed between the different datasets (Figure III-3); we thus assume that the combined dataset is homogeneous. Sinclair *et al.* (2005) and Gibson *et al.* (2007) also reported AFT and AHe data for 3 samples from the Barruera massif, just south of Maladeta, which show significantly younger ages as compared to the Maladeta and Marimaña samples at similar elevations (~ 20 Ma for AFT and $10\text{--}15$ Ma for AHe), interpreted to reflect local out-of-sequence thrusting. We decided to exclude these samples, as they would have further complexified the regional exhumation history while not adding to the overall understanding of it.

A combined age-elevation plot for all the data (Figure III-3) shows that the samples from different massifs line up along a common age-elevation relationship, consistent with the inference that exhumation of the southern central Axial Zone rocks results from uniform passive uplift of the Orri unit (Figure III-1) by stacking of underlying basement units. AFT data from above ~ 1500 m elevation show a steep slope with ages between 40 and 30 Ma, implying rapid exhumation during that time and fitting the long MTL. Lower samples record a decrease in exhumation rates from 30 Ma to at least 18 Ma. AHe ages mimic this pattern with a steep age-elevation slope between 20 and 30 Ma for samples from above ~ 2000 m and a lower slope below that. Fitzgerald *et al.* (1999) used the AFT age-elevation pattern from the Maladeta massif to predict exhumation rates between 2 and 4 km Myr^{-1} for the phase of rapid exhumation between 36 and 30 Ma, which subsequently strongly decreased to $\sim 0.06 \text{ km Myr}^{-1}$ until 6 Ma. They also suggested from thermal modeling that post-Miocene acceleration of exhumation had to occur to fit the age-elevation relationship. In

contrast, Gibson *et al.* (2007) found that their combined AFT and AHe data did not require such a late-stage acceleration in exhumation, a finding that was challenged by Babault *et al.* (2009; see also Sinclair *et al.* 2009).

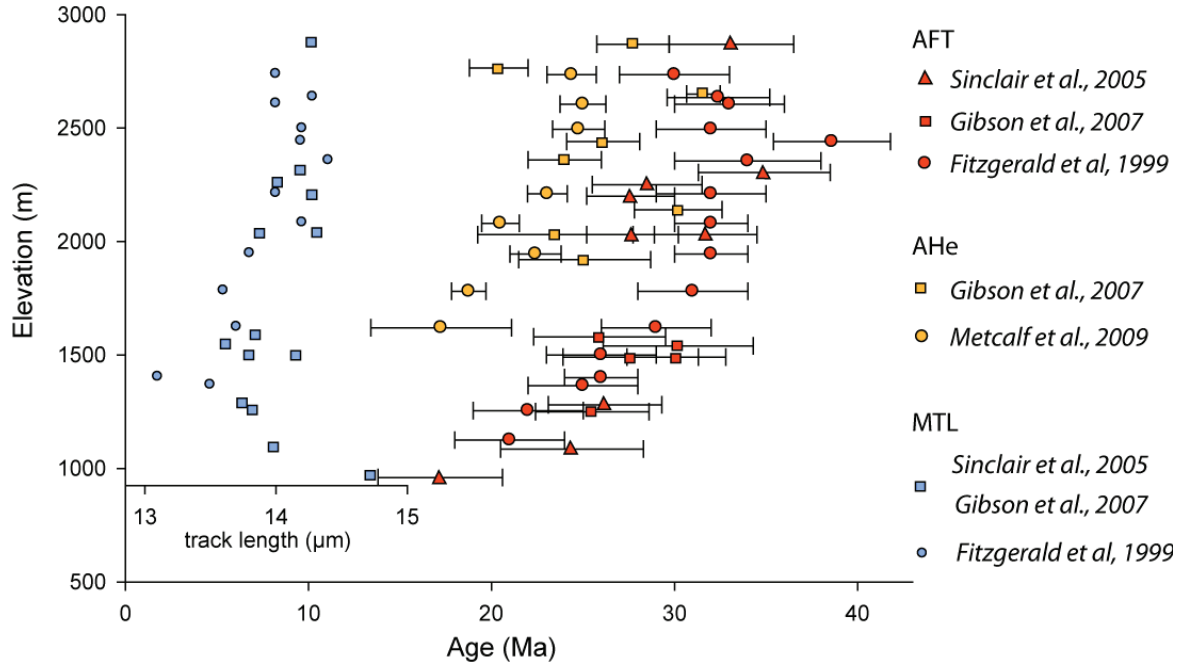


Figure III- 3. Combined age/elevation plot for all available low-temperature thermochronology data showing apatite fission-track ages (AFT in red), apatite (U-Th)/He ages (AHe in orange), and mean AFT track lengths (MTL in blue; note separate scale bar). Errors bars for AHe and AFT ages represent 1- σ error. Data from Fitzgerald *et al.* (1999), Sinclair *et al.* (2005), Gibson *et al.* (2007) and Metcalf *et al.* (2009).

Finally, Sinclair *et al.* (2005) published 4 zircon fission-track (ZFT) ages that range from 49.3 ± 2.6 Ma in the Maladeta and Marimaña massifs to 159 ± 33 Ma in the Noguerras zone, implying that total exhumation since 40 Ma was insufficient to exhume rocks with fully reset ZFT ages, consistent with recent combined modeling of AFT and K-feldspar $^{40}\text{Ar}/^{39}\text{Ar}$ time-temperature paths by Metcalf *et al.* (2009). We will include this constraint in our thermo-kinematic models as outlined below.

III-1.4 Numerical modeling

III-1.4a Model set up

Our thermo-kinematic modeling is based on *Pecube* (Braun 2003; see also Braun *et al.* in review), a finite-element code that solves the heat-transfer equation in 3 dimensions in a crustal block for a prescribed exhumation (rock advection) and topographic history as well as a number of fixed physical parameters. The crustal block has spatially constant material properties, representative of

the continental crust (Table III-1). In our case, we also adopt spatially constant vertical rock advection and model the area as a single uplifting block. As discussed previously, the thermochronology data record spatially homogeneous exhumation of the study area since ~40 Ma, allowing us to make this simplifying first-order assumption.

| Parameter | value |
|------------------------------|--------------------------------------|
| Crustal density | 2700 kg m ⁻³ |
| Mantle density | 3200 kg m ⁻³ |
| Equivalent elastic thickness | 25 km |
| Young's modulus | 10 ¹¹ Pa |
| Poisson ratio | 0.25 |
| Crustal thickness | 40 km |
| Thermal diffusivity | 25 km ² Myr ⁻¹ |
| Basal crustal temperature | 720 °C |
| Sea-level temperature | 15 °C |
| Atmospheric lapse rate | 4 °C km ⁻¹ |
| Crustal heat production | 0.95 μW m ⁻³ |

Table III - 1. Fixed thermo-kinematic and elastic parameters used in *Pecube* inversions. Crustal thickness is based on ECORS seismic profile (ECORS Pyrenees Team, 1988); basal temperature and crustal heat production are set to obtain a surface heat flow of 70 mW m⁻² and corresponding geothermal gradient of 33 °C km⁻¹ (e.g., Fernández & Banda, 1989; Fernández et al., 1998). Poisson ratio, Young's modulus and equivalent elastic thickness are used for calculating the isostatic rebound in response to relief change. Equivalent elastic thickness is constrained by flexural models (Zoetemeijer et al., 1990).

We aim to constrain the history of regional exhumation rates as well as the amount and timing of backfilling and re-excavation of the southern Pyrenees, using the available thermochronological data as constraints. The regional exhumation history is modeled as a number of exhumation phases, characterized by a constant exhumation rate between a beginning and end time. In order to maintain reasonable computing time, the topographic surface is obtained by downgrading the Shuttle Radar Topography Mission (SRTM) digital elevation model to a resolution of 1 km, sufficient to obtain accurate results as demonstrated by Valla *et al.* (2011). To test the hypothesis of backfilling by conglomerates, we have modified the way in which topographic evolution is parameterized in *Pecube*, in comparison to recent models (e.g., Valla et al. 2010; Glotzbach et al. 2011): here we impose a minimum elevation (H) to the topography to control the thickness of sediments infilling the valleys (Figure III-4). An increasing minimum elevation through time

models sedimentation in those areas where the present-day topography is lower than the prescribed minimum elevation, whereas a decreasing minimum elevation models erosion in those areas. The material added to fill the valleys has the same thermal properties as the crustal block. The total local erosion rates for locations at elevations lower than H are thus obtained by summing the regional exhumation rates and the local valley incision rate (rate of change in H).

The evolution from one topographic step to another can be either exponential or linear (Braun & Robert, 2005); we choose to let it evolve linearly in our models in order to limit the number of parameters. Valley infilling and incision is compensated by flexural isostasy, itself controlled by the value of the elastic thickness (25 km; Table III-1), constrained by flexural models of the Pyrenees (Zoetemeijer *et al.*, 1990). Hence, the elevation changes predicted by our modeling pertain to the isostatically balanced paleo-topography (*i.e.* the elevation changes are considered with respect to an external reference frame).

III-1.4b Pecube inversions

Pecube predicts time-temperature paths for each node that ends up at the surface at the end of the model run and uses these together with thermochronological age-prediction models to calculate thermochronometric ages. Here we use the AFT annealing model of Stephenson *et al.* (2006), the ZFT annealing model of Tagami *et al.* (1998), and the AHe diffusion model of Farley (2000). More elaborate models exist that take into account the kinetic effects of apatite composition for AFT and α -damage for AHe (e.g., Ketcham *et al.* 2007; Flowers *et al.* 2009; Gautheron *et al.* 2009). However, of the two AFT studies used here, Fitzgerald *et al.* (1999) did not report kinetic parameters, while the newer studies (Sinclair *et al.*, 2005; Gibson *et al.*, 2007) reported apatite kinetics (based on D_{par} values) very close to that of Durango apatite, on which the Stephenson *et al.* (2006) model is calibrated. Likewise, apatite U-Th concentrations reported by Gibson *et al.* (2007) and Metcalf *et al.* (2009) are typically a few tens of ppm, within the range where the conventional model of Farley (2000) predicts He-diffusion in apatite satisfactorily (Flowers *et al.*, 2009; Gautheron *et al.*, 2009). Predicted thermochronological ages are compared to the observed data to assess the overall fit of the model. To evaluate statistically the difference between modeled and observed ages, we use the objective function defined by Glotzbach *et al.* (see also 2011; Braun *et al.* in review):

$$\mu = \sum_{i=1}^n \left(\frac{m_i - o_i}{\sigma_i} \right)^2 \quad (1)$$

With μ the misfit value, n the number of data and, for each datapoint i , o_i the observed value (age or mean track length), m_i the modeled (predicted) value and σ_i the observed (1- σ) error. We thus fit the model to the set of thermochronological (AFT, AHe, ZFT) ages and mean AFT lengths.

Pecube attributes an age equal to the model onset time (40 Ma in our case) to thermochronological systems that were not sufficiently heated to be reset during the model run, which is the case for the ZFT data used here. We therefore include the constraint provided by the unreset ZFT ages by setting them to 40 Ma, with the same relative error as the original data.

The inverse approach couples *Pecube* with the Neighborhood Algorithm (Sambridge 1999a;b), allowing us to define an optimal model (i.e a best-fitting set of parameters) within a predefined parameter space (sampling stage), as well as to evaluate the level of precision with which each parameter is resolved the data (appraisal stage). In more detail, during the sampling stage the parameter space, as defined by the user, is divided into Voronoi cells centered on each model (combination of parameter values). During an initial iteration, 96 randomly chosen forward models are run and their misfit is assessed using Equation 1. Subsequent iterations also use 96 forward models but for which the parameter space is gradually restricted to the best-fitting 80 models from the previous iteration. The results presented here are obtained by 200 iterations after the initial seed and therefore each represent 19296 forward models. At the end of the sampling stage, we thus have a large collection of models that converge to an optimal combination of parameter values as a function of their misfit, but these solutions are strongly dependant on the calibration of the sampling stage itself (number of iterations, percentage of models resampled, etc; cf. Braun *et al.*, in review). Therefore, to more rigorously assess these results, a Bayesian estimate of parameter values is calculated during the appraisal stage by re-sampling the models and calculating the marginal posterior probability density function (PDF) of each parameter. For more details on the appraisal stage, see Valla *et al.* (2010) and Glotzbach *et al.* (2011).

III-1.4c Parameter space

There are four main sets of parameters that can vary in *Pecube*: topographic settings, kinematics (i.e., vertical exhumation rates), timing of change in topography or exhumation rates, and thermal parameters. We have run a total of about 45 inversions with varying degrees of freedom for these sets of parameters. We have found that optimal thermal parameters rapidly converge to values that are consistent with available data on the thermal structure of the Pyrenean foreland (Fernández and Banda 1989; Fernández *et al.* 1998): surface heat flow of $\sim 70 \text{ mW m}^{-2}$ and a corresponding geothermal gradient of $30\text{-}35 \text{ }^{\circ}\text{C km}^{-1}$. In the models shown here, therefore, thermal parameters are fixed to obtain a near-surface geothermal gradient of $33 \text{ }^{\circ}\text{C km}^{-1}$ (Table III-1). Similarly, the timing of major changes in exhumation rates converged rapidly in the earlier inversions; these timings were therefore also fixed in later inversions. We focus on the post-orogenic history of the southern Pyrenees here; the two main issues that we are interested in are whether the data require Pliocene acceleration of regional exhumation rates and whether they allow to quantitatively constrain valley infilling by conglomerates in terms of thickness and timing. We thus define

different phases of syn- and post-orogenic exhumation as well as minimum paleo-elevations of valley bottoms (H) at different times (Figure III-4).

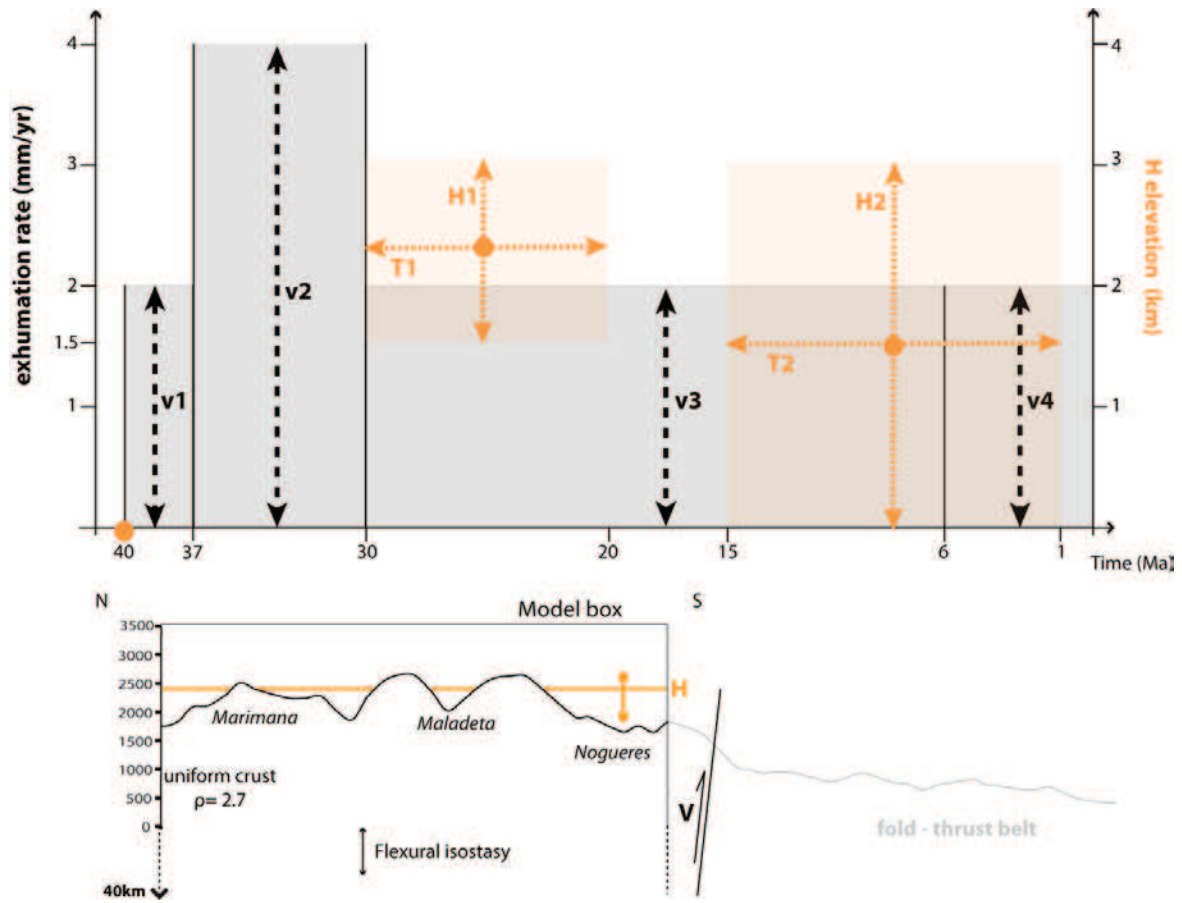


Figure III- 4. Free model parameters that are inverted for. (a) Evolution of exhumation rate (V1 – V4) and minimum elevation (H1, H2) through time. Grey shading and black arrows show prior range in parameters describing exhumation rates (V1-V4); yellow arrows show prior ranges in parameters describing topographic change and their timing (H1, H2, T1, T2). The timing of change in exhumation rate is fixed at 37 (V1 – V2), 30 (V2 – V3) and 6 (V3 – V4) Ma, respectively; the time of change in minimum elevation (T1, T2) is allowed to vary. Note that in model A all the parameters are independent, whereas H2 is set equal to H1 in model B. (b) Schematic north-south topographic cross-section across the study area, showing the extent of the modeled domain, the bounding fault controlling model exhumation and the implementation of the minimum-elevation value H through time.

We present here our two final inverse-model results that differ only with respect to the evolution of sediment infilling (minimum elevation of topography) during Miocene times. Both models start at 40 Ma and include four phases of exhumation, the timing of which is fixed (given rapid convergence on these times during earlier inversions) at 40-37, 37-30, 30-6 and 6-0 Ma (Figure

III-4). Velocities during these phases are allowed to vary between 0-2 km My⁻¹ during the 1st, 3rd and 4th phases (V1, V3, V4), while the exhumation rate between 37-30 Ma (V2) is allowed to vary between 0-4 km My⁻¹. V2 models the late Eocene-early Oligocene phase of rapid exhumation inferred from the thermochronology data by all authors (Fitzgerald et al. 1999; Sinclair et al. 2005; Gibson et al. 2007; Metcalf et al. 2009), while the post-orogenic time period is split in two phases (V3, V4) in order to specifically test for a Pliocene increase in exhumation rates, as argued for by Fitzgerald *et al.* (1999) and Babault *et al.* (2005b, 2009).

The topographic (valley infilling and excavation) history is modeled using three phases (Figure III-4). Infilling starts at the onset of the model run (40 Ma), as constrained by magnetostratigraphic data (Beamud et al. 2003, 2011). The models invert for the minimum elevation at the end of infilling (H1) and at the onset of excavation (H2). The minimum elevation at the end of infilling varies between 1.5 km (the preserved top of the conglomerate remnants; e.g., Beamud *et al.*, 2011) and 3 km, whereas the elevation at the onset of excavation is allowed to vary between 0-3 km. The timing of the end of infilling (T1) represents the time when the thickness of sediments was maximum; given the evidence for conglomeratic sedimentation at least up to 27-28 Ma (Beamud *et al.*, 2011), T1 is allowed to vary between 20-30 Ma. The timing of onset of excavation (T2) is allowed to vary between 1-15 Ma, in order to include all suggested times of establishment of a through-going Ebro River and associated incision (e.g. Coney et al. 1996, Garcia-Castellanos et al. 2003; Babault et al. 2005b, 2006). In model A (inversion 26) H1 and H2 are independent, whereas in model B (inversion 28) H2 is constrained to be equal to H1, so as to explicitly model a stable period without erosion or deposition between times T1 and T2. Thus, model A has 8 free parameters, while model B has 7. Table III-2 synthesizes the free parameters, their prior bounds and optimal values after inversion.

III-1.5 Results

Inversion results are presented in Figures III-5 (model A) and III-6 (model B), respectively, and synthesized in Figure III-7 and Table III-2. Figures III-5 and III-6 show scatter plots of individual forward-model misfit projected on planes defined by different sets of parameters, permitting to visualize the model convergence. They are associated with 1D and 2D posterior marginal probability density functions (PDFs) for the different parameters and parameter combinations. The optimal value for each parameter presented below and in Table III-2 corresponds to the modal (peak) value of the 1D marginal PDF and its uncertainty is calculated as the Gaussian half-width of the calculated PDF. Figure III-7 shows synoptic 2D marginal-probability plots that illustrate the evolution of regional exhumation rates (V) and valley filling (H) through time. Model B shows better-defined convergence during the sampling stage than model A, leading to more tightly constrained estimates of optimal parameter values after the appraisal stage. However, both models

are characterized by reasonably to well-defined parameter PDF's, from which optimal parameter values can be estimated with confidence, and by similar optimal misfit values.

III-1.5a Exhumation history

Predicted regional exhumation rates (V) for the 4 defined phases are similar for models A and B (Figures III-5-7; Table III-2): both models show fairly rapid exhumation between 40 and 37 Ma and very rapid exhumation from 37 to 30 Ma, followed by a major decrease to very slow rates until the present. In model A, exhumation rates increase from $V1 = 0.5 \pm 0.2 \text{ km Myr}^{-1}$ between 40-37 Ma to $V2 = 3.5 \pm 0.3 \text{ km Myr}^{-1}$ between 37-30 Ma. In model B, the increase is a bit less strong, from $V1 = 1.0 \pm 0.6 \text{ km Myr}^{-1}$ to $V2 = 2.8 \pm 0.3 \text{ km Myr}^{-1}$. Over the last 30 Ma, rates are constant, very slow and similar in both models: $V3 = V4 = 0.02 \pm 0.05 \text{ km Myr}^{-1}$. Neither model thus predicts or requires a recent increase in regional exhumation rates.

In both cases, the regional exhumation rates predicted by our inversions are in good agreement with a first-order analysis of the thermochronological data. The few ZFT ages limit exhumation rates prior to 30 Ma, whereas initial inversions without these data predicted unrealistically high exhumation rates of $\sim 6 \text{ km Myr}^{-1}$ during this time interval; the AFT ages and track lengths constrain the rapid exhumation phase and, finally, AHe ages allow to constrain the late-stage exhumation with better precision. Thus, exhumation for the “syn-orogenic” phases (40-30 Ma) is well defined and inferred rates are in agreement with previous studies. In contrast, the “post-orogenic” ($<30 \text{ Ma}$) exhumation rates are very low and the topographic changes play an important role in fitting the data.

III-1.5b Topographic evolution

We next consider the influence of the conglomerates infilling paleovalleys in modifying the relief and local burial/erosion histories. We focus here on the evaluation of 1) the maximum thickness of sediments infilling the valleys, 2) the timing and rates of incision of the valleys, and 3) the possibility that a stable filled topography existed for some time during the Oligocene-Miocene. It

Model A

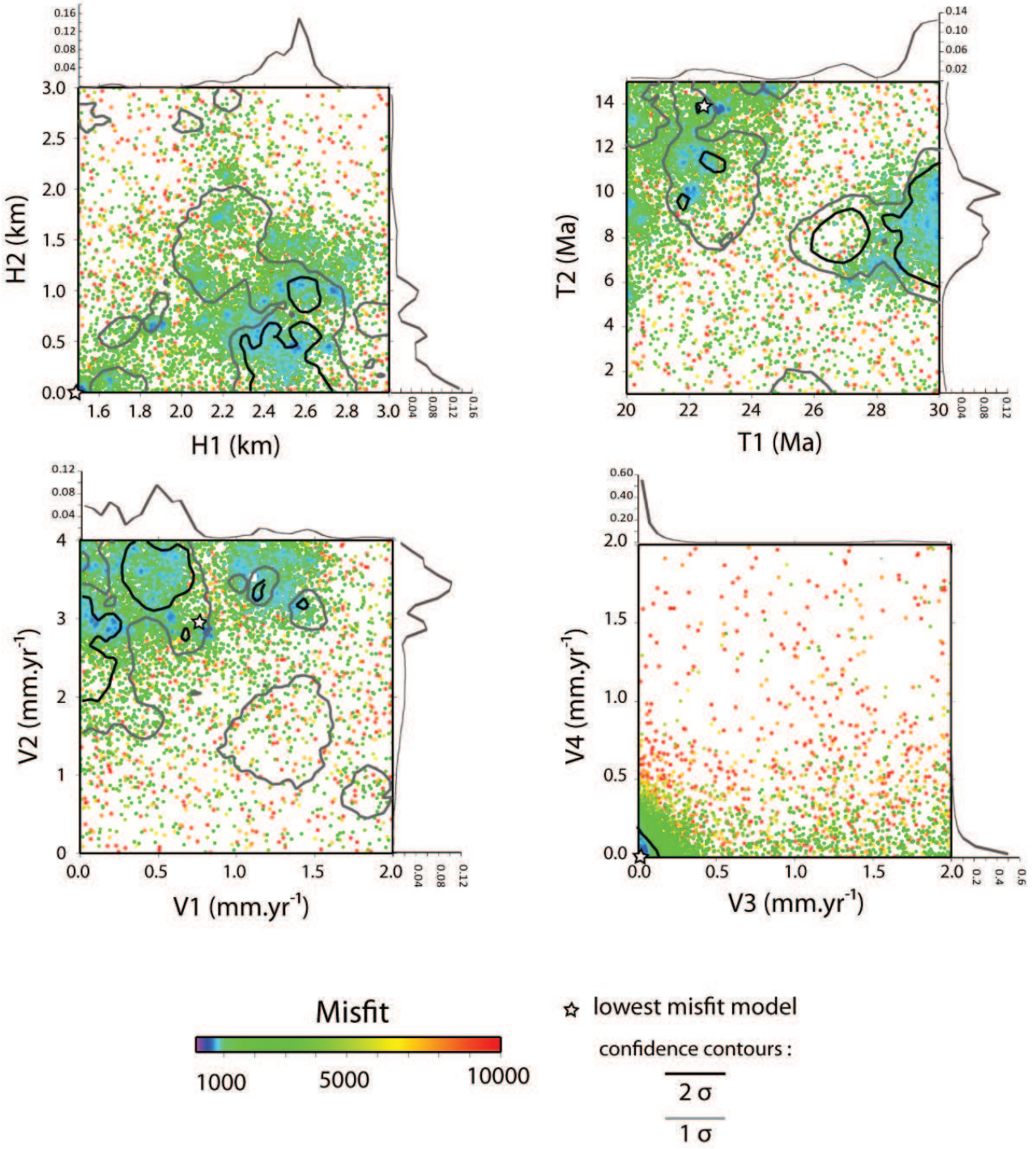


Figure III- 5. Inversion results for model A (inversion 26): Scatter plots are 2D projections of the 8-dimensional parameter space on planes defined by combinations of two parameters. Each dot indicates an individual forward-model run; dots are coloured according to misfit. Star indicates overall best-fit model. 1D and 2D marginal posterior parameter probabilities are also indicated as probability-density functions (PDF's) along each axis and 1- σ (67 % confidence) and 2- σ (95 % confidence) contours within the scatter plots, respectively. See text for discussion.

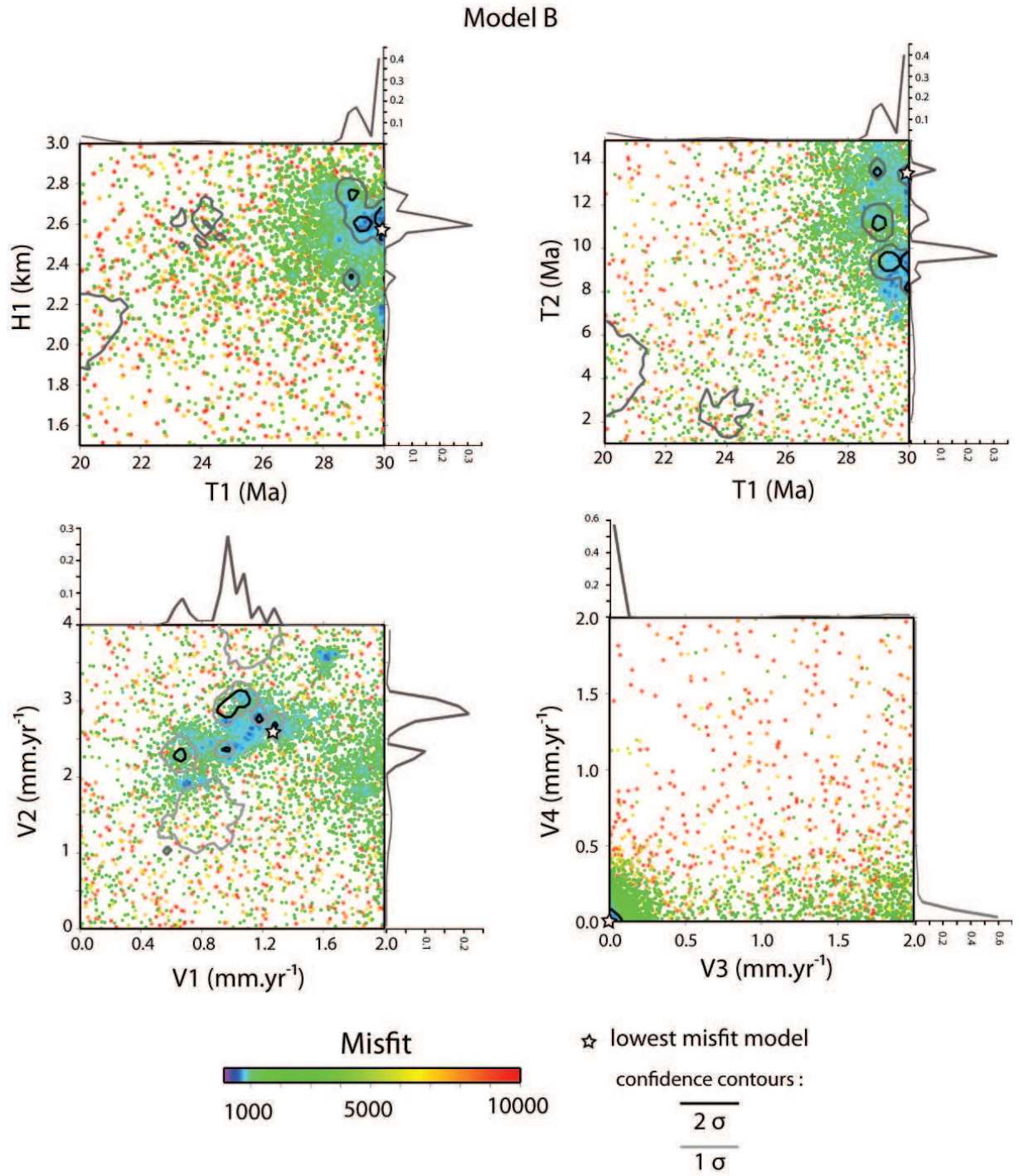


Figure III- 6. As Figure III-5 but for model B (inversion 28). Note that this is a 7-parameter model; since $H2$ is not an independent parameter ($H2 = H1$) in this inversion, it is not plotted here.

is worth noting that the highest current elevation in the study area is 3382 m, whereas the lowest is 212 m and the average valley-bottom elevation in the Nogueres zone (the lowest part of the study area) is around 800 m, so that H-values lower than 800 m mean that no relief changes are applied to the area. Moreover, the H-value expresses the minimum elevation of the model topography through time, so the present-day topography has to be subtracted from it to obtain the predicted local thickness of sediments.

In model A, the infilling elevation increases continuously from no infilling at 40 Ma to 2.6 ± 0.1 km (H1) at 29.8 ± 0.7 Ma (T1). These results imply infilling of the Axial Zone valleys at a maximum rate of ~ 0.23 km Myr⁻¹; the valleys reach their maximum fill immediately after the end of the rapid exhumation phase. The model subsequently predicts excavation of the valleys, with H2 = 0.0 ± 0.5 km at T2 = 9.9 ± 2.1 Ma, implying maximum erosion of 2.6 km in 20 Myr at a rate of ~ 0.13 km Myr⁻¹ during T1-T2. Thus, in this model valley excavation starts immediately after the peak infilling at ~ 30 Ma and, unexpectedly, incision rates drop during Late-Miocene times.

| Parameter | code | Unit | Prior range | Inversion results | |
|-----------------------------|------|----------------------|-------------|-------------------|-----------------|
| | | | | Model A | Model B |
| Exhumation rate 40-37 Ma | V1 | km Myr ⁻¹ | 0 – 2 | 0.5 ± 0.2 | 1.0 ± 0.6 |
| Exhumation rate 37-30 Ma | V2 | km Myr ⁻¹ | 0 – 4 | 3.5 ± 0.3 | 2.8 ± 0.3 |
| Exhumation rate 30-6 Ma | V3 | km Myr ⁻¹ | 0 – 2 | 0.02 ± 0.04 | 0.02 ± 0.05 |
| Exhumation rate 6-0 Ma | V4 | km Myr ⁻¹ | 0 – 2 | 0.02 ± 0.05 | 0.02 ± 0.05 |
| Valley infilling at time T1 | H1 | km | 1.5 – 3 | 2.6 ± 0.1 | 2.56 ± 0.02 |
| Valley infilling at time T2 | H2 | km | 0 – 3* | 0.0 ± 0.5 | 2.56 ± 0.02 |
| End of valley infilling | T1 | Ma | 30 - 20 | 29.8 ± 0.7 | 29.8 ± 0.3 |
| Onset of valley excavation | T2 | Ma | 15 - 0 | 9.9 ± 2.1 | 9.2 ± 0.5 |
| Number of parameters | | | | 8 | 7 |
| Lowest misfit μ | | | | 584 | 596 |

Table III - 2. Free kinematic, topographic and timing parameters used in Pecube inversions. Prior range is the predefined range within which the parameter values are allowed to vary; inversion results give modal value of parameter PDF and Gaussian half-width of the PDF after the NA appraisal stage. *Note that in model B (inversion 28), H2 is set equal to H1 and is thus not an independent parameter.

Model B was thus designed to include a phase of stable topography between the end of valley infilling and the onset of excavation, by setting H2 = H1. This model predicts a similar infilling scenario: from no infilling at 40 Ma to 2.56 ± 0.02 km (H1) at 29.8 ± 0.3 Ma (T1). However, in this

case, incision starts only at 9.2 ± 0.5 Ma (T2). Considering a mean elevation of 2400 m for the Maladeta / Marimaña area and 1400 m for the Nogueras zone, we evaluate a mean sediment thickness of 1200 m on top of the Nogueras zone, whereas the summits of the Maladeta and Marimaña massifs were not covered. This model predicts valley excavation at a rate of 0.28 ± 0.02 km Myr⁻¹ since late Miocene (Tortonian) times. Thus, Late-Miocene to recent local erosion rates varied between 0.02 ± 0.05 km Myr⁻¹ for areas above H2 to a maximum of 0.30 ± 0.07 km Myr⁻¹ for valley bottoms.

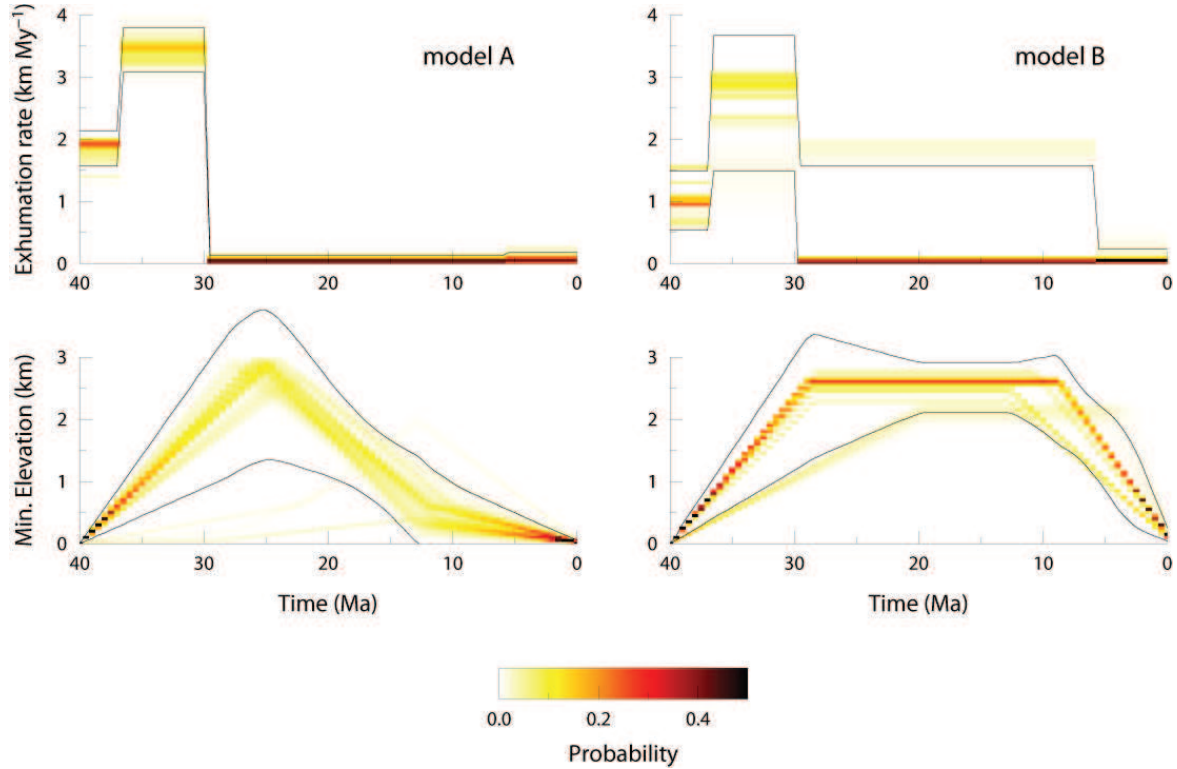


Figure III- 7. Synoptic probability-density plot showing evolution of exhumation rate (V) and valley filling (minimum elevation H) parameters through time for models A (inversion 26) and B (inversion 28). This plot synthesizes the inversion results by combining the PDF's calculated individually for parameters $V1-V4$ and $H1-H2$ (Figures III-5 and III- 6) as a function of time. The time-evolution of the H parameter is interpolated linearly between each value. Colour coding shows probability of any particular exhumation rate and minimum elevation as a function of time; thin black lines show 95% confidence contours.

The differences between the two models thus lie principally in the predicted post-orogenic excavation of the conglomerates infilling the valleys. Syn-orogenic infilling and the maximum amount of sediments are similar for the two models. However, model A predicts an immediate onset of excavation in Oligocene times, whereas model B predicts that incision started during the

late Miocene. Both models imply that an important amount of sediments has covered the southern Axial Zone and that incision started well before the Messinian or Pliocene, whatever the detailed evolution of topography during Neogene times. We will argue below that the scenario predicted by model B appears much more consistent with independent geological and geomorphological data for the evolution of the Ebro drainage system than that of model A.

III-1.5c Comparison with observed ages

Two forward models corresponding to the optimal values for exhumation rates and topographic changes inferred from the inversions were run to compare modeled and observed age patterns. Figure III-8 shows the observed and modeled ages plotted against elevation. AFT ages predicted by model A fit the steep age-elevation gradient above 1700 m elevation very well but fail to reproduce the distinct break-in-slope in the observed age-elevation relationship. AHe ages predicted by this model similarly line up along a steep age-elevation trend, toward the older limit of the observed ages.

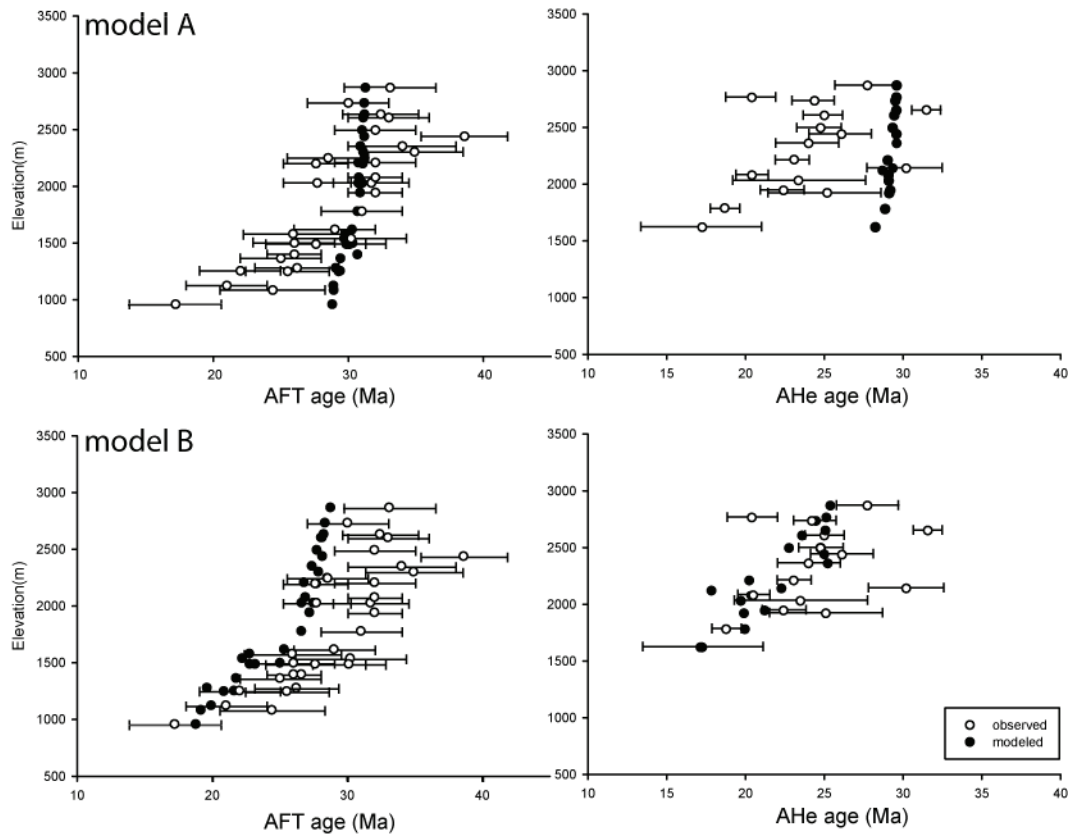


Figure III- 8. Fit of predicted ages (optimal models A and B, black circles) to observed ages (white circles with error bars); both are shown with respect to elevation (compare with Figure III-3).

Model B reproduces the AHe-age pattern much better. AFT ages predicted by this model show a similar pattern to that observed, including a clear break-in-slope, but the upper, steep part of the profile is offset by 1 to 3 Ma from the observed ages. Nevertheless, model B appears to better reproduce the observed age-elevation relationships for both thermochronometers; these results reinforce our preference for model B. This comparison also shows that the timing of final incision of the conglomerates is mainly constrained by the slope of the age-elevation relationship at low elevations, *i.e.* in localities that have been covered by conglomerates.

III-1.6 Discussion

III-1.6a Limitations of the model

Before we start exploring the implications of our model results for the late syn-orogenic and post-orogenic evolution of the southern Pyrenees and Ebro basin, it is appropriate to first outline some limitations of the model and assess their influence on the results. Most of these limitations tend to affect our inferred syn-orogenic exhumation and topographic history more strongly than the post-orogenic history.

First, we assume thermal parameters and physical properties of rocks to be constant. Heat production, thermal diffusivity and temperature at the base of the model were inverted for in initial inversions and the results systematically converged toward constant values that were consistent with measured heat flow in the region (Fernández and Banda 1989; Fernández et al. 1998). We therefore decided to fix these in order to limit the number of free parameters in the models and focus on the exhumation history and topographic evolution. However, potential variations in thermal conductivity, in particular sediment-blanketing effects, are not taken into account (see Section 6.3 for further discussion).

Another simplification is to model the whole area as a single vertically exhuming block. Obviously, the area is structured by several major thrusts (Figure III-1) that show a complicated activation sequence and potential re-activation or out-of sequence thrusting (cf. Section 2.1). There are, however, three main arguments to justify this approach. First, the main phase of exhumation in this part of the Pyrenees took place while the currently widely exposed Orri thrust sheet was uplifted as the passive roof of the underlying Rialp thrust sheet (Muñoz 1992; Beaumont et al. 2000); K-feldspar ^{40}Ar - ^{39}Ar data suggest that internal thrusting in the Orri thrust sheet had ceased by ~50 Ma (Metcalf et al. 2009). Secondly, as discussed in Section 3, the thermochronological data show a uniform age-elevation trend, implying uniform first-order patterns of exhumation, even though they are located in different thrust sheets. Thirdly, our main interest here is in the post-orogenic evolution of the study area, while the central Pyrenean topography was passively eroded. Our approach does not allow us to assess the effects of potential late-stage out-of-sequence thrusting in the study area, as suggested for the Barruera massif just south of Maladeta (Sinclair et

al. 2005; Gibson et al. 2007). We therefore exclude these more local complexities from our analysis, which focuses on the first-order exhumational and topographic history of the study area.

The topographic evolution is implemented in a very simple manner in *Pecube*, in this case by imposing an evolving minimum elevation to the model. This implies linear and constant erosion rates through time (we can control this parameter only by changing directly the relief parameters), and deposition consists in filling up the topography to the specified minimum elevation (cf. Section 4.1). We acknowledge that the topographic history may have been much more complex than this, although published provenance data for the preserved late-orogenic conglomerates suggest that planform drainage patterns have been relatively stable since the Eocene (Vincent 2001). However, this approach allows us to explore the first-order variation in post-orogenic topography with a minimum number of parameters.

Moreover, the initial topography at the onset of the model run is the same as the present-day topography. Several inversions were performed to try to quantify the initial topography, but these proved unsuccessful: none of the inversions converged to a clearly defined parameter set. Paleotopography has proven to be the most difficult parameter to constrain from inversion of thermochronological datasets (Valla et al. 2010; 2011) and as there are no published data that constrain the paleotopography of the Pyrenees, we choose to use the present-day topography as the initial topography. We note that stacking of the Noguères and Orri units was already well underway at 40 Ma so we expect significant topography to have existed at that time already.

Finally, one may be somewhat disappointed by the degree of fit of our optimal model predictions with the observed data (Figure III-8). Obviously, fitting a simple linear trend to the data provides a visually more satisfying concordance to the data. However, our model predictions result from a physically based model that aims to fit the entire dataset using realistic time-temperature paths for rock particles. In fact, we feel this is a strength rather than a weakness of the model, and we believe that the discrepancies between earlier interpretations result from consideration of a partial dataset and incomplete exploration of possible tectonic and geomorphic scenarios.

III-1.6b Neogene acceleration in exhumation rates?

The two main results of our modeling with respect to the exhumation history of the southern Pyrenees are: (1) there is a clear signal of rapid exhumation during the late Eocene-early Oligocene (37-30 Ma); and (2) there is no evidence for a late-Neogene or Quaternary acceleration in exhumation rates.

Although the syn-orogenic exhumation is not the main focus of this study, an assessment of the inferred rates and comparison with earlier studies is appropriate. Morris *et al.* (1998) modeled cooling histories for single AFT samples and concluded that most rapid exhumation took place between 35-30 Ma at rates of $\sim 0.25 \text{ km Myr}^{-1}$ to the east of the ECORS profile area; no data from the study area were available at that time. Fitzgerald *et al.* (1999) subsequently showed that the

AFT age-elevation relationship in the Maladeta massif requires much more rapid exhumation (2-4 km Myr⁻¹) during this time. Gibson *et al.* (2007) used *Pecube* forward modeling to suggest exhumation rates of 1-1.5 km Myr⁻¹ during the Late Eocene-Early Oligocene from their AFT and AHe data (but without taking Fitzgerald *et al.*'s (1999) data into account). Finally, Metcalf *et al.* (2009) suggested cooling rates of only ~10 °C Myr⁻¹ for this time period from thermal modeling of K-feldspar ⁴⁰Ar/³⁹Ar and AFT data, but without taking the age-elevation relationship into account. Our prediction of maximum exhumation rates of 2.5 km Myr⁻¹ at 37-30 Ma, while qualitatively comparable with these previous results, is at the high end of these estimates. These high rates are required by the nearly vertical AFT age-elevation trend for samples above ~1700 m elevation. They are limited by the inclusion of the ZFT data as well as the 4-8 Ma difference between AFT and AHe ages at similar elevations (Figure III-3), but the fact that only 4 ZFT ages are available and that their inclusion in the model is somewhat artificial (cf. Section 3.1) may limit their moderating effect on predicted syn-orogenic exhumation rates.

Both models consistently show very slow post-orogenic regional exhumation rates, of the order of 0.02 km Myr⁻¹. Our preferred model B implies such slow regional rates while the topography was largely buried under the conglomerates, and predicts the same value during excavation. In model A, exhumation rates also drop to close to zero immediately after 30 Ma. Such a rapid drop from very high to very low rates is inconsistent with conceptual models that suggest exponentially decreasing exhumation rates once orogenesis ceases (e.g. Baldwin *et al.* 2003), but supports earlier interpretations of the data (e.g., Fitzgerald *et al.*, 1999; Gibson *et al.*, 2007). It is possibly linked to rapid relief reduction due to conglomeratic infilling of the valleys, which nearly smothered the topography by 30 Ma (Figure III-9).

Neither of our two final scenarios supports a Late-Neogene or Quaternary acceleration in exhumation rates, as suggested by Babault *et al.* (2005b; 2009). In fact, such an acceleration was not predicted by any of our inversions. We conclude that regional denudation in the Pyrenees appears not to have been significantly affected by Late Neogene-Quaternary climate change (Zhang *et al.* 2001; Molnar 2004), providing some support for the suggestion that such changes may have had little influence on erosion rates (Willenbring and von Blanckenburg 2010).

III-1.6c Age and thickness of conglomerate deposits

Coney *et al.* (1996) first proposed that the conglomerates present today in the northern part of the south Pyrenean foreland (Figures III-1, III-2) once extended farther north, onlapping onto the Axial Zone. The magnetostratigraphic studies of Beamud *et al.* (2003, 2011) in the La Pobla de Segur area confirmed that the oldest sediments of the La Pobla massif were deposited in the paleovalley south of our study area at 40 Ma and then prograded northward, starting to infill the Senterada basin in the southern part of the Noguères Zone at 32 Ma. Northward progradation and onlapping of conglomerates is a logical outcome of our model when the minimum elevation H

increases, because the elevation of valley bottoms increases northward and valley infilling only occurs in the Axial Zone when ≥ 0.8 km, the minimum elevation in that area. Both models suggest onlapping of valley bottoms in the Axial Zone from ~ 37 Ma onward, in reasonable agreement with the magnetostratigraphic constraints.

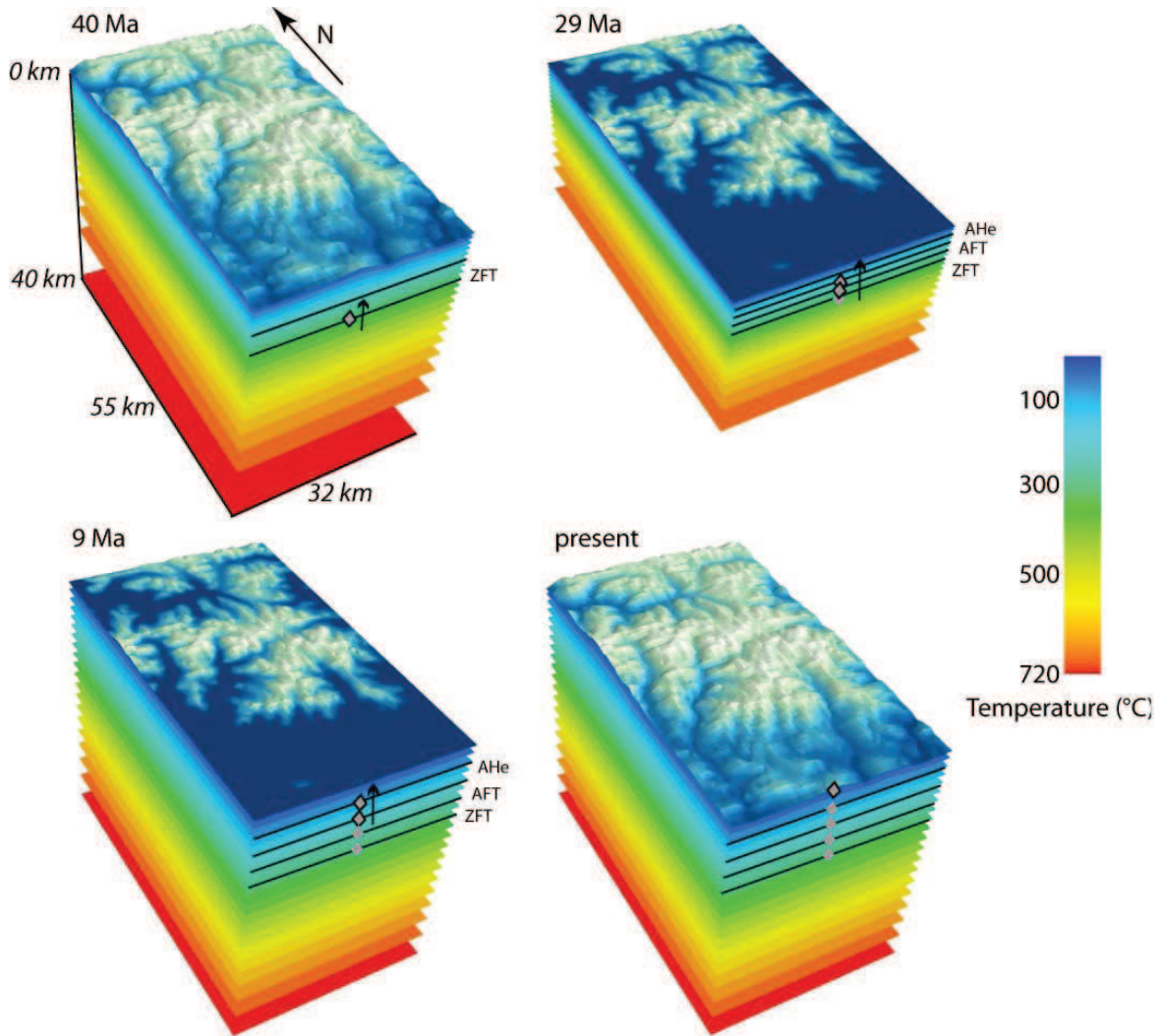


Figure III- 9. 3D visualization of the preferred scenario (model B) showing evolution of the thermal structure and topographic changes through time. Note strong compression of isotherms due to rapid exhumation between 37-30 Ma. Representative exhumation path for a rock sample in a valley bottom at the southern edge of the model is also shown.

Our models suggest that the conglomerate deposits reached an elevation of 2.6 km, implying a maximum thickness of about 2 km in the Axial Zone (Figure III-9); as stated previously, this estimate takes the isostatic response to topographic change into account. The total thickness in the foreland is difficult to extrapolate from our models, as they assume a simple horizontal upper

surface for the conglomerates, whereas in reality, these certainly wedged out toward the foreland. The thickness of sediments should have decreased toward the centre of the basin, or they would have overtopped the topographic barrier imposed by the Catalan Coastal Range (Garcia-Castellanos *et al.*, 2003). Although a thickness of ~2 km may seem large, it has been argued previously that such overburden is required to explain recent cooling recorded by AFT length distributions and AHe ages of low-elevation samples within the Axial Zone (Fitzgerald *et al.*, 1999; Metcalf *et al.*, 2009). Recently, two independent studies (Beamud *et al.*, 2011; Rahl *et al.*, 2011) have shown that AFT ages from granitic cobbles at the base of the conglomerate deposits in the foreland are partially reset, again implying that significant overburden once existed. The exact thickness of sediments may be modulated by the geothermal gradient within the covering conglomerates. We cannot place any constraint on that value; if the gradient in the conglomerates was much higher than the current 30-35 °C km⁻¹ measured in the Pyrenean foreland due to sediment-blanketing effects, the sediment thickness could have been correspondingly less. However, the conglomerates consist mainly of Axial Zone lithologies (Vincent 2001) so it is difficult to argue for significantly lower thermal conductivity (required for sediment blanketing) within them, in comparison to the underlying substrate. Moreover, rapid deposition, together with the relatively high permeability of the conglomerates, would lead to a decreased rather than an increased geothermal gradient (Dempster and Persano 2006) implying that our estimate of sediment thickness may be a minimum. In any case, our model predicts that there was sufficient overburden in the northern part of the south Pyrenean foreland to partially reset the AFT system and fully reset the AHe thermochronometer in underlying deposits. We are currently collecting such data to test the model.

A question that remains unanswered is what drove the relatively sudden deposition of these significant amounts of sediment. It is obvious from the provenance data (Vincent, 2001) and the simultaneity of rapid exhumation in the Axial Zone with conglomerate deposition (Beamud *et al.*, 2011; this study), that the Axial Zone was the major source for these proximal sediments. Thus, erosion of the Axial Zone became important enough to completely over-feed the drainage system. Costa *et al.* (2009) have recently shown that the connection of the Ebro basin to the Atlantic Ocean closed at 36 Ma, leading to endorheic conditions; closure of the basin could thus be linked with the “non-evacuation” of the conglomerates. However, conglomerate deposition probably started a few Myr before the basin became endorheic. Moreover, it is hard to imagine how distal closure of the basin (nearly 400 km from the study area) would lead to an immediate response in very proximal sites. Therefore, it appears that this important change in the depositional system was controlled by increased erosion of the source area rather than by basin closure. Huyghe *et al.* (2009) analyzed erosional and accretionary fluxes through time in the south-western Pyrenean foreland fold-and-thrust belt and suggested that climatic changes during the Eocene-Oligocene transition could be

the predominant factor in increasing denudation. However, our models do not allow us to decipher whether increased Axial Zone erosion was triggered by tectonics or climate change.

III-1.6d Timing of and controls on post-orogenic incision

Although closure of the Ebro basin cannot be directly linked to the onset of conglomerate deposition, the Neogene drainage evolution of the Ebro appears to have significantly influenced their subsequent incision. Given that our models do not provide support for Pliocene-Quaternary climatic control on post-orogenic erosion (cf. Section 6.2), re-excavation of the topography is most simply explained as being driven by a base-level drop, promoted by establishment of a connection between the Ebro Basin and the Mediterranean (Coney et al. 1996; Garcia-Castellanos et al. 2003). Our model B shows that the thermochronological data can be fit by imposing a stable filled topography between 29 and 9 Ma, with subsequent incision continuing to the present. Since propagation of the base-level drop at the outlet of the basin would take several Myr to propagate ~500 km to our study area (e.g. Whipple 2001, Loget and Van den Driessche 2009), this result sets a minimum age constraint for establishment of a connection to the Mediterranean. This timing is consistent with the model proposed by Garcia-Castellanos *et al.* (2003), who suggested an opening date between 13 and 8 Ma. It is also consistent with the presence of Tortonian lacustrine sediments in the center of the basin (Riba et al. 1983) and with the recent imaging of a major river system below the Messinian erosion surface in the Ebro delta area, as well as the presence of Serravalian-Tortonian deltaic sediments (Urgeles et al. 2011). Our modeling therefore strongly supports a Tortonian or earlier, rather than Messinian or Pliocene, connection of the Ebro Basin to the Mediterranean.

In contrast, the post-orogenic topographic evolution suggested by model A is not supported by independent data, which leads us to reject that model even though it has a similar optimal misfit to model B (Table III-2). Model A would imply that Ebro basin endorheism lasted only a few Myr, which is inconsistent with the field observations, such as the middle-Miocene lacustrine sediments in the center of the basin. Thus, it appears that base-level variations exert the major control on the post-orogenic erosion and topographic development of the southern Pyrenees, rather than tectonics or climate. In particular, endorheic conditions led to low erosion rates and kept the topography stable; whereas re-establishment of a through-going drainage system drove valley incision and re-excavation of the topography, much of which must have been already established during orogenesis.

III-1.7 Conclusions

By combining all available low-temperature thermochronology data and including appropriate patterns of topographic change through time, we have developed a consistent model for the post-orogenic evolution of the southern Pyrenees and show that this was controlled primarily by the

evolution of drainage patterns and base level within the Ebro basin. Our preferred model for the topographic and erosional evolution of the Pyrenees (Figure III-9) leads us to the following conclusions:

(1) The southern Axial Zone experienced rapid exhumation ($>2.5 \text{ km Myr}^{-1}$) from 37 to 30 Ma, simultaneous with the onset of valley infilling by conglomerates. Our results do not allow us to discriminate between a tectonic or climatic trigger for this strong pulse of exhumation. Subsequently, exhumation rates strongly decreased to 0.02 km Myr^{-1} from 30 Ma to the present, indicating a rapid transition to stable post-orogenic conditions and no discernable influence of late-Neogene / Quaternary climate change on erosion rates in the Pyrenees.

(2) By the end of the syn-orogenic phase at 30 Ma, the valleys were infilled by erosional products up to an elevation of 2.6 km and this valley-fill remained stable until $\sim 9 \text{ Ma}$. We interpret this pattern as the consequence of endorheism of the Ebro basin, which permitted the accumulation of a significant amount of sediments, from conglomeratic in our study area to lacustrine in the center of the basin. Therefore, triggering of the infilling would be the consequence of increased denudation of the Axial Zone, but the subsequent stability of the overfilled topography is due to endorheism of the basin.

(3) The model predicts a decrease of the maximum elevation of the conglomerates with a constant rate from 9 Ma to present, which we interpret as reflecting incision of the valleys. In the absence of a clear climatic trigger for this incision, it is most easily explained as reflecting the propagation of a major base-level drop, due to establishment of a connection to the Mediterranean, toward the headwaters of the Ebro basin. We thus propose that the opening of the basin occurred at the latest during Tortonian times and that late-Neogene / Quaternary climate change had little effect on the post-orogenic erosional history of the Pyrenees.

Acknowledgements

This study is supported by INSU-CNRS through the European Science Foundation Topo-Europe programme “Spatial and temporal coupling between tectonics and surface processes during lithosphere inversion of the Pyrenean-Cantabrian mountain belt (PyrTec)”. It forms part of CF's PhD project at Université Joseph Fourier, supported by the French Ministry for Research and Higher Education. We thank Jean Braun, Christoph Glotzbach and Pierre Valla for helpful discussions and comments, and Paul Fitzgerald and Hugh Sinclair for providing details on sample locations. Most calculations were performed on the r2d2 cluster at the Service Commun de Calcul Intensif de l'Observatoire de Grenoble (SCCI); final inversions were run on the CU-CSDMS High-Performance Computing Cluster. PvdB acknowledges CIRES at the University of Colorado, Boulder, for partial funding of a visiting fellowship during which this manuscript was written. We thank Ed Sobel and Daniel Garcia-Castellanos for constructive reviews, and Brian Horton for efficient editorial handling.

Chapter III-2 Quantifying the timing and extent of post-orogenic sedimentation in the southern Pyrenean foreland

III-2.1 Introduction

The southern central Pyrenees have figured prominently in studies of external wedge building, thrusting sequences and interactions between tectonics and surface processes. This is mainly due to the exceptional exposure of syn-tectonic strata (Puigdefabregas and Souquet 1986; Vergés and Muñoz 1990) and the quality of the ECORS seismic profile (ECORS Pyrenees Team 1988) shot through this area. Nevertheless, no low-temperature thermochronological data has been published from the foreland fold-and-thrust belt, except in the conglomeratic massifs (Beamud et al. 2011; Rahl et al. 2011), which revealed the timing of the episode of rapid erosional unroofing of the Axial Zone.

Using thermo-kinematic modeling of the thermal evolution of the Southern Axial Zone presented in the previous chapter (III-1), we have shown that the conglomerates could have prograded toward the hinterland until 30 Ma and remained stable until 9 Ma. From the late Miocene to the present, valley incision is necessary to reproduce the low-temperature thermochronology data; we interpreted the onset of the valley incision as resulting from excavation of the Ebro basin when it opened to the Mediterranean. Moreover, we estimated a thickness of ~2 km for the deposits on the southern flank of the Axial Zone. We thus have proposed a scenario of topographic evolution from Axial Zone data that we extrapolated to the southern Pyrenean foreland, but no data were available to test our model predictions.

Apatite (U-Th)/He thermochronology is a powerful tool to quantify the exhumation in fold-and-thrust belts as the closure temperature is relatively low (75 ± 15 °C, Wolf et al. 1998; Farley 2000). Yet, this thermochronometer is very sensitive and requires high-quality samples, making the application of this method quite difficult in sedimentary terrains.

In this chapter, we present new apatite fission-track (AFT, closure temperature 110 ± 10 °C) and apatite (U-Th)/He (AHe, closure temperature 75 ± 15 °C) data of sandstones collected in the Tremp-Graus and Ager basins to provide estimates of the thickness and extent of the overlying conglomerate deposits, as well as to further constrain the timing of excavation of the basin. We

will show that despite relatively scattered AHe ages, we could perform thermal modeling and obtain consistent Mesozoic to Cenozoic exhumation histories for 3 samples.

III-2.2 Tectono-sedimentary evolution

The south-central Pyrenean fold-and-thrust belt (also called South Central Unit, SCU) developed consequently to the collision of the Iberian plate and the European plate in Late Cretaceous times. The underthrusting of the Iberian plate created the Pyrenean doubly-vergent wedge. The southern Pyrenees evolved as the pro-wedge by inversion of Cretaceous extensional structures (Puigdefàbregas and Souquet 1986, Bond and McClay 1995) followed by in-sequence thrust propagation towards the South (Vergés and Muñoz 1990; Muñoz 1992; Vergés et al. 1995; Beaumont et al. 2000). The fold-and-thrust belt propagated further in the central part of the range, compared to the regions east and west of it, by sliding on a thick Triassic evaporitic layer. Thrusting is at first order in-sequence, with activation of the Boixols thrust in the Late Cretaceous, followed by the Montsec thrust from Paleocene to late Eocene, which transported the Tremp-Graus Basin in a piggy-back manner (Puigdefàbregas et al. 1992), and finally the frontal thrust (Sierras Marginales area), active from middle Eocene to late Oligocene times (see Figure III-10 for locations). There is, however, evidence of out-of sequence thrusting as well as reactivation of the Boixols and Montsec thrusts (Capote et al. 2002, Sinclair et al. 2005) simultaneously with the in-sequence wedge development (the thrusting sequence will be discussed in detail in Chapter IV-2). From the ECORS seismic profile (ECORS Pyrenees Team 1988; Choukroune and ECORS Team 1989), as well as modeling and thermochronological studies of the Southern Axial Zone (Beaumont et al. 2000; Sinclair et al. 2005; Fitzgerald et al. 2006; Gibson et al. 2007; Metcalf et al. 2009), the exhumation of the internal units (Noguères, Orri and Rialp) is known to have occurred by vertical stacking (Muñoz 1992; Vergés et al. 1995) and to have been focused during middle to late Eocene times. From the compilation of the important dataset of low-temperature thermochronology we modeled (see previous chapter) rapid exhumation at a rate of 2.8 ± 0.3 mm Myr⁻¹ between 37 and 30 Ma in that area.

This rapid exhumation was associated with strong erosion of the southern Axial Zone massifs, the products of which were deposited in pre-existing paleo-valleys as a thick discordant pile of conglomerates (Sis, Gorp and La Pobla massifs, Figures III-10 and III-11), which probably represent sediment transfer zones, supplying the Huesca fan system (Figure III-11, Vincent 2001).

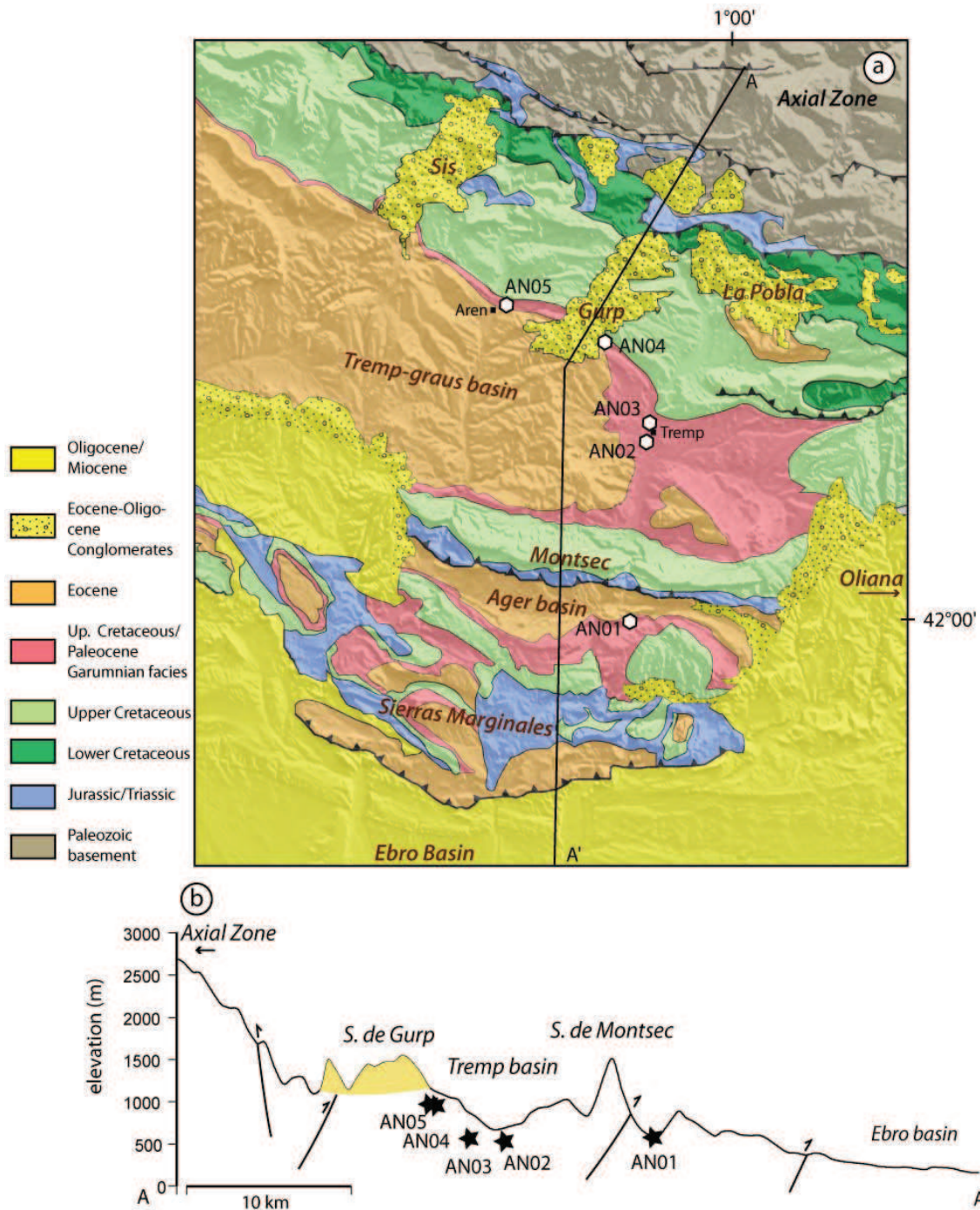


Figure III- 10. a) Simplified geological map of the southern central Pyrenees, (modified from ICC 2002), with sample positions. b) Topographic cross-section following the line A/A' in a), the sample positions have been projected on the section.

The link between the uplift of the internal massifs and deposition of the conglomerates massifs has been confirmed by pebble provenance studies (Vincent 2001) and by apatite fission-track analysis of pebbles from the Sis conglomerates (Beamud et al. 2011; Rahl et al. 2011), which both reveal unroofing of the Axial zone and deposition of its erosional products in the basin.

The present-day remnants of these major syn- to post-tectonic conglomerate deposits include the Senterada and La Pobla basins (Beamud et al. 2003; Beamud et al. 2011), the Sis conglomerates (Vincent, 2001), the Oliana fan (to the East of the CSU, Burbank et al. 1992b) and the Huesca fan (South-Southwest of our study area, Friend et al. 1996) and are ~1000 m thick at maximum. Magnetostratigraphic studies constrain the deposition of the Sis conglomerates at 40 to 27 Ma (Beamud et al. 2003; Beamud et al. 2011) and deposition of similar conglomerates to the east of the CSU, near the Oliana area (Burbank et al. 1992a) at 40 to 36 Ma.

The period of strong exhumation/erosion/deposition was synchronous with the closure of the Ebro foreland basin. Its connection to the Atlantic was closed at 36 Ma (Costa et al. 2009), and from that time the basin was endorheic until late Miocene times (Arenas and Pardo 1999; Garcia-Castellanos et al. 2003; Urgeles et al. 2011, previous chapter). During this period, the basin was progressively filled by conglomeratic deposits at its borders that graded to lacustrine sediments in its center, and developed into a large overfilled foreland basin.

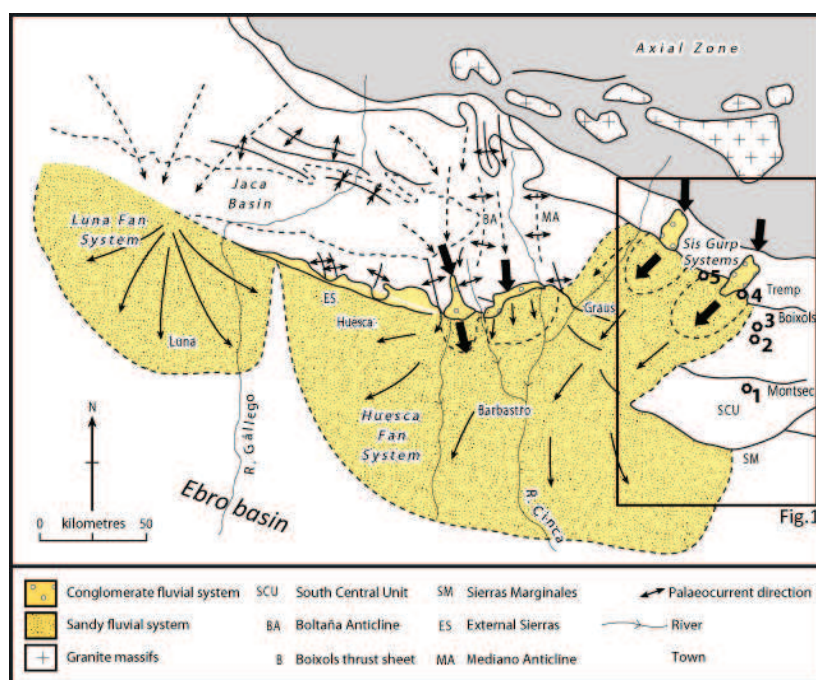


Figure III- 11. Reconstructed Oligocene-Miocene situation of the principal fan systems of the southern Pyrenean foreland basin, modified from Vincent (2001) and Jones (2004). The black box indicates the location of Figure III-10; number circles indicate sample locations.

III-2.3 Pre-depositional history

Recently, two independent studies have reported zircon fission-track, U-Pb and (U-Th)/He ages on zircons of samples located in the Tremp-Graus basin (Filleaudeau et al. 2011; Whitchurch et al. 2011). Zircon (U-Th)/He analysis of Garumnian sandstones of the Tremp basin (sample ORC2

collected at the same location than our sample AN03; Filleaudeau et al. 2011) shows 3 main age populations, interpreted to reflect distinct Mesozoic exhumation events: Triassic, Early Cretaceous and Late Cretaceous (Figure III-12a). Whitchurch et al. (2011) also published results of detrital zircon fission-track dating of samples collected from different sandstone and conglomerate formations of the southern Pyrenees. These authors found the same Early and Late Cretaceous exhumation events (Figure III-12b) in the Garumnian sandstones of the Ager basin (equivalent to our AN01 sample) together with Carboniferous (Variscan) ZFT ages. The sample collected from the Aren formation (stratigraphic unit just below the Garumnian in the Tremp basin) presents only an Early Cretaceous and a Carboniferous age peak. The combination of these two datasets have several implications for the Mesozoic exhumation and drainage patterns that we will not discuss here; however they both show the same phase of Early Cretaceous exhumation at 134 ± 15 Ma (all uncertainties combined), with less well expressed events at ~ 80 Ma, ~ 225 Ma and 300-330 Ma.

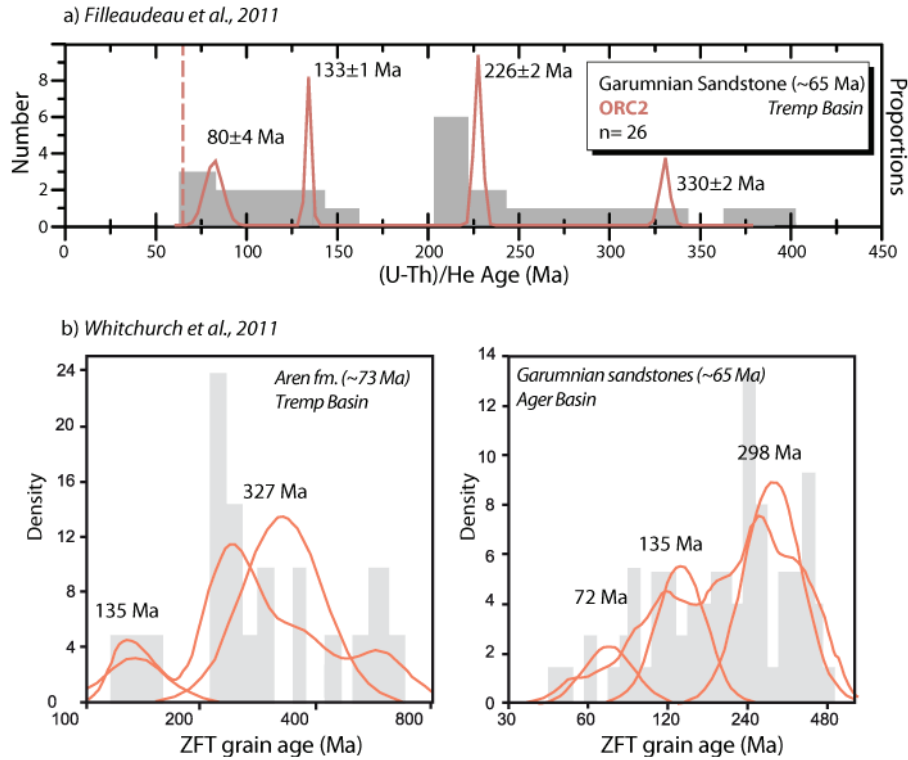


Figure III- 12. a) (U-Th)/He analysis on zircons from Garumnian sandstones of the Tremp basin (sample collected from same outcrop as AN03; Filleaudeau et al. 2011). b) Zircon fission-track age distribution for the Aren formation of the Tremp basin (depositional age 73 Ma) and the Garumnian formation of the Ager basin (corresponding to sample AN01), from Whitchurch et al. (2011).

III-2.4 Low-temperature thermochronology

During an initial sampling field trip, we collected sandstones from different formations of the Tremp basin: Santonian turbidites, earliest Paleocene “Garumnian” sandstones and Ilerdian sandstones. However, only the Garumnian sandstones yielded a sufficient amount of apatites to permit (U-Th)/He and fission-track analysis. A second sampling trip was thus necessary to collect Garumnian sandstones exclusively.

III-2.4a Apatite Fission-Track (AFT) thermochronology

The sample AFT preparation followed the analytical procedure described in Chapter I-2, samples were prepared and counted in Grenoble laboratory. Due to the low yield of grains in most samples, as many grains as possible were counted for each sample. Fission-track ages were calculated using the zeta-calibration method and the standard fission-track age equation (Hurford and Green, 1983). The χ^2 -test and age dispersion (Galbraith and Green 1990; Galbraith and Laslett 1993) were used to assess the homogeneity of AFT ages. Three samples yielded dispersed ages incompatible with a single age component, the grain-age distributions of these samples were decomposed into major grain-age components or peaks, using binomial peak fitting (Stewart and Brandon 2004, Table III-1). We were able to measure some horizontal confined track lengths and the widths of tracks crossing the etched internal surface (Dpar) in the four samples.

III-2.4b Apatite (U-Th)/He analysis

Apatites were extracted and carefully selected according to their morphology in the Grenoble laboratory (see Chapter I-2 for details). Each grain was placed into a platinum basket and sent to the thermochronology laboratory at Orsay-Paris-sud University (Cécile Gautheron). Between two to five replicates have been analyzed per sample. The platinum baskets were heated using a diode laser to 1030 ± 50 °C during 5 minutes, allowing total He degassing; a reheat under the same conditions allowed checking for the presence of He trapped in small inclusions. The ^4He content was determined by comparison with a $2\text{--}3 \times 10^{-7}$ ccSTP ^3He spike. After He extraction, platinum baskets were placed into single-use polypropylene vials. Apatite grains were dissolved one hour at 90°C in a $50\mu\text{l}$ HNO_3 solution containing a known content of ^{235}U and ^{230}Th , and then filled with 1 ml of ultrapure MQ water. The final solution was measured for U and Th concentrations by quadrupole ICP-QMS (series^{II} CCT Thermo-Electron at LSCE, Gif/Yvette France). A procedure similar to Evans et al. (2005) was followed. The analysis was calibrated using internal and external age standards, including Limberg Tuff, Durango and FOR3, with mean AHe ages of 16.8 ± 0.7 Ma, 31.8 ± 0.5 Ma, and 110.7 ± 7.0 Ma respectively. These values are in agreement with literature data, i.e. 16.8 ± 1.1 Ma (Kraml et al. 2006) for the Limberg Tuff, 31.02 ± 0.22 Ma (McDowell et al. 2005) for Durango and 112 ± 10 Ma for the internal FOR3 standard. The 1- σ error on AHe age should be

considered at 8%, reflecting the sum of errors in the ejection factor correction and age dispersion of the standards.

III-2.5 Results

III-2.5a Data

Apatite fission tracks were counted and measured in 4 samples located in the north (AN04), center (AN03, AN02) and south (AN01) of the basin (see Figure III-10 for location); the results are reported in Figure III-13 and Table III-3. Only the AN01 sample, located in another structural unit compared to the others, shows a single age component (144 ± 11 Ma) associated with very short mean track length (MTL, $10.1 \mu\text{m}$). Moreover, we note that the ZFT results for the Garumnian sample of the Ager formation is not fully consistent with our AFT age (AN01) of 144 ± 11 Ma, but this can be easily explained by the low number of grains (8) that we could count for this sample and which could have led us to “miss” some younger grains.

The three other samples have multiple age populations, but similar principal peak ages, with a main peak at 65.3 ± 3.7 Ma, 76.4 ± 4.2 Ma and 81.2 ± 4.7 Ma for samples AN02,03 and 04 respectively (Figure III-13); this peak gradually youngs toward the south. MTLs range from 11.3 to $12.2 \mu\text{m}$, indicating relatively slow long-term exhumation rates, and Dpar values are almost similar for the four samples (2.1 to $2.2 \mu\text{m}$). Apatite (U-Th)/He analyses were performed on 4 samples as well, AN01,02,03 and AN05; this last sample is located at the same level as AN04 but further West (near the town of Aren, Figure III-10). The first striking feature of the AHe ages is that the single-grain ages are not reproducible and scatter from 3.9 to 169 Ma. A more consistent dataset can be extracted from samples AN02 and AN03, which include 4 late Miocene-Pliocene ages (3.9 to 11.3 Ma). The ages cannot be interpreted directly, even though young ages probably imply Miocene burial and exhumation of the basin, which we want to test here. A first indication for the potential cause of the scatter in AHe ages is provided by the apparent relationship between sample ages and their uranium content (Figure III-14), which we examine in terms of the effective uranium concentration ($eU = [U] + 0.24 \times [\text{Th}]$, expressed in ppm). The eU content of the Garumnian samples present very low (4 ppm) to moderate (25 ppm) values and the AHe age vs eU correlation (Figure III-14) shows rapidly increasing ages for $eU > 15$ ppm, with less variation below this eU concentration, consistent with the variation of the AHe closure temperature with eU as predicted by Shuster et al.(2006) and Shuster and Farley (2009). Only sample AN05 does not fit this correlation, and we suspect that this may be related to its very high eU (and, in particular, quite extreme Th concentration) compared to the other samples. We thus make the hypothesis here that the age scatter is influenced by the eU content of the grains and could result from a similar thermal history.

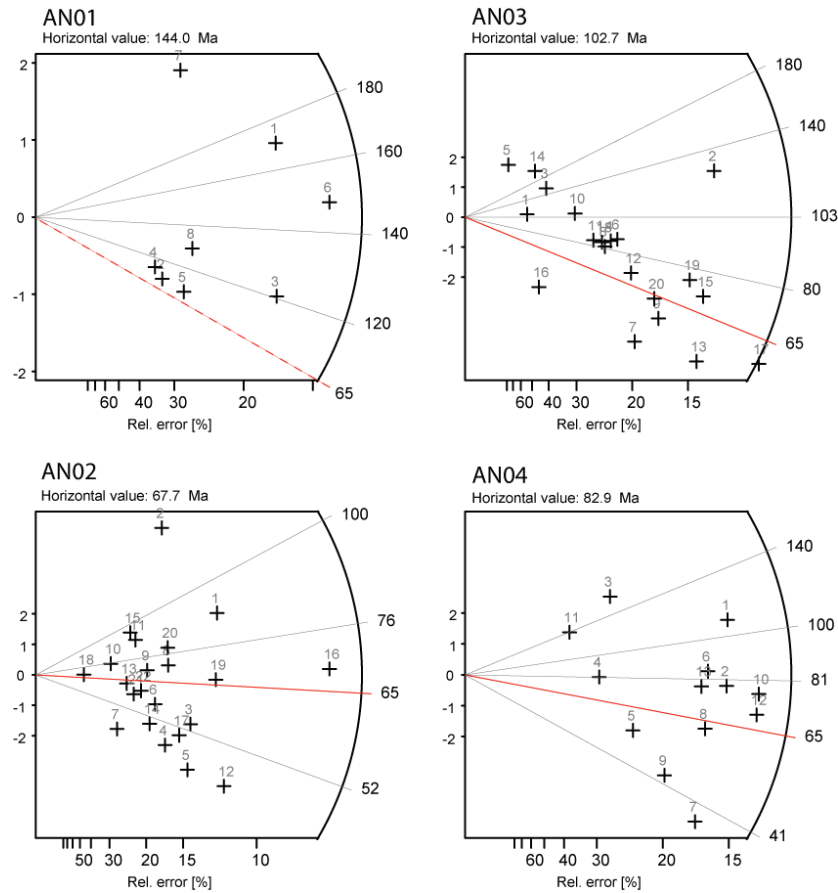


Figure III- 13. Radial plot representation of the counting data of samples AN01,02, 03, and 04. The radial plots are centered on the central value, and the red line represents the stratigraphic age (65 Ma.). Only the AN01 pass the X^2 -test.

In the following, we attempt to model the T-t paths with a thermal inversion model (Gallagher et al. 2009, Gallagher 2011) that also incorporates different kinetic models for He-diffusion.

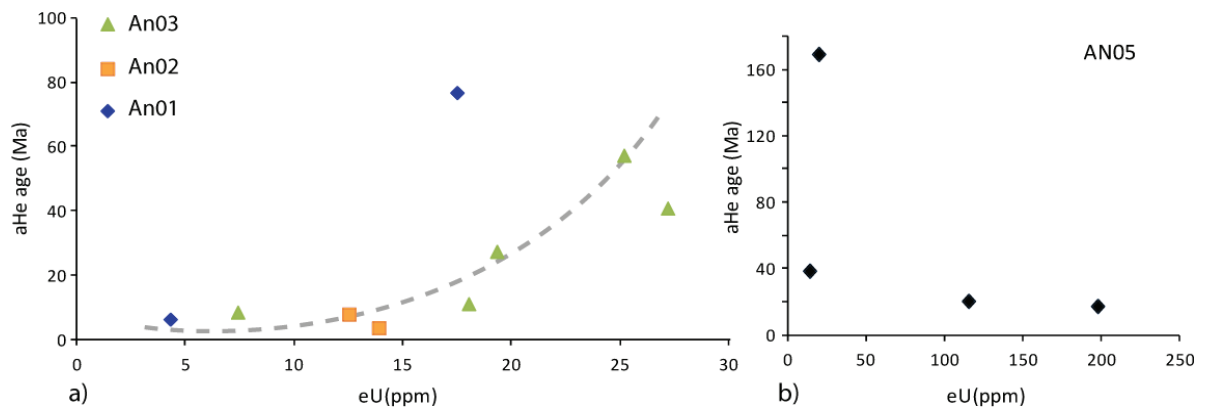


Figure III- 14. eU vs AHe ages for the four samples. Sample AN05 has been separated from the others due to its high uranium content, which contrasts with the other samples.

| Sample | position (lat/lon) | elevatio n(m) | no of grains | ps (Ns) (10^5 cm^{-2}) | pi (Ni) | pd (Nd) | PX ² (%) | Central age ($\pm 1 \sigma$, Ma) | P1 ($\pm 1 \sigma$) (Ma) | P2 ($\pm 1 \sigma$) (Ma) | P3 ($\pm 1 \sigma$) (Ma) | MTL (μm) | sd (μm) | Dpar (μm) | sd (μm) | no tracks |
|--------|-----------------------|------------------|-----------------|---------------------------------------|-----------------|------------|------------------------|---------------------------------------|-------------------------------|-------------------------------|-------------------------------|--------------------------|-------------------------|---------------------------|-------------------------|--------------|
| AN01 | 41.96/00.85 | 624 | 8 | 11.33 (489) | 6.32 (273) | 7.4(4262) | 32.34 | 144 \pm 11 | | | | 10.1 | 1.0 | 2.2 | 0.4 | 10 |
| AN02 | 42.16/00.89 | 436 | 20 | 7.641 (999) | 8.513 (1113) | 7.5 (4262) | << 1 | 76.9 \pm 6.2 | | 65.5 \pm 3.7 (75.5 %) | 125 \pm 19 (24.5 %) | 11.3 | 1.4 | 2.1 | 0.2 | 19 |
| AN03 | 42.18/00.89 | 504 | 22 | 12.64(1639) | 14.93 (1936) | 7.5(4262) | << 1 | 64.2 \pm 4.6 | 52.5 \pm 3.7 (39 %) | 76.4 \pm 4.2 (56.3 %) | 169 \pm 61 (4.7%) | 12.2 | 1.6 | 2.2 | 0.2 | 27 |
| AN04 | 42.22/00.84 | 902 | 13 | 10.715(810) | 12.05 (911) | 7.5 (4262) | << 1 | 74.1 \pm 7.6 | 41.0 \pm 5.8 (18%) | 81.2 \pm 4.7 (82 %) | | 11.3 | 2.2 | 2.1 | 0.1 | 19 |

Table III - 3. Apatite Fission-Track results. ρ_s and ρ_i are the spontaneous and induced track densities measured; ρ_d is the induced track density in the external detector, the number of tracks counted are in brackets; $P(X^2)$ is X^2 -probability (in %), $P(X^2) < 1$ indicates that the data distribution contains multiple populations (in this case, the single-grain ages were decomposed into grain-age populations P1, P2 and P3; MTL is the mean track length, with sd its standard deviation; Dpar is the average etch-pit width measured parallel to the C-axis. Measurements were performed by CF with a ζ -factor = 217.9 \pm 3.5 for IRMM-540 dosimeter glasses (cf Methodology chapter).

| S. Number | Sample | F_T | Weight (ng) | Length (μm) | Width (μm) | Thickness (μm) | $^4\text{He} \times 10^{-6}$ (cc/g) | U (ppm) | Th (ppm) | Th/U | eU (ppm) | Age (Ma) | Age corr. $\pm 1\sigma$ (Ma) |
|-----------|--------------|-------|----------------|-----------------------------|----------------------------|--------------------------------|--|---------|----------|------|----------|----------|------------------------------------|
| 2486 | AN011 | 0.76 | 2.9 | 128.02 | 101.25 | 94.82 | 122 | 12.9 | 19.2 | 1.5 | 17.5 | 58 | 76.9 \pm 7.1 |
| 2488 | AN012 | 0.8 | 5.7 | 180.86 | 122.86 | 108.13 | 4.1 | 2.8 | 6.3 | 2.3 | 4.3 | 5.2 | 6.5 \pm 0.6 |
| 2493 | AN022 | 0.76 | 3.4 | 145.9 | 106.3 | 92.63 | 9.4 | 9.9 | 11 | 1.1 | 12.5 | 6.2 | 8.1 \pm 0.7 |
| 2495 | AN023 | 0.84 | 6.7 | 156.28 | 139.2 | 132.51 | 5.4 | 5.8 | 33.6 | 5.8 | 13.9 | 3.2 | 3.9 \pm 0.3 |
| 2499 | AN031 | 0.76 | 3.9 | 187.51 | 100.52 | 84.67 | 48.5 | 9.8 | 39.6 | 4 | 19.3 | 20.9 | 27.6 \pm 2.5 |
| 2501 | AN032 | 0.87 | 5.3 | 177.4 | 135.28 | 116.96 | 117 | 22.3 | 20.5 | 0.9 | 27.2 | 35.7 | 41.0 \pm 3.8 |
| 2548 | AN033 | 0.69 | 10 | 150.75 | 77.14 | 67.19 | 120 | 12 | 54.9 | 4.6 | 25.2 | 39.6 | 57.4 \pm 5.3 |
| 1641 | AN034 | 0.84 | 11.5 | 200.0 | 150.0 | 187.5 | 20.6 | 15.9 | 8.9 | 0.56 | 18 | 9.5 | 11.3 \pm 1.0 |
| 1643 | AN035 | 0.8 | 5 | 150.0 | 125.0 | 112.5 | 6.2 | 4 | 14.2 | 3.55 | 7.4 | 6.9 | 8.7 \pm 0.8 |
| 2552 | AN051 | 0.8 | 4.6 | 190.56 | 113.2 | 97.05 | 326 | 49.2 | 616.3 | 12.5 | 197.1 | 13.8 | 17.2 \pm 1.6 |
| 2554 | AN052 | 0.8 | 5 | 147.47 | 119.98 | 111.78 | 224 | 27.9 | 362.4 | 13 | 114.9 | 16.3 | 20.3 \pm 1.9 |
| 1878 | AN053 | 0.85 | 12.6 | 275.0 | 175.0 | 125.0 | 53.2 | 6.4 | 29.9 | 4.67 | 13.6 | 32.6 | 38.5 \pm 3.5 |
| 1880 | AN054 | 0.8 | 12.8 | 262.5 | 162.5 | 162.5 | 335 | 10.6 | 36.5 | 3.43 | 19.4 | 144 | 169.1 \pm 15.6 |

Table III - 4. Apatite (U-Th)/He results (Orsay-Paris Sud University). These samples were collected from Garumnian (depositional age 70-60 Ma) continental sandstones. S_c number is the sample number which is the second replicate ^3He spike pipette number, F_T is the geometric correction factor for age calculation; age corr. is the age corrected by the F_T , the uncertainty 1σ was fixed at 8 % of the age. eU is the effective uranium concentration ($eU = [U] + 0.24[Th]$).

III-2.5b Thermal modeling

Due to the complexity of our dataset (large variations in AHe ages and eU), we use an inverse thermal model (Gallagher et al. 2009) that incorporates recent kinetic models of He diffusion proposed by Flowers et al. (2009) and Gautheron et al. (2009) (cf Chapter II-1) for a description of these models). The model allows to invert for both thermal history and AFT annealing/AHe diffusion parameters by a Markov chain Monte Carlo (MCMC) sampling method. During a first stage of modeling, an initial model (with initial T-t points and kinetic parameters) is tested to obtain a first model probability that fits the parameters. Then the model slightly perturbs the parameters to recalculate the probability. If the probability is higher than in the first-stage model, the new model is accepted; else, the previous model is retained. This procedure is repeated according to the number of iterations the user chooses, giving at the end a large number of models with their associated probabilities.

In this study, the parameter space (time, t , and temperature, T) has been subdivided into three T-t boxes: from 300 Ma (beginning of the model run) to 70 Ma with temperatures from 140°C to 0°C, from 70 to 60 Ma with temperatures of 10 ± 10 °C (e.g. surface conditions during deposition of the Garumnian series), and finally from 60 Ma to present, with temperature ranges of 140 °C-0 °C. By doing this, the only constraint we impose on the model is the deposition time. In a subsequent set of inversions, we tested the hypothesis of Eocene burial/exhumation related to the thrusting sequence of the southern Pyrenean fold-and-thrust belt, by adding a late Eocene near-surface temperature constraint on the samples AN02 and AN03.

The results are the products of 200000 iterations, which is a sufficient amount to obtain a stable and robust solution (see discussion in Gallagher 2011). The model of Ketcham et al. (2007) is used for fission-track annealing in apatite and the He diffusion models of Gautheron et al. (2009) and Flowers et al. (2009) which both take into account alpha-recoil damage and annealing will be used in this study. These two models include the influence of α -recoil damage on the He-diffusion process; this damage increases He retentivity using a linear (Gautheron et al. 2009) or cubic (Flowers et al. 2009) law. The main difference in the predicted AHe ages between the two models is found for low amounts of eU (15-25 ppm). As illustrated in Figure III-14, this is the case when the amount of α -damage of the apatite grains correspond to the slope change in the diffusion law defined by natural and experimental data (Shuster et al. 2006; Shuster and Farley 2009). The simulations will give us slight differences in the modeled thermal histories, but because no consensus has been found yet between these two models, we will present all results. Inversions performed with the two models are called respectively A (Gautheron et al. 2009) and B (Flowers et al. 2009) in the following. Moreover, we present results of inversions for samples AN01, 02 and 03, which were double-dated; the samples with only AFT analysis (AN04) or only AHe

measurements (AN05) were combined for a test model but do not provide sufficient thermal constraints to obtain a well-defined T-t path.

III-2.5c Inferred thermal histories

A general remark concerning the models is that they all predict very similar T-t paths, with burial from the deposition time to Miocene-Pliocene times followed by exhumation until the present-day. However, when comparing the maximum Cenozoic temperature of burial (T_{\max}), the B-models systematically predict lower values than the A-models, whereas the timing associated with the peak temperature (t_{\max}) does not vary systematically from one model to another. The T-t path of sample AN03 is quite different from one kinetic model to another (Figure III-15). Model A suggests a scenario in which sample AN03 was buried to 95 °C at ~20 Ma and then could have stayed at that temperature until no later than 12 Ma. From that time, exhumation is linear to the present.

The pre-deposition T-t path is poorly constrained, as is the case for the other models. The only exception is model B of sample AN03, which predicts a well-constrained pre-depositional history with linear cooling from the Early Cretaceous (130°C at 100 Ma) to the time of Garumnian deposition. That model predicts burial to 70 °C between 11 and 5 Ma, before being exhumed. This sample clearly shows difference in behavior of the two models: while model A predicts a variable pre-depositional history and important burial during the Miocene, model B fits the ages with a linear pre-deposition exhumation history associated with a lower Miocene maximum temperature. Finally it is worth noting that these two models return quite different probabilities for sample AN03; the probability is much better for model B. This could be explained by the fact that this sample has the largest proportion of grains with moderately high eU concentrations. As noted previously, in those circumstances, the model of Flowers et al. (2009) appears to better reproduce the kinetics of He diffusion, as it includes a transition from the little effect of eU on the kinetics to a rapid increase in retentivity.

| Model | Tmin (°C) | Mean Temperature | Tmax (°C) | Time min (Ma) | Mean Time | Time max (Ma) |
|-------|--------------|---------------------|--------------|------------------|-----------|------------------|
| AN03A | 77 | 86 | 95 | 12 | 16 | 20 |
| AN03B | 60 | 65 | 70 | 5 | 7.5 | 10 |
| AN02A | 95 | 100 | 105 | 5 | 6.5 | 8 |
| AN02B | 75 | 85 | 95 | 6 | 7 | 8 |
| AN01A | 82 | 87 | 92 | 1 | 2 | 3 |
| AN01B | 65 | 72.5 | 80 | 10 | 15 | 20 |

Table III - 5. Summary of the main modeling predictions for post-depositional reheating, graphically measured on Figure III-15.

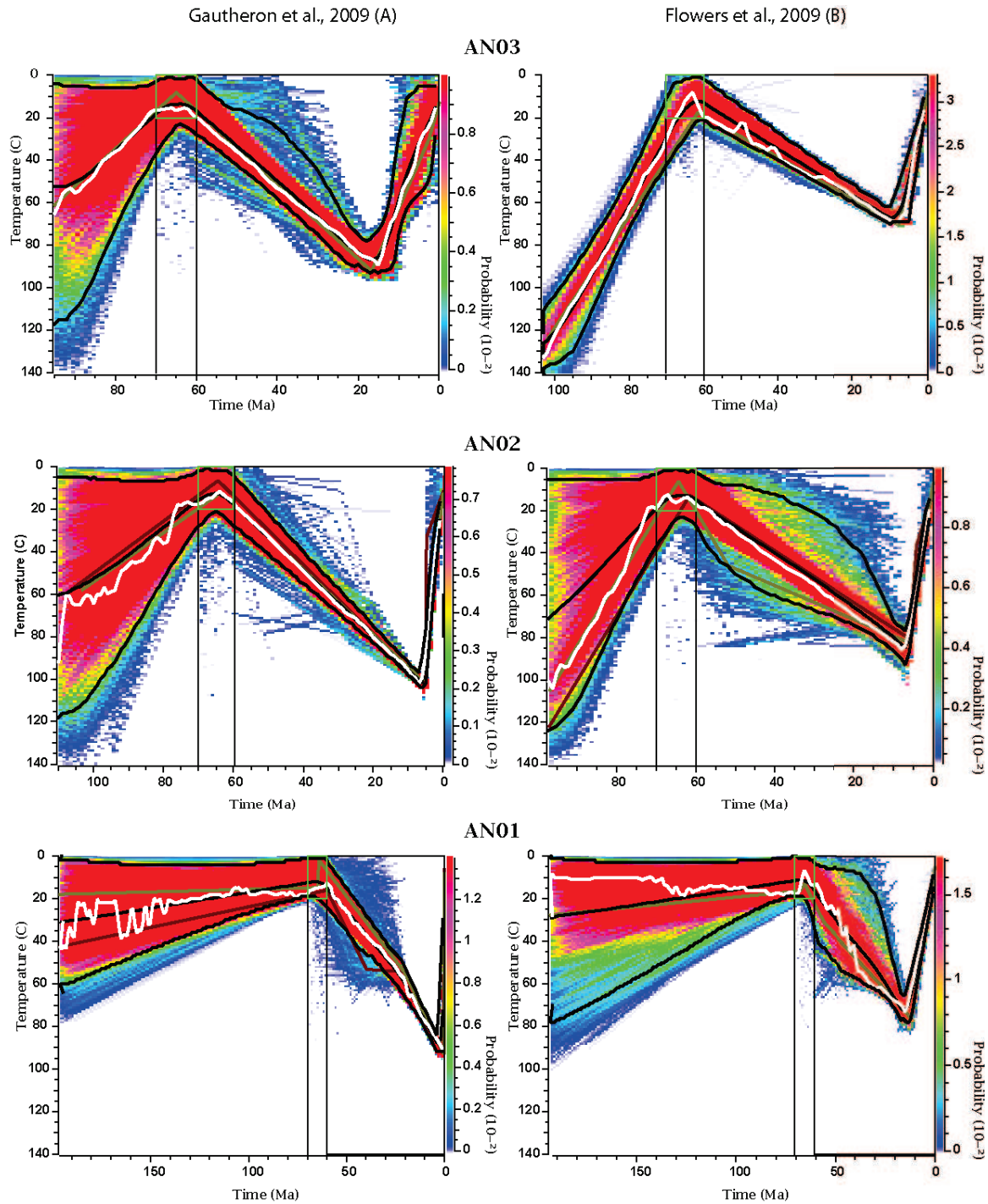


Figure III- 15. Modeled t - T paths for samples AN01, 02 and 03 and the two different models for He diffusion kinetics. The two black curves represent the 95% confidence interval for the t - T paths, the central black curve is the expected model (weighted mean model), the white curve is the mode model (combination of all models sampled) and the yellow the maximum likelihood model (best data fit). t - T paths are colored according to their probability (scale on the right hand side) which varies according to the models. The black boxes represent the parameter space explored; the horizontal scale is fixed from the oldest track to the present-day.

T-t paths predicted by both models for sample AN02 are much more similar. The burial is more important in model A; which predicts that the sample stayed at 105°C during the period 5-8 Ma, whereas model B predicts burial to a maximum of 95 °C between 6 and 8 Ma. Thus the results for this sample are very consistent; both models predict significant burial until the end of Miocene times. Finally, both models could not resolve a well-constrained pre-deposition T-t path.

Sample AN01 presents the most surprising results. This sample has the most contrasted AHe ages (7Ma and 77 Ma); its Early Cretaceous (144 Ma) AFT age consists of a single population. The sample is also furthest from the preserved conglomeratic massifs. Nevertheless, both models predict significant burial, to a maximum of 92°C and 80°C for models A and B respectively. Moreover, model A presents very young and rapid final exhumation (3 to 1 Ma), whereas model B predicts exhumation between 10 and 20 Ma, in better agreement with the other models presented previously.

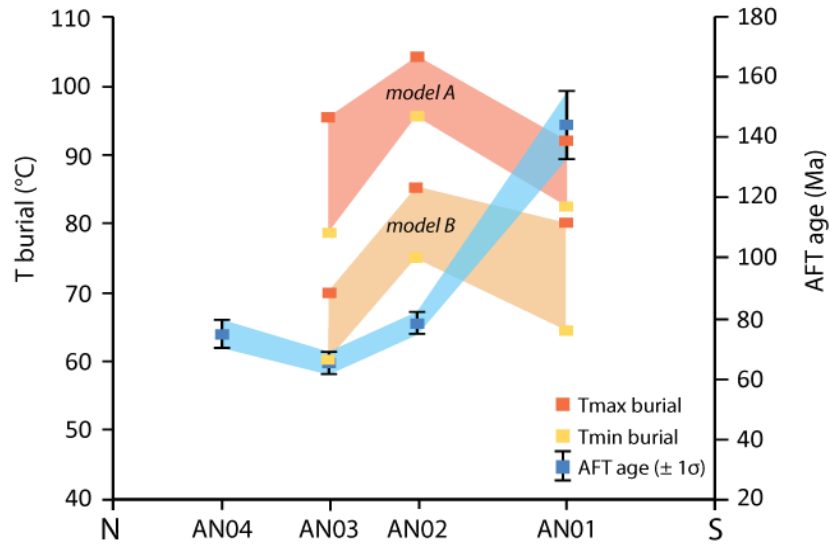


Figure III- 16. Burial temperature results plotted against central AFT ages, according to geographic position of the samples. T_{max} and T_{min} are the maximum and minimum temperature of Cenozoic burial.

Finally, we observe that the maximum Cenozoic burial temperatures predicted by the models are in agreement with their corresponding AFT ages (Figure III-16), T_{max} values are higher for samples with younger AFT ages, which is in favor of a more recent and deeper burial.

III-2.5d Eocene additional constraint

The first set of models does not resolve an Eocene signal of an exhumation linked to the tectonic activity of the fold-and-thrust belt. However, the late Eocene conglomerates generally rest unconformably on the earlier syn-tectonic sediments (Figure III-10), implying an initial period of burial and unroofing in the Late Cretaceous-Eocene. We thus test here the addition of a late

Eocene near-surface constraint, to possibly highlight the Paleogene thermal history of the samples. This constraint is represented by an additional T-t box at time 40 to 35 Ma and temperatures below 40°C. We only run this model for samples AN02 and AN03, since AN01 is located in the footwall of the Montsec thrust (Figure III-10) there is no reason to believe it was close to the surface in Eocene times. There is essentially no difference between predicted cooling paths for these two models for the AN02 and AN03 samples: the most probable paths show that the samples stayed close to the surface (or were shallowly buried) from their deposition to late Eocene times and then record the same first-order burial/exhumation histories as the previous models (Figure III-17). Moreover, the AN02-A model is not very well constrained, whereas the T-t paths were well-defined in the previous inversion. Therefore, we conclude that we cannot resolve the Eocene burial, because it was not important enough to be recorded by the AFT and AHe systems, or was completely overprinted by the subsequent (post-Eocene) burial and exhumation.

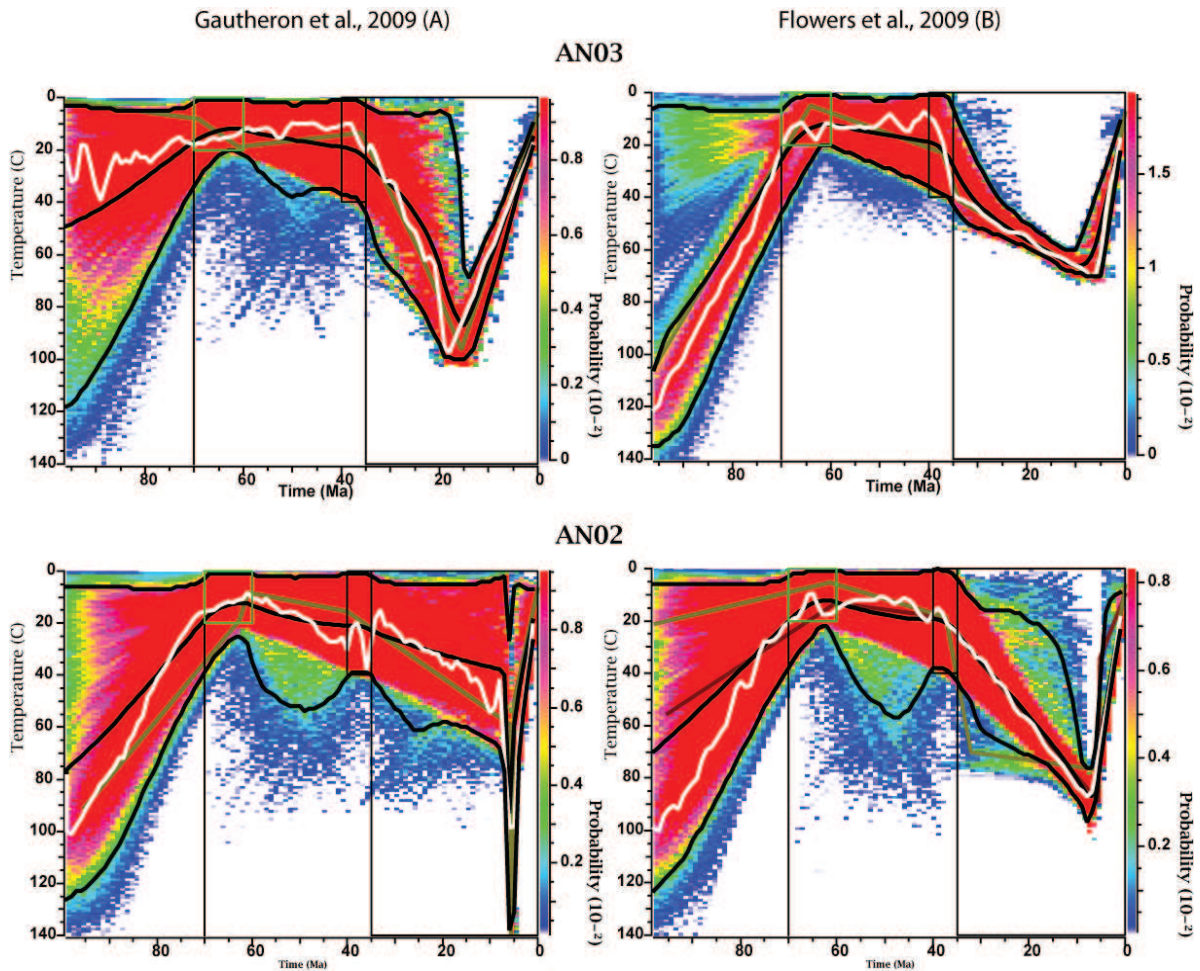


Figure III- 17. Summary of the thermal modeling results for the samples AN02 and AN03 with an additional constraint on the parameter space at Eocene times. Symbols and colors as in Figure III-15.

We will thus only discuss the results of the previous section (II-2.5c), which have been obtained by a more open parameter space and provide better constrained T-t paths.

III-2.6 Discussion

III-2.6a Exhumation scenario

Even if the modeling presents a variable range of maximum burial temperatures and associated timing, the first-order pattern of the T-t paths in all cases shows significant burial during post-Eocene times with subsequent exhumation starting in the late Miocene–early Pliocene. For samples AN02 and AN03, the modeling predicts post-depositional burial to a T_{\max} of 60°C to 105 °C, and an onset of final exhumation between 5 and 20 Ma. The average geothermal gradient in the SCU, commonly used for AFT interpretations (Beamud et al. 2011) has been constrained by numerical modeling (Zeyen and Fernández 1994) at 30 °C.km⁻¹, with theoretical values for the thermal conductivity of sediments (2.5 W.m⁻¹.K⁻¹). According to Fernández et al. 1998, the average geothermal gradient for the SCU area is $22 \pm 4^\circ\text{C/km}$, therefore lower than the value for the Pyrenean Axial Zone ($\sim 33^\circ\text{C/km}$); this discrepancy is apparently due to the high thermal conductivity measured (2.47 to 3.22 W.m⁻¹.K⁻¹) in the sediments. As there no consensus on the subject, we will use in the following a 30°C.km⁻¹ gradient to calculate estimates of thickness of the sediments, thus providing a minimal value of burial. The minimal burial can be estimated at 2 to 3.5 km of sediments and final exhumation rates at 0.1 to 0.7 km.Myr⁻¹. We interpret this burial as due to deposition of the Eocene-Oligocene conglomerates, products of the Axial Zone erosion. The results presented here are thus equal to or higher than the thermo-kinematic modeling results of low-temperature thermochronological data located in the southern Axial Zone (presented in the previous section), and allow us to extend our interpretations to the Pyrenean foreland.

Results from the thermo-kinematic model of the previous chapter imply a thickness of ~ 2 km of conglomeratic deposit, covering the southern central Pyrenees. The model also predicted re-incision of the conglomerates from Tortonian times (11.6 to 7.5 Ma) with an exhumation rate of 0.02 km Myr⁻¹ for the higher areas to 0.3 km Myr⁻¹ in the valley bottoms. We could not resolve the precise scenario for excavation (how long did it last, did it proceed at constant rates, etc), mostly because our dataset (youngest AFT age of 17.2 Ma in the Noguères zone) could not resolve Pliocene T-t histories. In this study, we measured younger AHe ages, that allow to more precisely resolve the Pliocene evolution; they imply that there was continuous excavation of the basin, from late Miocene-Pliocene to present.

III-2.6b Sedimentary extent

The inferred amounts of burial are consistent with what we expected for the samples AN02 and AN03, as these were sampled close to the conglomeratic massifs and the Axial Zone. A more

surprising result comes from sample AN01, which is located in another structural unit, south of the Montsec thrust, and quite far from the Axial Zone. The closest conglomeratic outcrops are located further east and have been dated by magnetostratigraphy at 40 to 36 Ma (Burbank et al. 1992a). Nevertheless, the inversion results suggest 2.6 to 3.0 km burial before onset of final exhumation between 2 and 15 Ma, and therefore excavation rates of 0.17 to 1.5 km Myr⁻¹. Thus, the Ager basin, South of the Montsec thrust (Figure III-10) seems to record the same post-Eocene burial/exhumation history as the Tresp basin, implying that infilling by the Huesca fan sediments extended to that basin (Figure III-11). These values are comparable to the ones of the northern samples. The burial of the Ager basin, which is not drawn in the paleo-geographic reconstructions (Figure III-11), could result from an extension of the Huesca fan further to the east, or from extension of the Oliana fan towards the west.

Moreover, as discussed previously (previous chapter, Garcia-Castellanos et al., 2003), the Ebro basin remained endorheic from 30 Ma to 9 Ma, accumulating an important amount of conglomeratic to lacustrine sediments from the border to the center of the basin. Our modeling result thus comforts the idea of an overfilled basin, by a significant amount of sediments (at least 2 km). This is also consistent with indications for partial resetting of the AFT system in the lower part of these deposits (Beamud et al. 2011; Rahl et al. 2011).

III-2.6c Sensitivity to eU variations

In the section 4.1, we formulated the hypothesis that the scatter in AHe ages could come from the variations in eU contents. We present in Figure III-18, a test of sensitivity of the model results to these variations. We extracted from the inverse modeling results the expected T-t paths and used them to predict AHe ages through HeFTy for eU varying from 5 to 30 ppm. It is worth noting that this test was performed with the He-diffusion model of Flowers et al. (2009), as the model of Gautheron et al. (2009) is not incorporated in HeFTy. When comparing the curves to our AHe data, we can see that the AN02 and AN03 samples are in excellent agreement with the modeled path. Therefore, this test shows that the scatter of these two samples can be largely explained by the eU content.

Conversely, the AN01 sample data does not follow the modeled path and so measured ages could have been influenced by another parameter, such as a different pre-depositional history. We will thus test that possibility in the next section.

III-2.6d Influence of the pre-depositional history

The modeling results provide values for the amount and timing of Cenozoic exhumation that range from 70 to 105 °C during 20 to 1 Ma; however, our dataset does not allow us to better define these intervals. The models are limited by the requirement of fitting the strongly variable AHe ages, which are only partly explained by varying eU content.

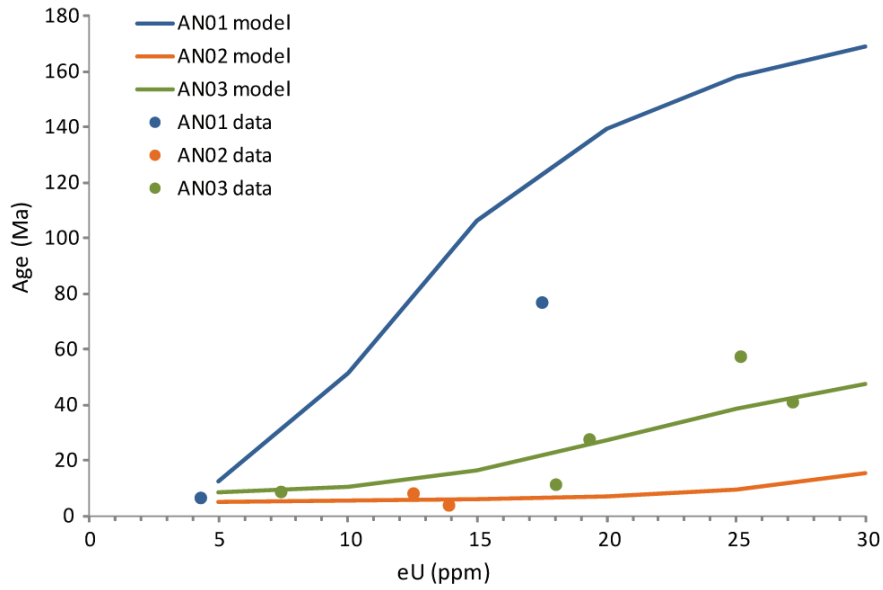


Figure III- 18. Sensitivity of the expected model to eU variations. The colored curves represent predicted AHe ages as a function of eU for the T-t paths of the expected B-models, and for eU varying from 5 to 30 ppm. The dots represent the data shown in Figure III-14.

The model cannot take into account the variable pre-depositional history of these detrital grains. Here, we will test to what degree such variable pre-depositional exhumation histories could explain the encountered variability of AHe ages.

We conclude from the higher-temperature data discussed in section 3 that detrital grains show variable pre-depositional exhumation ages, between ~80 and ~300 Ma. From this starting point, we tested the influence of the pre-depositional history and the eU content by performing forward modeling with HeFTy (Ketcham 2005), using the annealing modeling of Ketcham et al. (2007) for AFT and the He-diffusion model of Flowers et al. (2009), with a equivalent sphere radius of 100 μm , for AHe. We imposed the post-depositional scenario from the inversion results presented previously, and tested how the final AHe age varies as a function of eU values (from 5 to 30 ppm), post-depositional T_{max} (70, 80 and 90°C) and age of initial (pre-depositional) exhumation, as illustrated in Figure III-19. The results are presented in Figure III-20 for T_{max} of 70, 80 and 90°C, in which predicted ages are plotted as contours.

For the 3 T_{max} tested, the modeling reveals the same patterns, in agreement with the relationship we expect between AHe age, eU content and temperature of burial. The modeled ages are older when the initial exhumation starts earlier and when the grains have larger eU contents. The predicted ages are younger when T_{max} increases; the maximum modeled AHe ages are 165, 150 and 80 Ma, respectively, for T_{max} at 70, 80 and 90 °C. Moreover, for the same eU, the age scatter decreases with increasing T_{max} . For example, with an eU of 16 ppm (the average eU value of our

grains), the modeled ages vary from 20 to 130 Ma for T_{\max} 70°C; from 10 to 85 Ma for T_{\max} 80 °C, and from 10 to 20 Ma for T_{\max} 90°C.

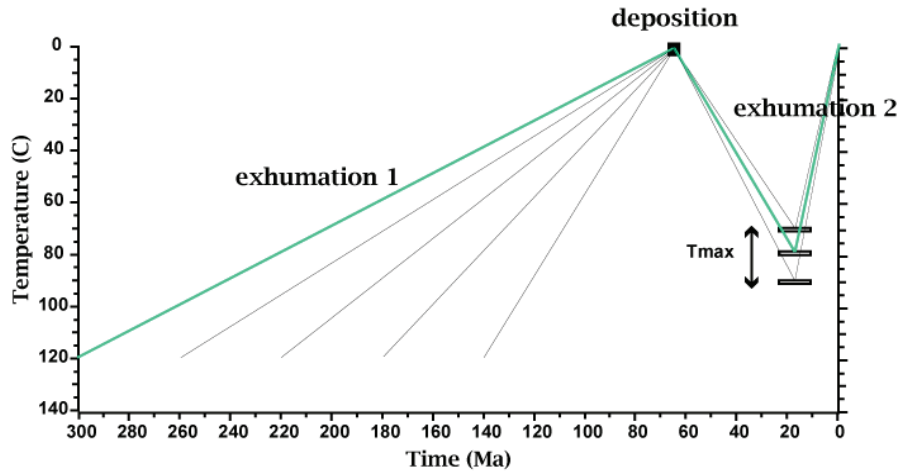


Figure III- 19. Schematic set up and methodology for the forward modeling runs using HeFTy. The green path represents one test and the grey ones the different combinations tested.

These forward models confirm the hypothesis that the pre-depositional history of the samples can have a major effect on AHe age variations.

With these results, we can also identify what variability in timing of pre-depositional exhumation would be required to explain the scatter in our AHe ages, by plotting our samples on the contour plots with their own age and eU values. First of all, the main observation is that the $T_{\max} = 80^{\circ}\text{C}$ plot provides the best-fit to the combined data; for both $T_{\max} = 70^{\circ}\text{C}$ and $T_{\max} = 90^{\circ}\text{C}$ there are several grains with ages that cannot be explained. Secondly, when looking at the 80°C -plot, we can conclude that all the grains except AN11 fit with a pre-depositional exhumation phase starting between 170 and 90 Ma, which is in good agreement with the ZHe and ZFT age distributions of Filleaudeau et al. (2011) and Whitchurch et al. (2011) that both record an Albian exhumation phase. These results are in agreement with the fact that the expected model for AN02 and AN03 predicts an onset of initial exhumation before Late Cretaceous times. Only the AN11 grain is outside of this range and suggests Permian initial exhumation. Our previous observations showed that the age dispersion between the two grains of this sample cannot be explained by the eU content only. We thus propose that variable pre-depositional exhumation histories, with at least one grain recording Permian initial cooling is another factor that explains the AN11 grain age.

To conclude, these forward models show that the pre-depositional history of a detrital sample can considerably influence the measured AHe ages as well as the inferred temperature of burial. In our

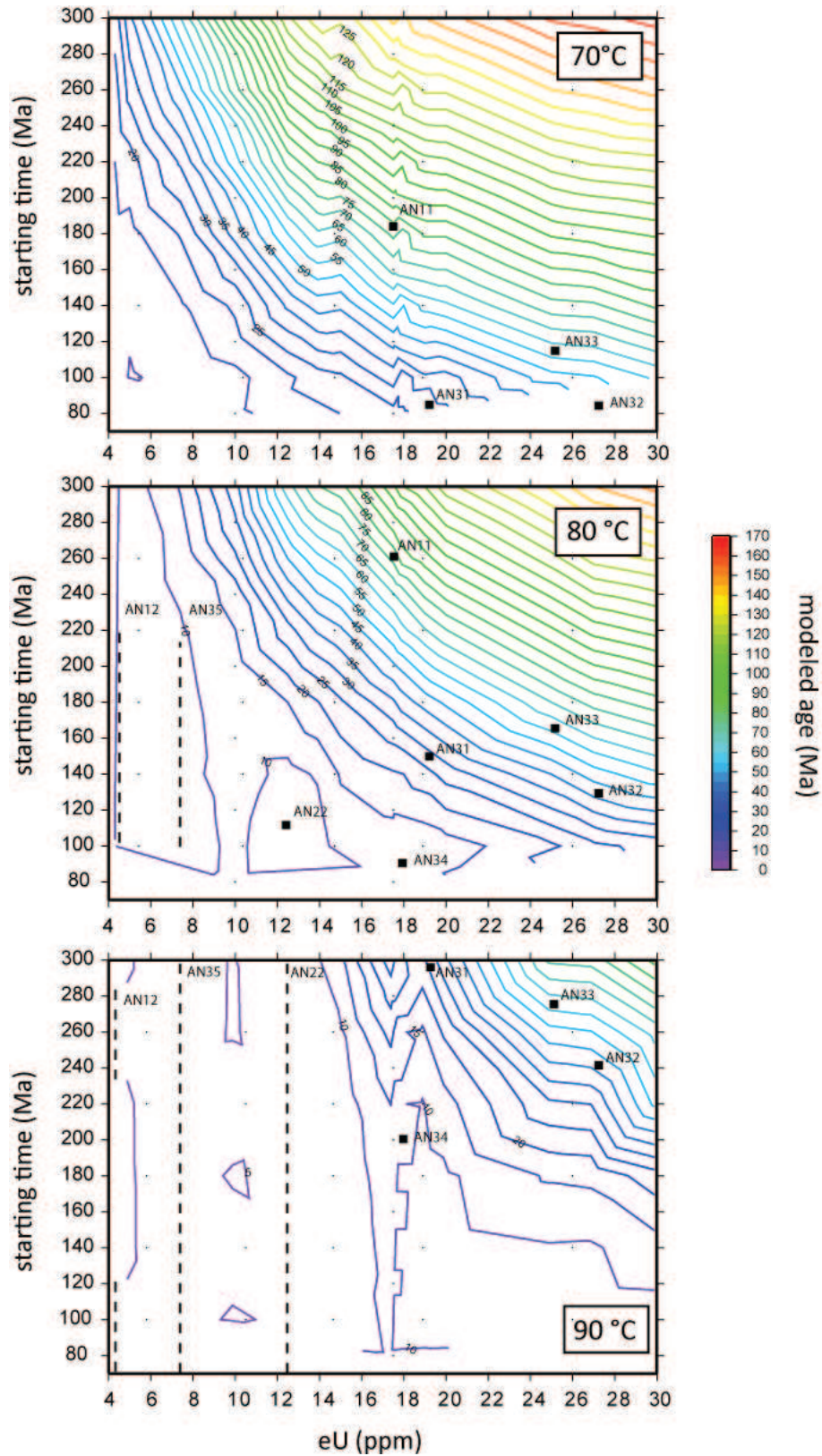


Figure III- 20. Test of pre-depositional exhumation history. AHe ages were calculated by HeFTy forward modeling, with the kinetic model of Flowers et al. (2009); for several eU contents, T_{max} and starting times of pre-depositional exhumation. Measured values of our samples were then plotted (black squares), or represented as dashed lines when they do not resolve a starting time.

case, it seems that a combination of variable eU and variable timing of initial exhumation, which is consistent with higher-temperature detrital ZHe and ZFT data, can explain the scatter in AHe ages. A T_{\max} of 80°C appears to best fit the combined AHe data; this T_{\max} is in the range of predictions for all the models of Figure III-15, except AN03B. Moreover, the forward models suggest that most apatite grains record an Albian pre-depositional exhumation phase.

III-2.7 Conclusions

We have succeeded in modeling our dataset of AFT and AHe double dating on sedimentary apatites to obtain consistent T-t paths using the He-diffusion kinetics that are a function of radiation damage and its annealing. This study reveals the importance of combining AFT and AHe jointly to provide sustainable constraints on thermal history in sedimentary rocks. Tests with constraining only the depositional time give more consistent and realistic results than the one with an additional constraint of an Eocene exhumation phase. The modeling of AN01, 02 and 03 samples all predict a burial from Late Cretaceous to Miocene-Pliocene times to reach temperatures of 60 to 105°C, equivalent to 1.8 to 3.2 km of burial. The timing for the onset of exhumation is from 20 to 1 Ma, with an average time of 9.5 Ma. From the study of the pre-depositional exhumation of the samples, we selected the post-Eocene history implying a T_{\max} of 80°C that precise our estimate of onset on exhumation at 7-18 Ma time period. We also infer from this modeling that an Albian exhumation phase is represented by a majority of grains.

The reason for age scatter of our AHe dataset were also investigated and reveal an important contribution of the eU content, as well as the influence of the pre-depositional history, for explaining these ages.

This modeling results showing a similar post-orogenic exhumation phase for the southern Pyrenean foreland and for the southern Axial Zone, are consistent with previous models (Chapter III-1) and suggest Late Miocene (pre-Messinian) onset of Ebro basin incision. They also confirm that an important amount of detrital sediments covered the southern Pyrenean flank, and filled the Ebro basin, consequently to the onset of endorheism. Additional low-temperature measurements in the Ager basin and in the Sierras Marginales could be useful to precise our observations. Sedimentological field studies on the Huesca and Oliana fans would also be helpful to understand the patterns of infilling of the Ebro basin.

Part IV- 2-D Modeling of the Southern Pyrenees

The amount and thickness of syn- to post-tectonic conglomeratic sedimentation have been précised in the previous chapter by thermo-kinematic modeling and low-temperature thermochronological data. These studies have shown that the thick Oligocene sedimentation was extending at least to the South of the Montsec thrust, in the southern fold-and-thrust belt. The first part of the previous chapter also confirms that the infilling started around 40 Ma , when the range was experiencing its main phase of exhumation. Therefore, this Chapter investigates the potential effects of the addition of this important amount of sediments on the evolution of the fold-and-thrust belt, and in particular on its thrusting sequence. Two level of syn-tectonic sedimentation will be applied to a 2D model of a thin-skinned wedge. In the first part, the effect of an early deposition of syn-tectonic sedimentation will be studied in general terms (this section was submitted to Geology). In the second part, we will apply a secondary sedimentation (representing the conglomeratic sedimentation) to a model of the Pyrenean pro-wedge, discuss on the consequences on the thrusting sequence and compare it to observations of out-of-sequence and reactivations in the southern Pyrenees.

Chapter IV-1 Syn-tectonic sedimentation effects on the growth of fold-and-thrust belts

Charlotte Fillon^{1,2}, Ritske Huismans² and Peter van der Beek¹

¹ Institut des Sciences de la Terre, Université Joseph Fourier, BP53, 38041 Grenoble, France

² Department of Earth Science, Bergen University, Bergen, N-5007, Norway

Submitted to *Geology*

IV-1.1 Abstract

We use two-dimensional dynamical modeling to investigate the effects of syn-tectonic sedimentation on fold-and-thrust belt development by testing variable syn-tectonic sediment thicknesses and flexural rigidities. Modeling results highlight the strong influence of these parameters on the structural style of a fold-and-thrust belt. In particular, there is a first-order control on the thrust sheet length and their spacing as well as the development of piggy-back basins. Thrust sheets are longer when sediment thickness and/or flexural rigidity increases, consistent with critical taper theory. A comparison of these results with observations from a number of several fold-and-thrust belt suggests that these natural systems record the first-order control exerted by syn-tectonic sedimentation.

IV-1.2 Introduction

The potential controls of surface processes on the tectonic evolution of mountain belts are slowly becoming better understood (e.g., Whipple 2009). Whereas erosion can strongly influence the growth of orogenic cores, syn-tectonic wedge-top sedimentation appears the dominant process influencing external, thin-skinned fold-and-thrust belts, as shown by both numerical and analogue models of fold-and-thrust belt development (Huiqi et al. 1992; Marshak and Wilkerson 1992; Boyer 1995; Storti and McClay 1995; Mugnier et al. 1997; Hardy et al. 1998; Simpson 2006; Stockmal et al. 2007; Malavieille 2010). Erosion products from the core of a mountain belt are transported to the foreland and deposited while the orogenic wedge continues to grow, thus interacting with the development of the foreland fold-and-thrust belt. This interaction can be understood in terms of both critical-taper (Davis et al. 1983; Dahlen 1984; 1990) and minimum-work (Hardy et al. 1998) theory: sedimentation on top of the wedge increases the taper angle and the work necessary to reactivate and create new internal thrusts, thus promoting wedge propagation on the décollement level; sedimentation on the lower part of the wedge having the opposite effect. The influence of sedimentation on the structural development of fold-and-thrust belts has been studied principally using analogue models. Storti and McClay (1995), for instance, showed that adding syn-orogenic sediments on top of a wedge reduces the number of thrusts, the internal shortening and the critical taper, and leads to longer thrust sheets. However, the surface taper and geometry of fold-and-thrust belts are also affected by flexural controls on plate bending, which are not easily incorporated in analogue models (but see Hoth et al. 2007a). Numerical models of fold-and-thrust belt formation more easily integrate these effects and have now reached sufficiently high numerical resolution that their predictions can be compared with observations in natural systems (Stockmal et al. 2007). In this paper we use two-dimensional forward dynamic models to investigate depositional controls on fold-and-thrust belt development. We focus in particular on the effects of syn-tectonic sedimentation and on the influence of flexure, and show that both exert first-order controls on wedge geometry and thrust propagation: increasing the thickness of syn-tectonic sediments and/or flexural rigidity leading to the activation of fewer and longer thrust sheets. We show that these general results are consistent with observational constraints on structure and wedge-top sedimentation in natural fold-and-thrust belts.

IV-1.3 Model set up

We use a 2D Arbitrary Lagrangian-Eulerian (ALE) finite element technique (Fullsack 1995) to model thin-skinned fold-and-thrust belt development. Model materials are frictional-plastic (Stockmal et al. 2007) and are characterized by a strain-dependent friction angle allowing for localization of deformation (Huisman and Beaumont 2003, see supplementary material for details).

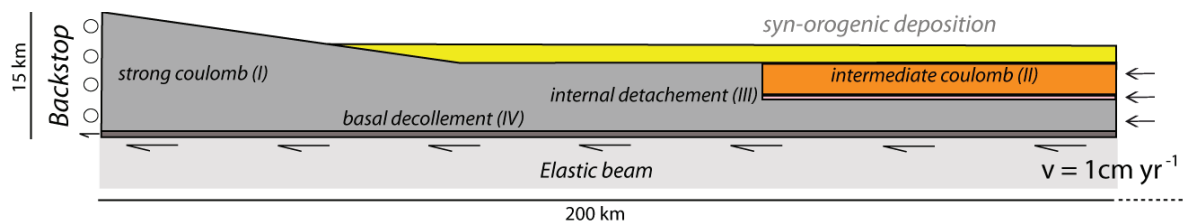


Figure IV - 1. Model geometry and boundary conditions. Dotted line on the right side of the box represents the continuity of the Lagrangian grid up to 800 km from the backstop; Eulerian grid extends to 400 km. Syn-tectonic deposition starts at 5 m.y. See text and Supplementary Table 1 for model parameter values.

The reference model 1 (Figure IV-1) consists of 4 materials: (I) a strong strain-weakening frictional-plastic material, with a high friction angle representing basement rocks; (II) an intermediate strength strain-weakening frictional-plastic material with lower friction angle for sediments, and (III) a very weak viscous internal décollement between these two layers, representing evaporites. A second weak viscous décollement (IV) is located at the base of the model. The initial geometry resembles a pre-existing wedge at critical taper and an adjacent, pre-existing sedimentary basin into which deformation propagates. A 1 cm yr⁻¹ velocity boundary condition is imposed on the right side and base of the model (Figure IV-1). The left side of the model domain is fixed horizontally, except at the base, where the basal décollement is evacuated at the same velocity. Gravitational loading is compensated by flexural isostasy, the wavelength of which is controlled by the flexural rigidity. Default parameter values for the models are provided in Supplementary Table 1.

In the models presented here, we focus exclusively on the effects of sedimentation, and therefore do not include erosional processes. Syn-orogenic sedimentation starts at 5 m.y, after some initial deformation, in models 2-6. From that moment, all topography below a fixed reference height representing base-level is filled with sediments (e.g., Figure IV-1). This representation of sedimentation is very simple but is consistent with the first-order infilling geometry pattern in an orogenic wedge and its foreland basin system (see DeCelles and Giles 1996, for example) : the accommodation space is filled by sediments that are subsequently deformed, and the elevation of the reference level forces sedimentation to occur only in the foreland fold-and-thrust belt domain. Varying base-level allows for testing the effect of varying sediment input in the foreland basin.

IV-1.4 Model Results

We present two sets of models that demonstrate the sensitivity of the model behavior to syn-tectonic sedimentation (Figure IV-2) and to flexural rigidity (Figure IV- 3). The first set includes three models with no (Model 1), moderate (Model 2) and strong (Model 3) syn-orogenic sedimentation. The second set investigates the response to changes in flexural rigidity (from 10^{21} to 10^{23} N m) for an intermediate sediment deposition model.

Reference Model, No Deposition - Model 1: During the initial stage, deformation only affects the strong coulomb “basement”, building an initial high-relief orogenic wedge with a system of pro- and retro- thrusts (pop-up structures; Figure IV- 2 at 5 m.y.), a common feature of all models presented. After 5 m.y., deformation migrates into the intermediate-coulomb “pre-tectonic sediments”; from this time on short thrusts develop in-sequence. All thrusts verge toward the foreland with similar lengths of about 17 km. No back-thrusts develop and there is almost no reactivation or out-of-sequence thrusting. By 12 m.y., nine thrust sheets have developed with a regular spacing.

Moderate Deposition - Model 2: Model 2 experiences syn-tectonic sedimentation up to an intermediate reference level after 5 m.y., (see Figure IV-1). At 5 m.y., the pre-tectonic sediments start forming a back-thrust towards the hinterland, favored by the development of a basement duplex. The first frontal thrust initiates at 7 m.y., creating a 34-km wide wedge-top basin. With further shortening, deformation migrates back into the internal parts of the wedge and is partitioned between frontal and basal accretion .At 9 m.y., a second thrust forms 112 km from the backstop. Flexural subsidence resulting from the weight of the growing internal wedge, provides more sediment accommodation space and the formation of a second smaller wedge-top basin between the two frontal thrusts. At 12 m.y. deformation is partitioned between the frontal thrust, the reactivated back-thrust and internal basement deformation. The average thrust-sheet length is 30 km and the maximum sediment thickness is 4 km.

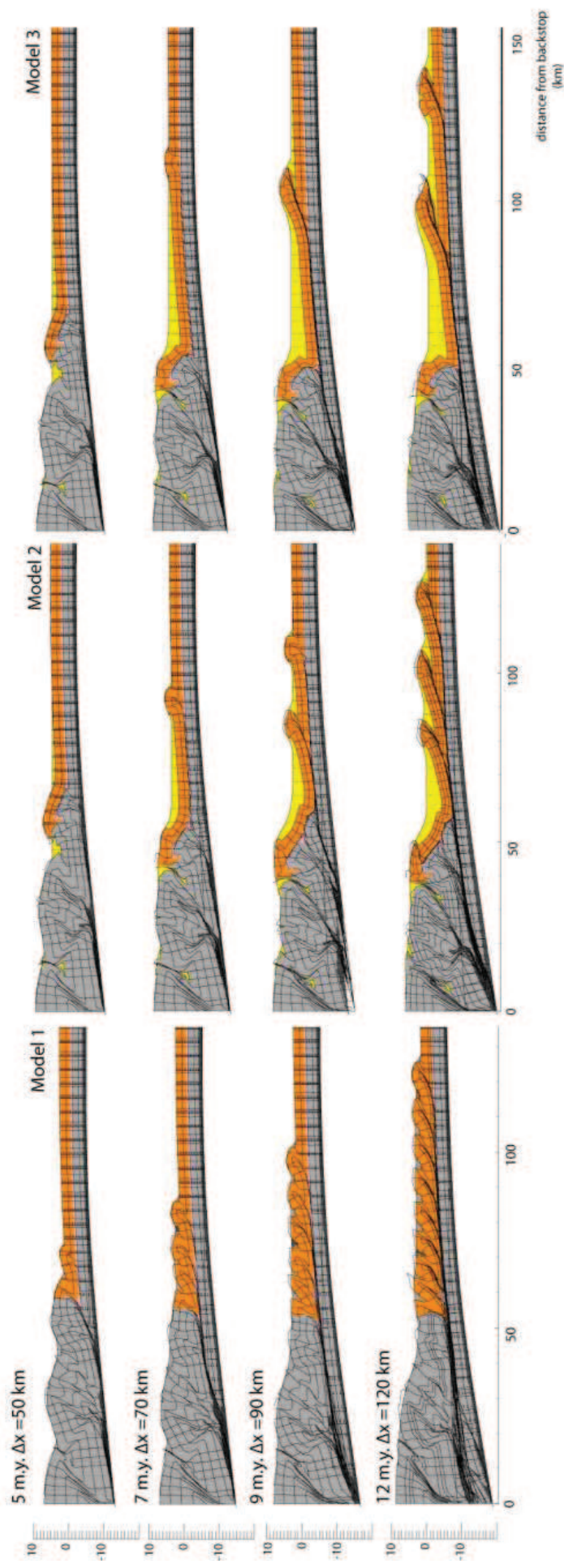


Figure IV - 2. Model evolution with different amounts of syn-tectonic sedimentation. Model 1: no syn-orogenic sedimentation; Model 2: syn-orogenic sedimentation up to 1.95 km elevation; Model 3: syn-orogenic sedimentation up to 2.25 km elevation. Panels are at 5, 7, 9 and 12 m.y. Flexural rigidity is 10^{22} N m.

Strong Deposition - Model 3: The generic behavior of Model 3 is similarly to Model 2 but the increased sediment thickness results in longer thrust sheets. At 5 m.y. a back-thrust is formed followed by emergence of the first external thrust around 7 m.y. at more than 100 km from the backstop. At 9 m.y., shortening is still accommodated by the frontal thrust, which accumulates more displacement than in model 2. A second thrust initiates just before 12 m.y. The wedge-top basin is around 43 km wide and the maximum sediment thickness is 6 km, for an average thrust-sheet length of 55 km.

Sensitivity to Flexural Rigidity – Models 4-6: We subsequently test the sensitivity to variations in flexural rigidity (10^{21} , 10^{22} , 10^{23} N) in models 4-6 with a constant intermediate base-level (Figure IV-3). The three models are all shown at 8 m.y. The evolution of Model 5, which has the reference model rigidity, is very similar to that of Model 2. The lower flexural rigidity in Model 4 favors a narrow foreland basin and the formation of a shorter 34-km thrust sheet. In contrast, Model 6 with a higher flexural rigidity favors the development of a wide foreland basin and the formation of a much longer 94-km thrust sheet. In all these models the location of initiation of the thrust sheets coincides with the edge of the foreland basin where sediments taper out.

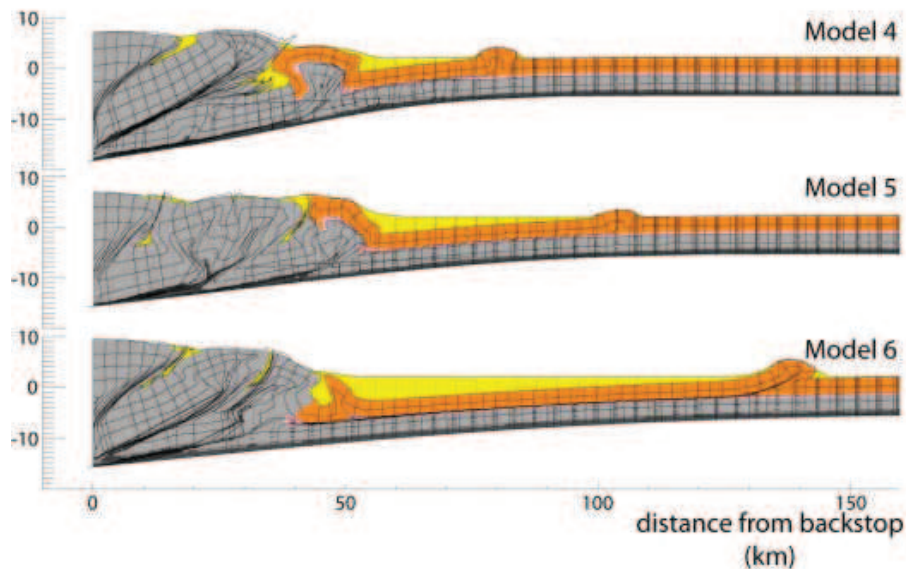


Figure IV - 3. Model panels at 8 m.y. for models with different flexural rigidity (Model 4: 10^{21} N m; Model 5: 10^{22} N m; Model 6: 10^{23} N m), corresponding to elastic thicknesses of 4.8, 10.4 and 22.4 km respectively (for Poisson ratio of 0.25 and Young modulus of 10^{11} N m⁻²). Models were run with syn-orogenic sedimentation reference level of 2.15 km.

IV-1.5 Discussion

A similar evolution characterizes wedge development in all models, independent of the amount of syn-tectonic sediments (Figure IV- 2, supplementary Fig.1) : 1) initiation of a frontal thrust; 2) out-of-sequence internal deformation and passive retreat of the external thrust belt; and 3) initiation of a new in-sequence thrust, resembling the frontal-accretion cycles described by Hoth et al. (2007). The main differences between the models are the locus and timing of thrust activation. The model without syn-orogenic sedimentation propagates most rapidly. Thrusts are very short, numerous, and do not accommodate much shortening, whereas the thrust sheets length increase with the amount of sediment depositing and activate later.

In all models the first external thrust and the subsequent frontal thrusts emerge at the point where the sediments taper out. This can be explained by two arguments. The fact that the sedimentary layer is very thin at that place induce that this zone is most stress-concentrated, making the localization of a thrust easier. Moreover, this place represents where the thrusting will need the less work to occur, the sediment column is thinner and so thrusting from the décollement level to the surface is easier. Thus, while sediments continue to deposit (Model 3), this zone migrates towards the foreland and so do the location of thrust activation.

The extent of syn-tectonic sedimentation asserts a first-order control on the location of the frontal thrusts. This extent is itself primarily governed by flexural parameters controlling the foreland basin shape. For lower flexural rigidities (Figure IV- 3, Model 4) a narrow and deep foreland basin is formed, limiting the extent of foredeep sedimentation with consequently shorter thrust sheets initiating where sediments taper out. In contrast, for higher flexural rigidities a wider foreland basin develops, promoting sedimentation much further out in the foreland and formation of longer thrust sheets.

The models presented here demonstrate that the extent and thickness of syn-tectonic sediments strongly affects the structural style of fold-and-thrust belts. The sediments are deposited horizontally, effectively stabilizing the wedge (e.g. Willett and Schlunegger 2010). In the most external parts where the sediments taper out and the angle of the basal décollement (β) tends to zero, the wedge reaches critical state. After the formation of the first thrust the surface attains a negative slope α , further stabilising the wedge (supplementary Fig.2). Further syn-tectonic sedimentation in front of the active thrust enlarges the stable wedge and promotes formation of a new frontal thrust. A second factor is the increased frictional strength resulting from loading by wedge top sedimentation, causing the new thrust to be formed where sediments are thinnest (Davis et al. 1983; Hardy et al. 1998). The evolution of taper angles α and β through time confirms that the wedge evolves according to critical taper theory: β ranges from 2 to 5 ° and α from -1 to +1 °, which is in good agreement with the typical values for these kind of thrust belts (Ford 2004). The activation of a new thrust corresponds to the moment in time when $\alpha + \beta$ is maximal.

IV-1.6 Comparison to natural systems

The numerical models presented here suggest that syn-tectonic wedge top sedimentation exerts a major control on foreland fold-and-thrust belt development. Other parameters, such as the relative strength of the décollement level, different rheologies, thickness of pre-orogenic sediments and pre-existing structures in the basement, are expected to play a role as well. We compare our results to observed structural style, sediment thickness, and flexural rigidity of several thin-skinned fold-and-thrust belts around the world (Figure IV-4; Supplementary Table 2 for data sources). Cross-sections for three different fold-and-thrust belts (Pyrenees, Canadian Rockies and Apennines) illustrate the correlation between thrust-sheet length and syn-tectonic sediment thickness and distribution (e.g. Figure IV-4a). The southern Pyrenean fold-and-thrust belt is characterised by a very thick succession of syn-orogenic sediments, thrust sheets up to 30 km in length and a wide piggy-back basin, comparable to the structure of Models 2 and 3 (Figure IV-2).

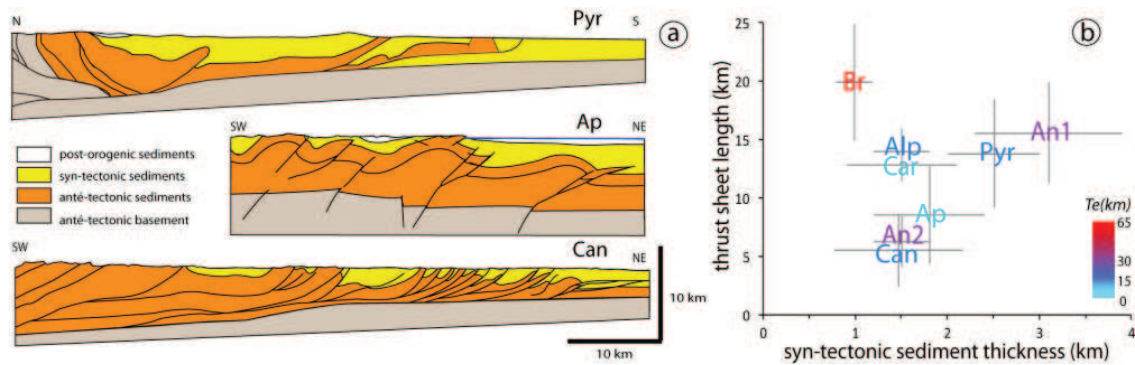


Figure IV - 4. (a) Cross-sections of fold-and-thrust belts with different thickness of syn-tectonic sediments and thrust sheet length, from top to bottom: ECORS section, Pyrenees Muñoz 1992, Apennines Butler et al. 2004 and Canadian Rockies Ollerenshaw 1978. (b) Average thrust-sheet length plotted against maximum sediment thickness for the Western Alps, France (Alp); Sub-Andean belt, North-West Bolivia (An1); Sub-Andean belt, South Bolivia (An2); Apennines (Ap); Brooks Ranges, Alaska (Br); Canadian Rockies (Can); Carpathians (Car) and southern Pyrenees (Pyr). The values for sediment thickness and thrust length were measured on at least three thrust sheets of the fold-and-thrust belt and then averaged; see Supplementary Table 2 for values and references.

The Apennines, with intermediate syn-tectonic sediment thickness are characterised by moderate thrust sheet length. The fold-and-thrust belt of the Canadian Rocky Mountains developed very short thrust sheets where syn-tectonic sediments are thin and longer thrust sheets where syn-tectonic sediments are thicker suggesting that temporal variations in sediment supply may lead to spatial variations in thrust-belt structure.

The average thrust-sheet length of a number of fold-and-thrust belts is plotted as a function of maximum syn-tectonic sediment thickness (Figure IV-4b). The belts are also discriminated according to their elastic thicknesses (See Supplementary table 2 for data sources). Although these fold-and-thrust belts differ strongly in age and tectonic setting, a clear correlation between syn-orogenic sedimentation and thrust-sheet length appears: belts with thicker and more extensive syn-tectonic deposits have systematically longer thrust sheets. The effect of flexural rigidity is less obvious, although ranges developed on thicker elastic lithosphere appear to be characterized by the longest thrust sheets.

Only the Brooks Range appears to lie outside the observed trend, what we can explain by a strong pulse of post-orogenic erosion that has removed several kilometers of sediment from this range (Cole et al. 1997; O'Sullivan et al. 1997), so that syn-tectonic deposits may have initially been much thicker.

IV-1.7 Conclusions

We have shown dynamical models provide a general explanation for the effect of syn-tectonic wedge top sedimentation on the formation of thin-skinned fold-and thrust belts. The model results show that an increase in syn-tectonic sedimentation leads to significantly longer thrust sheets. Variations in flexural rigidity enhance this effect by widening the basin and therefore extending the area of sediment deposition. A range of natural thin-skinned fold-and-thrust belts show a linear correlation between maximum sediment thickness and thrust-sheet length, confirming the inference from the numerical models.

Acknowledgments

This study is supported by INSU-CNRS through the European Science Foundation Topo-Europe programme “Spatial and temporal coupling between tectonics and surface processes during lithosphere inversion of the Pyrenean-Cantabrian Mountain belt (PyrTec)”. It forms part of CF's PhD project at Université Joseph Fourier and University of Bergen, supported by the French Ministry for Research and Higher Education.

IV-1.8 Supplementary Material

Supplementary methods

Rheology

In order to reproduce and localize deformation in fault zones, the model uses a classical yield criterion. Once yielding occurs, materials of the deformed area rapidly experience strain softening. In this model, the Drucker-Prager pressure-dependent yield criterion is used to model the plastic behavior for incompressible deformation in plane strain. Yielding occurs when:

$$(J'_2)^{\frac{1}{2}} = p \sin \phi_{eff} + c \cos \phi_{eff}. \quad (1)$$

Where $J'_2 = \frac{1}{2} \sigma'_{ij} \sigma'_{ij}$ is the second invariant of the deviatoric stress, p is the dynamic pressure (mean stress), c is the cohesion and ϕ_{eff} is the effective internal friction angle. The values of c and ϕ_{eff} were chosen to reproduce frictional sliding of rocks. The angle ϕ_{eff} includes the variations of Pore fluid pressure (P_f), which reduces the effective stress and is defined by

$$P \sin \phi_{eff} = (P - P_f) \sin \phi. \quad (2)$$

Several mechanisms can lead to brittle weakening of rocks (Huisman and Beaumont 2007 and references therein), including cohesion loss, mineral transformations, and increased pore fluid pressures. In the models presented here strain weakening is introduced using a parametric approach. The friction angle $\phi_{eff}(\varepsilon)$ decreases linearly with increasing strain in the range $0.5 < \varepsilon < 1.0$, where ε represents the square root of the second invariant of deviatoric strain.

Models parameters values

| Material number | Description | Internal friction angle Φ | |
|-----------------|---|--------------------------------|----------|
| | | $\Phi 1$ | $\Phi 2$ |
| I | Strong Coulomb , with strain softening | 38 | 25 |
| II | Intermediate Coulomb, with strain softening | 38 | 18 |
| III | Very weak internal décollement | 1 | |
| IV | Weak basal décollement | 10 | |
| Cohesion | 2 MPa | | |
| Density | 2.3 10 ³ km.m ⁻³ | | |
| Eulerian grid | 801 x 81 cells | 400 x 12.5 km | |
| Lagrangian grid | 1601 x 81 cells | 800 x 12.5 km | |

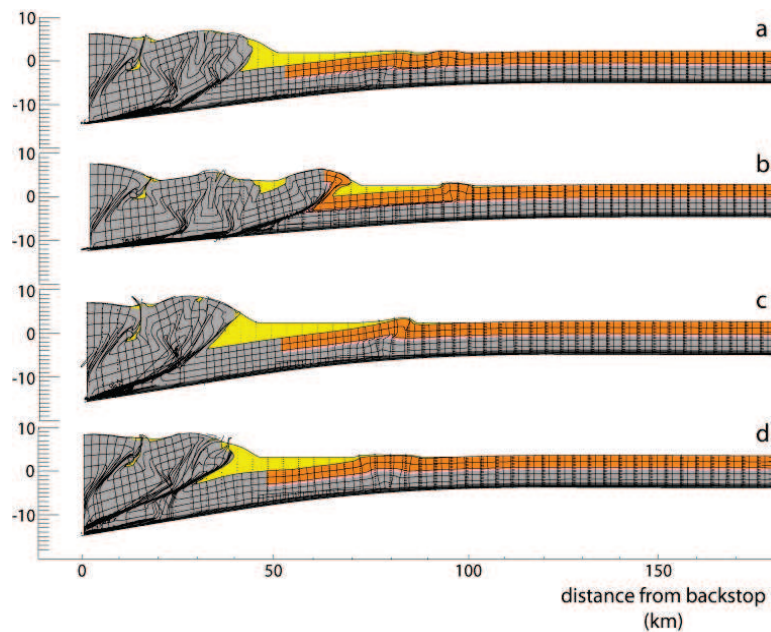
Supplementary Table 1: Fixed parameter values for numerical model runs.

Supplementary models

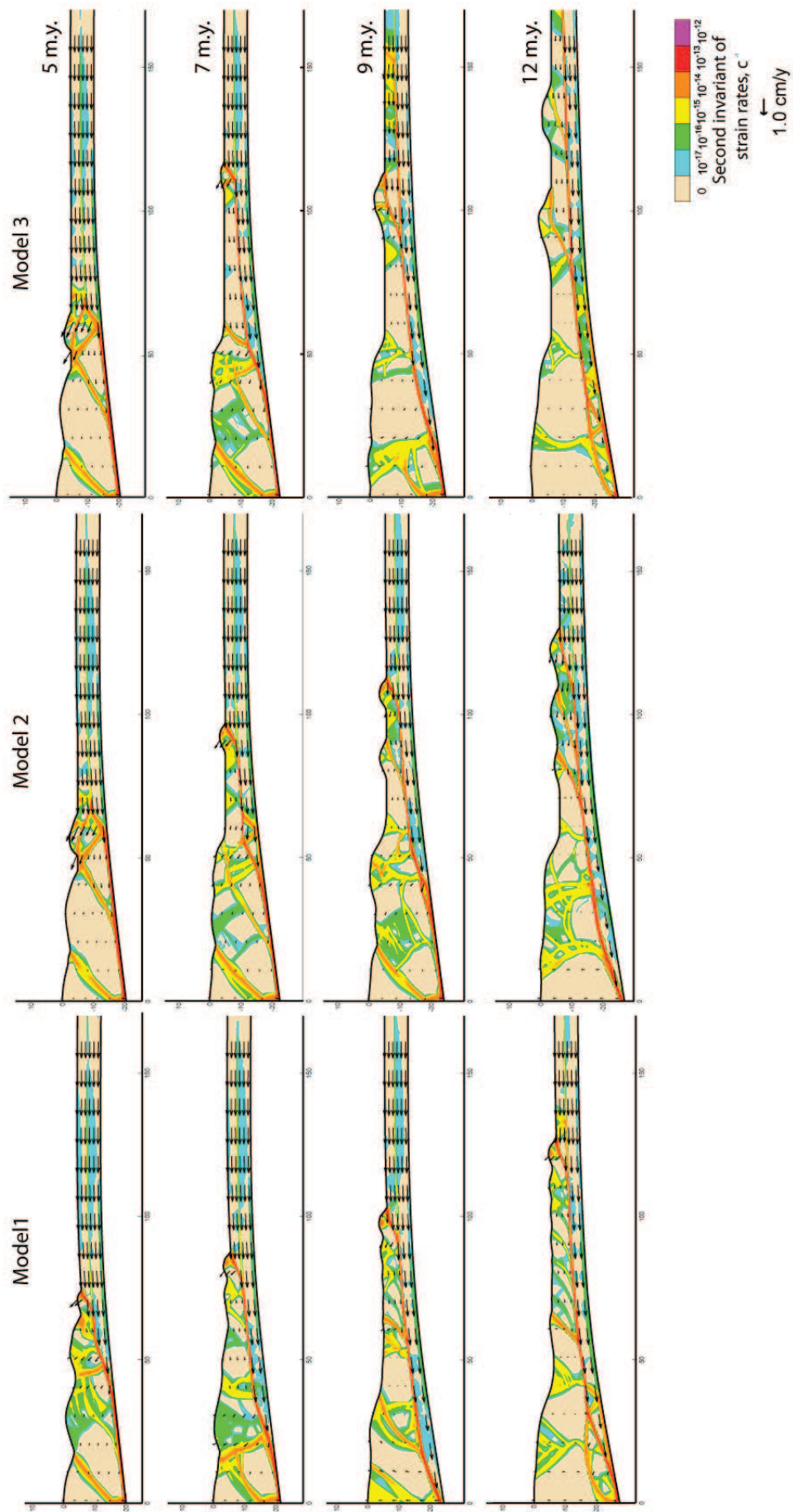
Influence of the strength of internal decollement strength on the thrust sheet lengths

The rheology of the internal decollement forms a major control on the wedge development. In order to test this influence, we run several models with increasing the strength of the internal décollement material (characterized by its internal friction angle ϕ_b). We present in supplementary Figure 2 snapshots of models with ϕ_b at 2.5°, 5°, 7.5°, and 10° at the time when their first external thrust activate. Syn-tectonic sedimentation in these supplementary models was set at the same level as in the models of Figure IV-2 but starts at 3 Myr.

Despite the differences in structural styles (in particular in model b), the first sedimentary thrust sheets are shortening with increasing ϕ_b . The first thrust activates at 98, 100 and 87 km from the backstop, in model a, b, c, and d respectively. We note that in model c ($\phi_b = 7.5^\circ$) the basement and the sedimentary layers deform jointly, because the difference in strength between the basement, the décollement and sedimentary layers is minimized. We thus conclude from this set of models that the rheology of the decollement level has an impact on the thrust sheet length by shortening them, but this effect is much less significant than the effect of syn-tectonic sediments on the wedge propagation and thrust sheet length.



Supplementary Figure 1: Tests of the influence of the strength of the internal decollement on the thrust sheet lengths. Model set up is the same than in Figure IV-2 but with syn-tectonic sedimentation starting at 3 Ma. Strength of the decollement is represented by the internal friction angle ϕ_b , that is 2.5°, 5°, 7.5°, and 10° for model a,b,c and d respectively.



Supplementary Figure 2: Evolution of principal strain rates and velocity field for models/snapshots shown in Figure IV-2.

Strain rates and velocity field

Supplementary Figure 2 documents the strain-rate evolution for the same models and at the same timesteps as shown in Figure IV-2. The green zones (at 7 m.y in models 1 and 3 for example) show the diffuse pattern of strain repartition, that is subsequently followed by localization on big faults. In the three models, most of the displacement coming from the right side of the model is accommodated by the frontal thrust and by underthrusting below the décollement level. In Model 1 (without syn-tectonic sedimentation), at 5 m.y, displacement is localized at the front but in the internal parts as well, with active backthrusting at around 50 km. Then this internal displacement progressively decreases to almost zero at 12 m.y. On the opposite, the velocity field in the fold-and-thrust belt shows that each thrust is active, but always less than the frontal thrust. Model 2 and 3 are very similar in terms of velocity field patterns. The backthrusting that occurs at 5 m.y. is very efficient at that time while the internal part experiences little displacement. At 7 m.y. the frontal thrust records most of the displacement, and the internal part (especially around 50 km from the backstop) show moderate and top-directed velocity field, this pattern is reproduced until the 9 m.y timestep. Finally, at 12 m.y, only the fold-and-thrust belt records displacement, the internal part become much less active. It is also worth noting that the velocity field shows very well the progression of underthrusting below the internal décollement level towards the left side of the model. Strain localization allows identifying the most active faults. In the three models, the strain is accumulated on 1) the frontal thrust , 2) the décollement level and 3) the largest faults in the internal parts. Among these structures, the décollement level is the one that concentrates most strain.

Data and references for natural systems

| Range | Average thrust length (km) | Maximum thickness of syn-tectonic sediments (km) | Reference for cross-sections | Elastic thickness (km) | Reference for Te |
|-----------------------------------|----------------------------|--|------------------------------|------------------------|---------------------------------|
| Canadian Rockies (Can) | 5.5 ± 3.1 | 1.5 ± 0.7 | <i>Ollerenshaw 1978</i> | 20 to 40 | <i>Flück et al. 2003</i> |
| Sub-andean belt (An2, S Bolivia) | 6.3 ± 2.2 | 1.5 ± 0.3 | <i>Horton 1998</i> | 30 to 40 | <i>DeCelles and Horton 2003</i> |
| Apennines (Ap) | 8.6 ± 4.1 | 1.8 ± 0.6 | <i>Butler et al. 2004</i> | 8 to 15 | <i>Royden and Karner 1984</i> |
| Carpathians (Car) | 12.9 ± 1.4 | 1.5 ± 0.6 | <i>Hippolyte et al. 1999</i> | 3 to 16 | <i>Zoetemeijer et al. 1999</i> |
| Pyrenees (Pyr) | 13.8 ± 4.6 | 2.5 ± 0.3 | <i>Muñoz 1992</i> | 20 to 30 | <i>Zoetemeijer et al. 1990</i> |
| Swiss molassic basin (Alp) | 14 ± 2 | 1.5 ± 0.3 | <i>Beck et al. 1998</i> | 5 to 15 | <i>Sinclair et al. 1991</i> |
| Sub-andean belt (An1, NW Bolivia) | 15.6 ± 4.3 | 3.1 ± 0.8 | <i>Baby et al. 1995</i> | 30 to 40 | <i>DeCelles and Horton 2003</i> |
| Brooks ranges (Br) | 20 ± 5 | 1 ± 0.2 | <i>Cole et al. 1997</i> | 65 to 75 | <i>Nunn et al. 1987</i> |

Supplementary Table 2: Sediment thicknesses, thrust-sheet lengths, and equivalent elastic thicknesses for natural fold-and-thrust belts. Measurements of thrust sheet length and their associated syn-tectonic sedimentation thickness was taken in three places of the fold-and thrust belt at least. The sediment thickness was measured at the place where the vertical thickness is maximum, i.e in the center of a piggy-back basin for example. The thrust sheet length was defined by the length from the place where the thrust is differentiating to its surface emergence.

Chapter IV-2 Influence of surface processes on the late-stage evolution of the southern Pyrenees

IV-2.1 introduction

The theoretical evolution of a thrusting sequence is controlled, at first-order, by the critical taper behavior that induces a cyclicity between thickening of the wedge and frontal accretion (Chapple 1978; Davis et al. 1983; Dahlen et al. 1984; Hoth et al. 2007b). Since wedge thickening is controlled not only by internal deformation but also by surface processes, there should be a feedback/coupling between wedge deformation and erosion/sedimentation (Willett 1999b; Willett 2010).

The effects of wedge-top sedimentation on an orogenic wedge have been studied by several authors using analogue and numerical modeling (Huiqi et al. 1992; Marshak and Wilkerson 1992; Boyer 1995; Storti and McClay 1995; Mugnier et al. 1997; Hardy et al. 1998; Simpson 2006; Malavieille 2010). In the previous chapter, we have shown by numerical modeling that the addition of syn-tectonic wedge-top sedimentation during the early stages of wedge development has the effect to perturb the patterns of thrust activation and to lengthen the thrust sheets. We concluded that these effects were the consequences of the taper angle modification by wedge-top sedimentation as well as forcing frontal accretion by minimizing the energy where sediments taper out. Similarly, the impact of erosion on the evolution of an orogenic wedge has been extensively studied by numerical and analogue modeling (Mugnier et al. 1997; Willett 1999b; Persson et al. 2004; Bonnet et al. 2007; Stockmal et al. 2007; Malavieille 2010).

In the southern Pyrenees, the rapid exhumation of the Axial Zone during late Eocene times produced a significant amount of sediments that were deposited to the south and covered the southern foreland (see Part III). Several field observations, geochronological studies and restored cross-sections (Burbank et al. 1992a; Puigdefàbregas et al. 1992; Meigs et al. 1996; Beaumont et al. 2000; Capote et al. 2002; Beamud et al. 2011) have shown that the southern Pyrenean wedge propagation was still active while these sediments were deposited, with evidence for exhumation in parts of the Southern Axial Zone, as well as in the center and south of the foreland fold-and-thrust belt, continuing until late Oligocene times.

The purpose of this chapter is to investigate how the erosion of the internal Massif and the deposition of resulting conglomerates on top of the fold-and-thrust belt could have influenced the thrusting sequence by stopping, enhancing or reactivating the thrust sheets. To reproduce the Pyrenean pro-wedge development, this modeling study incorporates a 2-step history of wedge-top sedimentation: wedge-top basins are filled to a prescribed base-level (as in the previous chapter) from the early stages of wedge development and an additional prograding wedge of sediments is added to the model when the fold-and-thrust belt is already developed. We will present several combinations of sedimentation geometries and discuss their influence on the thrusting sequence. Finally, these results will be compared to the southern Pyrenean thrusting sequence, in order to extract the critical parameters driving this sequence.

IV-2.2 Geological setting

IV-2.2a General context

The Pyrenean range is a collisional belt resulting from the convergence since the late Cretaceous of the Iberian and the European plates (Choukroune and ECORS Team 1989; Roure et al. 1989; Muñoz 1992; Beaumont et al. 2000). The underthrusting of the Iberian crust towards the North created a doubly-vergent orogen, the exhumation patterns and geometry of which are strongly asymmetric (Fitzgerald et al. 1999; Sinclair et al. 2005). The Pyrenean exhumation history can be divided into three phases (Figure IV-6): 1) From Late Cretaceous-Paleocene, exhumation in the Northern part (retro-side), contemporaneous with inversion of the Mesozoic basins in the South (Burbank et al. 1992b); then 2) development of the southern fold-and thrust belt (pro-side) and exhumation of the Noguères basement unit in the central Axial Zone (Paleocene to middle Eocene); and 3) simultaneous continuous southern foreland progression and stacking of the Orri and Rialp units under the Noguères unit to form the Axial Zone antiformal stack (Figure IV-5), Vergés and Muñoz 1990; Beaumont et al. 2000). The main exhumation phase inferred from thermochronological data occurred during Eocene times (Muñoz 1992; Fitzgerald et al. 1999; Beaumont et al. 2000; Vergés et al. 2002a; Sinclair et al. 2005). From Cenomanian to early Miocene times, Beaumont et al. (2000) calculated a total shortening of 165 km in the Central Pyrenees, which is a Maximum of several along-strike shortening estimates (Vergés et al. 1995; Teixell 1998).

The Pyrenean range is flanked to the North and South by two fold-and-thrust belts and foreland basins: the Aquitaine basin and the Ebro basin respectively. The southern pro-side of the Pyrenean wedge, is much better developed than the northern one and shows a very well exposed succession of Mesozoic and Cenozoic deposits (Late Cretaceous turbidites to Oligocene-Miocene conglomeratic deposits). The ECORS cross section through the Central Pyrenees (Figure IV-5) shows the thin-skinned development of the southern fold-thrust belt, favored by a thick and

continuous décollement level of Triassic evaporites that helped inverting the Mesozoic basins. This structural cross-section also shows the three main thrust sheet units transported by the Boixols thrust, the Montsec thrust and the Sierras Marginales frontal thrust, respectively. Further south, the Ebro foreland basin extends from the south of the Basque-Cantabrian basin (to the West) to the Mediterranean Sea (to the East), draining the Pyrenees, the Iberian range and the Catalan coastal range.

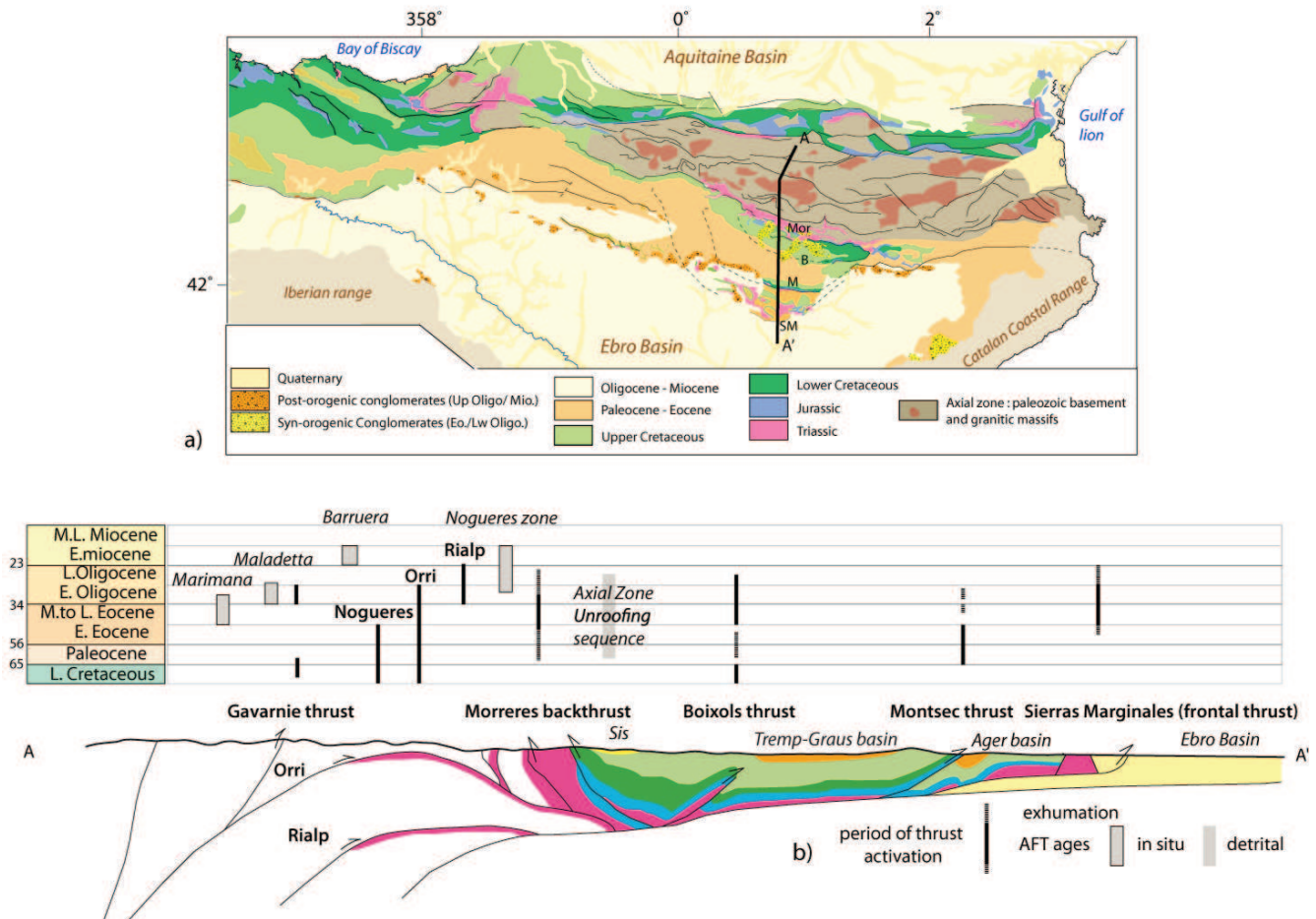


Figure IV - 5. a) Geological Map of the Pyrenees with location of the section A-A' shown below. b) Summary of the timing of exhumation and thrust activity from the literature. Timing of thrust activity was extracted from Muñoz (1992); Meigs et al (1996); Meigs and Burbank (1997); Capote et al.(2002); Sinclair et al.(2005); Rahl et al. (2011); thermochronological constraints are based on Fitzgerald et al.(1999) ; Sinclair et al.(2005) ; Gibson et al . (2007) ; Metcalf et al. (2009) and Beamud et al. (2011). Structural cross-section of the central Pyrenees is based on the ECORS seismic profile and redrawn from Muñoz (1992).

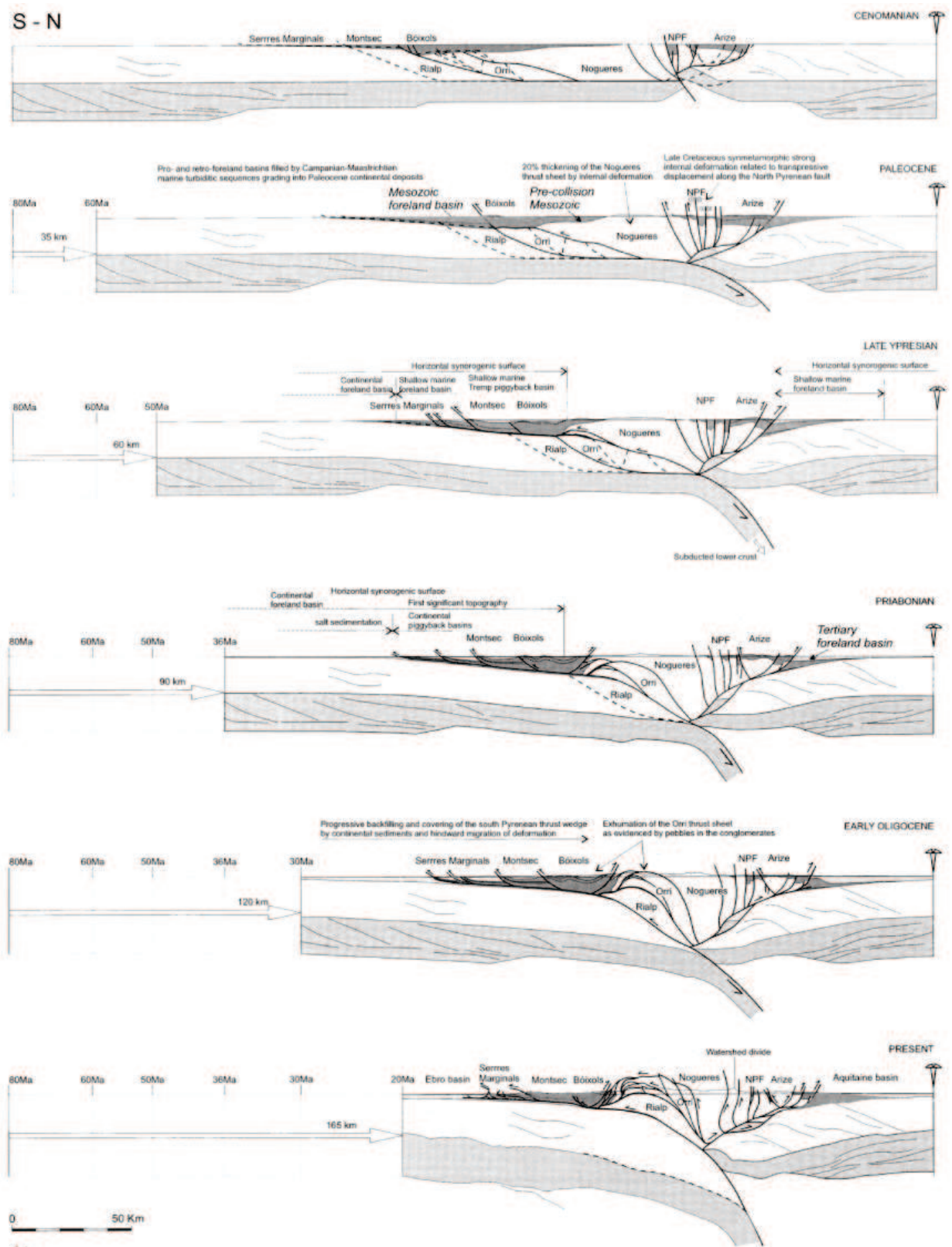


Figure IV - 6. 2-D geodynamic reconstruction of the central Pyrenees evolution from Late Cretaceous to present-day. From Beaumont et al. (2000).

Beamud et al. (2003, 2010) have dated the conglomeratic deposition from late Lutetian (~40 Myr) to Rupelian times (~28 Myr). Currently exposed remnants of these conglomeratic deposits are more than 1 km thick. Reconstruction of the extent of the conglomerates indicates that they prograded on the Southern flank of the Axial Zone during the Oligocene (e.g. Coney et al. 1996). We have shown in part II that their initial thickness was more than 2 km.

IV-2.2b South central Pyrenean thrusting sequence

The thrusting sequence in the southern Pyrenean pro-wedge (Figure IV-5) is at first order in-sequence: while the internal basement units were being emplaced (Nogueres, Orri, and Rialp), thrust sheets propagated over the décollement level of Triassic evaporites building the foreland fold-and-thrust belt. In the foreland, the first thrust to be activated was the Boixols thrust (to the east of the present-day Tremp basin), a former Mesozoic normal fault as shown by thickening of the Lower Cretaceous strata in its hangingwall. Then inversion of this structure in Late Cretaceous times (Bond and McClay 1995) formed the San Corneli anticline. There is some evidence for Late Eocene reactivation of this thrust; in particular the tilting of Bartonian-early Priabonian (40-37 Ma) conglomerates (lower Ermita, Pesonada units, Mellere 1993) deposited in the backlimb of the San Corneli anticline, whereas the Oligocene conglomerates above are horizontal. Further south, the thickening of the Garumnian formation strata (Late Cretaceous-Paleocene) indicates that the Montsec thrust was active during Paleocene time (Puigdefàbregas et al. 1992), dating therefore the southward in-sequence propagation of the thrust sequence and the initiation of the Tremp-Graus basin as a piggy-back basin. Montsec thrust activity lasted until the late Eocene, as dated by Magnetostratigraphy of the syn-tectonic conglomerates at the Eastern termination of the Montsec thrust (Burbank et al. 1992b). Activity of the present-day frontal thrust (Sierras Marginales) started earlier so that this thrust was active simultaneously with the Montsec (Burbank et al. 1992b); it stayed active until middle Oligocene times (26 Ma, Meigs et al. 1996). In detail, it is important to note that the relationships between Oligocene conglomeratic deposits and the structures in the Montsec-Sierras Marginales area show evidence for out-of sequence thrusting and reactivation at a smaller scale until late Oligocene times.

Going back toward the hinterland, the Morreres backthrust (Figure IV-5), is inferred to be active from early Eocene to Oligocene times (Mellere 1993; Capote et al. 2002) and delimits to the North the Boixols thrust sheet and the fold-and-thrust belt in general.

In the internal part of the wedge, exhumation occurred by stacking of the Nogueres, Orri and Rialp basement units. They were emplaced from Late Cretaceous to middle Eocene (Nogueres), from Paleocene to middle Oligocene (Orri), and during Oligocene (Rialp) times respectively (Muñoz 1992; Capote et al. 2002; Saura and Teixell 2006). Underthrusting by the Orri unit and resulting uplift of the Nogueres zone created rotated structures (called “têtes plongeantes”, Seguret 1972), of which the relationship with conglomeratic sediments documents the timing of activity.

The conclusions presented in Chapter II-1 from modeling of a combination of low-temperature thermochronological data (Fitzgerald et al. 1999; Sinclair et al. 2005; Gibson et al. 2007; Metcalf et al. 2009) provide constraints on the rate of exhumation of the southern Axial Zone. It documents a moderate exhumation rate (1 km.Myr^{-1}) from 40 to 37 Ma, followed by a rapid exhumation phase (2.8 km.Myr^{-1}) between 37 to 30 Ma, followed by a very slow exhumation phase (0.02 km.Myr^{-1}) from 30 Ma to present. The late Eocene-early Oligocene (37-30 Ma) exhumation of the axial zone is contemporaneous with significant infilling of the foreland by conglomerates. Nevertheless, these results do not incorporate the evidence for out-of sequence thrusting provided by structural observations presented before, as well as the young AFT and AHe ages in the Barruera area (Sinclair et al. 2005; Gibson et al. 2007).

In situ apatite fission-track ages range from early Eocene to Oligocene in the Marimaña, Maladeta and Barruera Massifs, with late Oligocene ages found in the southernmost Barruera Massif and in the Noguères zone (19.5 Ma and 17.2 Ma respectively). Moreover, Apatite (U-Th)/He results from Gibson et al. (2007) include 3 ages ranging from $10.5 \pm 0.8\text{ Ma}$ to $15.9 \pm 1.3\text{ Ma}$ in the Barruera Massif, and thus significantly younger than the other AFT data of the area. We have shown before that the syn-tectonic conglomeratic sedimentation was very thick and probably covered the southern Pyrenean foreland. In the following we will use dynamic models of fold and thrust belt formation to test if syn-tectonic wedge top conglomerate deposition could be the cause for the observed out-of-sequence thrusting.

IV-2.3 Model description

A 2D Arbitrary Lagrangian Eulerian (ALE) finite element model (Fullsack 1995) was used to investigate the relationships between the thin-skinned wedge development and wedge top sedimentation. This numerical model allows for visco-plastic rheologies but for our purpose, we limit its use to the upper crust, *e.g.* the first 15 km, and therefore do not include viscous deformation. The model reproduces localization of deformation by using a classical yield criterion and applying strain softening on the basement and sedimentary layers. Further details on the model and its parameters are further developed in the previous chapter (IV-1) and in the chapter I-2.

The superposition of the two grids (Lagrangian and Eulerian) allows for computation of large-scale deformation. The Lagrangian marker grid tracks the material, its properties, and the accumulated strain. Its position is updated according to the velocity field computed on the Eulerian grid. The Eulerian grid is 400 km long by 12.5 km thick and has a resolution of 801×81 cells respectively. The Lagrangian grid is two times longer (Table IV-1) to provide enough material to enter the system at the right-hand side of the model (1601×81 cells).

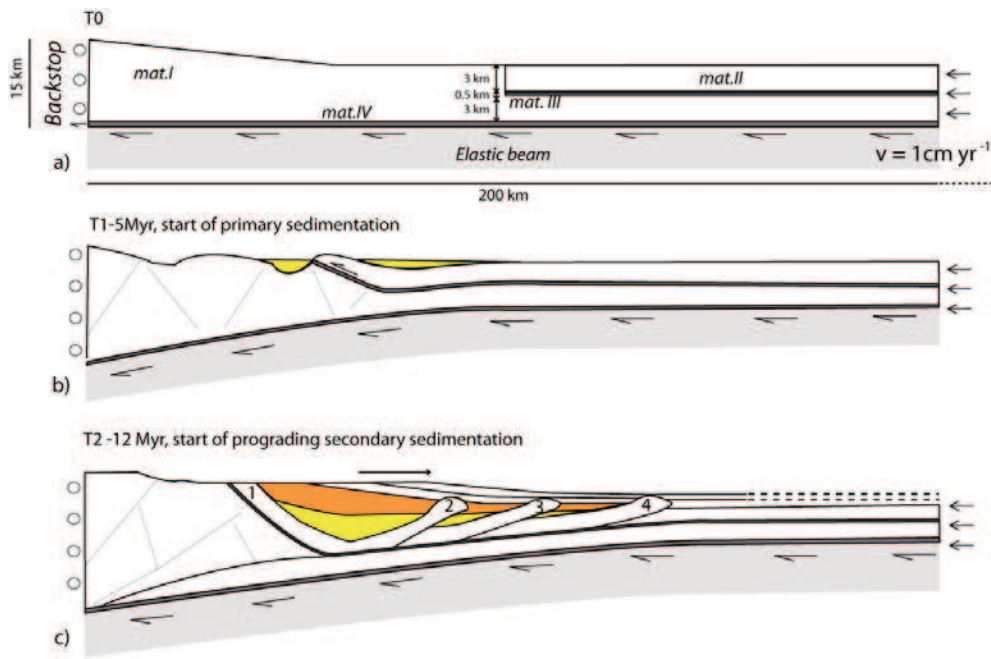


Figure IV - 7. Model set up. a) Situation at the beginning of the model run. b) Start of primary syn-tectonic sedimentation (same properties as Material II). c) Start of addition of a prograding syn-tectonic sedimentation. See Table IV-1 for the parameter properties

IV-2.3a Model geometry and Materials

The model domain is 200 km long and 15 km high at the left-hand side. The model includes different materials (see Table IV-1 and Figure IV-7): 1) a strong Coulomb material with a high friction angle and strain softening represents the basement (Mat. I); 2) an intermediate Coulomb material with moderate internal friction and strain softening (Mat. II); 3) a very weak internal décollement with a very low friction angle (Mat. III) located between the strong and the intermediate Coulomb materials and 4) a weak basal detachment with low friction angle at the base of the model box (Mat. IV). All materials have the same cohesion and the same density (see Table IV-1 for model parameters). Several runs testing the rheological parameters of the different materials were performed; the main modeling results are shown in the additional run section.

Material II (representing sediments) is 3-km thick and starts at 100 km from the backstop in order to produce a first “internal wedge” before deforming sediment, as it occurred in the Pyrenees. The initial topography has been slightly perturbed to favor the wedge development.

| Material number | Description | Internal friction angle ϕ | |
|-------------------|--|--|----------|
| | | $\Phi 1$ | $\Phi 2$ |
| I | Strong Coulomb , with strain softening | 38 | 25 |
| II | Intermediate Coulomb, with strain softening | 38 | 18 |
| III | Very weak internal décollement | 1 | |
| IV | Weak basal décollement | 10 | |
| Cohesion | 2 MPa | | |
| Density | 2.3 10 ³ kg.m ⁻³ | | |
| Eulerian grid | 801 x 81 cells | 400 x 12.5 km | |
| Lagrangian grid | 1601 x 81 cells | 800 x 12.5 km | |
| Erosion | Slope dependent, rate: 1mm.yr ⁻¹ for a 1:1 slope | | |
| Deposition | Primary sedimentation | reference level h=2.05 km Start at 5 Ma | |
| | Secondary sedimentation | Prograding half-Gaussian Start at 12 Ma | |
| Flexural rigidity | 1.10 ²² N.m ⁻¹ | | |

Table IV - 1. Main parameters for model runs. See Figure IV-7 for the geometric distribution of different materials in the model and the geometry of the sediment deposition.

IV-2.3b Boundary conditions

A constant velocity of 1 cm.yr⁻¹ is imposed on the right side and on the base of the model domain. The left side is fixed, except at the base where a slot allows for some weak Coulomb material to escape, to avoid the stacking of this material in the wedge. Gravitational loading is compensated by flexural isostasy, the wavelength of which is controlled by the flexural rigidity of an elastic beam below the basal décollement.

The effects of varying flexural parameters will not be tested here and all the models have the same flexural rigidity, that is 1.10²² N.m⁻¹ and so an elastic thickness (T_e) of 11.7 km with Poisson ratio of 0.25 and Young modulus of 7.10¹⁰. This value of T_e is the most satisfying when fitting the reconstructed flexural profile of the Pyrenees and with different modeling studies (Zoetemeijer et al. 1990a; Gaspar-Escribano et al. 2001) which predicted T_e of 10 to 20 km below the Ebro

foreland basin. We have performed several additional runs varying the flexural rigidity, a few of them are presented in the next section (additional runs).

IV-2.3c Surface processes

For models 2 to 6, we modify the sedimentation patterns twice during the model runs. “Primary sedimentation” fills up the topography to a reference level and starts at 5Myr (see previous section). A “secondary sedimentation” phase is modelled as prograding towards the right-hand side with a half-gaussian shape and starting at 12 Myr at which time the model shows a backthrust and 3 thrust sheets (representing the Boixols, the Montsec and Frontal thrusts). Model behavior is rate independent, which implies that the models can be interpreted at any desired time scale. The amount of convergence can be directly compared to the natural system, in the following we will consider that the model age has to be multiplied by 3 to obtain an average of “real” geological time. The parameters of prograding sedimentation can be chosen such to produce local or distributed sedimentation. The sedimentary body is allowed to evolve through time by prograding (towards the foreland) with an imposed velocity. In order not to cover the entire system with these sediments, we limit progradation to 2 Myr. After that time, the sedimentary body stays stable. However, the southern Pyrenees and Axial Zone also experienced episodes of strong erosion, which is not included in models 1 to 5; models including erosion will be presented in the last section of this chapter. The surface processes were simplified to focus exclusively on the effects of wedge-top sedimentation. In a first set of models the geometry of the sedimentary body is kinematically controlled (elevation, extent and shape).

IV-2.4 Results

We will present in the following the results of 6 model runs. In order to compare the thrusting sequence and the wedge behavior, the first model (Figure IV-8 and IV-9, model 1) do not include secondary sedimentation. The other models (models 2 to 5) investigate the effects of different geometries of deposition of the secondary sedimentation, tested with short (Figure IV-10), moderate (Figure IV-11) and long extent (Figure IV-12), and low and high elevation (Figure IV-13). The results will then be compared to the Pyrenean thrusting sequence (Figure IV-14). In the following, the fold-and-thrust belt thrusts will be referred to as F1, F2 F3 and F4 from the left to the right hand-side in order of their formation

| Model number | 1 st Sedimentation | Erosion | 2 nd Sedimentation | |
|--------------|-------------------------------|------------|-------------------------------|-----------------|
| | | | Elevation | Extent |
| 1 | Yes | No | | No |
| 2 | Yes | No | Low | Low |
| 3 | Yes | No | Low | Moderate |
| 4 | Yes | No | Low | High |
| 5 | Yes | No | High | Moderate |
| 6 | Yes | Yes | Low | Moderate |

Table IV - 2. Description of parameters for models 1-6.

IV-2.4a Base model (1) – no secondary sedimentation

This model includes only primary sedimentation, which starts at 5 Myr and consists of sedimentary material, similar to material II (Figure IV-7). Thrusting first occurs in the basement layer on the left-hand side of the box, creating the internal wedge. Then, the deformation in the sedimentary layers starts at 4.2 Myr, with backthrusting of the sediments onto the basement initiating the formation of the external wedge. The thrust sheets propagate in-sequence activation at 6.4, 8.6 and 11 Myr, respectively for the first, second and third thrust. As the syn-tectonic sedimentation thickness is one of the major controlling factors on the thrust sheets length (see previous chapter IV-1), the reference elevation of the sediments was tuned to 2.05 km to obtain thrust sheets with lengths comparable to those observed in the southern Pyrenees, which are ~30 km long (Figure IV-5). At 12 Myr, basement is deformed by large pro- and retro- thrusts and the external wedge resembles the late Eocene geometry of the South Pyrenean foreland fold-and-thrust belt as predicted by Beaumont et al. (2000) (Figure IV-6). To compare with the following models, we will now focus on details of the base model evolution between 12 and 14 Myr. Scaled to the Pyrenees evolution compared to the model, these 2 Myr can be taken to represent the 10 Myr period between 40 and 30 Ma, when strong erosion in Axial Zone and important deposition of its erosional products in the foreland occurred.

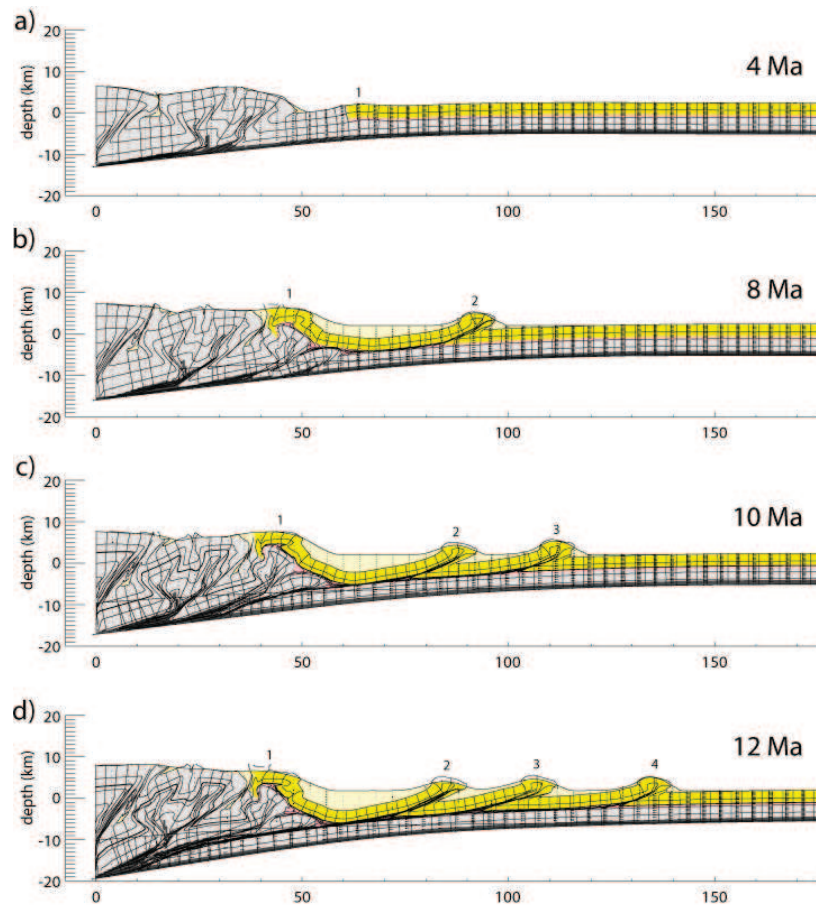


Figure IV - 8. Model 1 evolution from 4 to 12 Myr. The numbers correspond to the order of thrusts activation. The thrust are named in the text F1,2,3 and 4 following their order of appearance.

In the model (Figure IV-9) deformation in the internal zone is very active until 13.2 Myr and then decreases. At 12.2 Myr, the in sequence thrusts F3 and F4 are active (Figure IV-9a); between 12.8 and 13.6 Myr deformation moves to the rear of the wedge with most activity on F1 and the internal wedge which accommodate most of the displacement (Figure IV-9b-c). At 13.6 Myr, the décollement level is less efficient; deformation is localized on F2 with the major shear connecting to the basal décollement (Figure IV-9c). At 14.2 Myr, deformation moves again to the front of the wedge with F4 becoming the most active thrust (e.g. Figure IV-9d). A new frontal thrust initiates at 13.6 Myr but does not accommodate any significant shortening before 14.6 Myr.

The overall evolution of this model is characterized by distributed deformation on all the thrusting structures with cycling between frontal and rear accretion. The pattern of wedge propagation is firstly a wedge retreat with concentration of deformation on F2, and subsequently forward wedge propagation again by the new frontal thrust.

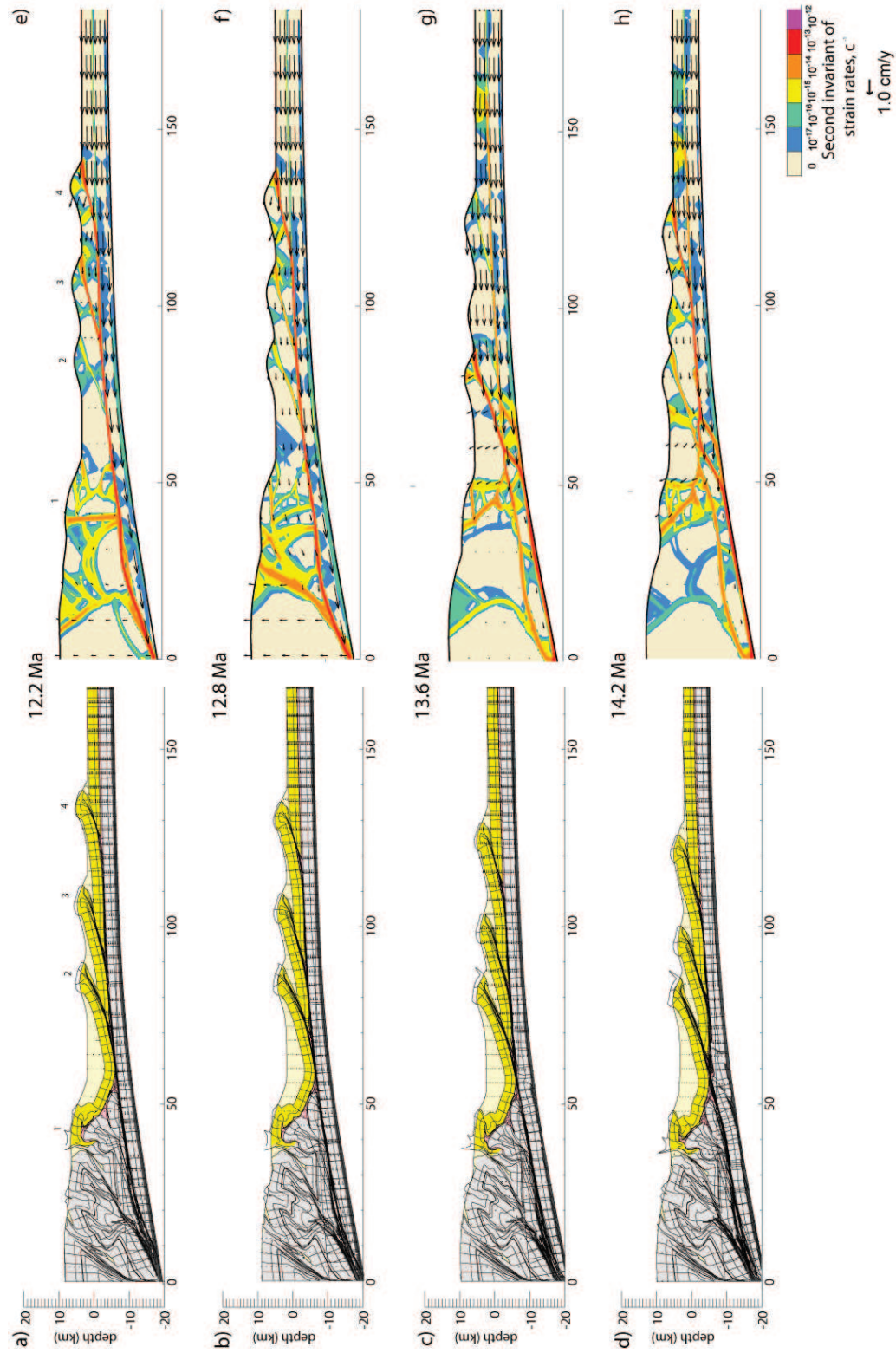


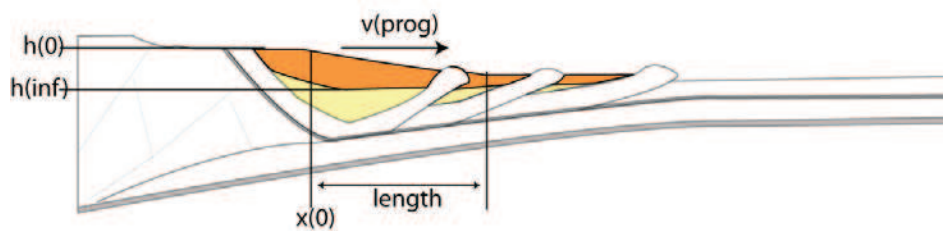
Figure IV - 9. Model 1 evolution from 12.2 to 14.2 Myr. The right panels show the second invariant of strain rate and the displacement field (black arrows) associated with deformation.

IV-2.4b Models including Secondary sedimentation

In the following models, we will test the effect of the deposition of a secondary prograding wedge with various geometries on the evolution of the wedge between 12 and 14 Myr (see Table IV-3 for parameters values).

Low elevation, short extent (model 2)

In model 2 we test the effect of a prograding wedge that has a low elevation and short extent covering only thrust F1 (Table IV-2). At 12.2 Myr, 3 zones are very active and accommodate most of the displacement: the frontal thrusts F3 and F4, and the shear zones in the internal zone of the wedge (e.g. Figure IV-10a-b). Secondary sedimentation decreases the activity on the backthrust in the internal area F1 in comparison to model 1. Strain starts to accumulate at 12.8 Myr at the future location of a new frontal thrust that will become efficient at 13.6 Myr (Figure IV-10b-c, f-g). At that time, F2 is completely deactivated. Deformation in the internal basement wedge localizes on a long pro-vergent thrust and the décollement level accommodates practically all the shortening. From 13.6 Myr there is a change in distribution of shortening; only the new frontal thrust accommodates displacement, the other shear zones are much less active. The internal zone is only deforming below the décollement level, with small conjugated shears that are equally spaced (e.g. Figure IV-10c and IV-10g). At 14.2 Myr, the new frontal thrust still accommodates most of the displacement, but shear zones F2, F3 and F4 and the internal zone are reactivated as well. The main difference with model 1 without secondary sedimentation is that the backthrust, F1 (the main locus of additional sedimentation) is completely deactivated.



| Model | $h(0)$ (km) | $h(inf)$ (km) | $x(0)$ (km) | length (km) | $v(prog)$ (cm.yr-1) |
|-------|-------------|---------------|-------------|-------------|---------------------|
| 2 | 6.5 | 2.05 | 40 | 20 | 0.5 |
| 3 | 6.5 | 2.05 | 40 | 45 | 0.5 |
| 4 | 6.5 | 2.05 | 40 | 70 | 0.5 |
| 5 | 7.5 | 2.05 | 40 | 40 | 0.5 |

Table IV - 3. Sedimentary wedge characteristics for models 2 to 5 presented in the following section, position of the corresponding parameters presented in the Figure above.

Low elevation, moderate extent (model 3)

In model 3 the prograding wedge has the same low elevation as in model 2 but an intermediate horizontal extent covering thrusts F1 and F2 initially and F3 after progradation at $t=14$ Ma (Table IV-2). The model behavior at 12.2 Myr is very similar to that of model 2, with the most of the deformation distributed between the front and the internal part of the wedge (e.g. Figure IV-11a and IV-11e). The only difference is that F2 is completely inactive in this model, as it is completely covered by the prograding wedge, while thrusts F3 and F4 are only partially covered. The model behavior at 12.8 Myr is also quite close to that of model 2, but the accumulation of strain in the frontal part of the wedge is more efficient, showing a faster activation of the new frontal thrust as compared to model 2 (Figure IV-11b and IV-11f). At 13.6 Myr model 3 exhibits uniform strain distribution over the entire wedge with all shear zones being moderately active (Figure IV-11c and IV-11g). Most of the strain is at this stage accumulated on the frontal and the most internal thrusts, and displacement is once again localized on the décollement level and the frontal thrust. The strain rate at 13.6 Myr (Figure IV-11g) also shows the delimitation of the secondary sediments, with propagation of deformation from material II through the secondary sediments. The basement below the middle décollement is intensively deformed by conjugated thrusts that are preferentially pro-verging. Finally, at 14.2 Myr, F2 becomes inactive, the internal zone is reactivated and most deformation is accommodated on shear zone F1 and the décollement (e.g. Figure IV-11d and IV-11h).

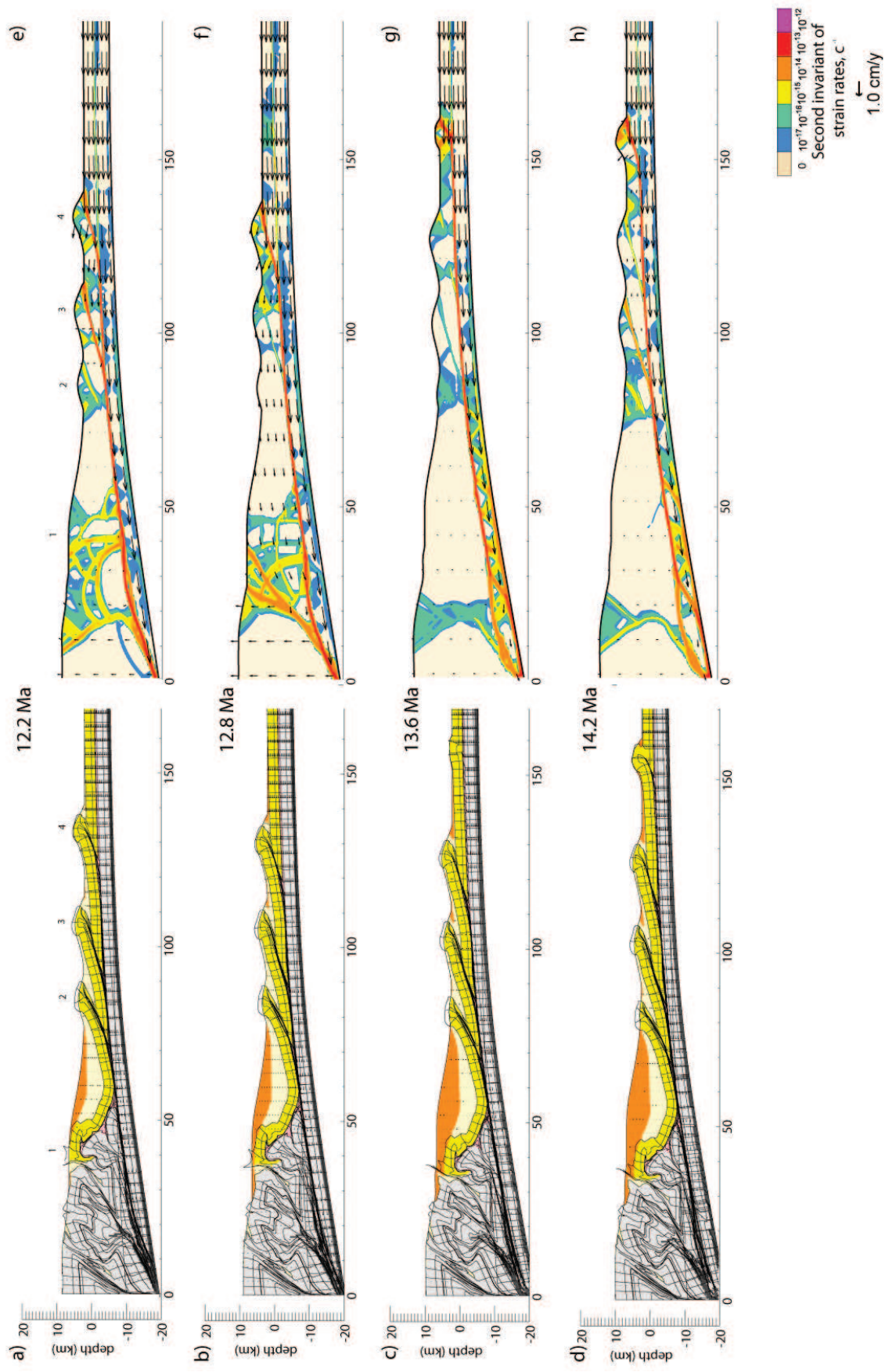


Figure IV - 10. Model 2 evolution from 12.2 to 14.2 Myr, same legend as in Figure IV-9.

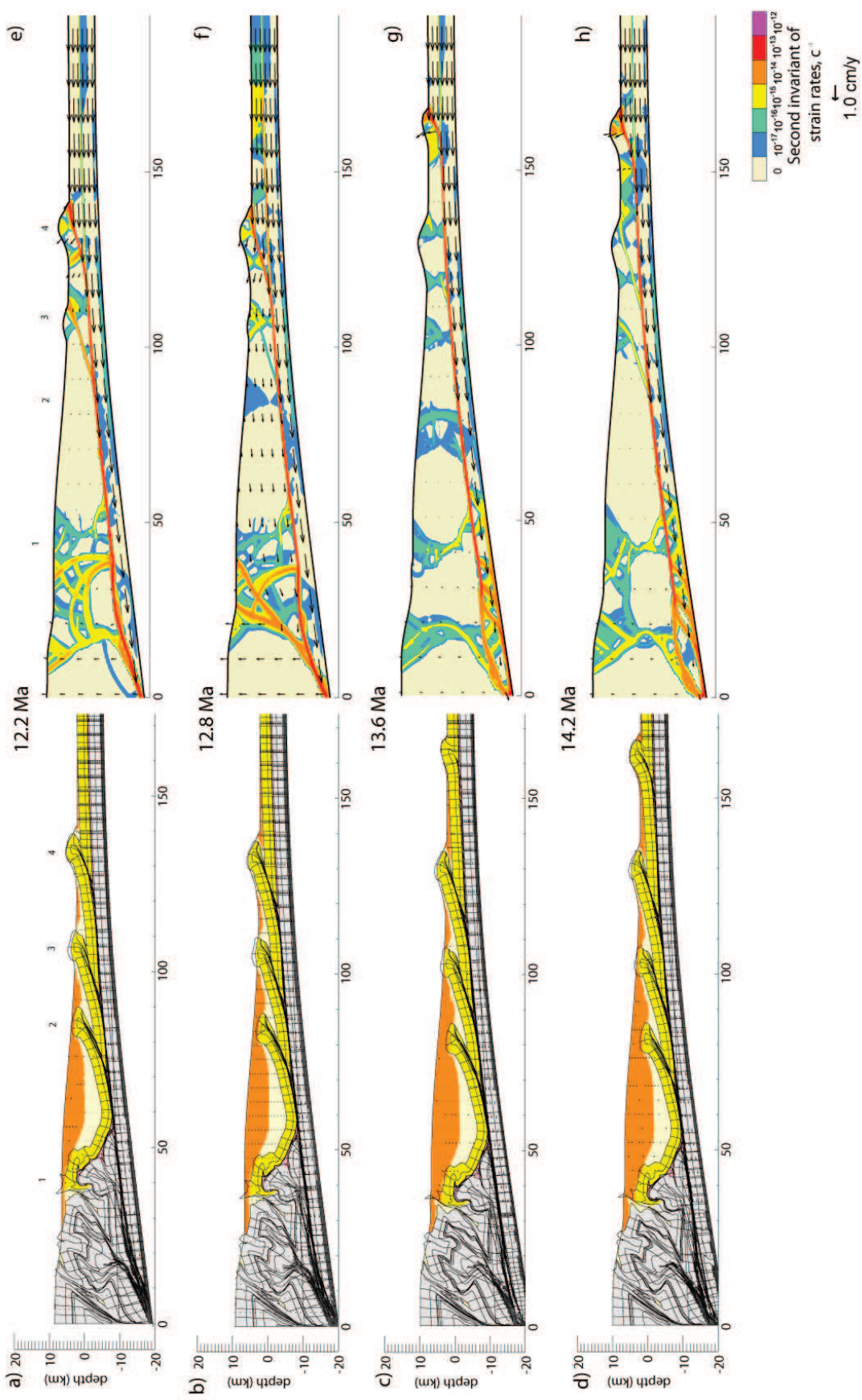


Figure IV - 11. Model 3 evolution from 12.2 to 14.2 Myr, same legend as in Figure IV-9.

Low elevation, long extent (model 4)

At 12.2 Myr, thrust F4 takes up most of the deformation. At the same time the new frontal thrust is starting to form as shown by the strain accumulation in the foreland (e.g. Figure IV-12a and IV-12e). Similar to models 2 and 3, the deformation is distributed between the frontal part of the wedge and the internal zones. F2 is completely covered by sediments and inactive at this stage. Between 12.8 and 13.6 Myr, most strain is accumulating on the new frontal thrust and in the internal area, thrust F3 is somewhat reactivated, and F4 is abandoned (Figure IV-12b and IV-12f). Finally, at 14.2 Myr, there is still small to moderate activity on all the faults but most of the shortening is localizing on the frontal thrust and a new frontal thrust is initiating (Figure IV-12d and IV-12h).

High elevation, moderate extent (model 5)

Model 5 (Figure IV-3) has the same prograding wedge extent as model 3 but a larger thickness providing a larger load in the internal area (Table IV-2). The top of the prograding wedge is 1.2 km higher than in models 2-4. This model is designed to test the consequences of aggrading conglomerates on the southern flank of the Axial Zone. Even if the sediments cover some faults of the Axial Zone in this set up, there are almost no differences in activity of these faults compared to model 3. Initiation of a new frontal thrust takes place at 12.8 Myr, no deformation is accommodated by F1. The subsequent evolution at 13.6 and 14.2 Myr is almost the same as in model 3, with the main activity on the frontal thrust and the Axial Zone thrusts and some distributed deformation on the other thrusts. The main difference with model 3 is that F4 continues to be active during the entire interval from 12-14 Myr.

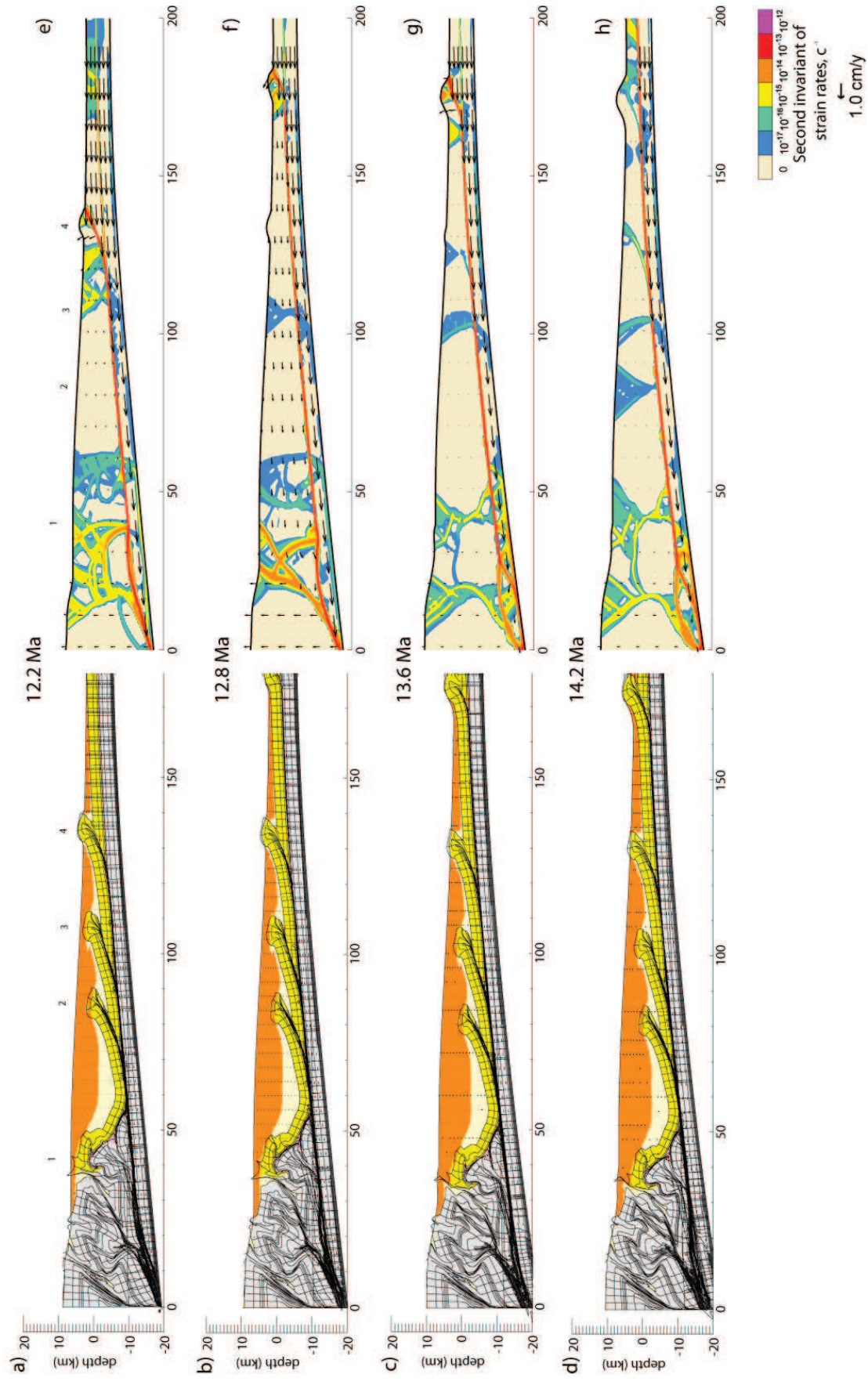


Figure IV - 12. Model 4 evolution from 12.2 to 14.2 Myr, same legend as in Figure IV-9.

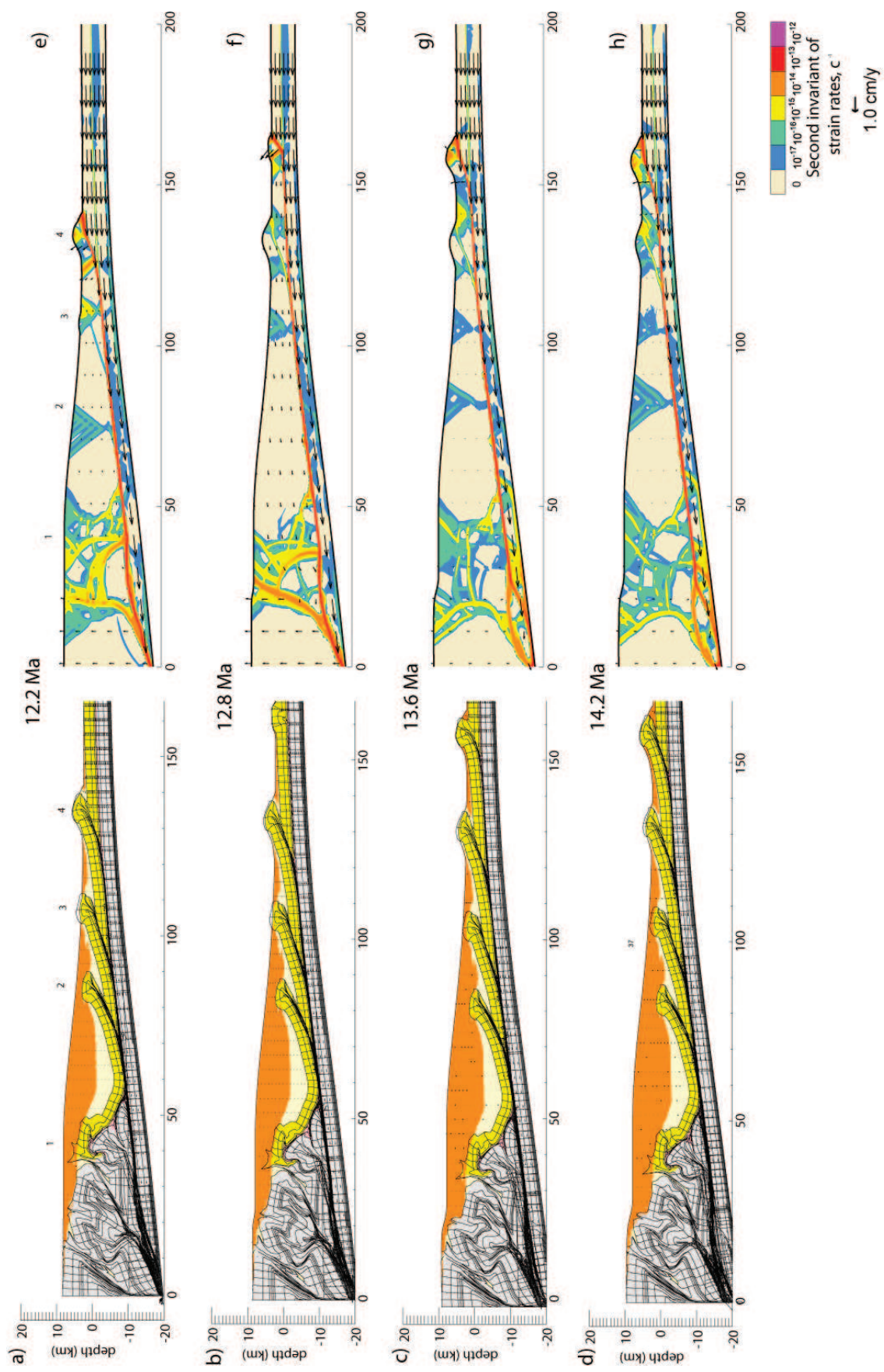


Figure IV - 13. Model 5 evolution from 12.2 to 14.2 Myr, same legend as in Figure IV-9.

IV-2.5 Interpretations and discussion

IV-2.5a Effects of secondary sedimentation on the thrusting sequence

The sequence of fault activation for the above models described is summarized in Figure IV-14. The model without secondary sedimentation shows a complex thrusting sequence with deformation cycling between in sequence frontal thrusting and wedge accretion, out of sequence thrusting in the internal area, and distributed deformation on the intermediate thrusts. A 2-step accretionary cycle is recognized. First, the wedge thickens with activity concentrated on the internal faults and on the backthrust; secondly, it propagates towards the foreland with the activation of a new frontal thrust. This sequence is very similar to the pro-wedge frontal accretion cycle described by Hoth et al (2007b) in their analogue modeling of a doubly-vergent orogen. In details, this complex thrusting sequence illustrates that accretion and wedge propagation require a complex deformational sequence activity. This inherent variability in the tectonic signal of frontal accretion and wedge thickening was also recognized by Naylor and Sinclair (2007) and occurs without perturbing the system with external processes.

The results from models with additional syn-tectonic secondary sedimentation show that the thrusting sequence is actually simplified by reducing the activity of several thrust in the center of the fold-and-thrust belt. Deformation in the most internal domain is similar for the various models run; the internal thrusts are always active although the details of strain localization differ. The models with the same extent but with different elevation of the secondary prograding sedimentary wedge (models 3 and 5) exhibit the same pattern of deformation for the most internal thrusts. Increasing the thickness of syn-tectonic sedimentation reduces the activity of the backthrust, showing that the activity is transferred from the most internal to the external thrusts to accommodate the addition of sediments. However, it should be noted that the internal thrusts are also very close to the left-hand side border and therefore probably influenced by the effect of the backstop.

Toward the foreland, the prograding wedge reduces deformation of the thrusts it covers in the piggy-back basin area; the stabilizing effect of the wedge appears proportional to the extent and thickness of sediments. As shown in Figure IV-14, this area of limited deformation (called “stable domain”) increases with extending sedimentation. However, in most cases, it does not mean that the thrusts are totally deactivated, as it was observed in the minimum work models of Hardy et al. (1998).

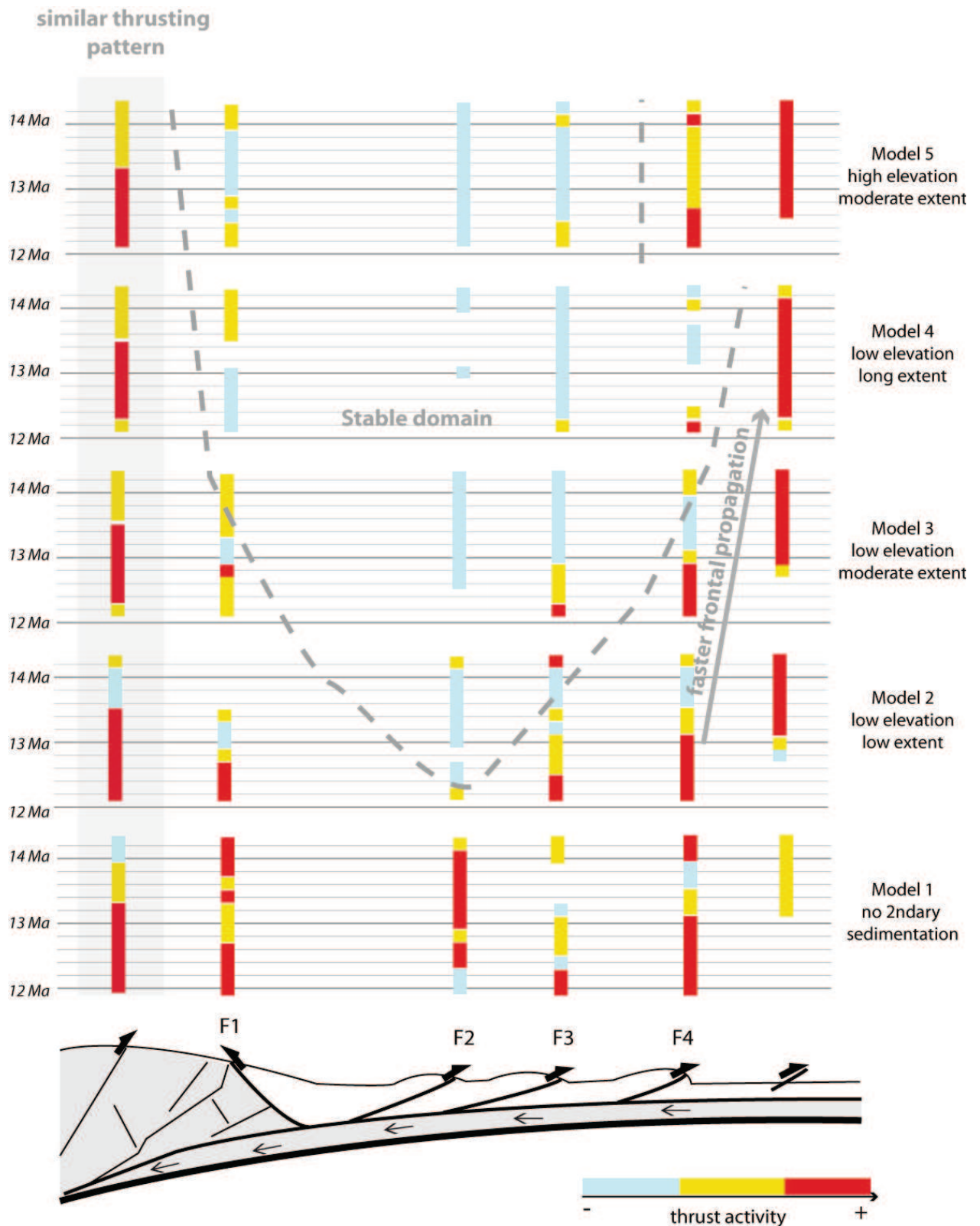


Figure IV - 14. Summary of the thrusting sequence of the models 1-5 presented in Figures IV-9 to IV-13. Thrust activity color code was simplified from the strain rate legend of the previous figures. Grey annotations are the Main interpretations.

Hardy et al. (1998) observed from 2D-kinematic-mechanical modeling that sedimentation, by increasing the frictional work on faults can “blanket” them. Our model results suggest that covering a thrust does not systematically lead to stopping its activity; this only happens in the models when 1) the thickness of sediments is large; 2) the thrust has just been covered by the sediments, in which case it is deactivated for a relatively short time interval of 0.2-0.4 Myr. In detail, the models indicate that during or after a thrust has been covered, strain will again localize on the thrust, which will also penetrate through the syn-tectonic sediments, as shown for instance by the conjugated faults patterns of model 5 at 70 km from the backstop at 14.2 Myr.

Finally, by reducing the activity of internal thrusts, the addition of secondary sedimentation favors frontal accretion; the further the secondary sedimentary wedge extends, the faster a new frontal thrust will activate. Models 1, 2, 3, and 4 with an increasingly extend of the secondary wedge show progressively earlier frontal thrust activation (e.g at 14.4, 13.2, 13 and 12.4 Myr respectively). The new thrusts also propagate further following the secondary sedimentation, with a locus at 145, 160, 165, and 180 km for the models with increasing extent of sediments. This last observation is in agreement with the conclusions of the previous chapter, showing that the thrust sheet length is controlled by the extent of syn-tectonic sedimentation.

The evolution of an orogen has been explained by several authors as following critical wedge behavior (Chapple 1978; Boyer and Elliott 1982; Davis et al. 1983; Dahlen et al. 1984; Boyer 1995). Following this theory, the wedge thickens by accommodating the convergence, until it attains a critical state (cf introduction). This state is defined by a critical value of the taper angle, the sum of topographic and basal slope, and by the internal and basal strength. Upon reaching the critical state, further addition of material to the wedge allows it to grow self similarly with deformation propagating towards the foreland by creating a new frontal thrust. As described in the previous section, this behavior is well reproduced by model 1 without secondary sedimentation (previous chapter). In the other models, we impose a secondary sedimentation geometry that is controlled at each timestep; however, the results from these models seem to follow a first-order critical behavior as well. By adding wedge-top sediments the load increases and consequently the flexure and the β angle. Therefore, critical state is reached earlier and the frontal accretion is favored.

IV-2.5b Comparison to the Pyrenees

From the studies presented in the previous sections (part III), we have evidence for a significant burial of the southern Pyrenean fold-and-thrust belt by late syn-orogenic conglomerates. Analysis of mechanical model results presented here suggests that the addition of this secondary sedimentation may have affected the thrusting sequence to different degrees, depending on the extent and elevation of the sedimentary deposits. Previous authors (Capote et al. 2002; Sinclair et al. 2005) note that the southern Pyrenean wedge thrusting sequence exhibited out-of-sequence

thrusting and reactivation of existing thrusts. The apatite (U-Th)/He measurements published by Gibson et al. (2007) are one of the main arguments for out of sequence deformation. These data indicate AHe ages of 15.9, 13.8, and 10.5 Myr on samples collected in the Barruera Massif, to the Southwest of the Maladeta Massif. These ages were interpreted (Gibson et al., 2007) as the “final pulses of activity” inherent to the natural wedge evolution as also proposed by Naylor and Sinclair 2007. From our modeling, we have shown (e.g. Figure IV-14) that the addition of secondary wedge-top sedimentation could effectively enhance the activity in the internal zone. Models 3, 4 and 5, indicate that the larger the extent and thickness of secondary sedimentation, the more deformation localizes in the internal zone. Despite this analogy, it is worth noting that we model here only one side of the orogen with plastic deformation only. Therefore, interpreting deformation of the internal part should be done with caution.

The other main expression of perturbation of the thrusting sequence is provided by field observations of deformation of the Oligocene conglomerates. As described in section IV-2.2b, deformation of the conglomerates is visible in the footwall of the Boixols thrust and also in the Sierras Marginales thrust sheet, close to the Montsec (Meigs et al. 1996). In our models, the Boixols thrust (compared to F2) exhibits moderate activity only following the addition of secondary sediments and we do not observe preferential reactivation of F2 as suggested by the data. Nevertheless as pointed out before, this does not necessarily mean that the thrust was totally deactivated. We indeed see some indications of strain concentration on this shear zone, even if it was covered by an important thickness of sediments. We also see evidence that deformation propagating through the secondary sediments. Finally, late deformation of the Sierras Marginales is to first order compatible with our modeling results. Whatever the thickness and extent of sediments is, the frontal area (F4 and frontal thrust) remain active during and after secondary deposition.

IV-2.5c Climatic triggering of the erosional pulse? Preliminary results

The deposition of a large amount of conglomerates during the late Eocene to Oligocene implies significant erosion of the Axial Zone during this time interval. Consequently we can ask the question what mechanism drives this important erosion (tectonics, climate, or both). In the Pyrenees, Huyghe et al. (2009) argue for a climatic control on the late Eocene exhumation, by summing the erosional and the accretionary fluxes through time, and showing that there was no increase in tectonic flux. They concluded that a major climate change such as the Eocene-Oligocene transition (Zachos et al. 2001) is more likely to explain the increase in erosional flux in the southern Axial Zone. This climatic transition has been associated by several authors to an increase in seasonality; which could lead to a more efficient erosion (Molnar 2004).

We present here the results of modeling an erosional pulse applied to the model 3 set-up (moderate extent and a low reference level of sedimentation), the resulting model (Model 6) is compared to

model 3 in Figure IV-15. By keeping the convergence rate the same and activating erosion at 10 Myr, we aim to reproduce a climatic forcing. Erosion starts at 10 Myr, and secondary sedimentation starts at 12 Myr, as in the other models. Erosion is proportional to the surface slope with a rate of 1 mm.yr^{-1} for a 45° slope.

Three Main differences can be observed between the model 3 and 6:

- 1) The frontal accretion occurs faster. In model 6, at 10 Myr, strain concentrates around 150 km, leading to activate the new frontal thrust 1 Myr earlier than in model 3. This pattern is reproduced at 13 Myr.
- 2) Reactivation of F4 is favored in model 6. At 12 Myr, and at 14 Myr, the thrust just behind the frontal thrust is very active and accommodates most of the deformation.
- 3) Appearance of stacking patterns in the internal units. From 11 Myr, strain localizes on curved faults that grow vertically.

These preliminary results show a thrusting sequence that is not very different from the models with secondary sedimentation only, and so could fit the thrusting sequence of the southern Pyrenees. The addition of erosion effectively reduces the taper and size of the wedge and therefore promotes thrusting in a more proximal position at F4 rather than allowing the wedge to grow and form a new thrust at F5. As mass removal by erosion is more efficient in the internal zone more mass is accreted to the base in this area. We also observe a stacking geometry in the internal zone that could be compared to the uplift mode of the Orri and Rialp units, exhumed from the early Eocene to late Oligocene.

This additional model has several limitations. Most notably, the surface processes are not mass conserving and the deformation is only plastic, rendering a direct comparison with the Pyrenean evolution less straightforward. Nevertheless, these observations are an interesting starting point for discriminating between a tectonic or a climatic trigger for the rapid late orogenic exhumation of the southern Pyrenees.

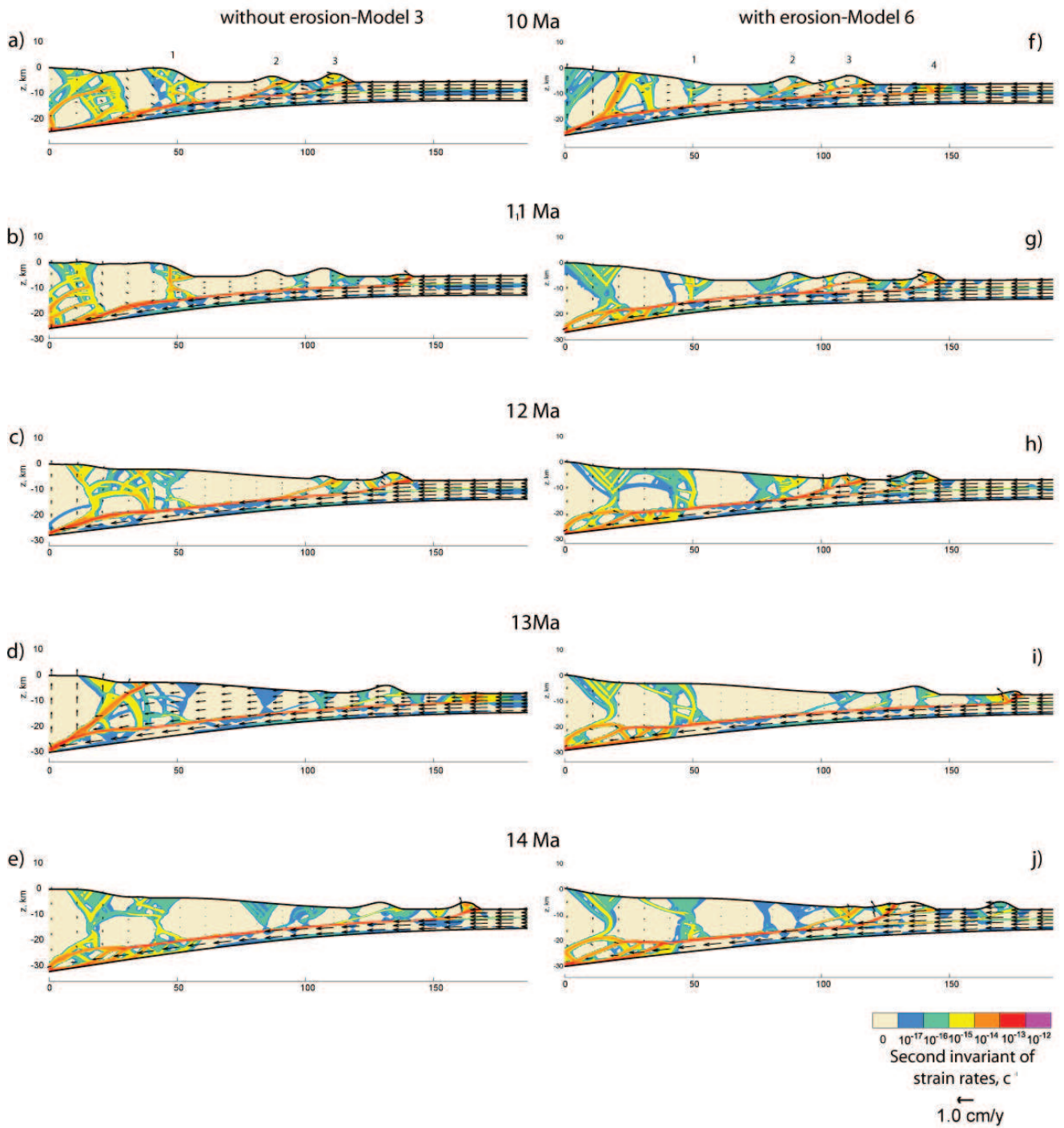


Figure IV - 15. left panel: Strain rate evolution from 10 Myr to 14 Myr for Model 3 (Figure IV-11). Right panel: strain rate evolution for model 6, equivalent to Model 3 but with slope-dependent erosion starting at 10 Myr.

IV-2.6 Conclusions

The southern Pyrenean wedge experienced an episode of strong erosion in late Eocene-Oligocene times, which produced a significant amount of sediments in the adjacent southern foreland basin, deposited as a thick series of conglomerates. The thickness of these sediments has been estimated at more than 2 km (part III), covering part of the southern fold-and thrust belt, while it was still actively deforming. Using a 2D mechanical model, we have studied what the effects of addition of these conglomeratic sediments may have been on the late stage evolution of the southern Pyrenean foreland. By modifying the wedge geometry, the secondary sedimentation affects the thrusting sequence, stabilizing the central part of the fold and thrust belt where the sediments are deposited, and favoring frontal accretion. The different geometries of the secondary sedimentary body that have been tested here show that even an extended and important sedimentation can reproduce the patterns of deformations in the southern Pyrenees, such as reactivation and out-of-sequence thrusting highlighted by several authors. The addition of erosion in the axial zone (e.g. model 6) show that 1) vertical stacking of the Axial Zone units could result from erosion rather than driving it, and 2) an increase in erosional efficiency related to a climatic change could be responsible for the strong exhumation of the southern Pyrenees during late Eocene-Oligocene times, however this hypothesis needs further investigation.

Additional runs

The models presented in the previous chapters (IV-1 and IV-2) are the result of a complete parameter study that I performed at the University of Bergen. In order to understand the model behavior and the control of each parameter on the wedge development, I first analyzed model results for varying material rheological behavior (by modifying the internal friction angle Φ) and varying flexural rigidity as well (see Table IV-4). A selection of the more representative model runs is thus presented in this section to illustrate the main characteristics of the wedge development when changing parameters. The Figures IV-16 to IV-19 illustrate the study on the effect of variable Φ for the materials I,II ,and III for weak or strong rheology; only the material IV was not tested. The surface processes were deactivated for these tests. Although the final set of parameter properties used in the previous model was chosen to correspond to the parameters used by Stockmal et al. (2007), we know from this parameter study what are the effects of the variations in Φ for each materials, and so can be more confident in interpreting our model runs.

The last two models runs (Figures IV-20 and IV-21) are showing results for changing the flexural rigidity with syn-tectonic sedimentation depositing at similar base-level (2.05 km). Snapshot of these models were already presented in the model results section of chapter IV-I. For comparison, all the models presented previously were preformed with an intermediate flexural rigidity of 1.10^{22} N.m⁻¹. From the model runs presented here, we see that the flexural rigidity is a first-order controlling parameter on the wedge shape and development, acting directly on the depth and extend of the foreland basin (see chapter IV-I for further discussion).

| Model number | Material I (Φ , °) | Material II (Φ , °) | Material III (Φ , °) | Flexural rigidity (D, N.m ⁻¹) |
|--------------|-----------------------------|------------------------------|-------------------------------|--|
| Sopen65 | 38-18 | 38-18 | 1 | 1.10^{22} |
| Sopen66 | 38-18 | 38-25 | 1 | 1.10^{22} |
| Sopen67 | 38-25 | 38-25 | 1 | 1.10^{22} |
| Sopen75S | 38-18 | 38-25 | 3.5 | 1.10^{22} |
| Sopen90_f21 | 38-18 | 38-25 | 1 | 1.10^{21} |
| Sopen90_f23 | 38-18 | 38-25 | 1 | 1.10^{23} |

Table IV - 4 Summary of the parameters changed in the additional runs presented in the following.

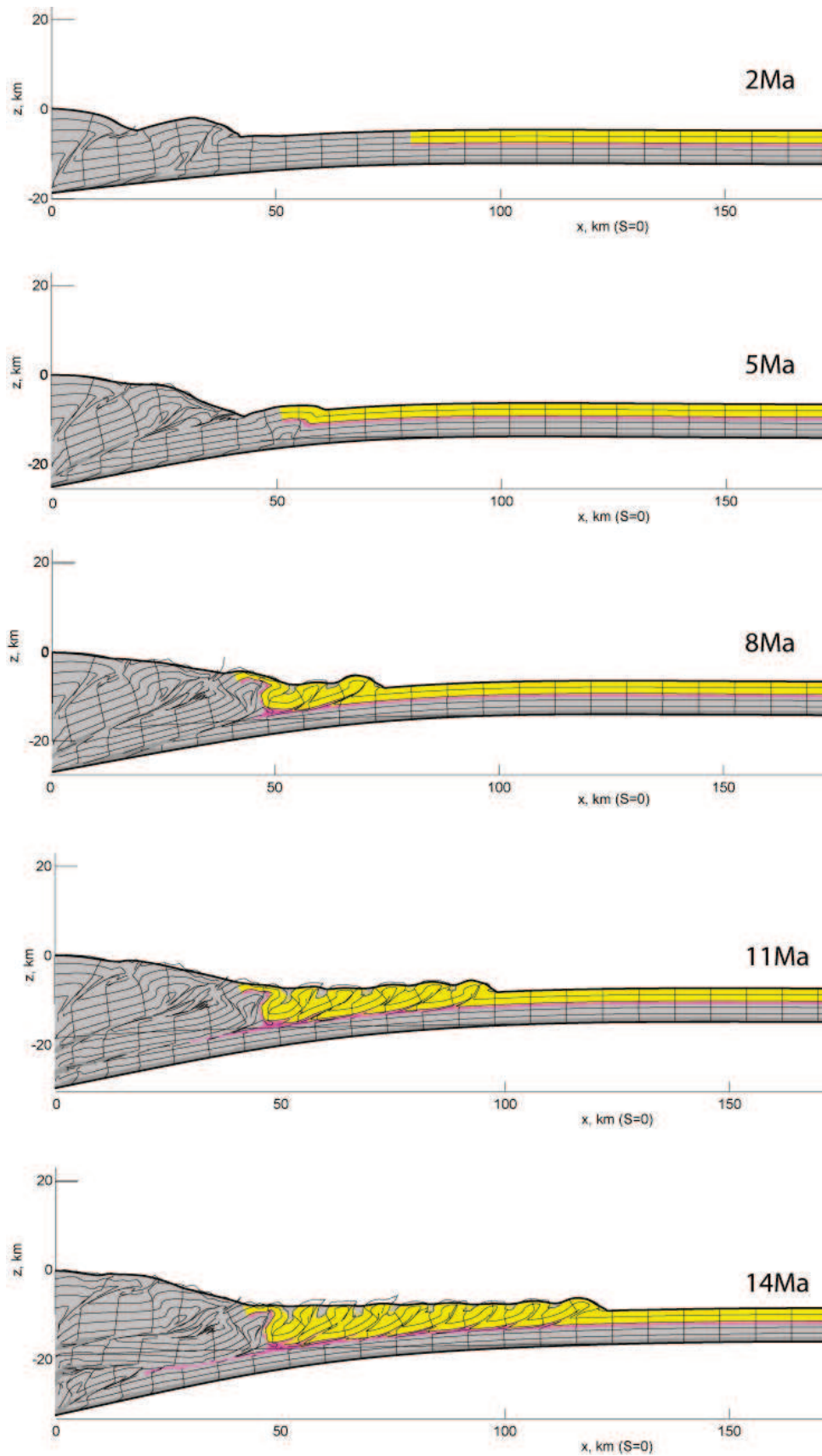


Figure IV - 16sopen65. Material I : $\Phi=38-18$; Material II : $\Phi=38-18$; Material III : $\Phi=1$. To be compared to sopen 67 for the effect of a stronger Material I. More shortening is accommodated on the basement thrust, creating longer thrusts (nappes).

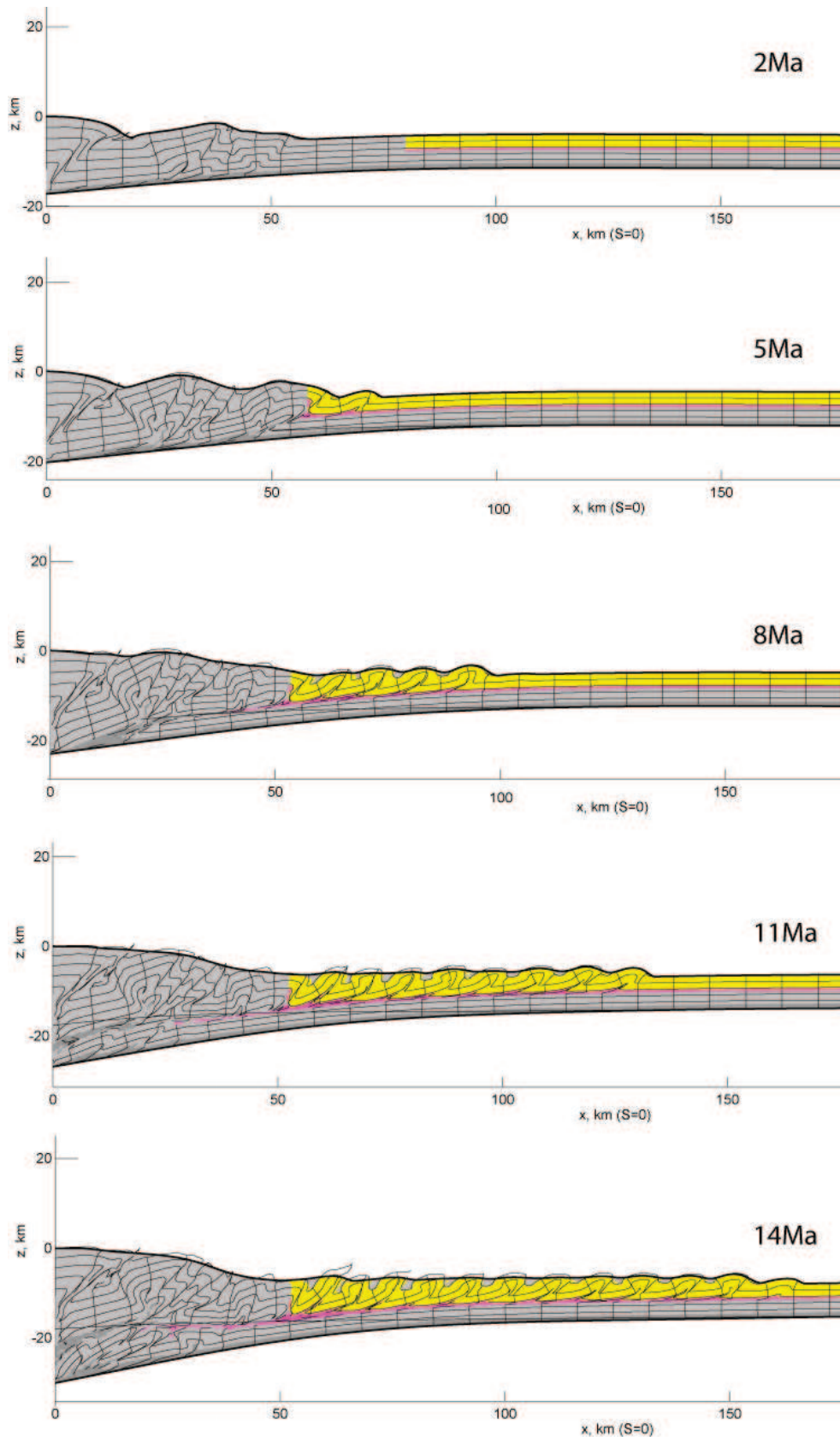


Figure IV - 17 sopen66 Material I : $\Phi=38-18$; Material II : $\Phi=38-25$; Material III : $\Phi=1$
 To be compared to sopen 67 for the effect of a stronger Material II. A stronger mat.II lead to propagate slightly further the thrust sheets.

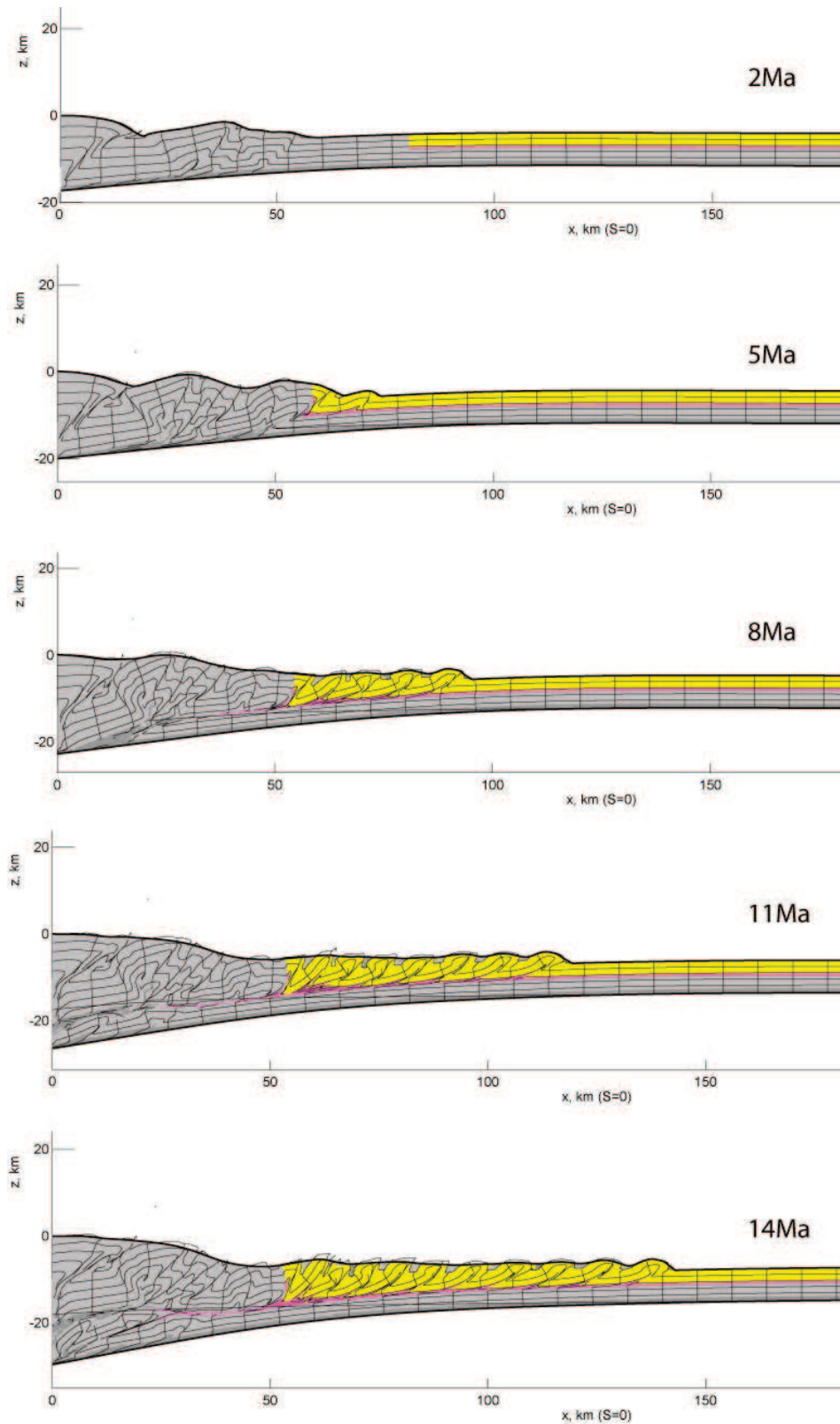


Figure IV - 18 sopen67 Material I : $\Phi=38-25$; Material II : $\Phi=38-25$; Material III : $\Phi=1$. To be compared to sopen 65 and 66 for the effect of a weaker Material I and II respectively; and to sopen75S for the effect of a weaker décollement level. A stronger mat.I mainly favors pop-up style deformation in the internal part.

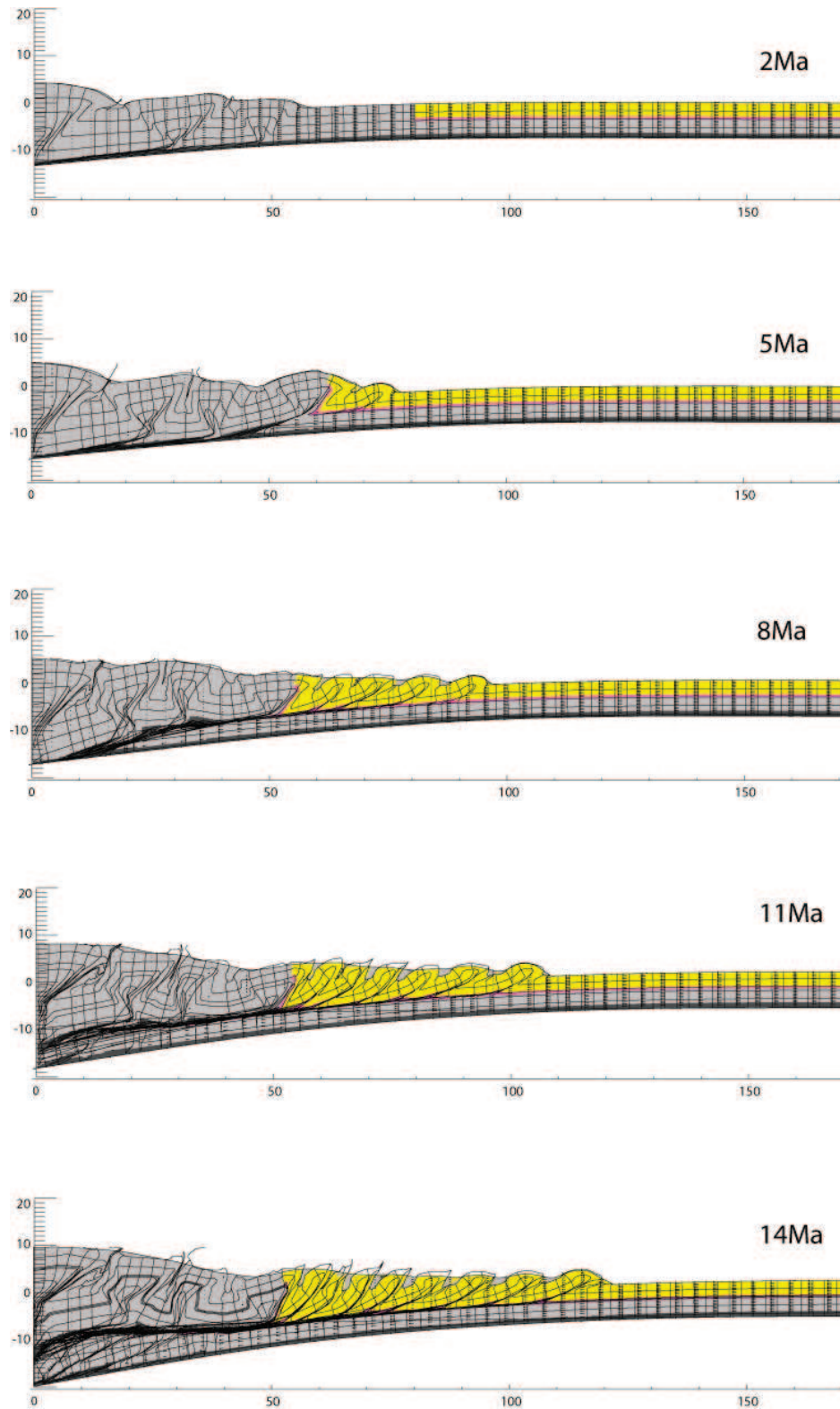


Figure IV - 19. *sopen75S. Material I : $\Phi=38-18$; Material II : $\Phi=38-25$; Material III : $\Phi=3.5$. To be compared to sopen67 for the effect of a stronger décollement level. With a stronger décollement level, the thrusts are activating closer to the internal wedge .*

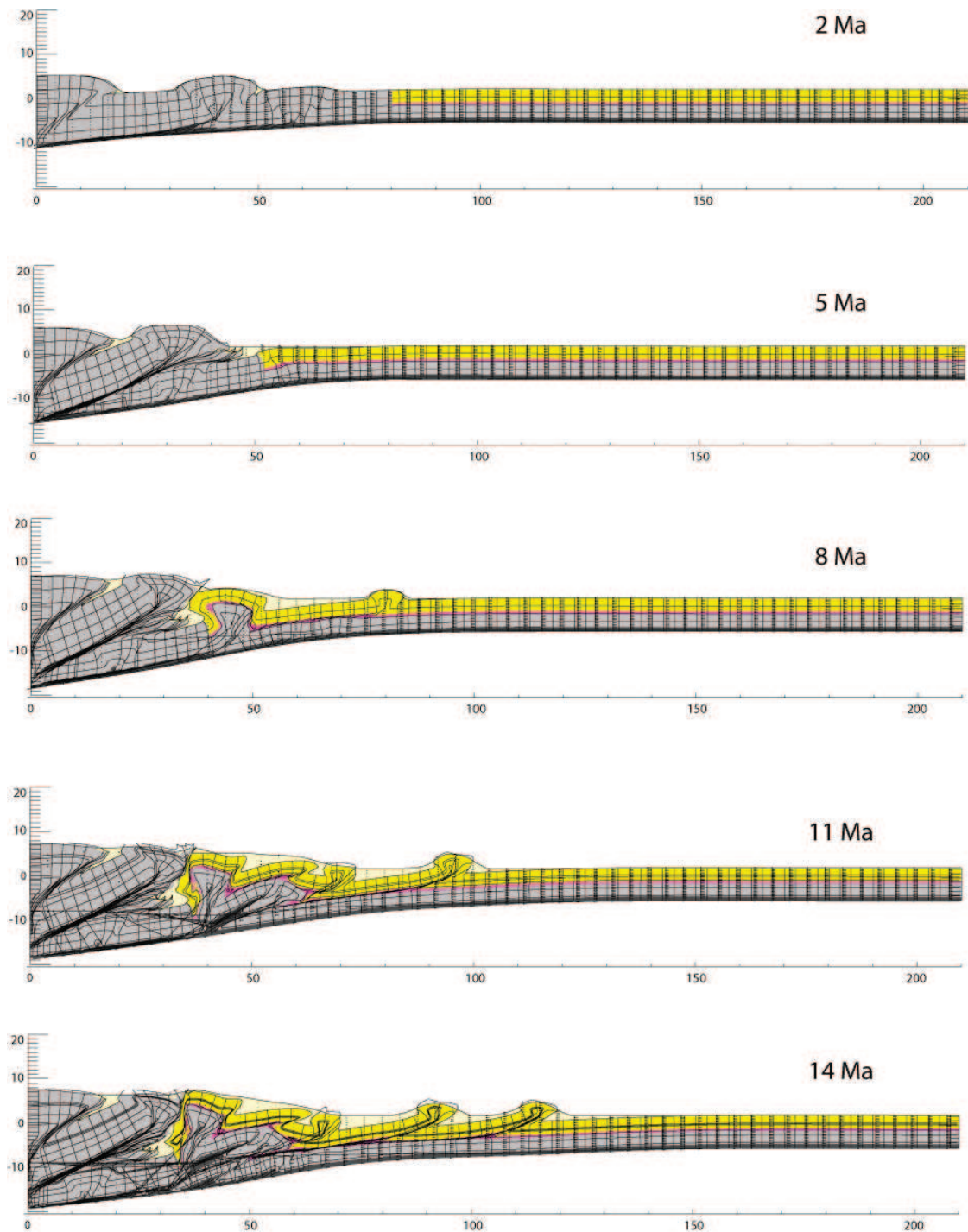


Figure IV - 20 *sopen90_f21*. Material I : $\Phi=38-18$; Material II : $\Phi=38-25$; Material III : $\Phi=1$. Flexural Rigidity: $D=1.10^{21} \text{ N.m}^{-1}$. To be compared to *sopen90_f23* for the effect of changing the flexural rigidity.

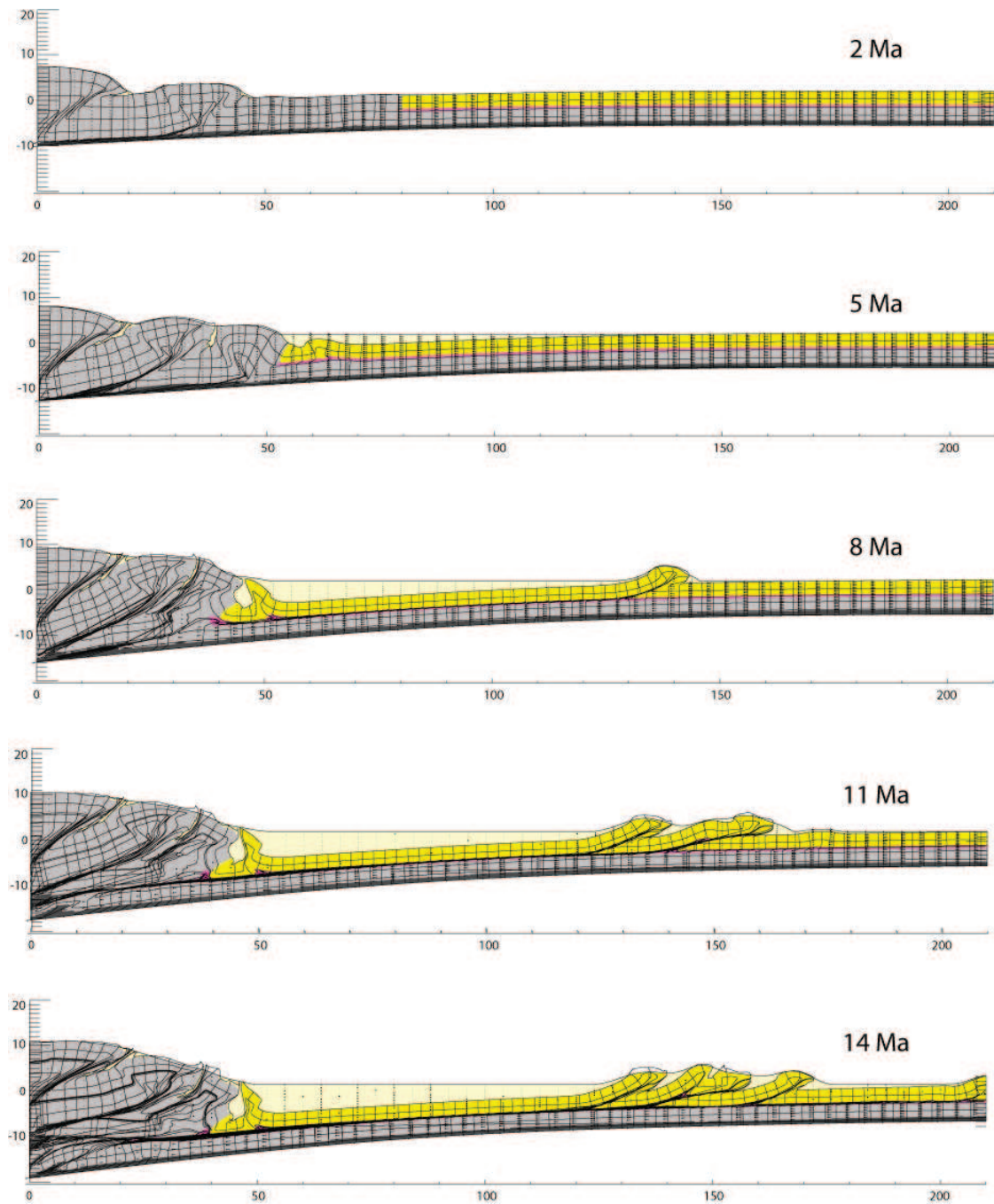


Figure IV - 21 *sopen90_f23*. Material I : $\Phi=38-18$; Material II : $\Phi=38-25$; Material III : $\Phi=1$. Flexural Rigidity: $D=1.10^{23} \text{ N.m}^{-1}$. To be compared to *sopen90_f21* for the effect of changing the flexural rigidity.

Part V - Synthesis and Outlook

By combining low-temperature thermochronology with different types of modeling, I have aimed to better constrain the lateral variability in exhumation of the Pyrenean-cantabrian mountain belt, as well as identify the feedbacks between the range and its foreland basins.

The different studies on both the central Pyrenees and the central Cantabrian Mountains presented in this manuscript lead me to focus particularly on the Eocene to Miocene times, when exhumation of the range and the erosion were important, combined to changes in drainage conditions from exorheic to endorheic in both the Duero and the Ebro basin. We can thus precise the evolution of the two study area as follows (Figure V - 1):

During **Eocene times**, the central Pyrenean fold-and-thrust belt propagates by frontal accretion of thrusting units. I have shown in Chapter IV-1 that the amount and extent of syn-tectonic sedimentation was a major factor controlling the thrust sheet length, pattern that appears to be reproduced in several natural thin-skinned fold-and-thrust belts. In particular, the Pyrenean fold-and-thrust belt develops with an overall in-sequence pattern, with the activation of the Boixols thrust, the Montsec thrust and the associated piggy-back Tremp-Graus basin, and finally the Sierras Marginales frontal thrust.

In **Bartonian times** (40-37 Ma), exhumation is moderate in the central Axial Zone with exhumation rates of 1 mm.yr^{-1} , derived from the thermo-kinematic modeling of the low-temperature thermochronological data (Chapter III-1).

At the same time, in the Central Cantabrian Mountains, the onset of Alpine inversion is documented in the retro fold-and-thrust belt offshore (Alonso et al. 1996; Alvarez-Marron et al. 1997), and highlighted by our new (U-Th)/He ages of zircons onshore. The ages of 37 and 39 Ma were measured in the center of the central section, south of the Cabuerniga fault (Part II).

Finally, in late Eocene times, the Ebro basin became endorheic (Costa et al. 2009) due to the closure of its connection to the Atlantic, while the Duero basin is already closed from the Paleocene onward (Santisteban et al. 1996).

The **Eocene-Oligocene transition** is marked by a pulse of erosion in the central Axial Zone of which the causes are still debated. In Chapter IV-2 I showed preliminary results in favor of a climatic control on this enhanced erosion; however this hypothesis needs to be confirmed by a more elaborated study.

In **Oligocene times**, I documented evidence for the continuation of Alpine deformation in the central Cantabrian Mountains. Several apatite fission track ages in the center of the Cantabrian section are Oligocene (30Ma and 27 Ma). While the central part of the range is still active, the erosion products are accumulating in the Northern margin of the Duero basin, developing a progressive unconformity along the range front.

In the central Pyrenees, exhumation rates strongly decreased to 0.02 km Myr^{-1} from 30 Ma to the present, indicating a rapid transition to stable post-orogenic conditions, possibly aided by partial burial of the range under its own erosional products.

By the end of the syn-orogenic phase at 30 Ma, the south Pyrenean valleys were infilled by erosional products up to an elevation of 2.6 km and this valley-fill remained stable until $\sim 9 \text{ Ma}$.

From (U-Th)/He measurements on apatites of the Southern foreland fold-and-thrust belt, we could extend these conclusions to the foreland. We thus extrapolated the thickness of the conglomeratic deposits of $\sim 2 \text{ km}$ until the south of the Montsec area, in the Ager basin, suggesting an extension of the paleogeographic location of the fluvial system.

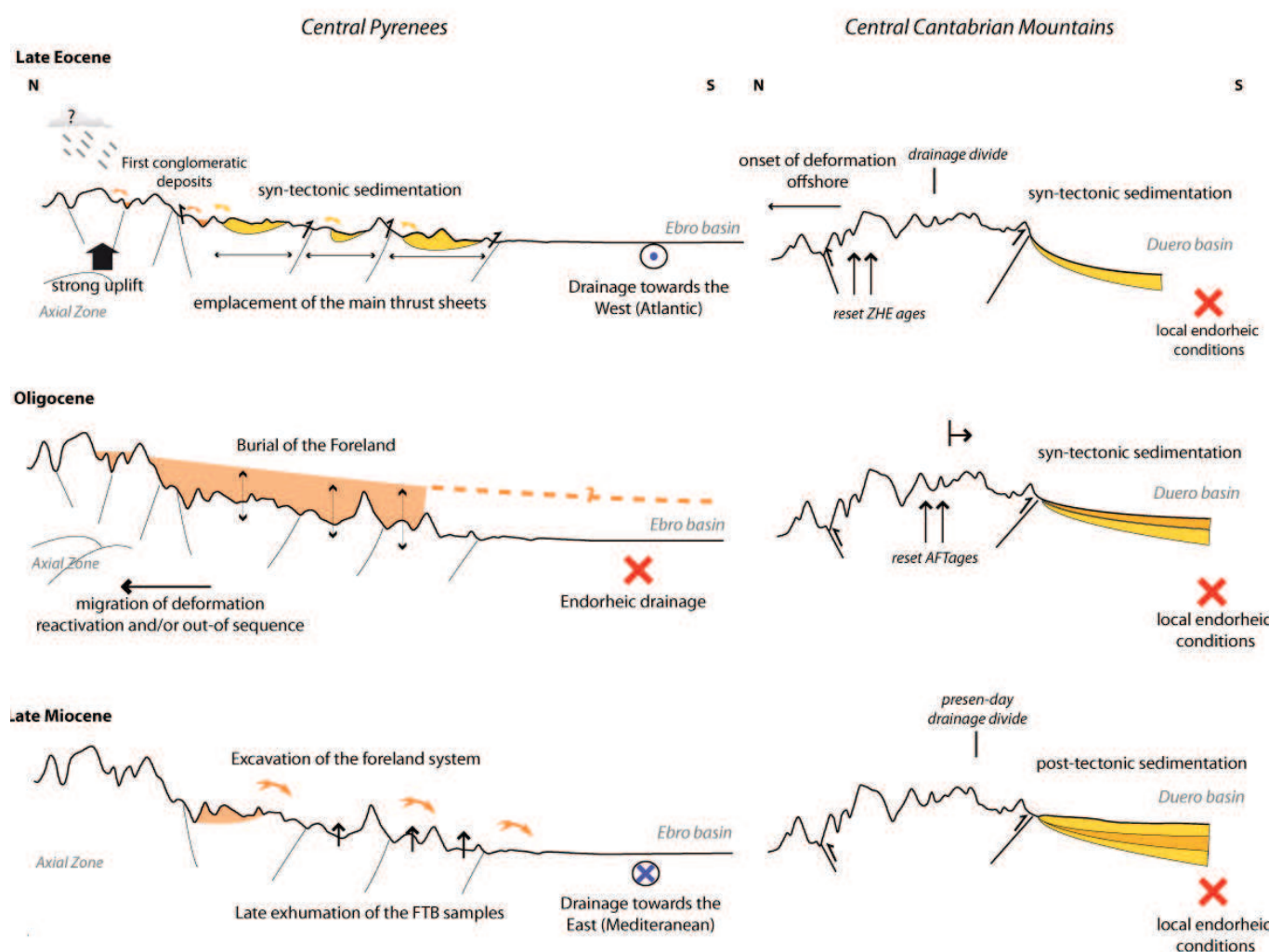


Figure V - 1 Summary of the main conclusions from this PhD work. Comparison of the Central Pyrenees and Central Cantabrians through time. The topographies have been modified from the present-day topography. This schematic representation is not to scale.

Consequences of this important burial on the thrusting sequence have been studied in Chapter IV-2. By modifying the wedge geometry, the secondary sedimentation perturbs the thrusting sequence, stabilizing the central part of the fold-and-thrust belt and promoting both frontal accretion and internal activity. The different geometries of the sedimentary body that have been tested inform us that even an extended and thick sedimentation can reproduce the patterns of deformations in the southern Pyrenees, such as reactivation and out-of-sequence thrusting highlighted by several authors (Gibson et al. 2007). However, such sedimentation does not promote out-of-sequence thrusting and the rapid erosion of the internal Axial Zone may be an important control.

Finally, both the thermo-kinematic modeling in the Axial Zone and the low-temperature data in the foreland predict an exhumation in **late Miocene times** (around 9 Ma). We interpret this exhumation as the consequence of the excavation of the Ebro basin, that unfilled the foreland and so exhumed the samples. We thus propose that the opening of the basin occurred at the latest during Tortonian times and that late-Neogene / Quaternary climate change had little effect on the post-orogenic erosional history of the Pyrenees.

To conclude, the approach combining thermochronology and numerical modeling allowed me to precise the Cenozoic evolution of the Pyrenean-Cantabrian mountain belt. The new thermochronological data from the Cantabrian Mountains, allow constraining the lateral variations in exhumation of the belt, from East to West. While the Pyrenees experienced a pulse of rapid exhumation in the late Eocene; exhumation starts in the Cantabrian Mountains. Then in Oligocene times, the central Pyrenees are mainly controlled by surface processes that led to the burial of the southern foreland. Simultaneously, the Cantabrian Mountains are still exhuming and deforming. Moreover, the constraints brought by the low-temperature thermochronological data allow us to refine the thickness of Mesozoic sediments that must have covered the Cantabrian Mountains and therefore the amount of inversion and the structure of the range.

The comparison of the evolution of the central Pyrenees and central Cantabrians also shows different patterns of control of syn-tectonic sedimentation and base-level changes on orogenic building. In the Pyrenees, I have shown that the Oligocene-Miocene burial and exhumation of the foreland and the Axial Zone can be interpreted in terms of surface processes. Therefore, the base-level of the Ebro strongly controlled the late evolution of the southern Pyrenees, and more generally, could influence the thrusting sequence when the amount of sediments is large enough. It is also interesting to compare the interactions between the range and its foreland in the Cantabrian Mountains. The present-day topography (Figure I-17) could effectively be comparable to the Oligocene topography of the Central Pyrenees.

But there are a few differences between the two areas. Firstly, the Cantabrian part of the belt does not present a wedge-top depozone and so the sediments directly deposit in the foredeep area. Secondly, the Cantabrian Mountains are of thick-skinned style whereas the Central Pyrenees are thin-skinned. Therefore, one can easily think that a more important amount of sediments will be needed to perturb the range growth, as we showed for the Southern Pyrenees. Finally, however the Duero basin is exorheic since Paleocene times and it has never been excavated as the Ebro basin did. Thus, with our dataset, we conclude that the influence of the Duero base-level on the Cantabrian range development is less than that of the Ebro basin for the Pyrenees. Yet, this interpretation may be challenged by combining our low-temperature ages with the AFT ages produced by Luis Barbero (University of Cadiz).

A few ideas for future work emerge from this PhD study; the Cantabrian Mountain area is the place where a lot of work still needs to be done.

For instance, the western central section still lacks low-temperature thermochronological ages. As the lithologies are very poor in apatites, more ZHe analyses could be performed.

From the central section, we are now working on an re-interpretation of the upper crustal structure, which could also change some patterns on the deeper structure; in particular, there is still a strong debate on the indenting lower crust under the Cantabrian Mountains. Moreover, numerical modeling could also document the evolution of this part of the belt, at the crustal scale, and also at shallower scale to test the influence of the Duero base-level on the Cantabrian deformation sequence.

In the Pyrenean part, the investigation of a climatic influence on the wedge development could be very interesting. However, the surface processes could not be correctly modeled through a 2-D model and 3-D will be needed to reproduce the fluvial and alluvial behavior.

References

- Alonso-Zarza, A. M. and J. P. Calvo (2000). "Palustrine sedimentation in an episodically subsiding basin: the Miocene of the northern Teruel Graben (Spain)." *Paleogeography, Paleoclimatology, Paleoecology* **160**: 1-21.
- Alonso, J. L., J. A. Pulgar, J. C. Garcia-Ramos and P. Barba (1996). Tertiary basins and Alpine tectonics in the Cantabrian Mountains (NW Spain). *Tertiary Basins of Spain: The Stratigraphic Record of Crustal Kinematics*. P. F. Friend and C. J. Dabrio. New York, Cambridge Univ. Press: 214– 227.
- Alvarez-Marron, J., A. Perez-Estaun, A. Danobeitia, J. A. Pulgar, J. R. Martinez Catalen, A. Marcos, F. Bastida, P. Ayarza Arribas, J. Aller, J. Gallart, F. Gonzalez-Lodeiro, E. Banda, M. C. Comas and D. Cordoba (1996). "Seismic structure of the northern continental margin of Spain from ESCIN deep seismic profiles." *Tectonophysics* **264**: 153-174.
- Alvarez-Marron, J., E. Rubio and M. Torne (1997). "Subduction-related structures in the North Iberian Margin." *Journal of Geophysical Research* **102**(B10): 22497-22511.
- Arche, A., G. Evans and E. Clavell (2010). "Some considerations on the initiation of the present SE Ebro river drainage system: Post- or pre-Messinian?" *Journal of Iberian Geology* **36**(1): 73-85.
- Arenas, C., J. I. Casanova and G. Pardo (1997). "Stable-isotope characterization of the Miocene lacustrine systems of Los Monegros (Ebro Basin, Spain): palaeogeographic and palaeoclimatic implications." *Palaeogeography, Palaeoclimatology, Palaeoecology* **128**(1-4): 133-155.
- Arenas, C. and G. Pardo (1999). "Latest Oligocene-Late Miocene lacustrine systems of the north-central part of the Ebro Basin (Spain): sedimentary facies model and palaeogeographic synthesis." *Palaeogeography, Palaeoclimatology, Palaeoecology* **151**(1-3): 127-148.
- Babault, J. (2004). Dynamique de l'érosion dans une chaîne de montagnes: Influence de la sédimentation de piedmont. L'exemple des Pyrénées. Rennes, Université de Rennes I. **PhD**: 218.
- Babault, J., S. Bonnet, A. Crave and J. Van Den Driessche (2005a). "Influence of piedmont sedimentation on erosion dynamics of an uplifting landscape: An experimental approach." *geology* **33**(4): 301–304.
- Babault, J., S. Bonnet, G. Ruiz and J. Van Den Driessche (2009). "A comment on 'Late- to post-orogenic exhumation of the Central Pyrenees revealed through combined thermochronological data and modelling' by M. Gibson, H. D. Sinclair, G. J. Lynn and F. M. Stuart." *Basin Research* **21**(1): 139-141.
- Babault, J., N. Loget, J. Van Den Driessche, S. Castelltort, S. Bonnet and P. Davy (2006). "Did the Ebro basin connect to the Mediterranean before the Messinian salinity crisis?" *Geomorphology* **81**(1-2): 155-165.
- Babault, J., J. Van Den Driessche, S. Bonnet, S. Castelltort and A. Crave (2005b). "Origin of the highly elevated Pyrenean peneplain." *Tectonics* **24**: TC2010, doi:10.1029/2004TC001697.
- Baby, P., R. Limachi, I. Moretti, E. Mendez, J. Oller, B. Guillier and M. Specht (1995). Petroleum system of the northern and central Bolivian sub-Andean zone. *Petroleum Basins of South America*. A.J. Tankard, R. Suarez and H. J. Welsink. **American Association of Petroleum Geologists Memoir**, **62**: 445-458.

- Baldwin, J. A., K. X. Whipple and G. E. Tucker (2003). "Implications of the shear stress river incision model for the timescale of postorogenic decay of topography." *Journal of Geophysical Research* **108**: 2158.
- Barbarand, J., A. Carter, I. Wood and T. Hurford (2003). "Compositional and structural control of fission-track annealing in apatite." *Chemical Geology* **198**(1-2): 107-137.
- Barnolas, A. and V. Pujalte (2004). La Cordillera Pirenaica. *Geología de España*. J. Vera. Madrid, SGE-IGME: 231-343.
- Beamud, E., M. Garcès, L. Cabrera, J. A. Munoz and Y. Almar (2003). "A middle to late Eocene continental chronostratigraphy from NE Spain." *Earth and Planetary Science Letters* **216**: 501-504.
- Beamud, E., J. A. Muñoz, P. G. Fitzgerald, S. L. Baldwin, M. Garcés, L. Cabrera and J. R. Metcalf (2011). "Magnetostratigraphy and detrital apatite fission track thermochronology in syntectonic conglomerates: constraints on the exhumation of the South-Central Pyrenees." *Basin Research* **23**(3): 309-331.
- Beaumont, C., J. A. Muñoz, J. Hamilton and P. Fullsack (2000). "Factors controlling the Alpine evolution of the central Pyrenees inferred from a comparison of observations and geodynamical models." *Journal of Geophysical Research* **105**: 8121-8145.
- Beck, C., E. Deville, E. Blanc, Y. Philippe and M. Tardy (1998). Termination of the Savoy Molasse Basin (northwestern siliciclastic accumulation (Upper Marine Molasse) in the southern Alps/southern Jura). *Cenozoic Foreland Basins of Western Europe*. A. Mascle, C. Puigdefàbregas, H. P. Luterbacher and M. Fernández. **Geological Society, London, Special Publication, 134**: 263-278.
- Bond, R. and K. McClay (1995). Inversion of a Lower Cretaceous extensional basin, south central Pyrenees, Spain. *Basin Inversion*. J. Buchanan, Buchanan, P., Geological Society of London Special Publications. **88**: 415-431.
- Bonnet, C., J. Malavieille and J. Mosar (2007). "Interactions between tectonics, erosion, and sedimentation during the recent evolution of the Alpine orogen: Analogue modeling insights." *Tectonics* **26**(6): TC6016.
- Boyer, S. E. (1995). "Sedimentary basin taper as a factor controlling the geometry and advance of thrust belts." *Am J Sci* **295**(10): 1220-1254.
- Boyer, S. E. and D. Elliott (1982). "Thrust systems." *AAPG Bulletin* **66**(9): 1196-1230.
- Braun, J. (2003). "Pecube: a new finite-element code to solve the 3D heat transport equation including the effects of a time-varying finite amplitude surface topography." *Computers & Geosciences* **29**: 787-794.
- Braun, J., P. A. van der Beek, P. Valla, X. Robert, F. Herman, C. Glotzbach, V. Pedersen, C. Perry, T. Simon-Labric and C. Prigent (in review). "Quantifying rates of landscape evolution and tectonic processes by thermochronology and numerical modeling of heat transport in the crust using PECUBE." *Tectonophysics*.
- Burbank, D. W. and R. S. Anderson (2005). *Tectonic Geomorphology*, Blackwell Science.

- Burbank, D. W., C. Puigdefabregas and J. A. Muñoz (1992a). "The chronology of the Eocene tectonic and stratigraphic development of the eastern Pyrenean foreland basin, northeast Spain." *Geological Society of America Bulletin* **104**: 1101-1120.
- Burbank, D. W., J. Vergés, J. A. Muñoz and P. Benthams (1992b). "Coeval hindward- and forward-imbricating thrusting in the south-central Pyrenees, Spain: Timing and rates of shortening and deposition." *Geological Society of America Bulletin* **104**: 3-17.
- Butler, R. W. H., S. Mazzoli, S. Corrado, M. De Donatis, D. Di Bucci, R. Gambini, G. Naso, C. Nicolai, D. Scrocca, P. Shiner and V. Zucconi (2004). Applying thick-skinned tectonic models to the Apennine thrust belt of Italy—Limitations and implications. *Thrust tectonics and hydrocarbon systems*. K. R. McClay. **82**: 647– 667.
- Camara, P. (1997). "The Basque-Cantabrian basin's Mesozoic tectono-sedimentary evolution." *Mém. Soc. géol. France* **171**: 187-191.
- Capote, R., J. A. Muñoz, J. L. Simón, C. L. Liesa and L. E. Arlegui (2002). Alpine tectonics I: the Alpine system north of the Betic Cordillera. *The Geology of Spain*. W. Gibbon and T. Moreno. London, The Geological Society: 367–400.
- Carlson, W. D., R. A. Donelick and R. A. Ketcham (1999). "Variability of apatite fission-track annealing kinetics; I, Experimental results." *American mineralogist* **84**(9): 1213-1223.
- Carretier, S. and F. Lucazeau (2005). "How does alluvial sedimentation at range fronts modify the erosional dynamics of mountain catchments?" *Basin Research* **17**: 361-381.
- Carrière, K. L. (2006). Neoproterozoic to Holocene tectonothermal evolution of the southern Cantabrian Mountains NW Iberia, revealed by apatite fission-track thermochronology. Geologisch-Paläontologisches Institut. Heidelberg, Ruprecht-Karl Universität Heidelberg. **PhD**: 289.
- Carslaw, H. S. and C. J. Jaeger (1959). *Conduction of Heat in Solids, 3rd Edition.*, Clarendon Press, Oxford.
- Casas-Sainz, A. M. and G. de Vicente (2009). "On the tectonic origin of Iberian topography." *Tectonophysics* **474**(1-2): 214-235.
- Cavagnetto, C. and P. Anadón (1996). "Preliminary palynological data on floristic and climatic changes during the Middle Eocene-Early Oligocene of the eastern Ebro Basin, northeast Spain." *Review of Paleobotany and Palynology* **92**: 281-305.
- Chapple, W. M. (1978). "Mechanics of thin-skinned fold-and-thrust belts." *Geological Society of America Bulletin* **89**(8): 1189-1198.
- Choukroune, P. and ECORS Team (1989). "The ECORS Pyrenean deep seismic profile reflection data and the overall structure of an orogenic belt." *Tectonics* **8**: 23-39.
- Cloetingh, S., E. Burov, F. Beekman, B. Andeweg, P. A. M. Andriessen, D. Garcia-Castellanos, G. de Vicente and R. Vegas (2002). "Lithospheric folding in Iberia." *Tectonics* **21**(5): 1041.
- Cole, F., K. J. Bird, J. Toro, F. Roure, P. B. O'Sullivan, M. Pawlewicz and D. G. Howell (1997). "An integrated model for the tectonic development of the frontal Brooks Range and Colville Basin 250 km west of the Trans-Alaska Crustal Transect." *Journal of Geophysical Research* **102**(B9): 20685-20708.

- Coney, P. J., J. A. Muñoz, K. R. McClay and C. A. Evnechick (1996). "Syntectonic burial and post-tectonic exhumation of the southern Pyrenees foreland fold-thrust belt." *Journal of the Geological Society, London* **153**(1): 9-16.
- Costa, E., M. Garces, M. Lopez-Blanco, E. Beamud, M. Gomez-Paccard and J. Cruz Larrasoana (2009). "Closing and continentalization of the South Pyrenean foreland basin (NE Spain): magnetochronological constrains." *Basin Research* **22**(6): 904-917.
- Coxall, H. K., P. A. Wilson, H. Palike, C. H. Lear and J. Backman (2005). "Rapid stepwise onset of Antarctic glaciation and deeper calcite compensation in the Pacific Ocean." *Nature* **433**(7021): 53-57.
- Dahlen, F. A. (1984). "Noncohesive critical Coulomb wedges: An exact solution." *Journal of Geophysical Research* **89**(B12): 10125-10133.
- Dahlen, F. A. (1990). "Critical taper model of fold-and-thrust belts and accretionary wedges." *Annual Review of Earth and Planetary Sciences* **18**(1): 55-99.
- Dahlen, F. A., J. Suppe and D. Davis (1984). "Mechanics of fold-and-thrust belts and accretionary wedges:cohesive Coulomb theory." *Journal of Geophysical Research* **89**(B12): 10087-10101.
- Davis, D., J. Suppe and F. A. Dahlen (1983). "Mechanics of fold-and-thrust belts and accretionary wedges." *Journal of Geophysical Research* **88**: 1153-1172.
- de Vicente, G., R. Vegas, A. Muñoz Martín, P. G. Silva, P. Andriessen, S. Cloetingh, J. M. González Casado, J. D. Van Wees, J. Alvarez, A. Carbó and A. Olaiz (2007). "Cenozoic thick-skinned deformation and topography evolution of the Spanish Central System." *Global and Planetary Change* **58**(1-4): 335-381.
- DeCelles, P. and K. A. Giles (1996). "Foreland basin systems." *Basin Research*(8): 105-123.
- DeCelles, P. and B. K. Horton (2003). "Early to middle Tertiary foreland basin development and the history of Andean crustal shortening in Bolivia." *Geological Society of America Bulletin* **115**(1): 58-77.
- Dempster, T. J. and C. Persano (2006). "Low-temperature thermochronology: Resolving geotherm shapes or denudation histories?" *Geology* **34**(2): 73-76.
- Densmore, A. L., P. A. Allen and G. Simpson (2007). "Development and response of a coupled catchment fan system under changing tectonic and climatic forcing." *Journal of Geophysical Research* **112**(F1): F01002.
- Desegaulx, P. and I. Moretti (1988a). "Subsidence history of the Ebro basin." *Journal of Geodynamics*(10): 9-24.
- Desegaulx, P. and I. Moretti (1988b). "Subsidence history of the Ebro basin." *Journal of Geodynamics* **10**: 9-24.
- Dumitru, T. A. (1993). "A new computer-automated microscope stage system for fission-track analysis." *Nucl. Tracks Radiat. Meas.* **21**(4): 575-580.
- ECORS Pyrenees Team (1988). "The ECORS deep seismic profile reflection survey across the Pyrenees." *Nature* **331**: 508-811.

- Elliott, D. (1976). "The motion of thrust sheets." *Journal of Geophysical Research* **81**(5): 949-963.
- Espina, R. G., G. De Vicente and A. Muñoz Martin (1996). "Análisis poblacional de fallas alpinas en el borde occidental de la Cuenca Vasco-Cantábrica (Cordillera Cantábrica, NO de España)." *Geogaceta* **20**(4): 936-938.
- Evans, N. J., J. P. Byrne, J. T. Keegan and L. E. Dotter (2005). "Determination of uranium and thorium in zircon, apatite, and fluorite: Application to laser (U-Th)/He thermochronology." *Journal of Analytical Chemistry* **60**(12): 1300-1307.
- Farley, K. A. (2000). "Helium diffusion from apatite: general behavior as illustrated by Durango fluorapatite." *J. Geophys. Res.*(105): 2903-2914.
- Farley, K. A. (2002). (U-Th)/He Dating: Techniques, Calibrations, and Applications. *Mineralogy and Geochemistry : Noble Gases in Geochemistry and Cosmochemistry*. D. Porcelli, C. J. Ballentine and R. Wieler. Washington D.C., Mineralogical Society of America. **47**: 819-844.
- Farley, K. A., R. A. Wolf and L. T. Silver (1996). "The effects of long alpha-stopping distances on (U-Th)/He ages." *Geochimica et cosmochimica acta* **60**(21): 4223-4229.
- Fernández-Suárez, J., G. R. Dunning, G. A. Jenner and G. Gutiérrez-Alonso (2000). "Variscan collisional magmatism and deformation in NW Iberia: constraints from U-Pb geochronology of granitoids." *Journal of the Geological Society of London* **157**: 565-576.
- Fernández-Viejo, G., J. Gallart, J. A. Pulgar, D. Córdoba and J. J. Dañobeitia (2000). "Seismic signature of Variscan and Alpine tectonics in NW Iberia: Crustal structure of the Cantabrian Mountains and Duero basin." *Journal of Geophysical Research* **105**(B2): 3001-3018.
- Fernández-Viejo, G., J. Gallart, J. A. Pulgar, J. Gallastegui, J. J. Dañobeitia and D. Córdoba (1998). "Crustal transition between continental and oceanic domains along the North Iberian Margin from wide angle seismic and gravity data." *Geophys. Res. Lett.* **25**(23): 4249-4252.
- Fernández, M., I. Marzán, A. Correia and E. Ramalho (1998). "Heat flow, heat production, and lithospheric thermal regime in the Iberian Peninsula." *Tectonophysics* **291**(1-4): 29-53.
- Filleaudeau, P. Y., F. Mouthereau and R. Pik (2011). "Thermo-tectonic evolution of the south-central Pyrenees from rifting to orogeny: insights from detrital zircon U/Pb and (U-Th)/He thermochronometry " *Basin Research* **in press**.
- Fitzgerald, P. G., S. L. Baldwin, L. E. Webb and P. B. O'Sullivan (2006). "Interpretation of (U-Th)/He single grain ages from slowly cooled crustal terranes: A case study from the Transantarctic Mountains of southern Victoria Land." *Chemical Geology* **225**(1-2): 91-120.
- Fitzgerald, P. G., J. A. Muñoz, P. J. Coney and S. L. Baldwin (1999). "Asymmetric exhumation across the Pyrenean orogen: implications for the tectonic evolution of a collisional orogen." *Earth and Planetary Science Letters* **173**: 157-170.
- Flemings, P. B. and T. E. Jordan (1989). "A synthetic stratigraphic model of foreland basin development." *Journal of Geophysical Research* **94**: 3851-3866.

- Flowers, R. M., R. A. Ketcham, D. L. Shuster and K. A. Farley (2009). "Apatite (U-Th)/He thermochronometry using a radiation damage accumulation and annealing model." *Geochimica et Cosmochimica Acta* **73**(8): 2347-2365.
- Flück, P., R. D. Hyndman and C. Lowe (2003). "Effective elastic thickness T_e of the lithosphere in western Canada." *Journal of Geophysical Research* **108**(B9): 2430.
- Ford, M. (2004). "Depositional wedge tops: interaction between low basal friction external orogenic wedges and flexural foreland basins." *Basin Research* **16**(3): 361-375.
- Friend, P. F., M. J. Lloyd, R. McElroy, J. Turner, A. Van Gelder and S. J. Vincent (1996). Evolution of the central part of the northern Ebro basin margin, as indicated by its Tertiary fluvial sedimentary infill. *Tertiary basins of Spain*. C. J. D. P.F. Friend, Cambridge University press: 166-172.
- Fullsack, P. (1995). "An arbitrary Lagrangian-Eulerian formulation for creeping flows and its application in tectonic models." *Geophys. J. Int.* **120**: 1-23.
- Galbraith, R. F. and P. F. Green (1990). "Estimating the component ages in a finite mixture." *Nuclear Tracks and Radiation Measurements* **17**(3): 197-206.
- Galbraith, R. F. and G. M. Laslett (1993). "Statistical models for mixed fission track ages." *Nuclear Tracks and Radiation Measurements* **21**(4): 459-470.
- Gallagher, K. (2011). "Transdimensional inverse thermal history modelling for quantitative thermochronology." *Journal of Geophysical Research* **in press**.
- Gallagher, K., K. Charvin, S. Nielsen, M. Sambridge and J. Stephenson (2009). "Markov chain Monte Carlo (MCMC) sampling methods to determine optimal models, model resolution and model choice for Earth Science problems." *Marine and Petroleum Geology* **26**(4): 525-535.
- Gallastegui, J. (2000). "Estructura cortical de la cordillera y margen continental cantabricos: perfiles ESCI-N." *Trabajos de Geología* **22**: 234.
- Garcia-Castellanos, D. (2007). "The role of climate during high plateau formation. Insights from numerical experiments." *Earth and Planetary Science Letters* **257**(3-4): 372-390.
- Garcia-Castellanos, D., J. Vergés, J. Gaspar-Escribano and S. Cloetingh (2003). "Interplay between tectonics, climate, and fluvial transport during the Cenozoic evolution of the Ebro Basin (NE Iberia)." *Journal of Geophysical Research* **108**(B7): 2347, doi:10.1029/2002JB002073.
- Garcia-Ramos, J. C. and M. Gutierrez-Claveral (1995). La cobertura Mesozoico-Terciaria. *Geología de Asturias*. Trea. Gijón, C. Aramburu, F. Bastida.
- Gaspar-Escribano, J. M., J. D. Van Wees, M. Ter Voorde, S. Cloetingh, E. Roca, L. Cabrera, J. A. Muñoz, P. A. Ziegler and D. Garcia-Castellanos (2001). "Three-dimensional flexural modelling of the Ebro Basin (NE Iberia)." *Geophysical Journal International* **145**(2): 349-367.
- Gautheron, C. and L. Tassan-Got (2010). "A Monte Carlo approach of diffusion applied to noble gas/helium thermochronology." *Chemical Geology* **273**: 212-224.

- Gautheron, C., L. Tassan-Got, J. Barbarand and M. Pagel (2009). "Effect of alpha-damage annealing on apatite (U-Th)/He thermochronology." *Chemical Geology* **266**(3-4): 157-170.
- Gautheron, C., L. Tassan-Got and K. A. Farley (2006). "(U-Th)/Ne chronometry." *Earth Planet. Sci. Lett.* **243**: 520-535.
- Gibson, M., H. D. Sinclair, G. J. Lynn and F. M. Stuart (2007). "Late- to post-orogenic exhumation of the Central Pyrenees revealed through combined thermochronological data and modelling." *Basin Research* **19**(3): 323-334.
- Glotzbach, C., P. A. van der Beek and C. Spiegel (2011). "Episodic exhumation and relief growth in the Mont Blanc massif, Western Alps from numerical modelling of thermochronology data." *Earth and Planetary Science Letters* **304**(3-4): 417-430.
- Gomez-Fernandez, F., R. A. Both, J. Mangas and A. Arribas (2000). "Metallogenesis of Zn-Pb carbonate-hosted mineralization in the southeastern region of the picos de europa (Central Northern Spain) province: geologic, fluid inclusion, and stable isotope studies." *Economic Geology* **95**(1): 19-40.
- Green, P. F., P. V. Crowhurst, I. R. Duddy, P. Japsen and S. P. Holford (2006). "Conflicting (U-Th)/He and fission track ages in apatite: Enhanced He retention, not anomalous annealing behaviour." *Earth and Planetary Science Letters* **250**(3-4): 407-427.
- Green, P. F. and I. R. Duddy (2006). "Interpretation of apatite (U-Th)/He ages and fission track ages from cratons." *Earth and Planetary Science Letters* **244**(3-4): 541-547.
- Green, P. F., I. R. Duddy, A. J. W. Gleadow, P. R. Tingate and G. M. Laslett (1986). "Thermal annealing of fission tracks in apatite: 1. A qualitative description." *Chemical Geology: Isotope Geoscience section* **59**: 237-253.
- Grobe, R. W., J. Alvarez-Marrón, U. A. Glasmacher and R. Menéndez-Duarte (2010). "Low-temperature exhumation history of Variscan-age rocks in the western Cantabrian Mountains (NW Spain) recorded by apatite fission-track data." *Tectonophysics* **489**(1-4): 76-90.
- Gunnell, Y. and M. Calvet (2006). "Comment on "Origin of the highly elevated Pyrenean peneplain" by Julien Babault, Jean Van Den Driessche, Stéphane Bonnet, Sébastien Castelltort, and Alain Crave." *Tectonics* **25**.
- Gunnell, Y., M. Calvet, S. Bricau, A. Carter, J.-P. Aguilar and H. Zeyen (2009). "Low long-term erosion rates in high-energy mountain belts: Insights from thermo- and biochronology in the Eastern Pyrenees." *Earth and Planetary Science Letters* **278**(3-4): 208-218.
- Hardy, S., C. Duncan, J. Masek and D. Brown (1998). "Minimum work, fault activity and the growth of critical wedges in fold and thrust belts." *Basin Research* **10**: 365-373.
- Hendriks, B. W. H. and T. F. Redfield (2005). "Apatite fission track and (U-Th)/He data from Fennoscandia: An example of underestimation of fission track annealing in apatite." *Earth and Planetary Science Letters* **236**(1-2): 443-458.
- Herrero, A., G. Alonso-Gavilán and J. R. Colmenero (2010). "Depositional sequences in a foreland basin (north-western domain of the continental Duero basin, Spain)." *Sedimentary geology* **223**: 235-264.

- Hippolyte, J. C., D. Badescu and P. Constantin (1999). "Evolution of the transport direction of the Carpathian belt during its collision with the east European Platform." *Tectonics* **18**(6): 1120-1138.
- Horton, B. K. (1998). "Sediment accumulation on top of the Andean orogenic wedge: Oligocene to late Miocene basins of the Eastern Cordillera, southern Bolivia." *Geological Society of America Bulletin* **110**(9): 1174-1192.
- Hoth, S., A. Hoffmann-Rothe and N. Kukowski (2007a). "Frontal accretion: An internal clock for bivergent wedge deformation and surface uplift." *Journal of Geophysical Research* **112**.
- Hoth, S., A. Hoffmann-Rothe and N. Kukowski (2007b). "Frontal accretion: An internal clock for bivergent wedge deformation and surface uplift." *Journal of Geophysical Research* **112**: B06408.
- Huiqi, L., K. R. McClay and D. Powell (1992). Physical models of thrust wedges. *Thrust tectonics*. K. R. McClay, Chapman & Hall: 71-81.
- Huismans, R. S. and C. Beaumont (2003). "Symmetric and asymmetric lithospheric extension: Relative effects of frictional-plastic and viscous strain softening." *J. Geophys. Res.* **108**(B10): 2496.
- Huismans, R. S. and C. Beaumont (2007). Roles of lithospheric strain softening and heterogeneity in determining the geometry of rifts and continental margins. *Imaging, Mapping and Modelling Continental Lithosphere Extension and Breakup*. G. D. Karner, Manatschal, G., & Pinheiro, L.M. , Geological Society, London, Special Publications: 107-134.
- Hurford, A. J. and P. F. Green (1983). "The zeta age calibration of fission-track dating." *Chemical Geology* **41**: 285-317.
- Hurford, A. J. and K. Hammerschmidt (1985). "⁴⁰Ar/³⁹Ar and K/Ar dating of the Bishop and Fish Canyon Tuffs: Calibration ages for fission-track dating standards." *Chemical Geology: Isotope Geoscience section* **58**(1-2): 23-32.
- Huyghe, D., F. Mouthereau, S. Castelltort, P. Y. Filleaudeau and L. Emmanuel (2009). "Paleogene propagation of the southern Pyrenean thrust wedge revealed by finite strain analysis in frontal thrust sheets: Implications for mountain building." *Earth and Planetary Science Letters*(288): 421-433.
- ICC (2002). Mapa geològic de Catalunya 1:250 000. I. C. d. Catalunya.
- Jammes, S., G. Manatschal, L. Lavie and E. Masini (2009). "Tectonosedimentary evolution related to extreme crustal thinning ahead of a propagating ocean: Example of the western Pyrenees." *Tectonics* **28**: TC4012.
- Johnson, D. D. and C. Beaumont (1995a). Preliminary Results from a Planform Kinematic Model of Orogen Evolution, Surface Processes and the Development of Clastic Foreland Basin Stratigraphy. *Stratigraphic Development in Foreland Basins*. S. L. Dorobek and G. M. Ross, Soc. Econ. Paleont. Mineral. Spec. Publ. **52**: 3-24.
- Johnson, D. D. and C. Beaumont (1995b). Preliminary results from a planform kinematic model of orogen evolution, surface processes and the development of clastic foreland basin stratigraphy. *Stratigraphic development in foreland basins*. S. L. Dorobek and G. M. Ross, Soc. Econ. Paleont. Mineral. Spec. Publ., **52**: 3-24.

- Jolivet, M., P. Labaume, P. Monié, M. Brunel, N. Arnaud and M. Campani (2007). "Thermochronology constraints for the propagation sequence of the south Pyrenean basement thrust system (France-Spain)." *Tectonics* **26**.
- Jones, S. J. (2004). "Tectonic controls on drainage evolution and development of terminal alluvial fans, southern Pyrenees, Spain." *Terra Nova* **16**(3): 121-127.
- Julivert, M. (1971). "Decollement tectonics in the Hercynian Cordillera of Northwest Spain." *American Journal of Science* **270**(1): 1-29.
- Katz, M. E., K. G. Miller, J. D. Wright, B. S. Wade, J. V. Browning, B. S. Cramer and Y. Rosenthal (2008). "Stepwise transition from the Eocene greenhouse to the Oligocene icehouse." *Nature Geosci* **1**(5): 329-334.
- Ketcham, R. A. (2005). Forward and reverse modeling of low-temperature thermochronology data. *Low-Temperature Thermochronology: Techniques, Interpretations and Applications*. P. W. R. T. A. Ehlers, Rev. Mineral. Geochem. **58**: 275-314.
- Ketcham, R. A., A. Carter, R. A. Donelick, J. Barbarand and A. J. Hurford (2007). "Improved modeling of fission-track annealing in apatite." *American Mineralogist* **92**: 789-798.
- Kooi, H. and C. Beaumont (1996). "Large-scale geomorphology: Classical concepts reconciled and integrated with contemporary ideas via a surface processes model." *Journal of Geophysical Research* **101**(B2): 3361-3386.
- Kraml, M., R. Pik, M. Rahn, R. Selbekk, J. Carignan and J. Keller (2006). "A new multi-mineral age reference material for $^{40}\text{Ar}/^{39}\text{Ar}$, (U-Th)/He and fission track dating methods: The Limberg t3 tuff." *Geostandards and Geoanalytical Research* **30**(2): 73-86.
- Krijgsman, W., F. J. Hilgen, I. Raffi, F. J. Sierro and D. S. Wilson (1999). "Chronology, causes and progression of the Messinian salinity crisis." *Nature* **400**(6745): 652-655.
- Lear, C. H., T. R. Bailey, P. N. Pearson, H. K. Coxall and Y. Rosenthal (2008). "Cooling and ice growth across the Eocene-Oligocene transition." *Geology* **36**(3): 251-254.
- Lepvrier, C. and E. Martinez-Garcia (1990). "Fault development and stress evolution of the post-Hercynian Asturian Basin (Asturias and Cantabria, northwestern Spain)." *Tectonophysics* **184**(3-4): 345-356.
- Loget, N. and J. Van den Driessche (2009). "Wave Train Model for Knickpoint Migration." *Geomorphology* **106**: 376-382.
- Malavieille, J. (2010). "Impact of erosion, sedimentation, and structural heritage on the structure and kinematics of orogenic wedges: Analog models and case studies." *GSA Today* **20**(1): 4-10.
- Marshak, S. and M. S. Wilkerson (1992). "Effect of overburden thickness on thrust belt geometry and development." *Tectonics* **11**(3): 560-566.
- Martin-Gonzalez, F., L. Barbero, R. Capote, N. Heredia and G. Gallastegui (2011). "Interaction of two successive Alpine deformation fronts: constraints from low-temperature thermochronology and structural mapping (NW Iberian Peninsula)." *International Journal of Earth Sciences*: 1-12.

- Martin-Gonzalez, F. and N. Heredia (2011). "Complex tectonic and tectonostratigraphic evolution of an Alpine foreland basin: The western Duero Basin and the related Tertiary depressions of the NW Iberian Peninsula." *Tectonophysics* **502**(1-2): 75-89.
- Maurel, O., P. Moniè, R. Pik, N. Arnaud, M. Brunel and M. Jolivet (2007). "The Meso-Cenozoic thermo-tectonic evolution of the Eastern Pyrenees: an Ar/Ar fission track and (U-Th)/He thermochronological study of the Canigou and Mont-Louis massifs." *International Journal Earth Sciences* **97**: 565-584.
- Mayayo, M., J., A. Yuste, A. Luzon and B. Bauluz (2011). "Clay mineral assemblages as palaeoclimatic indicators in a shallowing carbonate lacustrine system: Oligocene-Miocene, central Ebro Basin (NE Spain)." *Clay Minerals* **46**: 355-370.
- McDowell, F. W., W. C. McIntosh and K. A. Farley (2005). "A precise ^{40}Ar - ^{39}Ar reference age for the Durango apatite (U-Th)/He and fission-track dating standard." *chemical geology* **214**(3-4): 249-263.
- McMillan, M. E., P. L. Heller and S. L. Wing (2006). "History and causes of post-Laramide relief in the Rocky Mountain orogenic plateau." *Geological Society of America Bulletin* **118**(3-4): 393-405.
- Mediavilla, R., C. J. Dabrio, A. Martin-Serrano and J. L. Santisteban (1996). Lacustrine neogene systems of the Duero Basin: evolution and controls. *Tertiary basins of Spain : the stratigraphic record of crustal kinematics*. P. F. Friend and C. J. Dabrio, Cambridge University Press: 228-236.
- Meesters, A. G. C. A. and T. J. Dunai (2002). "Solving the production–diffusion equation for finite diffusion domains of various shapes Part I. Implications for low-temperature (U–Th)/He thermochronology." *chemical geology*(186): 333-344.
- Meigs, A. J. and D. W. Burbank (1997). "Growth of the South Pyrenean orogenic wedge." *Tectonics* **16**(2): 239-258.
- Meigs, A. J., J. Verges and D. W. Burbank (1996). "Ten-million-year history of a thrust sheet." *Geological Society of America Bulletin* **108**(12): 1608-1625.
- Mellere, D. (1993). Thrust-Generated, Back-Fill Stacking of Alluvial Fan Sequences, South-Central Pyrenees, Spain (La Pobla De Segur Conglomerates). *Tectonic Controls and Signatures in Sedimentary Successions*, Blackwell Publishing Ltd.: 259-276.
- Metcalf, J. R., P. G. Fitzgerald, S. L. Baldwin and J. A. Munoz (2009). "Thermochronology of a convergent orogen: Constraints on the timing of thrust faulting and subsequent exhumation of the Maladeta Pluton in the Central Pyrenean Axial Zone." *Earth and Planetary Science Letters* **287**(3-4): 488-503.
- Molnar, P. (2004). "Late Cenozoic increase in accumulation rates of terrestrial sediment: How might climate change have affected erosion rates?" *Annual Review of Earth and Planetary Sciences* **32**(1): 67-89.
- Molnar, P. and P. England (1990). "Late Cenozoic uplift of mountain ranges and global climate change: chicken or egg?" *Nature* **346**(6279): 29.
- Morris, R. G., H. D. Sinclair and A. J. Yelland (1998). "Exhumation of the Pyrenean orogen: Implications for sediment discharge." *Basin Research* **10**: 69-86.

- Mugnier, J. L., P. Baby, B. Colletta, P. Vinour, P. Bale and P. Leturmy (1997). "Thrust geometry controlled by erosion and sedimentation: A view from analogue models." *Geology* **25**(5): 427-430.
- Muñoz, J. A. (1992). Evolution of a continental collision belt: ECORS Pyrenees crustal balanced cross section. *Thrust Tectonics*. K. R. McClay. London, Chapman & Hall: 235-246.
- Naylor, M. and H. D. Sinclair (2007). "Punctuated thrust deformation in the context of doubly vergent thrust wedges: Implications for the localization of uplift and exhumation." *Geology* **35**(6): 559-562.
- Nelson, C. H. and A. Maldonado (1990). "Factors controlling late Cenozoic continental margin growth from the Ebro Delta to the western Mediterranean deep sea." *Marine Geology* **95**: 419-440.
- Nunn, J. A., M. Czerniak and R. H. J. Pilger (1987). "Constraints on the structure of Brooks Range and Colville Basin, Northern Alaska, from flexure and gravity analysis." *Tectonics* **6**(5): 603-617.
- O'Sullivan, P. B., J. M. Murphy and A. E. Blythe (1997). "Late Mesozoic and Cenozoic thermotectonic evolution of the central Brooks Range and adjacent North Slope foreland basin, Alaska: Including fission track results from the Trans-Alaska Crustal Transect (TACT)." *Journal of Geophysical Research* **102**(B9): 20821-20845.
- Olivet, J.-L. (1996). "La cinématique de la plaque Ibérique." *Bull. Cent. Rech. Explor. Prod. Elf Aquitaine* **20**: 131-195.
- Ollerenshaw, N. C. (1978). Geology, Calgary, Alberta-British Columbia. Geological Survey of Canada Map 1457A.
- Ori, G. G. and P. F. Friend (1984). "Sedimentary basins formed and carried piggyback on active thrust sheets." *Geology* **12**(8): 475-478.
- Pedreira, D. (2005). Estructura cortical de la zona de transición entre los Pirineos y la Cordillera Cantábrica. Oviedo, Spain, Universidad de Oviedo. **Ph.D. thesis**: 343.
- Pedreira, D., J. A. Pulgar, J. Gallart and J. Diaz (2003). "Seismic evidence of Alpine crustal thickening and wedging from the western Pyrenees to the Cantabrian Mountains (north Iberia)." *Journal of Geophysical Research* **108**(B4).
- Pedreira, D., Pulgar, J.A., Gallart, J., Torné, M. (2007). "Three-dimensional gravity and magnetic modeling of crustal indentation and wedging in the western Pyrenees-Cantabrian Mountains " *Journal of Geophysical Research* **112**(B12405).
- Pérez-Estaún, A., F. Bastzda, J. L. Alonso, J. Marqufnez, J. Aller, J. Alvarez-Marron, A. Marcos and J. A. Pulgar (1988). "A thin-skinned tectonics model for an arcuate fold and thrust belt : the cantabrian zone (variscan ibero-armoric arc)." *Tectonics* **7**(3): 517-537.
- Pérez-Rivarés, F. J., M. Garcés, C. Arenas and G. Pardo (2004). "Magnetostratigraphy of the Miocene continental deposits of the Montes de Castejón (central Ebro basin, Spain): geochronological and paleoenvironmental implications." *Geologica Acta* **2**(3): 221-234.
- Persano, C., F. M. Stuart, P. Bishop and D. N. Barfod (2002). "Apatite (U-Th)/He age constraints on the development of the Great Escarpment on the southeastern Australian passive margin." *Earth and Planetary Science Letters* **200**(1-2): 79-90.

- Persson, K. S., D. Garcia-Castellanos and D. Sokoutis (2004). "River transport effects on compressional belts: First results from an integrated analogue-numerical model." *Journal of Geophysical Research* **109**(B1): B01409, doi:10.1029/2002JB002274.
- Puigdefàbregas, C., J. A. Muñoz and J. Vergés (1992). Thrusting and foreland basin evolution in the southern Pyrenees. *Thrust Tectonics*. K. R. McClay. London, Chapman & Hall: 247-254.
- Puigdefàbregas, C. and P. Souquet (1986). "tectosedimentary cycles and depositional sequences of the Mesozoic and tertiary from the Pyrenees." *tectonophysics* **129**: 173-203.
- Pulgar, J. A., J. L. Alonso, R. G. Espina and J. A. Marín (1999). "La deformación alpina en el basamento varisco de la Zona Cantábrica." *Trabajos de Geología, Universidad de Oviedo* **21**: 283-294.
- Pulgar, J. A., J. Gallart, G. Fernandez-Viejo, A. Perez-Estaun, J. Alvarez-Marron and E. Group (1996). "Seismic image of the Cantabrian Mountains in the western extension of the Pyrenees from integrated ESCIN reflection and refraction data." *Tectonophysics* **264**(1-4): 1-19.
- Pulgar, J. A., J. Pérez-Estaun, J. Gallart, J. Alvarez-Marron, J. Gallastegui, J. L. Alonso and E. Group (1997). "The ESCI-N2 deep seismic reflection profile: A traverse across the Cantabrian Mountains and adjacent Duero basin." *Rev. Soc. Geol. Esp.* **8**(4): 383-394.
- Rahl, J. M., S. H. Haines and B. A. van der Pluijm (2011). "Links between orogenic wedge deformation and erosional exhumation: Evidence from illite age analysis of fault rock and detrital thermochronology of syn-tectonic conglomerates in the Spanish Pyrenees." *Earth and Planetary Science Letters* **307**(1-2): 180-190.
- Reiners, P. W., K. A. Farley and H. J. Hickes (2002). "He diffusion and (U-Th)/He thermochronometry of zircon: initial results from Fish Canyon Tuff and Gold Butte." *Tectonophysics* **349**(1-4): 297-308.
- Reiners, P. W., T. L. Spell, S. Nicolescu and K. A. Zanetti (2004). "Zircon (U-Th)/He thermochronometry: He diffusion and comparisons with ⁴⁰Ar/³⁹Ar dating." *Geochimica et cosmochimica acta* **68**(8): 1857-1887.
- cuenca terciaria del Ebro. *Libro Jubilar J. M. Ríos, Geología de España*. J. Comba. Madrid (Spain), Instituto Geológico y Minero de España: 131–159.
- Roest, W. R. and S. P. Srivastava (1991). "Kinematics of the plate boundaries between Eurasia, Iberia, and Africa in the North Atlantic from the Late Cretaceous to the present." *Geology* **19**(6): 613-616.
- Roure, F., P. Choukroune, X. Berastegui, J. A. Muñoz, A. Villien, P. Matheron, M. Bareyt, M. Seguret, P. Camara and J. Deramond (1989). "ECORS deep seismic data and balanced cross sections: geometric constraints on the evolution of the Pyrenees." *Tectonics* **8**(1): 41-50.
- Royden, L. and G. D. Karner (1984). "Flexure of Lithosphere Beneath Apennine and Carpathian Foredeep Basins: Evidence for an Insufficient Topographic Load." *AAPG Bulletin* **68**.

- Sambridge, M. (1999a). "Geophysical inversion with a neighbourhood algorithm-II.Appraising the ensemble." *geophysical Journal International* **138**: 727-746.
- Sambridge, M. (1999b). "Geophysical inversion with a neighbourhood algorithm—I.Searching a parameter space." *geophysical Journal International* **138**: 479-494.
- Santisteban, J. L., R. Mediavilla, A. Martin-Serrano and C. J. Dabrio (1996). The Duero Basin: a general overview. *Tertiary basins of Spain : the stratigraphic record of crustal kinematics*. P. F. Friend and C. J. Dabrio, Cambridge University Press: 183-187.
- Saura, E. and A. Teixell (2006). "Inversion of small basins: effects on structural variations at the leading edge of the Axial Zone antiformal stack (Southern Pyrenees, Spain)." *journal of structural geology* **28**(11): 1909-1920.
- Schmitz, B. and V. Pujalte (2007). "Abrupt increase in seasonal extreme precipitation at the Paleocene-Eocene boundary." *Geology* **35**(3): 215-218.
- Seguret, M. (1972). Etude tectonique des nappes et séries décollés de la partie centrale du versant sud des Pyrénées. Caractère synsédimentaire, rôle de la compression et de la gravité., Université de Montpellier: 210.
- Shuster, D. L. and K. A. Farley (2009). "The influence of artificial radiation damage and thermal annealing on helium diffusion kinetics in apatite." *Geochimica et cosmochimica acta* **73**(1): 183-196.
- Shuster, D. L., R. M. Flowers and K. A. Farley (2006). "The influence of natural radiation damage on helium diffusion kinetics in apatite." *Earth and Planetary Science Letters* **249**(3-4): 148-161.
- Sibuet, J.-c., S. P. Srivastava and W. Spakman (2004). "Pyrenean orogeny and plate kinematics." *Journal of Geophysical Research* **109**(B08104).
- Simpson, G. D. H. (2006). "Modelling interactions between fold-thrust belt deformation, foreland flexure and surface mass transport." *Basin Research* **18**: 125-143.
- Sinclair, H. D., B. J. Coakley, P. A. Allen and A. B. Watts (1991). "Simulation of Foreland Basin Stratigraphy using a diffusion model of mountain belt uplift and erosion: An example from the central Alps, Switzerland." *Tectonics* **10**(3): 599-620.
- Sinclair, H. D., M. Gibson, G. Lynn and F. Stuart (2009). "The evidence for a Pyrenean resurrection: a response to Babault et al. (2008)." *Basin Research* **21**(1): 143-145.
- Sinclair, H. D., M. Gibson, M. Naylor and R. G. Morris (2005). "Asymmetric growth of the Pyrenees revealed through measurement and modeling of orogenic fluxes." *American Journal of Science* **305**: 369-406.
- Sobel, E. R., G. E. Hilley and M. R. Strecker (2003). "Formation of internally drained contractional basins by aridity-limited bedrock incision." *Journal of Geophysical Research* **108**(B7): 2344, doi:10.1029/2002JB001883.
- Spiegel, C., B. Kohn, D. Belton, Z. Berner and A. Gleadow (2009). "Apatite (U-Th-Sm)/He thermochronology of rapidly cooled samples: The effect of He implantation." *Earth and Planetary Science Letters* **285**(1-2): 105-114.

- Srivastava, S. P., W. R. Roest, L. C. Kovacs, G. Oakey, S. LÃ©vesque, J. Verhoef and R. Macnab (1990). "Motion of Iberia since the Late Jurassic: Results from detailed aeromagnetic measurements in the Newfoundland Basin." *Tectonophysics* **184**(3-4): 229-260.
- Srivastava, S. P., J.-c. Sibuet, S. Cande, W. R. Roest and I. D. Reid (2000). "Magnetic evidence for slow seafloor spreading during the formation of the Newfoundland and Iberian margins." *Earth and Planetary Science Letters*(182): 61-76.
- Stephenson, J., K. Gallagher and C. C. Holmes (2006). "A Bayesian approach to calibrating apatite fission track annealing models for laboratory and geological timescales." *Geochim. Cosmochim. Acta*(70): 5183–5200.
- Stewart, R. J. and M. T. Brandon (2004). "Detrital-zircon fission-track ages for the 'Hoh Formation': Implications for late Cenozoic evolution of the Cascadia subduction wedge." *Geological Society of America Bulletin* **116**(1-2): 60-75.
- Stockmal, G. S., C. Beaumont, M. Nguyen and B. Lee (2007). Mechanics of thin-skinned fold-and-thrust belts: Insights from numerical models. *Whence the Mountains? Inquiries into the Evolution of Orogenic Systems: A Volume in Honor of Raymond A. Price*. J. W. Sears, T. A. Harms and C. A. Evenchick, Geological Society of America. **433**: 63-98.
- Storti, F. and K. McClay (1995). "Influence of syntectonic sedimentation on thrust wedges in analogue models." *Geology* **23**(11): 999-1002.
- Tagami, T., R. F. Galbraith, R. Yamada and G. M. Laslett (1998). Revised annealing kinetics of fission tracks in zircon and geological implications. *Advances in Fission-Track Geochronology*. P. Van den haute and F. De Corte. Dordrecht, Netherlands, Kluwer Academic Publishers: 99 - 112.
- Teixell, A. (1998). "Crustal structure and orogenic material budget in the west central Pyrenees." *Tectonics* **17**(3): 395–406.
- Teixell, A. (2004). Estructura cortical de la Cordillera Pireneica. *Geologia de España*. J. Vera. Madrid, Geol. de Esp., Inst., Geol. y Minero de Esp.: 320-321.
- Urgeles, R., A. Camerlenghi, D. Garcia-Castellanos, B. De Mol, M. Garcés, J. Vergés, I. Haslam and M. Hardman (2011). "New constraints on the Messinian sealevel drawdown from 3D seismic data of the Ebro Margin, western Mediterranean." *Basin Research* **23**(2): 123-145.
- Valla, P. G., F. Herman, P. A. van der Beek and J. Braun (2010). "Inversion of thermochronological age-elevation profiles to extract independent estimates of denudation and relief history -- I: Theory and conceptual model." *Earth and Planetary Science Letters* **295**(3-4): 511-522.
- Valla, P. G., P. A. van der Beek and J. Braun (2011). "Rethinking low-temperature thermochronology data sampling and modelling strategies for quantification of denudation and relief histories." *Earth and Planetary Science Letters* **in press**.
- Vera, J. (2004). *Geologia de España*. Madrid, Instituto Geológico y Minero de España.
- Vergés, J., M. Fernández and A. Martínez (2002a). "The Pyrenean orogen: pre-, syn-, and post-collisional evolution." *Journal of the Virtual Explorer* **8**: 57 - 76.
- Vergés, J., M. Marzo and J. A. Muñoz (2002b). "Growth strata in foreland settings." *Sedimentary geology* **146**(1-2): 1-9.

- Vergés, J., H. Millan, E. Roca, M. J. A., M. Marzo, J. Cites, T. Den Bezemer, R. Zoetemeijer and S. Cloetingh (1995). "Eastern Pyrenees and related foreland basins: pre-, syn- and post-collisional crustal-scale cross-sections." *Marine and Petroleum Geology* **12**(8): 893-915.
- Vergés, J. and J. A. Muñoz (1990). "thrust sequences in the southern central Pyrenees." *Bull. Societe geologique de france* **8**(2): 265-271.
- Vincent, S. J. (2001). "The Sis palaeovalley: a record of proximal fluvial sedimentation and drainage basin development in response to Pyrenean mountain building." *Sedimentology* **48**(6): 1235-1276.
- Watts, A. B. (2001). *Isostasy and Flexure of the Lithosphere*. Cambridge, Cambridge University Press.
- Whipple, K. X. (2001). "Fluvial Landscape Response Timescale: How Plausible Is Steady-State Denudation? ." *American Journal of Science* **301**: 313-325.
- Whipple, K. X. (2009). "The influence of climate on the tectonic evolution of mountain belts." *Nature Geoscience* **2**(2): 97-104.
- Whitchurch, A. L., A. Carter, H. D. Sinclair, R. A. Duller, A. C. Whittaker and P. A. Allen (2011). "Sediment routing system evolution within a diachronously uplifting orogen: Insights from detrital zircon thermochronological analyses from the South-Central Pyrenees." *American Journal of Science* **311**(5): 442-482.
- Willenbring, J. K. and F. von Blanckenburg (2010). "Long-term stability of global erosion rates and weathering during late-Cenozoic cooling." *Nature* **465**: 211-214.
- Willett, S. (1999a). "Rheological dependence of extension in wedge models of convergent orogens." *Tectonophysics* **305**(4): 419-435.
- Willett, S. (2010). "Erosion on a line." *Tectonophysics* **484**(1-4): 168-180.
- Willett, S., C. Beaumont and P. Fullsack (1993). "Mechanical model for the tectonics of doubly vergent compressional orogens." *Geology* **21**: 371-374.
- Willett, S. D. (1992). Dynamic and kinematic growth and change of a Coulomb wedge. *Thrust tectonics*. E. R. McClay. London, Chapman & Hall.
- Willett, S. D. (1999b). "Orogeny and orography: The effects of erosion on the structure of mountain belts." *Journal of Geophysical Research* **104**(B12): 28957-28981.
- Willett, S. D. and F. Schlunegger (2010). "The last phase of deposition in the Swiss Molasse Basin: from foredeep to negative-alpha basin." *Basin Research* **22**(5): 623-639.
- Wobus, C. W., G. E. Tucker and R. S. Anderson (2010). "Does climate change create distinctive patterns of landscape incision?" *Journal of Geophysical Research* **115**(F4): F04008.
- Wolf, R. A., K. A. Farley and D. M. Kass (1998). "Modeling of the temperature sensitivity of the apatite (U–Th)/ He thermochronometer." *chemical geology*(148): 105-114.
- Yelland, A. J. (1990). "Fission track thermotectonics in the Pyrenean orogen." *Nucl. Tracks Radiat. Meas.* **17**(3): 293-299.

- Zachos, J., M. Pagani, L. Sloan, E. Thomas and K. Billups (2001). "Trends, rhythms, and aberrations in global climate 65 Ma to present." *Science* **292**(5517): 686-693.
- Zeyen, H. and M. Fernández (1994). "Integrated lithospheric modeling combining thermal, gravity, and local isostasy analysis : Application to the NE Spanish Geotranssect." *Journal of Geophysical Research* **99**(B9): 18,089 - 18,102.
- Zhang, P., P. Molnar and W. R. Downs (2001). "Increased sedimentation rates and grain sizes 2-4 Myr ago due to the influence of climate change on erosion rates." *Nature* **410**: 891-897.
- Zoetemeijer, R., P. Desegaulx, S. Cloetingh, F. Roure and I. Moretti (1990a). "Lithospheric Dynamics and Tectonic-stratigraphic Evolution of the Ebro basin." *Journal of Geophysical Research* **95**(B3): 2701-2711.
- Zoetemeijer, R., P. Desegaulx, S. Cloetingh, F. Roure and I. Moretti (1990b). "Lithospheric dynamics and tectonic-stratigraphic evolution of the Ebro basin." *Journal of Geophysical Research* **95**(B3): 2701-2711.
- Zoetemeijer, R., C. Tomek and S. Cloetingh (1999). "Flexural expression of European continental lithosphere under the western outer Carpathians." *Tectonics* **18**(5): 843-861.